Hydrocracking of n-C_{16} over MFI Zeolite Nano-sheets – Effect of the Si/Al Ratio

Mohamed Habeeb Parker

Submitted in partial fulfilment of the requirements
of the degree of Master of Science in Chemical Engineering

April 2018

Supervised by:

Prof. Dr. Patricia J. Kooyman

Dr. Roald Brosius

Centre for Catalysis Research

Department of Chemical Engineering

University of Cape Town

Cape Town

South Africa

Declaration

I know the meaning of plagiarism and declare that all the work in the document, save for that which is properly acknowledged, is my own. This thesis/dissertation has been submitted to the Turnitin module (or equivalent similarity and originality checking software) and I confirm that my supervisor has seen my report and any concerns revealed by such have been resolved with my supervisor.

Name: Mohamed Habeeb Parker

Signature: Signed by candidate

Date: 20 April 2018

Acknowledgements

This project would not be possible without the contributions of many individuals and organizations. The author would like to acknowledge all involved in the successful completion of this project, specifically:

- **Prof. Dr. Patricia J. Kooyman**, project supervisor, for the opportunity to conduct this research and her time, supervision, dedication and helpful insight.
- **Dr. Roald Brosius**, project co-supervisor, for his time, supervision, assistance, dedication and helpful insight.
- **UCT Department of Chemical Engineering**, **Centre for Catalysis Research** and **c*change**, for allowing the use of their laboratories, equipment, resources and various other facilities.
- **The South African Research Chairs Initiative (SARChI)**, **National Research Foundation (NRF)**, for the financial assistance during this project.
- **Dr. Jaco Brand**, Nuclear Magnetic Resonance (NMR) Unit, Central Analytical Facilities (CAF), Stellenbosch University, for the ^{27}Al MAS SSNMR experiments.
- **Ms. Zulfa le Riche**, Analytical Laboratory, Department of Chemical Engineering, UCT, for the N_2 physisorption and ICP-OES experiments.
- **Dr. Innocent Shuro** and **Mr. Mohammed A. Jaffer**, Electron Microscope Unit (EMU), Department of Chemical Engineering, UCT, for all the help in acquiring the TEM micrographs.
- **Mr. Pete Roberts**, NMR Centre, Department of Chemistry, UCT, for the ^{1}H NMR experiments.

Abstract

The combination of MFI zeolite nano-sheets with competitive adsorption of water (H_2O) in hydrocracking of long-chain paraffins presents a promising opportunity to produce diesel with high yield and with high cetane number. Thus, in wet hydrocracking of a long-chain paraffin (n-hexadecane (n-C_{16})) over MFI nano-sheets, it was investigated whether catalytic activity increased with increasing number of Brønsted acid (H^+) sites (decreasing silicon-to-aluminium (Si/Al) ratio), while secondary cracking remained completely suppressed. Also, it was investigated whether more Al atoms could be incorporated into the framework of MFI nano-sheets by modifying the new synthesis method.

It was demonstrated that the new synthesis method, which utilizes $C_{22}H_{45}–N^+(CH_3)_2–C_6H_{12}–N^+(CH_3)_2–C_6H_{13}$ ($C_{22\text{-}6\text{-}6}$) as structure-directing agent (SDA), could be extended to various Si/Al ratios in the range 25 – 100. The nano-sheets exhibited extra-framework Al (EFAl) species. Nano-sheets with Si/Al = 75 exhibited an oddly large amount of EFAl species compared to the other nano-sheets. For nano-sheets with Si/Al = 75, a high fraction of the EFAl species may have formed during calcination of the ammonium form and may encompass flexible Al species with predominantly Al in octahedral coordination (Al^{VI}).

Nano-sheets were loaded with 0.9 wt% platinum (Pt) via incipient wetness impregnation (IWI). Pt/nano-sheets with Si/Al = 25, 50 and 100 exhibited similar and high Pt dispersion (γ_{Pt}). In contrast, Pt/nano-sheets with Si/Al = 75 exhibited a very low γ_{Pt}, which was probably a result of the abundance, nature and/or location of EFAl species present in the support.

In dry hydrocracking of n-C_{16}, the catalytic activity increased with decreasing Si/Al ratio, strongly suggesting that the number of H^+ sites increased with decreasing Si/Al ratio. Nano-sheets with Si/Al = 75 most likely contained Al^{VI} species associated with Brønsted acidity, supporting the presence of flexible Al^{VI} species.

In wet hydrocracking of n-C_{16}, at a constant and sufficiently high γ_{Pt}, the activity increased with increasing number of H^+ sites (decreasing Si/Al ratio), while secondary cracking remained completely suppressed. Pt/nano-sheets with Si/Al = 75 displayed a lower activity than Pt/nano-sheets with Si/Al = 100, which may be a result of the very low γ_{Pt} of Pt/nano-sheets with Si/Al = 75, underlining the importance of high γ_{Pt}. For Pt/nano-sheets with Si/Al = 25, 50 and 100, H_2O favoured linear cracking products at low cracking yields. In contrast, for Pt/nano-sheets with Si/Al = 75, H_2O favoured branched cracking products, which may be a result of Pt sites on the external surface of the support being too far from the H^+ sites inside the micropores.

The new synthesis method could be extended to a modified SDA, namely $C_{22}H_{45}–N^+(CH_3)_2–C_6H_{12}–N^+(CH_3)_2–C_3H_7$ ($C_{22\text{-}6\text{-}3}$), at various Si/Al ratios in the range 25 – 100. Replacing the terminal $–C_6H_{13}$ group in $C_{22\text{-}6\text{-}6}$ with $–C_3H_7$ resulted in an increase in the framework Al (FAl) content of MFI nano-sheets with Si/Al ≥ 50, with the increase being the most pronounced for nano-sheets with Si/Al = 50. This was due to the increased occupancy of the zeolite framework by the hydrophilic region of $C_{22\text{-}6\text{-}3}$ in comparison to the hydrophilic region of $C_{22\text{-}6\text{-}6}$ under the given set of synthesis conditions, since $–C_3H_7$ was less bulky than $–C_6H_{13}$.

Calcined nano-sheets were loaded with 1 wt% Pt via competitive ion exchange (CIE). In dry and wet hydrocracking of n-C_{16}, the activity increased with decreasing Si/Al ratio and in wet hydrocracking, secondary cracking was not completely suppressed up to high conversions. This was probably due to the presence of additional H^+ sites generated after SDA removal. H_2O favoured linear cracking products at low cracking yields.

Sodium (Na^+) ion-exchanged nano-sheets were loaded with 1 wt% Pt via CIE. The average Pt size (d_{Pt}) of the Pt/Na^+ nano-sheets were larger than the d_{Pt} of the Pt/calcined nano-sheets, which may be a result of the nature and/or location of EFAl species present in the Na^+ supports. In dry and wet hydrocracking of n-C_{16}, differences in activity were observed and in wet hydrocracking, secondary cracking was not completely suppressed up to high conversions. This was probably due to insufficient intimacy between H^+ sites and Pt sites such that the rate was controlled by diffusion of olefinic intermediates from H^+ sites to Pt sites and vice versa. H_2O favoured linear cracking products at low cracking yields.

Contents

Chapter 1. Introduction

Hydrocracking is a process that involves the breaking down, i.e. "cracking" of heavy hydrocarbons into lighter hydrocarbons in the presence of hydrogen (H_2). The process is based on bifunctional catalysts with a metal function (e.g. platinum (Pt)) and Brønsted acid function (e.g. zeolites). In the reaction mechanism, the metal has a (de)hydrogenation function, whereas the acid catalyses two important steps, namely isomerization followed by the actual cracking step. The process remains the key technology to produce diesel in high yield from heavy oils or from Fischer-Tropsch (FT) waxes, with the latter derived from alternative sources such as natural gas and renewables (Brosius, Kooyman & Fletcher, 2016).

Regarding automotive fuels (gasoline, diesel), diesel is the preferred fuel. The efficiency of a diesel-fuelled engine is higher than that of a gasoline-fuelled engine. This implies that a diesel-fuelled car would travel more kilometres per unit of fuel. Also, diesel is more fully-hydrogenated and thus would, on complete combustion, produce relatively less carbon dioxide (CO_2) and more water (H_2O) than gasoline (Dry, 2001).

The cetane number (CN) of diesel is a quantity indicating the ignition properties of diesel fuel relative to cetane as a standard. The higher the CN, the easier it is to start a standard diesel engine (Business Dictionary, n. d.). Dramatic reductions in the emissions of unburnt hydrocarbons and carbon monoxide (CO) have been achieved via diesel with a high CN. Also, this high-quality diesel allows large exhaust gas recirculation that reduces nitrogen oxides (NO_x) and soot emissions (Lilik & Boehman, 2011; Brosius, Kooyman & Fletcher, 2016). The market requires minimum CNs typically in the range 40 – 51 (Dry, 2001; Bacha *et al.*, 2007; Toma, 2016).

In hydrocracking of heavy oils, diesel CN is improved by hydrotreating molecules with the lowest CN such as aromatics under high H_2 pressure operating conditions (Brosius, Kooyman & Fletcher, 2016). Diesel with CNs typically above 55 can be achieved (Van Veen, 2002). However, the high-pressure conditions make the process quite expensive (Dufresne *et al*., 1987; Valavarasu, Bhaskar & Balaraman, 2007). Currently, the best option for producing high CN diesel is via FT wax hydrocracking. Unlike oil feedstocks, FT waxes are essentially linear paraffins and virtually free from aromatics. Consequently, diesel with very high CNs typically above 70 can be achieved (Sie, Senden & van Wechem, 1991; Dry, 2001; Bouchy *et al.*, 2009). Diesel with high CNs would be required in regions where the specifications for diesel are very stringent. Alternatively, below specification, oil-derived diesel can be upgraded by blending in the required amount of FT diesel (Dry, 2001).

Zeolites are crystalline, microporous aluminosilicates with a three-dimensional (3D) framework structure. They are widely used as Brønsted acid catalysts in oil refining and petrochemistry. The large pore zeolite, namely zeolite Y, has made significant inroads in commercial operations of the hydrocracking process (Vermeiren & Gilson, 2009). Pure primary cracking can be achieved up to high conversions, a feature required for production of diesel in high yields (Schulz & Weitkamp, 1972). On the other hand, the medium pore MFI zeolite shows secondary cracking already at low conversions due to hindered diffusion of the largest fragments imposed by the medium pores (Weitkamp, Jacobs & Martens, 1983). The original catalytic dewaxing process, the Mobil Distillate Dewaxing (MDDW) process, demonstrated the unsuitability of MFI zeolite in maximizing diesel yield, as the zeolite over-cracks long-chain paraffins into gasoline and lighter products (Chen *et al.*, 1977; Meisel *et al.*, 1977). As a result, a diesel-selective variant of the process was developed, the Mobil Isomerization Dewaxing (MIDW) process, based on a proprietary noble metal-zeolite catalyst (Buyan *et al.*, 1995). Despite secondary cracking displayed by MFI zeolite, compared to zeolite Y, MFI zeolite displays a higher selectivity towards linear cracking products due to transition-state shape-selectivity imposed by the medium pores (Weitkamp, Jacobs & Martens, 1983). This is a useful property, considering improvement of diesel CN.

Recently, co-feeding of H_2O in hydrocracking of a long-chain paraffin, namely n-hexadecane (n-C_{16}), over Pt/bulk MFI zeolite and Pt/MFI zeolite nano-sheets resulted in two major advantages (Brosius, Kooyman & Fletcher, 2016). H_2O suppressed secondary cracking up to high conversions and secondary isomerization at low cracking yields through competitive adsorption at the Brønsted acid (H^+) sites. This new strategy for long-chain paraffin hydrocracking selectivity control, i.e. the combination of MFI zeolites with competitive adsorption of H_2O presents a promising opportunity to further improve the CN of diesel produced from FT wax, while maintaining a high diesel yield. The effects were more pronounced on the nano-sheets, thus making them better candidates than their bulk counterparts. Thus, for MFI nano-sheets, this project further investigated whether the catalytic activity could increase with increasing number of H^+ sites (decreasing silicon-to-aluminium (Si/Al) ratio), while secondary cracking remained completely suppressed. Also, it was investigated whether more Al atoms could be incorporated into the framework of MFI nano-sheets with various Si/Al ratios by modifying the new synthesis method (Brosius, Kooyman & Fletcher, 2016).

Chapter 2. Literature Review

2.1. Fischer-Tropsch Synthesis (FTS) Process

The Fischer-Tropsch synthesis (FTS) process converts synthesis gas comprising a mixture of CO and H_2 over a suitable catalyst into a wide range of hydrocarbons. H_2O is formed as a by-product. The overall FTS reaction is shown in reaction 1 (Dry, 2001):

$$CO + 2.15H_2 \rightarrow \text{hydrocarbons} + H_2O \qquad \textbf{Reaction 1}$$

Currently, the commercial FTS process has two modes of operation: a high temperature FTS (HTFT) process and a low temperature FTS (LTFT) process. The HTFT process mainly produces gasoline and lower olefins over iron-based catalysts at temperatures in the range 300 – 350 °C. On the other hand, the LTFT process mainly produces linear waxes over cobalt- or iron-based catalysts at lower temperatures in the range 200 – 240 °C (Dry, 2002). Typical product distributions for the HTFT and LTFT processes from Sasol are shown in table 1 (Jager, 1998).

Table 1: Typical product distributions for the HTFT and LTFT processes from Sasol (Adapted from Jager, 1998).

Products (wt%)	HTFT	LTFT
Methane	7	4
$C_2 – C_4$ olefins	24	4
$C_2 – C_4$ paraffins	6	4
Gasoline	36	18
Middle distillates (diesel + kerosene)	12	19
Wax	9	48
Oxygenates	6	3

2.2. Hydrocracking Process

The hydrocracking process involves the breaking down, i.e. “cracking” of heavy hydrocarbons into lighter hydrocarbons in the presence of H_2. The overall hydrocracking reaction is shown in reaction 2, where i represents the carbon number of the reactant and j the carbon number of the cracking products:

$$C_iH_{2i+2} + H_2 \rightarrow C_jH_{2j+2} + C_{(i-j)}H_{2(i-j)+2} \qquad \textbf{Reaction 2}$$

Hydrocracking is based on bifunctional catalysts containing a metal and Brønsted acid support. Metals employed typically include:

- Noble metals (Pt, palladium (Pd))

- Transition metals from group VIA (molybdenum (Mo), tungsten (W)) and group VIIIA (cobalt (Co), nickel (Ni)), usually applied as sulphides or oxides

Brønsted acid supports employed typically include:

- Amorphous silica-aluminas (ASAs)
- Halogen-doped aluminas (Al_2O_3)
- Zeolites

Three types of hydrocracking processes can be distinguished, namely:

- Conventional hydrocracking
- Mild hydrocracking
- LTFT wax hydrocracking

Table 2 compares typical process conditions and catalysts employed in the three processes.

Table 2: Typical process conditions and catalysts employed in conventional, mild and LTFT wax hydrocracking (Adapted from Dufresne *et al.*, 1987; Shah *et al*., 1988; Sie, Senden & van Wechem, 1991; Scherzer & Gruia, 1996; Marcilly, 2003; Calemma, 2005; Leckel, 2007; Valavarasu, Bhaskar & Balaraman, 2007; Bouchy *et al.*, 2009; Vermeiren & Gilson, 2009).

	Conventional hydrocracking	**Mild hydrocracking**	**LTFT wax hydrocracking**
Temperature (°C)	350 – 430	380 – 440	324 – 372
H_2 pressure (bar)	100 – 140	30 – 70	10 – 50
H_2/feedstock (m^3/m^3)	800 – 2000	400 – 800	500 – 1800
LHSV (h^{-1})	0.2 – 2	0.2 – 2	0.5 – 3
Conversion (%)	70 – 100	20 – 40	20 – 100
Metal	• Pt, Pd • Sulphides of Ni-Mo, Ni-W and Co-Mo	• Oxides of Ni, Mo and W	• Pt, Pd • Sulphides of Ni-Mo, Ni-W and Co-Mo
Brønsted Acid	• ASA • Halogen-doped Al_2O_3 • Zeolite (Y, USY) • Combinations thereof	• ASA • Halogen-doped Al_2O_3 • Zeolite (Y) • Combinations thereof	• ASA • Halogen-doped Al_2O_3 • Zeolite (Y, USY) • Combinations thereof

Hydrocracking remains the key technology to produce middle distillates such as diesel and kerosene (jet fuel). Regarding automotive fuels (gasoline, diesel), diesel is the preferred fuel (see chapter 1). Also, high CN diesel presents several advantages (see chapter 1). The market requires

minimum CNs typically in the range 40 – 51 (Dry, 2001; Bacha *et al.*, 2007; Toma, 2016). Table 3 compares typical diesel yields and CNs that can be obtained by the three processes.

Table 3: Typical diesel yields and CNs obtained by conventional, mild and LTFT wax hydrocracking (Adapted from Dufresne *et al.*, 1987; Maxwell, 1987; Sie, Senden & van Wechem, 1991; Pappal, Hunter & Groeneveld, 1997; Van Veen, 2002; Valavarasu, Bhaskar & Balaraman, 2007; Bouchy *et al.*, 2009).

	Conventional hydrocracking	**Mild hydrocracking**	**LTFT wax hydrocracking**
Diesel yield (%)	42 – 76	15 – 30	60
Diesel CN	> 55	40 – 56	> 70

2.2.1. Conventional Hydrocracking

Conventional hydrocracking involves conversion of heavy hydrocarbons into lighter, valuable products, mainly diesel and to a lesser extent kerosene (Maxwell *et al.*, 1997; Van Veen, 2002), under high H_2 operating pressure conditions (table 2). Typical feedstocks include (Dufresne *et al*., 1987; Scherzer & Gruia, 1996; Vermeiren & Gilson, 2009):

- Heavy crude oil
- Vacuum gas oil (VGO)
- Fluid catalytic cracking light cycle oil
- Coker gas oil
- Deasphalted oil

Prior to hydrocracking, the feedstock undergoes hydrotreatment reactions such as organic sulphur (S)-removal reactions (hydro-desulphurization), organic nitrogen (N)-removal reactions (hydro-denitrogenation) and hydrogenation of aromatics. At least three types of process configurations can be distinguished, namely:

- Two-stage configuration
- One-stage configuration
- Series-flow configuration

The two-stage configuration is the most conventional one in which the hydrotreatment and hydrocracking reactions are carried out in separate stages, with inter-stage product removal. An inter-stage product removal sends a feed almost free from the hydrotreatment by-products such as hydrogen sulphide (H_2S) and ammonia (NH_3) to the hydrocracking stage. The one-stage configuration is the simplest one in which the hydrotreatment and hydrocracking reactions are

carried out in a single stage, without inter-stage product removal. The series flow configuration is a more modern, less expensive configuration, which is similar to the two-stage configuration, but without inter-stage product removal (Maxwell, 1987; Maxwell & Stork, 2001; Vermeiren & Gilson, 2009).

Reducing the content of S and N compounds and aromatics is important regarding product quality. For instance, in diesel, reducing the content of S and N compounds and aromatics results in reduced emissions of pollutants from the engine. Also, reducing the content of aromatics results in higher CN. In addition, reducing the content of S and N compounds provides less poisoning conditions for hydrocracking (Dufresne *et al*., 1987).

In practice, most diesel fuels are produced from the conventional process. However, the high-pressure operating conditions (table 2) make the process quite expensive (Dufresne *et al*., 1987; Dry, 2001; Valavarasu, Bhaskar & Balaraman, 2007).

2.2.2. Mild Hydrocracking

Mild hydrocracking involves conversion of heavy hydrocarbons into lighter, valuable products, mainly middle distillates (diesel and kerosene), under mild H_2 pressure conditions (table 2). The main feedstock in mild hydrocracking is VGO, but other feedstocks used in the conventional process may be used.

To achieve mild hydrocracking, refiners have been revamping existing VGO hydrotreatment process units, mainly hydro-desulphurization units, into mild hydrocracking units since the early 1980s. These one-stage units operate at mild pressures (table 2) that are consistent with the typical design pressures for existing hydrotreatment units (Dufresne *et al*., 1987; Valavarasu, Bhaskar & Balaraman, 2007). The feedstock undergoes mild hydrotreatment (e.g. hydro-desulphurization, hydro-denitrogenation and hydrogenation of aromatics) prior to hydrocracking. The mild pressures result in a lower level of hydrotreatment compared to the conventional process. This in turn results in lower conversions (table 2), higher poisoning conditions and slightly lower quality products compared to conventional hydrocracking. However, the quality of the products is still reasonably good (Dufresne *et al*., 1987; Pappal, Hunter & Groeneveld, 1997; Shorey, Lomas & Keesom, 1999; Marcilly, 2003; Valavarasu, Bhaskar & Balaraman, 2007).

Mild hydrocracking is very attractive in that it enables increased middle distillates production at a reduced cost compared to conventional hydrocracking. For instance, existing VGO hydrotreatment process units can be easily converted to mild hydrocracking units, simply by

changing the temperature or catalyst and can thus save investment costs. Also, hydrocracking at mild pressures saves investment costs significantly (Maier *et al.*, 1984; Sonnemans, Plantenga & Desai, 1984; Basta, 1986; Dufresne *et al*., 1987; Valavarasu, Bhaskar & Balaraman, 2007). The reduced cost of mild hydrocracking offsets the lower product quality obtained by the mild process.

2.2.3. Low Temperature Fischer-Tropsch (LTFT) Wax Hydrocracking

In LTFT wax hydrocracking, an LTFT stage is combined with a hydrocracking stage as in the Shell Middle Distillate Synthesis (SMDS) Process. In the combined, two-stage process, LTFT produces predominantly waxes in the first stage, which in turn undergo hydrocracking in the second stage to produce mainly diesel or kerosene (Sie, Senden & van Wechem, 1991).

Currently, the best option for producing a high CN diesel virtually free from S and N compounds and aromatics is via LTFT wax hydrocracking. Unlike oil feedstocks, LTFT products are essentially linear paraffins and virtually free from aromatics and S and N compounds (Dry, 2001). The linearity of paraffins and absence of aromatics favour the CN of diesel. Consequently, diesel produced from the SMDS process has very high CNs (table 3) (Sie, Senden & van Wechem, 1991). Diesel with high CNs would be required in regions where the specifications for diesel are very stringent. Alternatively, below specification, oil-derived diesel can be upgraded by blending in the required amount of LTFT diesel (Dry, 2001).

The absence of aromatics and S and N compounds in LTFT waxes eliminates the need for hydrotreatment reactions such as hydro-desulphurization, hydro-denitrogenation and hydrogenation of aromatics, which can thus save investment costs (i.e. equipment, catalysts and high-pressure conditions for these hydrotreatment reactions are not required). Also, a one-stage hydrocracking unit is advantageous over a two-stage hydrocracking unit, as investment costs for inter-stage product removal are saved. Furthermore, due to the absence of catalyst poisons such as S and N compounds and the high reactivity of waxes, the less-expensive mild operating pressures enable high conversions of LTFT waxes (table 2), which can thus save investment costs.

2.3. The Classical Hydrocracking Mechanism

Currently, the most accepted hydrocracking mechanism is the “classical” hydrocracking mechanism. It was initially proposed by Mills *et al*. (1953) and Weisz and Swegler (1957) and is shown in figure 1. In the mechanism, the metal dehydrogenates an n-paraffin into an n-olefin. The n-olefin desorbs from the metal site and diffuses to a Brønsted acid site on which it adsorbs. The acid site protonates the n-olefin into a secondary carbenium ion. The carbenium ion is a reactive intermediate and undergoes skeletal isomerization followed by cracking at the

carbon – carbon bond in the β position with respect to the carbon atom (C) carrying the positive charge (β-scission), resulting in the formation of a smaller carbenium ion and an olefin.

The smaller carbenium ion can be cracked further or deprotonated into olefins. The resulting smaller olefins can be protonated to form another carbenium ion. Smaller olefins can desorb from acid sites and diffuse to a metal site on which they adsorb. Finally, the metal hydrogenates the olefin fragments into paraffinic cracking products.

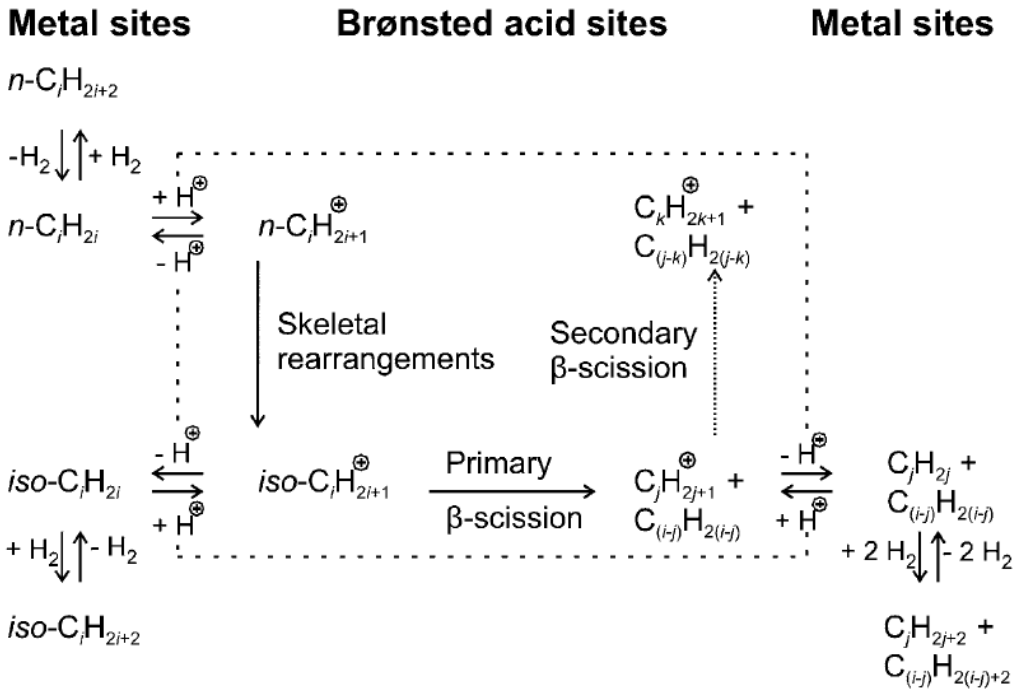

Figure 1: The classical hydrocracking mechanism over bifunctional hydrocracking catalysts (Weitkamp, 2012).

2.3.1. Carbenium Ion Isomerization

There are two mechanisms by which a carbenium ion can undergo isomerization: type A isomerization and type B isomerization. In type A isomerization, the degree of branching of the carbenium ion does not change, but the alkyl substituents undergo a positional change via a 1,2-alkyl and hydride shift, for example (Marcilly, 2003; Bouchy *et al.*, 2009):

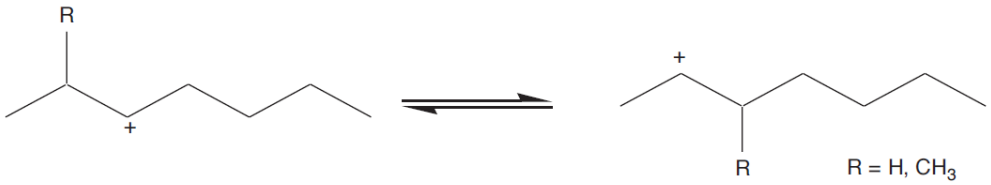

In type B isomerization, the degree of branching of a carbenium ion is increased or decreased via formation of cyclic carbonium ion intermediates such as protonated cyclopropane (PCP), for example (Chevalier, Guisnet & Maurel, 1977; Bouchy *et al.*, 2009):

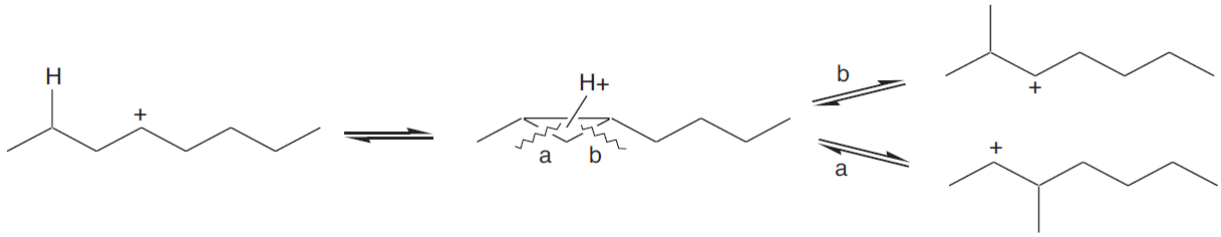

Several studies showed that type A isomerization is much faster than type B isomerization (Chevalier, Guisnet & Maurel, 1977; Ribeiro, Marcilly & Guisnet, 1982). Evidence for type B isomerization emerged from the isomerization of n-pentane and carbon-13 (^{13}C)-labelled n-butane in fluoroantimonic acid (HF-SbF_5) (Brouwer & Oelderik, 1968) and from selectivities of isomerization of the homologous n-paraffins with 8 – 15 carbons on a zeolite (Weitkamp, 1982).

2.3.2. Carbenium Ion Cracking (β-Scission)

The hydrocracking step occurs via scission of the C – C bond in the β position of the positively charged carbon of an isomerized carbenium ion, with the step termed "β-scission". There are five mechanisms by which a carbenium ion can undergo β-scission: Type A, Type B1, Type B2, Type C and Type D β-scission (figure 2) (Weitkamp, Jacobs & Martens, 1983; Weitkamp, Ernst & Karge, 1984). The rate of β-scission increases with increasing stability of a carbenium ion (figure 2). Type D β-scissions are highly unlikely due to the high energy content of the primary carbenium ions involved (Weitkamp, 2012).

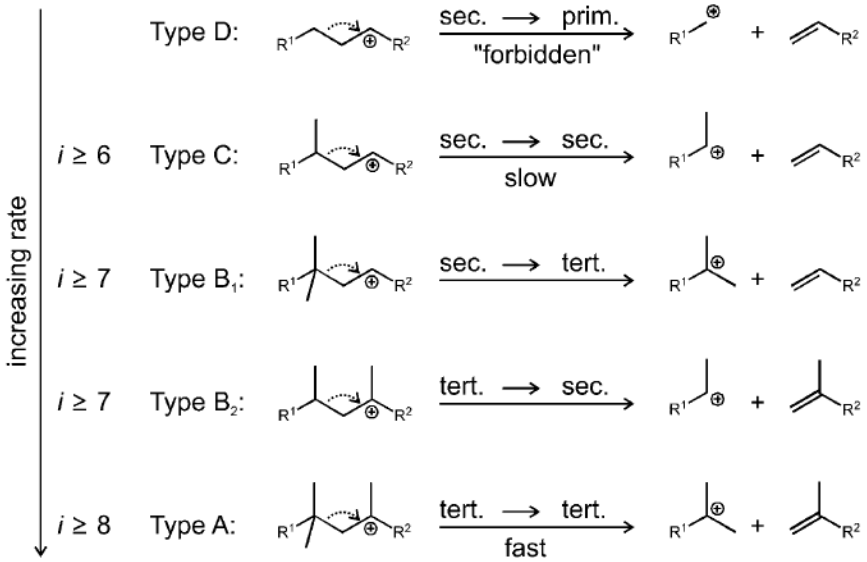

Figure 2: Classification of β-scission reactions of carbenium ions (Weitkamp, 2012).

2.3.3. The Weisz Intimacy Criterion

The classical mechanism involves diffusion of olefinic intermediates from a metal site to an acid site and vice-versa. To ensure that these diffusion steps are not rate-limiting for the overall reaction, the two functions must be sufficiently close. This has been quantified and is known as the Weisz intimacy criterion (equation 1) (Weisz, 1962):

$$R^2 < 1.2\ 10^5 \frac{P_0 D_0}{T dN/dt} \qquad \textbf{Equation 1}$$

Where:

R = Average distance between metal and acid (m)

P_0 = Partial pressure of olefins (MPa)

T = Reaction temperature (K)

D_0 = Diffusivity of olefins (m^2/s)

dN/dt = Reaction rate ($mol/s/m^3$)

2.4. Ideal Hydrocracking

Ideal hydrocracking is a special case of bifunctional hydrocracking. Key features of ideal hydrocracking include:

- A low reaction temperature (Schulz & Weitkamp, 1972; Weitkamp, 1975; Thybaut *et al.*, 2005)

- Consecutive skeletal isomerization and β-scission reactions (Schulz & Weitkamp, 1972; Weitkamp, 1982; Weitkamp, 2012)
- The possibility of high yields of skeletal isomers (Schulz & Weitkamp, 1972; Weitkamp, 1975; Weitkamp, 1982; Weitkamp, 2012)
- The possibility of pure primary cracking up to high conversions (Coonradt & Garwood, 1964; Schulz & Weitkamp, 1972; Weitkamp, 1975; Steijns *et al.*, 1981; Marcilly, 2003; Bouchy *et al.*, 2009)
- Product flexibility in the conversion of heavy feedstocks (Hedden & Weitkamp, 1975; Sie, Senden & van Wechem, 1991; Weitkamp, 2012)
- The absence of C_1 and C_2 products (Schulz & Weitkamp, 1972; Weitkamp, 2012)
- Fewer C_3 products compared to C_4 products (Schulz & Weitkamp, 1972; Weitkamp, 2012)

Based on the classical hydrocracking mechanism (see 2.3), the n-paraffin transformation involves (de)hydrogenation steps on the metal sites, skeletal isomerization and cracking (β-scission) steps on the acid sites and diffusion steps of the olefinic intermediates from metal sites to acid sites and vice versa.

In an ideal hydrocracking catalyst, a certain threshold in the (de)hydrogenation activity is surpassed at which quasi-equilibration of the (de)hydrogenation reactions is established. At quasi-equilibrium, the concentration of n-olefinic intermediates is considered high enough for rapidly displacing the isomeric or cracked olefinic intermediates from the acid sites through competitive adsorption/desorption and the isomeric or cracked intermediates are rapidly hydrogenated by the metal. In such a catalyst, the acid-catalysed consecutive steps, namely skeletal isomerization and β-scission, are rate-limiting for the overall reaction (Coonradt & Garwood, 1964; Weitkamp, 1975; Weitkamp, 1978; Weitkamp, 2012).

For a bifunctional hydrocracking catalyst to be termed “ideal”, the following criteria must be met:

- The metal should be in sufficient quantity (content and dispersion) and have sufficient strength relative to the acid to balance the acid function. This ensures that the reaction rate is not limited by the metal function (Coonradt & Garwood, 1964; Schulz & Weitkamp, 1972; Guisnet *et al.*, 1987; Alvarez *et al.*, 1989; Degnan & Kennedy, 1993; Alvarez *et al.*, 1996; Patrigeon *et al.*, 2001; Bouchy *et al*., 2009).
- The metal and acid sites must be at short mutual distance such that the Weisz intimacy criterion is satisfied. This ensures that the reaction rate is not limited by diffusion of olefinic intermediates from the metal sites to the acid sites and vice versa (Weisz, 1962; Blomsma, Martens & Jacobs, 1997; Bouchy *et al*., 2009; Kim *et al.*, 2013).

Ideal hydrocracking catalysts allow a refiner to run a plant with maximal yield of either diesel, kerosene, or gasoline, in response to the needs of the market, simply by varying the severity of the reaction (Hedden & Weitkamp, 1975).

2.5. Zeolites

Zeolites are microporous, crystalline aluminosilicates with a 3D framework structure. The micropores are uniformly-sized with molecular dimensions (0.3 – 1 nm). The framework contains Si atoms and Al atoms in tetrahedral coordination with oxygen atoms (O). Each AlO_4 tetrahedron in the framework carries a net negative charge, which is typically counter-balanced by group IA and group IIA cations such as sodium ions (Na^+), potassium ions (K^+), calcium ions (Ca^{2+}) and magnesium ions (Mg^{2+}) (Breck, 1974; Flanigen, 2001). According to Löwenstein's rule, only a single Al tetrahedral environment, namely $Al(SiO)_4$, exists in the zeolite framework, whereas AlOAl pairings are forbidden (Löwenstein, 1954). There are currently 235 zeolite structures with unique framework types registered by the International Zeolite Association (IZA) (IZA Structure Commission, 2017).

Zeolites are used in various commercial applications such as:

- Selective adsorption in drying, purification and separation (Marcilly, 2004; Méthivier, 2005; Kresge, 2006; Vermeiren & Gilson, 2009; Guild Associates, Inc, 2016)
- Catalysis in oil refining and petrochemistry (Doolan & Pujado, 1989; Avidan, 1993; Vermeiren & Gilson, 2009)

In the latter, some properties of zeolites are keys to their success. These include (Maxwell, 1987; Vermeiren & Gilson, 2009):

- Strong acidity
- High thermal and hydrothermal stability
- High resistance to S and N compounds
- Low coke-forming tendency
- Shape-selectivity properties

Zeolite Y (and USY) is a large pore zeolite and thus suitable for hydrocracking of heavy feedstocks. This zeolite has made significant inroads in commercial operations of the hydrocracking process (Vermeiren & Gilson, 2009).

The sole presence of micropores in zeolites may impose significant diffusional limitations. Catalytic performance can be seriously limited by diffusion of reactants or products. Reactants

and products with sizes beyond the micropore dimensions cannot diffuse into and out of zeolite crystals, respectively (see 2.5.3). Bulk zeolite crystals are often several thousand times larger than the pore diameter. In such a diffusion-controlled regime, less than 10% of Brønsted acid sites on the external surface of the bulky crystal might actually participate in a catalytic reaction, simply due to the limited diffusion of reactants to and from the acid sites on the external surface (Pérez-Ramírez, 2008; Na, Choi & Ryoo, 2013). Also, slow diffusion of products inside micropores can cause the products to form coke that cover acid sites inside the micropores, resulting in catalyst deactivation (Na, Choi & Ryoo, 2013).

Several strategies have been developed to overcome diffusional limitations. Mesopores (2 – 50 nm) can be generated into a zeolite framework post-synthetically. However, some mesopores are isolated as internal cavities and do not contribute in overcoming diffusional limitations (Scherzer, 1978; de Jong *et al*., 2010). Also, the raw zeolite samples should be treated very carefully, to prevent complete dissolution or the loss of crystallinity (Tao *et al.*, 2006; Egeblad *et al.*, 2008; Na, Choi & Ryoo, 2013).

Mesopores can be generated into a zeolite framework during crystallization by incorporating a hard template such as carbon nanoparticles into the reactant mixture. However, this process is thermodynamically unfavourable in terms of entropy. Hence, zeolite crystallization should be directed to occur in a confined space between the template particles or inside the template pores, in a manner similar to dry-gel synthesis (Jacobsen *et al.*, 2000; Schüth, 2003; Na, Choi & Ryoo, 2013).

Zeolites in the form of small nanoparticles can be developed for rapid diffusion. However, the synthesis conditions must be controlled very delicately to stop crystallization before growth to bulk crystals, and often must stop at a very low yield. Also, the zeolite nanoparticles are usually obtained in a colloidal dispersion, which is difficult to filter. From the viewpoint of catalyst preparation, the synthesis of zeolite nanoparticles is considered impractical as yet (Tosheva & Valtchev, 2005; Na, Choi & Ryoo, 2013).

2.5.1. Brønsted Acidity of Zeolites

Since the mid-1960s, Brønsted acidic zeolites (H-zeolites) have been employed as a hydrocracking co-catalyst (Maxwell & Stork, 1991). H-zeolites are typically prepared by ion exchanging a synthesized zeolite in the Na^+ form (Na-zeolite) with ammonium (NH_4^+) followed by calcining the NH_4^+ form (NH_4-zeolite) at temperatures in the range 300 – 550 °C to release NH_3 (Uytterhoeven, Christner & Hall, 1965; Ward, 1967; Stevenson, 1971; Choi *et al.*, 2009). The Brønsted acidity of H-zeolites arises due to the weakening of the bond in the hydroxyl (OH) group bridging Si and Al

(figure 3). The O atom donates electron density to Al and as a result withdraws electron density from the hydrogen atom (H), thus weakening the O – H bond resulting in the Brønsted acidity.

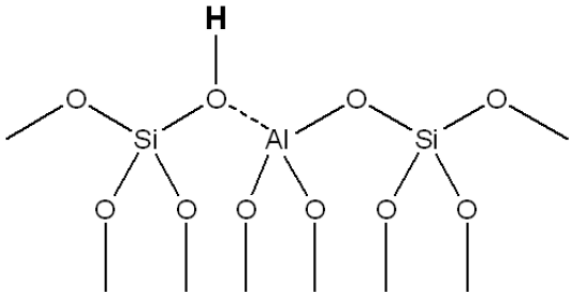

Figure 3: Brønsted acidity due to weakening of the O – H bonds (Adapted from Kukard, 2008).

Generally, for H-zeolites, the number of H^+ sites decreases with increasing Si/Al ratio. The Brønsted acid catalytic activity was found to be linearly proportional to the number of H^+ sites (Olson, Haag & Lago, 1980; Scholle *et al.*, 1985).

2.5.2. Extra-framework Aluminium (EFAl) of Zeolites

Zeolites may contain extra-framework Al (EFAl) species. For EFAl, octahedral or pentahedral coordination of Al with oxygen atoms have been identified by spectroscopic and computational methods. EFAl species with octahedral Al include:

- Charged $[Al(H_2O)_6]^{3+}$ complex (Fyfe *et al.*, 1982; Klinowski *et al.*, 1983)
- Alumina-like polymeric phases (Yingcai *et al.*, 1996)
- Lattice defects such as $Al(SiO)_2(OH)(H_2O)_3$ and $Al(SiO)(OH)_2(H_2O)_3$ (Wouters, Chen & Grobet, 1998; Lamberov *et al.*, 2000)
- Neutral complexes such as $Al(OH)_3(H_2O)_3$ (Benco *et al.*, 2002)

EFAl species with pentahedral Al include:

- Charged $Al(OH)^{2+}$ and AlO^+ entities coordinated by four framework oxygen atoms (Jiao *et al.*, 2005; Huang *et al.*, 2008)
- Neutral complexes such as $Al(OH)_3(H_2O)_2$ (Lisboa, Sánchez & Ruette, 2008)

In addition, Al in the charged Al complex and entities, lattice defects and neutral complexes are Lewis acid centres.

2.5.3. Molecular Shape-Selectivity

Molecular shape-selectivity, or simply shape-selectivity, is defined as the reaction specificity that results from the presence of a sterically confined environment in which the molecules are

converted. Shape-selectivity involves a subtle matching of size and shape of reactants, products and transition-states with the size and shape of the pores of a porous catalyst, respectively. A net shape-selective effect requires that the shape-selective environment is repeated many times throughout the catalyst (Martens & Jacobs, 2001).

Shape-selectivity was initially discovered by Weisz and Frilette (1960). Later, Csicsery (1976) distinguished three main types of shape-selectivities, namely:

- Reactant shape-selectivity
- Product shape-selectivity
- Transition-state shape-selectivity

Reactant shape-selectivity occurs when a reactant(s) is too bulky to diffuse into catalyst pores. For instance, in dehydration of alcohols over CaA zeolite. In a 1-butanol:iso-butanol mixture, 1-butanol is selectively dehydrated by CaA, since iso-butanol is too bulky to diffuse into the catalyst pores (Weisz & Frilette, 1960).

Product shape-selectivity occurs when a product(s) formed within catalyst pores is too bulky to diffuse out as an observed product(s). The product(s) is either converted to a less bulky molecule or eventually deactivates the catalyst by coking. For instance, in cracking of n-paraffins over CaA. n-Paraffins are selectively cracked by CaA into linear products instead of isomeric products, since isomeric products are too bulky to diffuse out of the catalyst pores (Weisz & Frilette, 1960).

Transition-state shape-selectivity occurs when a reaction(s) is prevented because the corresponding transition-state is too bulky to form in the catalyst pores. For instance, in trans-alkylation of dialkylbenzenes over ASA. 1-methyl-3-ethylbenzene is selectively trans-alkylated by ASA into 1-methyl-3,5-diethylbenzene instead of various other trialkyl benzenes, since the transition-states that would form via the other reaction pathways are too bulky to form in the catalyst pores (Csicsery, 1967; Csicsery 1976).

“Pore mouth catalysis” and “key-lock catalysis” are peculiar forms of shape-selectivity. The term “pore mouth catalysis” was introduced by Venuto (1977) to indicate that conversion of a molecule occurs at the pore opening of a zeolite (interrupted cages, channel intersections, or channels) and not deeper inside the crystal. For conversion of a molecule with two or more atom groups adsorbed simultaneously on two or more adjacent pore openings, the term “key-lock catalysis” is used (Martens *et al.*, 1995).

2.5.4. Bulk MFI Zeolite

ZSM-5 (bulk MFI) zeolites are medium pore zeolites composed of pentasil units. The micropore system comprises straight 10-ring channels along the *b*-axis intersected by 10-ring sinusoidal channels along the *a*-axis. A representation of the pore system is shown in figure 4. The straight and sinusoidal channels have pore openings of approximately 5.3 x 5.6 Å and approximately 5.1 x 5.5 Å, respectively. The intersection cavities are approximately 9 Å (Kokotailo *et al.*, 1978; Database of Zeolite Structures, 2017).

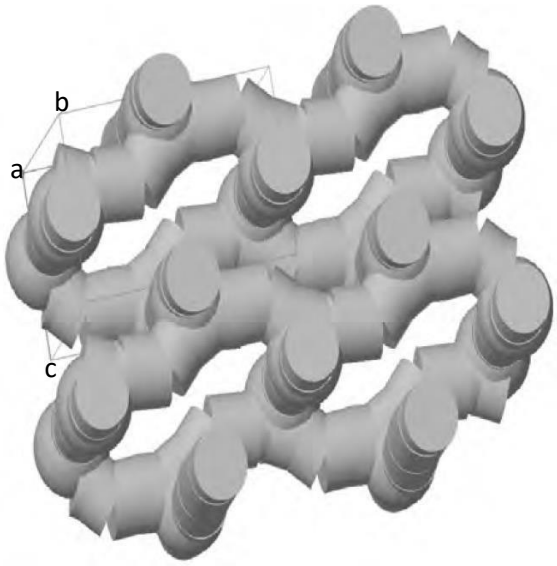

Figure 4: Pore system of bulk MFI (Adapted from Koen, 2014).

Bulk MFI was discovered in 1965 as a direct result of Mobil's investigation of quaternary amines as SDAs in zeolite synthesis (Argauer & Landolt, 1972). Due to their medium pore size, bulk MFI zeolites impose molecular shape-selectivity effects. This feature has made them attractive for use in various catalytic applications. Applications typically utilize reactant and product shape-selectivity, as in the separation and cracking of undesirable molecules, respectively, to produce useful products and/or improve the quality of existing products.

For instance, shape-selective catalytic technology based on bulk MFI has been demonstrated in the original catalytic dewaxing process, the MDDW process, to improve cold flow properties of diesel (Chen *et al.*, 1977; Meisel *et al.*, 1977). Cold flow properties of diesel define the flowability of the fuel at low temperatures. In the diesel fraction, wax has a poor solubility in the other hydrocarbons. At low temperature, wax crystallizes, affecting the cold flow properties of the fuel that can prevent engine start-up. Diesel fuels have specifications on cold flow properties. The MDDW process has been developed to upgrade the fuels to meet these specifications

(ExxonMobil Research and Engineering Company [EMRE], 2002; EMRE, 2011). The process utilizes bulk MFI to separate wax from diesel and selectively crack the wax into gasoline, while cold flow properties of the diesel are improved. The process was widely commercialized; however, although successful, a small amount of the diesel was cracked into gasoline and lighter fragments during the process (Chen *et al.*, 1977; Meisel *et al.*, 1977; Ireland *et al.*, 1979; EMRE, 2011). The process demonstrated the unsuitability of bulk MFI in maximizing diesel yield, as the zeolite over-cracks long-chain paraffins due to hindered diffusion of the largest fragments imposed by the medium pores.

Research continued by Mobil, with the goal of increasing the diesel yield. As a result, a diesel-selective variant of the process was developed, the MIDW process, based on a proprietary noble metal-zeolite catalyst, very likely the larger pore zeolite-β loaded with Pt and/or Pd. The catalyst separates wax from diesel and isomerizes and selectively cracks wax into diesel. Some of the diesel-range material is isomerized rather than cracked during the process. While cold flow properties of the diesel are improved, the higher retention of diesel-range material results in a higher diesel yield compared to the original process (Buyan *et al.*, 1995; EMRE, 2011; Vogt *et al.*, 2015). Furthermore, in fluid catalytic cracking (FCC), bulk MFI is used as a co-catalyst to separate n-paraffins from gasoline and selectively crack the n-paraffins into lower olefins to improve the octane quality of gasoline (Henz *et al.*, 1986; Martens & Jacobs, 2001).

2.5.5. MFI Zeolite Nano-sheets

Recently, Choi *et al.* (2009) approached the synthesis of MFI zeolite nano-sheets (Si/Al = 50) by designing a di-quaternary ammonium surfactant, namely $C_{22}H_{45}–N^+(CH_3)_2–C_6H_{12}–N^+(CH_3)_2–C_6H_{13}$, designated as $C_{22\text{-}6\text{-}6}$ (figure 5). The surfactant contains a hydrophobic tail group comprising a long-chain alkyl group ($C_{22}H_{45}$–, "C22"), and a hydrophilic head group comprising two quaternary ammonium groups linked by a hexyl spacer (–C_6H_{12}–, "C6 linkage"). The terminal ammonium group contains a hexyl (–C_6H_{13}) substituent. The remaining substituents on the ammonium groups are methyl groups (–CH_3).

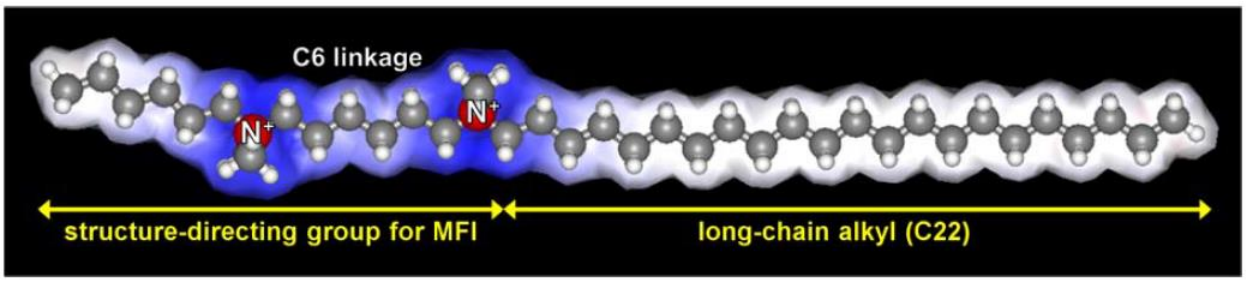

Figure 5: 3D molecular structure of $C_{22\text{-}6\text{-}6}$ (Choi *et al.*, 2009 (Suppl.)).

For the first time in zeolite synthesis, an SDA did dual structure-directing functions at the micro- and meso-length scales simultaneously owing to the hydrophilic and hydrophobic groups, respectively. The hydrophilic group functioned as an effective structure-directing agent (SDA) for the zeolite framework, while the hydrophobic tail group induced formation of mesoscale micelles via hydrophobic interaction between the tails. The alkyl tails suppressed crystal growth of the zeolite beyond the ammonium region due to their strong hydrophobic character (Choi *et al*., 2009). The resultant product took the form of MFI nano-sheets. In contrast to bulk MFI, MFI nano-sheets exhibited wide *ac* planes, ultra-short micropores along the *b*-axis, and inter-crystalline mesopores (Choi *et al*., 2009). Depending on synthesis conditions, the nano-sheets formed a randomly stacked (unilamellar), regularly stacked (multilamellar) or nano-sponge-like morphology (Choi *et al*., 2009; Jo *et al.*, 2014).

Park *et al.* (2011) found that the thickness of nano-sheets increased with increasing number of ammonium groups in the surfactant. It is noteworthy that surfactants with similar structures containing one ammonium group did not function as SDAs for nano-sheets, generating amorphous MCM-41 or bulk MFI instead (Kresge *et al.*, 1992; Beck *et al.*, 1994; Park *et al.*, 2011). Hence, at least two ammonium groups are necessary for directing the structure of nano-sheets.

The nano-sheets exhibited surprisingly strong Brønsted acidity and high thermal and hydrothermal stability and mechanical strength (Choi *et al*., 2009; Na *et al.*, 2011). Also, the nano-sheets showed improved catalytic performance compared to bulk MFI in various catalytic reactions. For instance, the nano-sheets showed:

- Higher catalytic activity in conversion of bulky molecules due to a larger number of H^+ sites on the external surfaces (Choi *et al.*, 2009; Jung *et al.*, 2012)
- Improved coke tolerance in methanol-to-gasoline conversion due to facile diffusion of coke precursors out of the ultrashort micropores (Choi *et al.*, 2009)

Jo *et al.* (2014) observed a rapid (≈ four-fold) increase in the crystallization rate of MFI nano-sheets and a uniform mesopore pore size distribution (PSD) when bulk MFI was included in a synthesis mixture. Bulk MFI functioned as a crystallization-accelerating seed. It was found that an MCM-41-like phase is initially formed, followed by zeolite formation. Both materials exhibited similar mesopore PSDs. It is thought that bulk MFI seeds disintegrate into numerous sub-nanometre nuclei, which could be embedded everywhere in the MCM-41-like pore walls and could thereby result in rapid zeolite formation and the similarity of mesopore sizes between the MCM-41-like phase and nano-sheets.

Framework aluminium (FAl) and EFAl content of MFI nano-sheets (Si/Al = 20 – 50) were investigated (Wu *et al.*, 2014; Zhu *et al.*, 2015). Initially, for nano-sheets with Si/Al = 30 – 50, it was reported that 25 – 40% Al are EFAl (Wu *et al.*, 2014). Later, it was reported that the FAl content of nano-sheets with Si/Al = 20 increased from 40% to 70% after replacing $C_{22\text{-}6\text{-}6}$ with a modified surfactant in a synthesis mixture (Zhu *et al.*, 2015). Compared to $C_{22\text{-}6\text{-}6}$, the modified surfactant contained a terminal propyl group ($–C_3H_7$) instead of the terminal $–C_6H_{13}$ group in the hydrophilic region. The modified surfactant is designated as $C_{22\text{-}6\text{-}3}$. Based on modelling simulations, it was found that the framework occupancy by the hydrophilic region increased when $–C_6H_{13}$ was changed to $–C_3H_7$, since $–C_3H_7$ is less bulky than $–C_6H_{13}$ (figure 6) (Zhu *et al.*, 2015). The higher occupancy explains the higher FAl content of the nano-sheets synthesized under the given set of synthesis conditions.

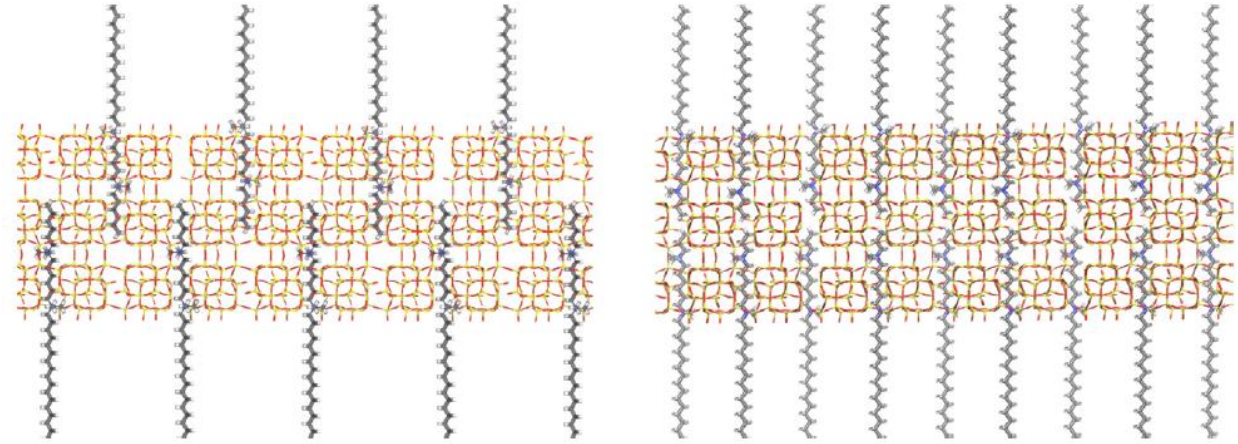

Figure 6: Minimum-energy configuration of (left) $C_{16}H_{33}N^+(CH_3)_2–C_6H_{12}–N^+(CH_3)_2–C_6H_{13}$ and (right) $C_{16}H_{33}N^+(CH_3)_2–C_6H_{12}–N^+(CH_3)_2–C_3H_7$ in a nano-layered silicalite-1. Simulations done with the CVFF forcefield in Materials Studio (Zhu *et al.*, 2015).

For H-zeolites, H^+ compensates the negatively charged framework $Al(SiO)_4$ tetrahedra. Increasing the FAl content of H-zeolites can lead to a higher Brønsted acid activity (Olson, Haag & Lago, 1980; Olson, Haag & Borghard, 2000).

2.6. Catalytic Properties of Hydrocracking Catalysts

Research into the improvement of hydrocracking catalysts is an ever-ongoing process. Although much more expensive, noble metals can be quite effective in hydrocracking of pure hydrocarbons due to the absence of S and N compounds that are poisons to the metals (Scherzer & Gruia, 1996; Bartholomew, 2001). Also, in hydrocracking of pure hydrocarbons, noble metals have a stronger (de)hydrogenation activity than transition metals and are thus better for ideal hydrocracking of LTFT wax (see 2.4) (Coonradt & Garwood, 1964).

Ideal hydrocracking has been observed since the earliest description of n-C_{16} hydrocracking over Pt/ASA (Coonradt & Garwood, 1964). Later, it has been observed in large pore zeolites, namely Pt/Y zeolite (Schulz & Weitkamp, 1972; Weitkamp, 1975; Weitkamp, 1978) and Pt/USY zeolite (Steijns & Froment, 1981). Also, in these catalysts, due to the absence of shape-selectivity effects in cracking, primary cracking products rich in iso-paraffins are formed. This can be explained by the occurrence of predominantly type A β-scissions and some type B β-scissions (see 2.2.3) (Weitkamp, Jacobs & Martens, 1983).

In contrast, the medium pore Pt/bulk MFI zeolite does not display ideal hydrocracking behaviour (Weitkamp, Jacobs & Martens, 1983). Secondary cracking is observed already at low conversions due to product shape-selectivity imposed by the medium pores. The largest fragments are hindered from diffusing out of the zeolite pores and thus undergo secondary cracking. Despite this, compared to ASA and zeolite Y, MFI zeolite displays a higher selectivity towards linear cracking products due to transition-state shape-selectivity imposed by the medium pores. Type C β-scission is favoured over type A and B β-scissions since the transition-state that would form via type A or B β-scission is too bulky to form in the medium pores, thus favouring linear cracking products (see 2.3.2) (Weitkamp, Jacobs & Martens, 1983). In MFI zeolites, isomerization of primary cracking products is controlled by competitive adsorption (Weitkamp, Jacobs & Martens, 1983). The higher selectivity towards linear cracking products in MFI zeolites is advantageous, considering the improvement of diesel CN (see 2.2.3).

A new synthesis method for MFI nano-sheets was developed, which utilizes $C_{22\text{-}6\text{-}6}$ as SDA (Brosius, Kooyman & Fletcher, 2016). In hydrocracking of n-C_{16}, the Pt/MFI nano-sheets (Si/Al = 50) showed a lower degree of secondary cracking than Pt/bulk MFI due to enhanced diffusion of primary cracking products across the ultra-short micropores of the nano-sheets (Brosius, Kooyman & Fletcher, 2016). However, the enhanced diffusion was insufficient to completely suppress secondary cracking.

H_2O is a major by-product of the FTS process (reaction 1). The effects of H_2O in hydrocracking were investigated in the early 1970s (Yan, 1972) and recently (Brosius, Kooyman & Fletcher, 2016). Yan (1972) reported that H_2O suppresses the cracking activity of Pt/Y, but enhances the cracking activity of Pt/Rare-Earth (RE)X. In the former, the activity is suppressed because H_2O competes with the feed for adsorption at the H^+ sites. Although competitive adsorption can occur in the latter, it can be overcompensated by hydration of RE ions into additional H^+ sites. In the more recent study (Brosius, Kooyman & Fletcher, 2016), the suppression of activity by H_2O due to competitive adsorption was demonstrated in Pt/HY, Pt/bulk MFI and Pt/MFI nano-sheets.

However, in the more recent study (Brosius, Kooyman & Fletcher, 2016), despite the loss of activity, H_2O was found to be advantageous with regards to selectivity. It essentially enables the otherwise non-ideal hydrocracking catalysts, namely Pt/MFI bulk and Pt/MFI nano-sheets, to approach ideal hydrocracking behaviour. Also, it further improves selectivity towards linear cracking products at low cracking yields. H_2O eliminates secondary cracking completely up to high conversions and increases formation of linear cracking products at low cracking yields, with the effect more pronounced on the nano-sheets. This is due to competitive adsorption of H_2O. H_2O suppresses further cracking of isomerized primary cracking products and isomerization of the primary cracking products.

Thus, the effects of enhanced diffusion are modest in comparison to the effects of competitive adsorption of H_2O. This new strategy for long-chain paraffin hydrocracking selectivity control, i.e. the combination of MFI zeolites with competitive adsorption of H_2O, presents a promising opportunity to further improve the CN of diesel produced from LTFT wax, while maintaining a high diesel yield.

For H-zeolites with varying Si/Al ratios loaded with a constant and sufficient amount of metal, provided the metal dispersion is constant and sufficiently high, the catalytic activity can be controlled by varying the number of H^+ sites (Si/Al ratio), while remaining in the zone of ideal hydrocracking (Guisnet *et al.*, 1987; Alvarez *et al.*, 1996; Patrigeon *et al.*, 2001).

Chapter 3. Hypotheses and Key Questions

3.1. Hypotheses

In H-zeolites, H^+ compensates negatively charged framework $Al(SiO)_4$ tetrahedra. The Brønsted acid catalytic activity is linearly proportional to the number of H^+ sites (Olson, Haag & Lago, 1980; Scholle *et al.*, 1985). In wet hydrocracking over medium pore MFI zeolites, secondary cracking is completely supressed up to high conversions (Brosius, Kooyman & Fletcher, 2016). For H-zeolites with varying Si/Al ratios loaded with a constant and sufficient amount of metal, provided the metal dispersion is constant and sufficiently high, the catalytic activity can be controlled by varying the number of H^+ sites (Si/Al ratio), while remaining in the zone of ideal hydrocracking (Guisnet *et al.*, 1987; Alvarez *et al.*, 1996; Patrigeon *et al.*, 2001). Thus, in wet hydrocracking, for MFI nano-sheets with varying Si/Al ratios loaded with a constant and sufficient amount of metal, provided the metal dispersion is constant and sufficiently high, it can be hypothesized that the catalytic activity should increase with increasing number of H^+ sites (decreasing Si/Al ratio), while secondary cracking remains completely suppressed.

A new synthesis method for MFI nano-sheets was developed, which utilizes the conventional surfactant $C_{22\text{-}6\text{-}6}$ (Brosius, Kooyman & Fletcher, 2016). In a different synthesis method, replacing the terminal $–C_6H_{13}$ group in the conventional surfactant with a $–C_3H_7$ group resulted in an increase in the FAl content of MFI nano-sheets at a given Si/Al ratio and under a given set of synthesis conditions (Zhu *et al.*, 2015). Thus, it can be hypothesized that replacing the terminal $–C_6H_{13}$ group in the surfactant $C_{22\text{-}6\text{-}6}$ with a $–C_3H_7$ group in the new synthesis method should result in an increase in the FAl content of MFI nano-sheets with various Si/Al ratios.

3.2. Key Questions

This study will focus on answering the following key questions:

- Can the new synthesis method be extended to various Si/Al ratios?
- Does the number of H^+ sites increase with decreasing Si/Al ratio?
- Does varying the Si/Al ratio significantly influence the metal dispersion?
- In wet hydrocracking, at a constant and sufficiently high metal dispersion, does the catalytic activity increase with increasing number of H^+ sites, and, if so, is secondary cracking completely suppressed up to high conversions?
- Can the new synthesis method be extended to $C_{22\text{-}6\text{-}3}$ at various Si/Al ratios?
- In the new synthesis method, compared to $C_{22\text{-}6\text{-}6}$, does $C_{22\text{-}6\text{-}3}$ give rise to a higher FAl content for MFI nano-sheets at a given Si/Al ratio and, if so, to what extent?

Chapter 4. Experimental

4.1. Synthesis

4.1.1. Synthesis of Structure-Directing Agents (SDAs)

The SDAs for MFI zeolite nano-sheets synthesis were di-quaternary ammonium surfactants, namely $[C_{22}H_{45}–N^+(CH_3)_2–C_6H_{12}–N^+(CH_3)_2–C_6H_{13}]Br_2$ ($C_{22\text{-}6\text{-}6}Br_2$) and $[C_{22}H_{45}–N^+(CH_3)_2–C_6H_{12}–N^+(CH_3)_2–C_3H_7]Br_2$ ($C_{22\text{-}6\text{-}3}Br_2$). Synthesis of the SDAs involves two reaction steps. The first step involves formation of an intermediate, namely $[C_{22}H_{45}–N^+(CH_3)_2–C_6H_{12}–N(CH_3)_2]Br$ ($C_{22\text{-}6\text{-}0}Br$). The second step involves alkylation of the intermediate, resulting in formation of the SDA. The synthesis procedures of the SDAs are described in subsequent sections.

4.1.1.1. Synthesis of $C_{22\text{-}6\text{-}6}Br_2$

For the first reaction step, initially, 86 g (0.500 mol) of *N,N,N',N'*-tetramethyl-1,6-diaminohexane (Sigma-Aldrich, 99%) and 19.5 g (0.050 mol) of 1-bromodocosane (TCI) were dissolved in 500 ml of a acetonitrile/toluene mixture (1:1 vol/vol) and heated at 60 °C for 10 hours (Choi *et al.*, 2009). After cooling to room temperature, the solution was cooled in a refrigerator at 4 °C for 1 hour (Wu *et al.*, 2013). Thereafter, the product ($C_{22\text{-}6\text{-}0}Br$) was filtered, washed with cold acetonitrile (Machoke *et al.*, 2014) followed by cold diethyl ether (Choi *et al.*, 2009) and dried at room temperature for 2 days (Machoke *et al.*, 2014).

For the second reaction step, initially, 28.1 g (0.050 mol) of $C_{22\text{-}6\text{-}0}Br$ and 12.4 g (0.075 mol) of 1-bromohexane (Sigma-Aldrich) were dissolved in 250 ml of acetonitrile and heated at 70 °C for 10 hours (Choi *et al.*, 2009; Machoke *et al.*, 2014). After cooling to room temperature, the solution was cooled in a refrigerator at 4 °C for 1 hour (Wu *et al.*, 2013). Thereafter, the product ($C_{22\text{-}6\text{-}6}Br_2$) was filtered, washed with cold diethyl ether (Choi *et al.*, 2009) and dried at room temperature for 24 hours (Machoke *et al.*, 2014). 31.2 g of $C_{22\text{-}6\text{-}6}Br_2$ product was obtained (86% overall yield). The product was identified by Proton Nuclear Magnetic Resonance Spectroscopy (^{1}H NMR). The spectrum is shown in figure A1 in appendix 1. The spectrum corresponds well with a spectrum reported previously (Benavent *et al.*, 2012).

4.1.1.2. Synthesis of $C_{22\text{-}6\text{-}3}Br_2$

For the first reaction step, $C_{22\text{-}6\text{-}0}Br$ was prepared by the same synthesis procedure as in 4.1.1.1. For the second reaction step, $C_{22\text{-}6\text{-}3}Br_2$ was prepared by the same synthesis procedure as in 4.1.1.1 with the following exception: 28.1 g (0.050 mol) of $C_{22\text{-}6\text{-}0}Br$ was reacted with 9.2 g (0.075 mol) of 1-bromopropane (Sigma-Aldrich) (Zhu *et al.*, 2015). 24.9 g of $C_{22\text{-}6\text{-}3}Br_2$ product was

obtained (73% overall yield). The product was identified by ^{1}H NMR. The spectrum is shown in figure A2 in appendix 1.

4.1.2. Synthesis of MFI Zeolite Nano-sheets

The zeolite preparation method was adopted from Machoke *et al.* (2015) and modified to allow for secondary nucleation assisted hydrothermal crystallization (Jo *et al.*, 2014; Brosius, Kooyman & Fletcher, 2016 (Suppl.)). The zeolite samples are coded as follows: NS-x-yz, with

- NS abbreviating nano-sheets,
- x the number of carbons in the terminal alkyl group of the SDA,
- y the target Si/Al molar ratio, and
- z the order in which the samples were synthesized at a given target Si/Al ratio.

The various zeolites, SDAs used, target Si/Al ratios, and gel molar compositions are shown in table 4.

Table 4: Zeolites, SDAs used, target Si/Al ratios, and gel molar compositions.

Zeolite	SDA	Target Si/Al ratio	Gel molar composition						
			SiO_2	Al_2O_3	SDA	H_2SO_4	Na_2O	H_2O	EtOH
NS-6-25a	$C_{22\text{-}6\text{-}6}Br_2$	25	100	2	10	21	30	4000	400
NS-6-50a	$C_{22\text{-}6\text{-}6}Br_2$	50	100	1	10	21	30	4000	400
NS-6-75a	$C_{22\text{-}6\text{-}6}Br_2$	75	100	0.67	10	21	30	4000	400
NS-6-100a	$C_{22\text{-}6\text{-}6}Br_2$	100	100	0.50	10	21	30	4000	400
NS-6-25b	$C_{22\text{-}6\text{-}6}Br_2$	25	100	2	10	21	30	4000	400
NS-6-50b	$C_{22\text{-}6\text{-}6}Br_2$	50	100	1	10	21	30	4000	400
NS-6-75b	$C_{22\text{-}6\text{-}6}Br_2$	75	100	0.67	10	21	30	4000	400
NS-6-100b	$C_{22\text{-}6\text{-}6}Br_2$	100	100	0.50	10	21	30	4000	400
NS-3-25a	$C_{22\text{-}6\text{-}3}Br_2$	25	100	2	10	21	30	4000	400
NS-3-50a	$C_{22\text{-}6\text{-}3}Br_2$	50	100	1	10	21	30	4000	400
NS-3-75a	$C_{22\text{-}6\text{-}3}Br_2$	75	100	0.67	10	21	30	4000	400
NS-3-100a	$C_{22\text{-}6\text{-}3}Br_2$	100	100	0.50	10	21	30	4000	400

NS samples with a target mass of 3 g were prepared. In the preparation of NS samples, initially, 1.2 g of sodium hydroxide (NaOH, Sigma-Aldrich) was dissolved in 27.3 g of millipore H_2O (10 MΩ.cm @ 25 °C) in a 500 ml polyethylene bottle, forming a 1.1 M basic solution. Then,

0.15 g of bulk MFI (H-MFI-90, Si/Al = 45, Süd Chemie AG) was added as a crystallization-accelerating seed and the resulting mixture was left to stir at 60 °C for 12 hours to form a seed solution. After cooling to room temperature, the SDA (3.624 g of $C_{22\text{-}6\text{-}6}Br_2$ or 3.424 g of $C_{22\text{-}6\text{-}3}Br_2$) was added under vigorous stirring and the resulting solution was left to stir vigorously for 4 hours. This mixture is denoted as solution A.

Aluminium sulphate octadecahydrate ($Al_2(SO_4)_3 \cdot 18H_2O$, Riedel de Haën) and sulphuric acid (H_2SO_4, Kimix, 98%) were dissolved in H_2O in a 100 ml polyethylene bottle, forming an acidic solution. The masses of $Al_2(SO_4)_3 \cdot 18H_2O$, H_2SO_4 (98%) and H_2O used for NS samples with Si/Al ratios of 25 – 100 are shown in table 5. This mixture is denoted as solution B.

Table 5: Masses of $Al_2(SO_4)_3 \cdot 18H_2O$, H_2SO_4 (98%) and H_2O used for nano-sheets with Si/Al ratios 25 – 100.

Si/Al ratio	**$Al_2(SO_4)_3 \cdot 18H_2O$ (g)**	**H_2SO_4 (98%) (g)**	**H_2O (g)**
25	0.6664	0.738	8.24
50	0.3332	0.885	8.35
75	0.2221	0.934	8.38
100	0.1666	0.959	8.40

After stirring solution A for 4 hours, solution B was added dropwise at a rate of 1 drop/5 s to solution A and the resulting solution was left to stir for 1 hour. Thereafter, 10.417 g of tetraethylorthosilicate (TEOS, Sigma-Aldrich) was added at once under vigorous stirring and the resulting solution was left to stir vigorously for 4 hours.

For NS samples synthesized with $C_{22\text{-}6\text{-}6}Br_2$, a viscous and pourable hydrogel was formed. On the other hand, for NS samples synthesized with $C_{22\text{-}6\text{-}3}Br_2$, a solid hydrogel was formed. The gel was transferred to four Teflon lined stainless steel autoclaves (21 ml) to precisely 67% of the available volume. The autoclaves were placed in a zeolite oven, rotated at 60 rpm and heated from room temperature to 150 °C (heating rate: 5 °C/min, temperature ramp time: 30 minutes). At 150 °C, hydrothermal crystallization starts and occurs over a period of 2.5 days. After cooling to room temperature, the product was filtered and washed with 1 x 2.5 l H_2O using 6 bar of compressed air in a pressure filtration unit and dried at 120 °C for 12 hours.

4.1.3. Post-treatment of MFI Zeolite Nano-sheets

4.1.3.1. SDA Removal

To remove the SDA, the as-synthesized NS samples were calcined in static air at 550 °C for 8 hours (heating rate: 1 °C/min, temperature ramp time: 8 hours 45 minutes) (Brosius, Kooyman & Fletcher, 2016 (Suppl.)). The NS-6-ya samples were calcined once. The remaining samples were calcined twice since for the NS-6-yb samples, a fraction of the sample appeared brown, whereas for the NS-3-ya samples, the whole sample appeared brown. The brown colour implies that SDA is still present. Also, the NS-6-yb and NS-3-ya samples were treated the same to eliminate any differences that may arise from calcination, since these samples were compared to investigate whether $C_{22\text{-}6\text{-}3}$ could result in a higher FAl content than $C_{22\text{-}6\text{-}6}$ at a given Si/Al ratio. The target masses, masses of as-synthesized and calcined NS (C-NS) samples, and yields of C-NS samples are shown in table 6.

Table 6: Target masses, masses of as-synthesized and C-NS samples, and yields of C-NS samples.

Zeolite	Target mass (g)	Mass as-synthesized (g)	Mass calcined (g)	Yield (%)
C-NS-6-25a	3	3.86	2.72	90.7
C-NS-6-50a	3	3.69	2.60	86.7
C-NS-6-75a	3	4.12	2.82	94.0
C-NS-6-100a	3	4.17	2.76	92.0
C-NS-6-25b	3	4.09	2.71	90.3
C-NS-6-50b	3	3.92	2.63	87.7
C-NS-6-75b	3	4.07	2.84	94.7
C-NS-6-100b	3	4.16	2.75	91.7
C-NS-3-25a	3	4.37	2.79	93.0
C-NS-3-50a	3	4.16	2.76	92.0
C-NS-3-75a	3	4.15	2.73	91.0
C-NS-3-100a	3	4.26	2.80	93.3

4.1.3.2. Protonation

Protonation of the zeolites was obtained by either of the following two methods:

- C-NS samples were ion exchanged with ammonium chloride (NH_4Cl), followed by calcination, or

- C-NS samples or Na^+ ion-exchanged NS (Na-NS) samples were loaded with Pt by competitive ion exchange (CIE), followed by *in-situ* calcination and reduction (See 4.1.3.3 for metal loading, 4.1.3.3.2 for Pt loading by CIE, 4.3.2.2 for *in-situ* calcination and 4.3.2.3 for *in-situ* reduction).

For the former method, initially, 500 ml of H_2O was added to 1.3365 g of NH_4Cl and C-NS sample. The masses of the C-NS samples used in this ion exchange are shown in table 7. The solutions were left to stir at room temperature for 12 hours. Thereafter, the products were filtered and washed with 1 x 2.5 l H_2O. The ion exchanges were repeated once more. Thereafter, the products were filtered and washed with 4 x 2.5 l H_2O to rinse away all chloride (Cl^-) ions (Brosius, Kooyman & Fletcher, 2016 (Suppl.)).

Table 7: Masses of C-NS samples ion exchanged with NH_4^+.

Zeolite	Mass (g)
C-NS-6-25a	2.72
C-NS-6-50a	2.60
C-NS-6-75a	2.82
C-NS-6-100a	2.76
C-NS-6-25b	0.8
C-NS-6-50b	0.8
C-NS-6-75b	0.8
C-NS-6-100b	0.8
C-NS-3-25a	0.8
C-NS-3-50a	0.8
C-NS-3-75a	0.8
C-NS-3-100a	0.8

To test for the presence of Cl^- ions, a few drops of 0.1 M silver nitrate ($Ag(NO_3)_2$) solution was added to a 250 ml sample of the filtrate after each washing step. When a $Ag(NO_3)_2$ solution is added to a solution containing Cl^- ions, silver chloride (AgCl) is precipitated as a white precipitate since it is insoluble in H_2O, confirming the presence of Cl^- (BBC - GCSE Bitesize, n. d.; Whitten *et al.*, 2013; Department of the Interior, 1993). After the fourth washing step, no Cl^- ions were detected. The NH_4^+ forms of the NS (NH_4-NS) samples were then dried at 120 °C for 12 hours. Thereafter, the NH_4-NS samples were calcined in static air at 550 °C for 1 hour

(heating rate: 3 °C/min, temperature ramp time: 3 hours) to release NH_3, resulting in the protonated (H^+) forms (Brosius, Kooyman & Fletcher, 2016 (Suppl.)).

For the latter method, after reducing Pt-loaded zeolites (see 4.1.3.3.2 and 4.3.2.3), H^+ as well as Pt^0 clusters are generated as shown in equation 2 (Philippaerts *et al.*, 2010):

$$Pt^{2+} + H_2 + Z^{2-} \rightarrow 2Pt^0 + (H^+)_2Z^{2-} \qquad \textbf{Equation 2}$$

4.1.3.3. Metal Loading

Pt was loaded onto the zeolites via two different techniques, namely incipient wetness impregnation (IWI) or competitive ion exchange (CIE) (Philippaerts *et al.*, 2010; Philippaerts *et al.*, 2011). Table 8 shows the zeolites loaded with Pt, corresponding techniques used to load Pt, and the corresponding target Pt loadings.

Table 8: Zeolite, techniques used to load Pt, and Pt loadings.

Zeolite	Technique	Pt loading (wt%)
H-NS-6-25a	IWI	0.9
H-NS-6-50a	IWI	0.9
H-NS-6-75a	IWI	0.9
H-NS-6-100a	IWI	0.9
Na-NS-6-25b	CIE	1
Na-NS-6-50b	CIE	1
Na-NS-6-75b	CIE	1
Na-NS-6-100b	CIE	1
C-NS-3-25a	CIE	1
C-NS-3-50a	CIE	1
C-NS-3-75a	CIE	1
C-NS-3-100a	CIE	1

4.1.3.3.1. Incipient Wetness Impregnation (IWI)

Prior to IWI, the total H_2O sorption capacities (incipient wetness points) of the H-NS-6-ya samples were determined by adding H_2O dropwise to 1 g of dry sample and mixing thoroughly. The incipient wetness points are shown in table 9.

Table 9: Incipient wetness points of the H-NS-6-ya samples.

Zeolite	Incipient wetness point (ml/g)
H-NS-6-25a	1.53
H-NS-6-50a	1.61
H-NS-6-75a	1.70
H-NS-6-100a	1.79

For IWI, 0.3226 g of tetrammine platinum (II) nitrate solution ($Pt(NH_3)_4(NO_3)_2$, Alfa Aesar, 2.79%) was diluted with H_2O up to the corresponding incipient wetness points (table 9). Thereafter, the solutions were added at once to the corresponding 1 g dry samples, mixed thoroughly and dried at room temperature for 2 – 3 days (Brosius, Kooyman & Fletcher, 2016 (Suppl.)).

4.1.3.3.2. Competitive Ion Exchange (CIE)

For CIE, the C-NS-3-ya samples were used. On the other hand, prior to CIE, the C-NS-6-yb samples were ion exchanged via 2 successive steps to ensure that the samples are completely in their Na^+ forms. In the first step, the C-NS-6-yb samples were converted into the NH_4-NS-6-yb forms. Initially, the samples were ion exchanged with NH_4^+ in a 1 l ammonium hydroxide (NH_4OH) solution with pH 10 (Philippaerts *et al.*, 2010). For each sample, this step was carried out in duplicate. The masses of the samples used in each case are shown in table 10. Solutions were shaken for 15 minutes. Then, for each sample, the products were filtered sequentially. Thereafter, the products were washed with 3 x 2.5 l H_2O and dried at 120 °C for 3 hours.

Table 10: Masses of C-NS-6-yb ion exchanged with NH_4^+.

Zeolite	Mass (g)
C-NS-6-25b	0.95
C-NS-6-50b	0.91
C-NS-6-75b	1.02
C-NS-6-100b	0.97

In the second step, the NH_4-NS-6-yb samples were converted into the Na-NS-6-yb forms. 300 ml of H_2O was added to 17.532 g of sodium chloride (NaCl) and NH_4-NS sample. The masses of the NH_4-NS samples used in this ion exchange step are shown in table 11. The solutions were left to stir at room temperature for 16 hours (Philippaerts *et al.*, 2010). Thereafter, the products were filtered, washed with 4 x 2.5 l H_2O to rinse away all Cl^- ions and dried at 120 °C for 3 hours.

Table 11: Masses of NH_4-NS-6-yb ion exchanged with Na^+.

Zeolite	Mass (g)
NH_4-NS-6-25b	1.76
NH_4-NS-6-50b	1.72
NH_4-NS-6-75b	1.87
NH_4-NS-6-100b	1.82

For CIE, 300 ml of H_2O was added to 0.1122 g of NaCl, 0.0270 g of tetraammine platinum (II) chloride monohydrate ($Pt(NH_3)_4Cl_2 \cdot H_2O$, Alfa Aesar) and 1.5 g of C-NS-3-ya or Na-NS-6-yb sample. The solution was left to stir at room temperature for 48 hours (Philippaerts *et al.*, 2010). Thereafter, the sample was filtered, washed with 4 x 2.5 l H_2O to rinse away all Cl^- ions and dried at room temperature for 2 – 3 days.

4.2. Characterization

4.2.1. Characterization of SDAs

The SDAs were identified by ^1H NMR Spectroscopy. The spectra were recorded on a 400 MHz Varian Unity NMR spectrometer. The ^1H chemical shifts were externally referenced to deuterated chloroform ($CDCl_3$). In a typical experiment, 10 mg of SDA was dissolved in 0.7 ml of $CDCl_3$ (Institute of Chemistry, the Hebrew University of Jerusalem, n. d.). The ^1H content in the SDAs was determined by integration of the NMR signals using the MestReNova version 11.0 software package.

4.2.2. Characterization of Catalysts

MFI zeolite nano-sheets were characterized by various characterization techniques including X-ray Diffraction (XRD), Bright-field Transmission Electron Microscopy (TEM), Nitrogen (N_2) Physisorption, Ammonia Temperature Programmed Desorption (NH_3-TPD) and ^{27}Aluminium Magic Angle Spinning Solid-State Nuclear Magnetic Resonance (^{27}Al MAS SSNMR) Spectroscopy. Bulk MFI (H-MFI-90, Si/Al = 45, Süd Chemie AG) was used as a reference sample. Pt-loaded nano-sheets were characterized by TEM, Inductively Coupled Plasma Optical Emission Spectrometry (ICP-OES) and Carbon Monoxide (CO) Chemisorption. The information obtained by the various techniques is given in table 12.

Table 12: Information obtained by the various characterization techniques.

Technique	Information
XRD	MFI framework topology
TEM	Confirmation of nano-sheets, thickness range and average thickness of nano-sheets, Pt particle size distribution, average Pt particle size, Pt dispersion
N_2 Physisorption	Micropore volume, external surface area, mesopore pore size distribution
NH_3-TPD	Acid site strength, total acid site concentration
^{27}Al MAS SSNMR Spectroscopy	% Al distribution: • % FAl (Al^{IV}) • % EFAl in pentahedral coordination (Al^{V}) • % EFAl in octahedral coordination (Al^{VI})
ICP-OES	Pt content (wt%)
CO Chemisorption	Average Pt size

4.2.2.1. X-ray Diffraction (XRD)

X-ray Diffraction (XRD) was performed on a Bruker D8 Advance diffractometer equipped with a position-sensitive detector and an X-ray tube comprising a cobalt (Co) Kα radiation source. Measurements were made with the X-ray tube at 35 kV and 40 mA. The wavelength of Kα1 ($\lambda_{K\alpha1}$) emitted by Co was 1.78897 Å. The XRD patterns were recorded in the 2θ range 5 – 80° with a step size of 0.03174° and dwell time of 1.04835 s per step.

4.2.2.2. Transmission Electron Microscopy (TEM)

Bright-field Transmission Electron Microscopy (TEM) micrographs were acquired using an FEI Tecnai F20 instrument equipped with a field emission gun and operated at 200 kV. Each sample was suspended in ethanol and dispersed over a carbon film-coated copper grid prior to measurements. Nano-sheet thickness and Pt size were measured using the ImageJ 1.50i software. For determining the thickness range and average thickness of nano-sheets, 100 nanosheets were measured for each sample. For determining Pt particle size distribution and average Pt particle size (d_{Pt}), 300 Pt particles were counted assuming spherical particles (Dune Sciences, Inc., 2011). The Pt dispersion (γ_{Pt}) was calculated using equation 3 (Verheyen *et al.*, 2013):

$$\gamma_{Pt} = \frac{101.6}{d_{Pt}}$$ **Equation 3**

4.2.2.3. Nitrogen (N_2) Physisorption

Nitrogen (N_2) Physisorption was performed on a MicroMeritics TriStar II 3020 instrument. Prior to physisorption, 0.2 g of sample was degassed at 350 °C under vacuum for 12 hours to remove any moisture and other adsorbates from the sample (Brosius, Kooyman & Fletcher, 2016). N_2 physisorption was performed at liquid N_2 temperature (-196 °C), with 10 s allowed for equilibration at each pressure. The micropore volume (V_{micro}) and external surface area (S_{ext}) were calculated using the *t*-plot method, with statistical thickness of adsorbed N_2 in the range 0.35 – 0.60 nm (Hudec *et al.*, 2002; Lowell *et al.*, 2004). The mesopore pore size distribution (PSD) was calculated using the Barret-Joyner-Halenda (BJH) model from the desorption branch of the isotherm (Barrett, Joyner & Halenda, 1951).

4.2.2.4. Ammonia Temperature Programmed Desorption (NH_3-TPD)

Ammonia Temperature Programmed Desorption (NH_3-TPD) was performed on a MicroMeritics Autochem 2920 instrument equipped with a thermal conductivity detector (TCD). 0.25 g of sample was heated to 600 °C at 10 °C/min under a helium (He) flow of 50 cm^3/min to remove any moisture and other adsorbates from the sample. The sample was cooled to 100 °C and saturated with NH_3 under a 1 mol % NH_3 in He flow of 50 cm^3/min for 30 minutes. The sample was exposed to a He flow of 50 cm^3/min for 2 hours to remove physisorbed NH_3. The NH_3-TPD profile was obtained while heating from 100 °C to 600 °C at 5 °C/min under a He flow of 50 cm^3/min (Brosius, Kooyman & Fletcher, 2016). The total acid site concentration ([TAS]) was derived from the NH_3-TPD profiles using equations 4 – 7 assuming one NH_3 molecule chemisorbed per acid site:

$$[TAS] = \frac{n_{NH_3\ Chemisorbed}}{m_{Dry\ zeolite}} \times 1000$$ **Equation 4**

$$n_{NH_3\ Chemisorbed} = \frac{\int_{t_3}^{t_4} I_{TCD\ signal}(t)\,dt \times n_{NH_3\ Adsorbed}}{\int_{t_1}^{t_2} I_{TCD\ signal}(t)\,dt}$$ **Equation 5**

$$n_{NH_3\ Adsorbed} = \frac{\int_{t_1}^{t_2} I_{TCD\ signal}(t)\,dt \times n_{NH_3\ in\ He}}{[I_{TCD\ signal}(t_1) - I_{TCD\ signal}(t_2)] \times [t_2 - t_1]}$$ **Equation 6**

$$n_{NH_3\ in\ He} = \frac{F_{1\%\ NH_3\ in\ He} \times [t_2 - t_1]}{V_m} \times 1\%\ NH_3\ in\ He \qquad \textbf{Equation 7}$$

Where:

$[TAS]$ = Total acid site concentration (mmol/g)

$n_{NH_3\ Chemisorbed}$ = moles of NH_3 chemisorbed

$n_{NH_3\ Adsorbed}$ = moles of NH_3 adsorbed

$n_{NH_3\ in\ He}$ = moles of NH_3 in He

$m_{Dry\ zeolite}$ = mass of dry zeolite (g)

$I_{TCD\ signal}\ (t)$ = Intensity of TCD signal as a function of time (t) (a.u.)

t_1 = 0.5 min

t_2 = 30 min

t_3 = 150 min

t_4 = 250 min

$F_{1\%\ NH_3\ in\ He}$ = 1% NH_3 in He gas flow rate (l/min)

V_m = Standard molar volume = 22.4 (l/mol)

The theoretical Al concentration ($[Al]_T$) was determined using equation 8:

$$\left.\begin{aligned} [Al]_T &= \frac{x_{Al,T}}{M_{Zeolite}} \times 1000 \\ x_{Al,T} &= \frac{1}{1 + (Si/Al)_T} \end{aligned}\right\} [Al]_T = \frac{1000}{M_{Zeolite}(1 + (Si/Al)_T)} \qquad \textbf{Equation 8}$$

Where:

$[Al]_T$ = Theoretical Al concentration (mmol/g)

$x_{Al,T}$ = Theoretical mole fraction of Al in zeolite

$M_{Zeolite}$ = Molar mass of zeolite (g/mol)

$(Si/Al)_T$ = Theoretical Si/Al ratio (mol/mol)

4.2.2.5. ^{27}Aluminium Magic Angle Spinning Solid-State Nuclear Magnetic Resonance (^{27}Al MAS SSNMR) Spectroscopy

^{27}Aluminium Magic Angle Spinning Solid-State Nuclear Magnetic Resonance (^{27}Al MAS SSNMR) spectra were recorded on an Agilent VNMRS Wide Bore 500 MHz NMR spectrometer with a ^{27}Al frequency of 130.196 MHz and ^{1}H frequency of 500 MHz using 4 mm zirconia rotors and a 4 mm

T3 HX Magic Angle Spin NMR probe. For the ^{27}Al Single Pulse (SP) MAS experiments, a single excitation pulse of 1.2 µs and MAS rate of 10 kHz were used with high power ^{1}H decoupling. The ^{27}Al chemical shifts (δ) were externally referenced to a saturated aluminium nitrate nonahydrate ($Al(NO_3)_3 \cdot 9H_2O$) aqueous solution. Prior to NMR measurements, the samples were fully hydrated in a desiccator. In a typical experiment, approximately 50 mg of hydrated sample was packed in the rotor (Almutairi *et al.*, 2013; Wu *et al.*, 2014; Zhu *et al.*, 2015). From the spectra obtained, the % Al distribution was estimated using peak areas obtained from spectral deconvolution of the respective signal components using the MestReNova version 11.0 software package.

4.2.2.6. Inductively Coupled Plasma Optical Emission Spectrometry (ICP-OES)

Inductively Coupled Plasma Optical Emission Spectrometry (ICP-OES) was performed using a Varian ICP-OES 730 series spectrometer. Argon (Ar) was used as plasma source and carrier gas. 50 mg of sample was digested in a mixture containing 6 ml of hydrochloric acid (HCl), 2 ml of hydrofluoric acid (HF) and 2 ml of nitric acid (HNO_3). The resulting mixture was left overnight at room temperature to allow the sample to dissolve. Thereafter, the solution was placed in a MARS-5 microwave digester in which the sample was heated to 180 °C for 25 minutes and kept at this temperature for 40 minutes. Following digestion, the sample was diluted up to concentrations within the calibration range of the ICP-OES instrument (200 – 5000 ppb).

4.2.2.7. Carbon Monoxide (CO) Chemisorption

Carbon Monoxide (CO) Chemisorption was performed on a MicroMeritics ASAP 2020 instrument equipped with a Pfeiffer MVP015-2 vacuum pump. Prior to chemisorption, 0.1 g of sample was calcined at 350 °C for 1 hour (heating rate: 0.3 °C/min) in the presence of oxygen (O_2) (flow rate: 120 cm^3/min). The sample was cooled to 35 °C (heating rate: 10 °C/min) then evacuated at 35 °C for 15 minutes. The sample was reduced at 225 °C for 1 hour (heating rate: 0.4 °C/min) in the presence of H_2 (flow rate: 120 cm^3/min). The sample was cooled to 35 °C (heating rate: 10 °C/min) then evacuated at 35 °C for 15 minutes. An automated leak test was performed at 35 °C for 1 minute with a maximum allowed outgas rate of 100 µmHg/min. The sample was evacuated at 35 °C for 40 minutes. CO chemisorption was performed by dosing the sample with CO at 35 °C and various pressures in the range 0.1 – 600 mmHg, with 20 s allowed for equilibration at each pressure. The average Pt particle size was calculated using equation 9:

$$d_{Pt} = \frac{6}{A_{Sm}\gamma_{Pt}\rho_{Pt}} \times 10^9 \qquad \textbf{Equation 9}$$

Where:

d_{Pt} = Average Pt particle size (nm)

A_{Sm} = Active area per gram of pure Pt (m^2/g)

γ_{Pt} = Pt dispersion (%)

ρ_{Pt} = Density of Pt = 21.45 g/cm^3

A_{Sm} was calculated using equation 10:

$$A_{Sm} = \frac{V_{mon} N_A F_S A_{CO}}{\frac{m_{Pt}(\%)}{100} V_m} \qquad \textbf{Equation 10}$$

Where:

V_{mon} = Monolayer volume adsorbed at STP (m^3/g) determined using the average of the final four values of the volume adsorbed on the difference curve

N_A = Avagadro's number

F_S = Stoichiometry factor = 1 for CO adsorption on Pt

A_{CO} = Cross-sectional area of CO = 7.87 x 10^{-20} m^2

$m_{Pt}(\%)$ = wt% of Pt determined by ICP-OES

V_m = Standard molar volume = 2.24 x 10^{-2} m^3/mol

γ_{Pt} was calculated using equation 11:

$$\gamma_{Pt} = \frac{\frac{V_{mon}}{V_m}}{\frac{m_{Pt}(\%)}{M_{Pt}}} \qquad \textbf{Equation 11}$$

Where:

M_{Pt} = Molar mass of Pt (g/mol)

4.3. Hydrocracking of n-Hexadecane (n-C_{16})

4.3.1. Hydrocracking Test Unit

A process flow diagram of the hydrocracking test unit is shown in figure 7. The unit consists of a trickle-phase reactor equipped with a vaporizer and on-line gas chromatography flame ionization detector (GC-FID). Two units are operated in parallel. Various components of the unit and the hydrocracking procedures applied are described in the following sections.

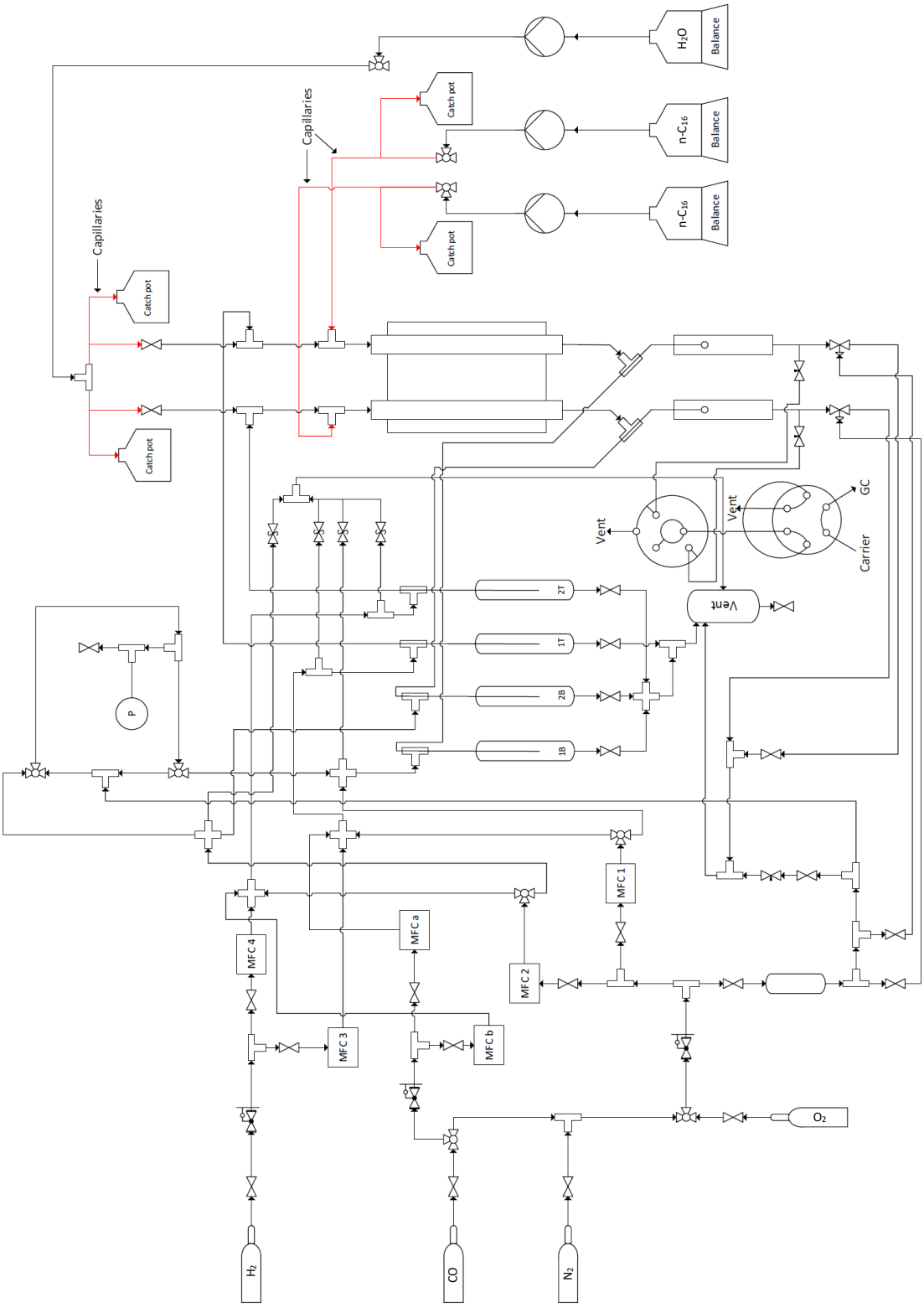

Figure 7: Process flow diagram of hydrocracking test unit.

4.3.1.1. Gas Feed Supply

The gas feed (N_2, O_2 or H_2) was supplied from the main house lines at 100 bar pressure. Tescom pressure-reducing regulators were used to step down the pressure to 50 bar. Brooks thermal mass flow controllers (MFCs) were used to measure and control the gas flow rate. The gas feed from the MFCs flows through a dip-tube into a guard catch pot. Subsequently, the flow proceeds under pressure through the dip-tube to the reactor. Also, the guard catch pot provides a safety mechanism for the MFCs by preventing back-flow of liquid from the reactors to the MFCs. Any back-flow of liquid from the reactors would first flow through the dip-tube and collect into the guard catch pot before flowing up the dip-tube to the MFCs.

4.3.1.2. Liquid Feed Supply

The liquid feed pots containing n-C_{16} or H_2O were placed on A & D GX-4000 or Mettler Toledo laboratory balances, respectively, to verify the liquid feed rate. Lab Alliance Series 1 high pressure liquid chromatography (HPLC) pumps were used to pump liquid to the reactor. Each pump was equipped with a pulse dampener to ensure a smooth flow of liquid. A set of fused silica capillaries (50 µm internal diameter (ID)) was used to administer H_2O to the reactor.

4.3.1.3. Reactor

The reactor consists of the following components:

- ¾" Stainless steel cylindrical tube with an ID of 16 mm and a length of 360 mm.
- Internally embedded thermowell with an outer diameter (OD) of 3 mm passing through the length of the reactor.
- Reactor head comprising two inlet ports, one for the gaseous feed and the other for the liquid feed.

A brass housing serves as a heating block for two reactor tubes. The heating block was heated by four individually controlled heating elements. The temperature was controlled using Gefran 800P temperature controllers. The reactor was operated at 225 °C in the isothermal catalyst bed zone. The heating block was well insulated with an insulating jacket.

4.3.1.4. Vaporizer

The vaporizer was made of stainless steel with an ID of 10.2 mm, length of 500 mm and wall thickness of 1.25 mm. The vaporizer was housed in a metal conduit with an ID of 25 mm. A heating wire was wrapped around the metal conduit to allow the temperature along the length of the vaporizer to gradually increase. The temperature was controlled using Gefran 600P

temperature controllers. The vaporizer was well insulated with glass wool and was filled with silicon carbide (SiC).

The reactor effluent, partly liquid and partly vapour, flows into the top of the vaporizer where it spreads over the SiC packing 5 cm above the point where the dilution gas enters through a dip-tube. The reactor effluent cools down to 175 °C between the reactor and vaporizer. A constant flow of N_2 dilution is fed to the vaporizer, where it brings about partial evaporation of the reactor effluent. Full evaporation is achieved gradually along the length of the vaporizer due to the temperature gradient of approximately 1.5 °C/cm from 175 °C to 235 °C. The needle valve at the bottom of the vaporizer releases a small stream of the diluted, fully gaseous effluent to an online gas chromatograph (GC). The bulk of the diluted effluent passes through the back-pressure regulator to the vent (Brosius & Fletcher, 2014; Brosius, Kooyman & Fletcher, 2016 (Suppl.)).

4.3.2. Catalyst Pretreatment

4.3.2.1. Reactor Loading

The reactor tube was placed in an upright position in a bench vise. The reactor is equipped with a metal grid and felt basket in the isothermal zone. For all experiments conducted, 1 g of Pt-loaded catalyst was loaded into the reactor. Glass wool was placed on top of the catalyst bed. Another basket and stainless steel coiled wire was slid down the reactor tube using a 15 mm OD rod with a groove for the wire to close the catalyst zone. The reactor head was fitted with a gasket onto the reactor body.

4.3.2.2. Calcination

Catalysts were calcined *in-situ* at 350 °C for 1 hour (heating rate: 0.2 °C/min) in the presence of O_2. The O_2 flow rates for the various catalysts are shown in table 13. Thereafter, catalysts were cooled to 225 °C under N_2.

Table 13: O_2 flow rates during calcination.

Catalyst	O_2 flow rate (ml/min)
Pt/H-NS-6-25a	120
Pt/H-NS-6-50a	120
Pt/H-NS-6-75a	120
Pt/H-NS-6-100a	120
Pt/C-NS-3-25a	250
Pt/C-NS-3-50a	250
Pt/C-NS-3-75a	250
Pt/C-NS-3-100a	250
Pt/Na-NS-6-25b	250
Pt/Na-NS-6-50b	250
Pt/Na-NS-6-75b	250
Pt/Na-NS-6-100b	250

4.3.2.3. Reduction

Catalysts were reduced *in-situ* at 225 °C (heating rate: 0.2 °C/min) in the presence of H_2 (flow rate: 120 ml/min). The reduction times for the various catalysts are shown in table 14.

Table 14: Reduction times.

Catalyst	Reduction time (hours)
Pt/H-NS-6-25a	8
Pt/H-NS-6-50a	8
Pt/H-NS-6-75a	8
Pt/H-NS-6-100a	8
Pt/C-NS-3-25a	24
Pt/C-NS-3-50a	24
Pt/C-NS-3-75a	24
Pt/C-NS-3-100a	24
Pt/Na-NS-6-25b	24
Pt/Na-NS-6-50b	24
Pt/Na-NS-6-75b	24
Pt/Na-NS-6-100b	24

4.3.3. Hydrocracking Procedure

4.3.3.1. Start-up Procedure

The following procedure was used for the start-up of all experiments conducted:

- Clean the reactors with acetone to remove residual catalyst, reactants and products.
- Follow the procedure for reactor loading (see 4.3.2.1).
- Place the reactors in the appropriate heating blocks.
- For each reactor:
  - Fit the gas line with a gasket onto the gas feed inlet of the reactor.
  - Fit a cap onto the liquid feed inlet of the reactor to prevent reduction of the metal by reducing agents in the n-C_{16} line after calcination.
  - Fit the product outlet of the reactor with a gasket onto the vaporizer.
- Cover the base of the reactors with glass wool.
- Cover the heating block with the insulating jacket.
- Open the N_2 gas two-way valve.
- Set the back-pressure regulators to 20 bar.
- Open the O_2 gas two-way valve. Follow the procedure for catalyst calcination. Close the O_2 gas two-way valve.

- Open the N_2 dilution gas two-way valve. Set the N_2 feed inlet MFC to a N_2 flow rate of 120 ml/min. This removes any remaining O_2 in the reactors preventing production of H_2O during reduction.
- Open the H_2 gas two-way valve. Follow the procedure for catalyst reduction.
- For each reactor:
    - Remove the cap from the liquid feed inlet of the reactor. Fit the n-C_{16} line with a gasket onto the liquid feed inlet of the reactor.
- Open the N_2 dilution gas two-way valve. Set the N_2 feed inlet MFC to a N_2 flow rate of 250 ml/min. Allow the reactors to pressurize for 1 hour. This helps to increase the flow of n-C_{16} through the capillary into the liquid feed inlet of the reactor, preventing backflow of n-C_{16} into the catch pots.
- Set the temperature of the reactors to their reaction temperatures. Switch on the temperature controllers to maintain the set temperatures.
- Set the n-C_{16} liquid feed inlet valves away from the reactors. Prime the n-C_{16} HPLC pumps for approximately 30 s. Collect the liquid feed in catch pots during priming.
- Fill the n-C_{16} pots with recycled n-C_{16} collected from catch pots. Re-zero the balances before loading the n-C_{16} pots.
- Set the n-C_{16} liquid feed inlet valves towards the reactors. Set the n-C_{16} flow rate to 0.09 ml/min on the HPLC pump. Set the H_2 flow rate to 16 ml/min to feed n-C_{16} with a flow rate of 0.02 ml/min. Collect the excess n-C_{16} (0.07 ml/min) in catch pots.
- Record the time and feed pot balance for n-C_{16} feed verification calculations.
- Start the on-line gas chromatogram sampling.

4.3.3.2. Co-feeding of H_2O

- Set the H_2O liquid feed inlet valves away from the reactors. Prime the H_2O HPLC pumps for approximately 30 s. Collect the liquid feed in catch pots during priming.
- Fill the H_2O pots with H_2O. Re-zero the balances before loading the H_2O pots.
- Set the H_2O liquid feed inlet valves towards the reactors. Set the H_2O flow rate to 0.16 ml/min on the HPLC pump.
- Record the time and feed pot balance for H_2O feed verification calculations.

4.3.3.3. On-line Procedure

4.3.3.3.1. Temperature

The temperature is adjusted using a set of Gefran 800P temperature controllers. H_2 and n-C_{16} flow commences at 225 °C. Steady state is reached after 24 hours on stream. Sample each of four

parallel reactors for 12 hours time-on-stream at steady state before changing the temperature. In the absence of H_2O (dry hydrocracking) and presence of H_2O (wet hydrocracking), the hydrocracking temperatures for the various catalysts are shown in tables 15 – 17. For each catalyst, temperatures are shown from the start to the end of an experiment.

Table 15: Dry and wet hydrocracking temperatures for the Pt/H-NS-6-ya catalysts.

Catalyst	Temperature (°C)										
	Dry hydrocracking							Wet hydrocracking			
Pt/H-NS-6-25a	225	215	205	195	185	-	-	235	245	255	265
Pt/H-NS-6-50a	225	215	205	195	185	-	-	235	245	255	265
Pt/H-NS-6-75a	225	215	205	195	230	235	245	245	255	265	275
Pt/H-NS-6-100a	225	215	205	195	230	235	245	245	255	265	275

Table 16: Dry and wet hydrocracking temperatures for the Pt-H/C-NS-3-ya catalysts.

Catalyst	Temperature (°C)									
	Dry hydrocracking					Wet hydrocracking				
Pt-H/C-NS-3-25a	225	215	205	195	185	235	245	255	265	275
Pt-H/C-NS-3-50a	225	215	205	195	185	235	245	255	265	275
Pt-H/C-NS-3-75a	225	215	205	235	245	245	255	265	275	285
Pt-H/C-NS-3-100a	225	215	205	235	245	245	255	265	275	285

Table 17: Dry and wet hydrocracking temperatures for the Pt-H/Na-NS-6-yb catalysts.

Catalyst	Temperature (°C)												
	Dry hydrocracking						Wet hydrocracking						
Pt-H/Na-NS-6-25b	225	215	205	195	235	-	235	245	255	265	275	285	295
Pt-H/Na-NS-6-50b	225	215	205	195	235	-	235	245	255	265	275	285	295
Pt-H/Na-NS-6-75b	225	215	205	195	235	245	245	255	265	275	285	295	-
Pt-H/Na-NS-6-100b	225	215	205	195	235	245	245	255	265	275	285	295	-

4.3.3.4. Shutdown Procedure

The following procedure describes a normal shut-down procedure, which excludes the cooling of the vaporizer, GC-FID selection/injection valves and the overhead lines:

- Stop the sampling on the on-line GC.
- Switch off all HPLC pumps.

- Close all liquid feed inlet valves.
- Set all gas MFCs to closed.
- Close all gas manifold valves.
- Gradually lower the pressure in reactors to 1 bar and allow to cool.
- Gradually lower the back-pressure regulators to 1 bar.

4.3.4. Product Analysis

4.3.4.1. Gas Chromatography (GC)

The reactor products were analyzed by gas chromatography (GC) using a Varian CP-3900 on-line gas chromatograph equipped with a non-polar CP-Sil 5 CB column (25 m, 0.15 mm ID, 2 µm thickness stationary phase) and flame ionization detector (FID) and the Galaxie Chromatography Data System software package. H_2 was used as a carrier gas and fuel for the FID. Pressurized synthetic air was used to operate the automatic selection valve and as an oxidant source for the FID flame.

4.3.4.1.1. Sampling Procedure

The sampling procedure makes use of a 4-way selection valve and a 6-way injection valve. To sample the individual reactors, the following general procedure was executed:

- The selection valve is set to sample *a* inlet and the injection valve is set to the vent allowing the sample loop to be filled with product from reactor *a*.
- The injection valve is switched to the GC-FID allowing product from reactor *a* to be injected onto the column. Reactor *a* is vented through the injection valve while reactor *b* remains vented through the selection valve.
- The selection valve is switched to sample *b* inlet and the injection valve is switched back to the vent allowing the sample loop to be filled with product from reactor *b*.
- The carrier gas and product from reactor *a* flow through the GC-FID. The product from the reactor *a* is analyzed.
- The system is flushed, and the injection valve is switched to the GC-FID allowing product from reactor *b* to be injected onto the column. Reactor *b* is vented through the injection valve while reactor *a* remains vented through the selection valve.
- Following reactor *b* product analysis and system flush, the selection valve and injection valve are switched back to their initial state. The process repeats itself.

4.3.4.1.2. Gas Chromatography Flame Ionization Detector (GC-FID) Data Determination

The raw data output from GC-FID comprised a standard gas chromatogram with peak identification and variable baseline for integration. Peak areas in a chromatogram are directly proportional to the number of carbon atoms in a molecule (i) and molar flow rate of a carbon molecule (F_{C_i}). For each run, C_1 and C_2 products were grouped separately. The groupings of remaining carbon number fractions are shown in table 18. Grouping is necessary due to the difficulty in separating and identifying individual molecule fractions with high carbon numbers.

Table 18: Groupings of carbon number fractions.

Carbon number fraction	Grouping
C_3	• Paraffins • Olefins
$C_4 – C_5$	• Linear paraffins • Linear olefins • Paraffinic isomers • Olefinic isomers
$C_6 – C_{12}$	• Linear paraffins • Linear olefins • Mono-branched paraffinic isomers • Multi-branched paraffinic isomers • Olefinic isomers
$C_{13} – C_{16}$	• Linear paraffins • Mono-branched paraffinic isomers • Multi-branched paraffinic isomers

The conversion of n-C_{16} ($X_{n\text{-}C_{16}}$) was determined by equation 12:

$$X_{n-C_{16}} = \left(1 - \frac{Area\ n{-}C_{16}\ peak}{\sum_{i=1}^{i=16} Area\ C_i\ peak}\right) \qquad \textbf{Equation 12}$$

The reaction rate (r) was determined by equation 13:

$$r = \frac{F_{n-C_{16}} X_{n-C_{16}}}{m} \qquad \textbf{Equation 13}$$

Where:

$F_{n-C_{16}}$ = Molar flow rate of n-C_{16} (mol/g/s)

m = mass of catalyst (g)

The yield of isomerization products (Y(iso-C_{16})) was determined by equation 14:

$$Y(iso - C_{16}) = X_{n-C_{16}} \times \frac{Area\ iso{-}C_{16}\ peak}{\sum_{i=1}^{i=16} Area\ C_i\ peak} \qquad \textbf{Equation 14}$$

The yield of cracking products (Y(C_1-C_{15})) was determined by equation 15:

$$Y(C_1 - C_{15}) = X_{n-C_{16}} \times \left(1 - \frac{Area\ iso{-}C_{16}\ peak}{\sum_{i=1}^{i=16} Area\ C_i\ peak}\right) \qquad \textbf{Equation 15}$$

The C_4/C_{12} molar ratio was determined by equation 16:

$$\frac{C_4}{C_{12}} = \frac{F_{C_4}}{F_{C_{12}}} = \frac{12 \times Area\ C_4\ peak}{4 \times Area\ C_{12}\ peak} \qquad \textbf{Equation 16}$$

Chapter 5. Results and Discussion

5.1. Characterization of MFI Zeolite Nano-sheets

5.1.1. NS-6-ya

H-NS-6-ya samples were characterized by XRD, TEM, N_2 physisorption, NH_3-TPD and ^{27}Al MAS SSNMR spectroscopy. Bulk MFI (Si/Al = 45) was used as a reference sample.

5.1.1.1. XRD

XRD was used to confirm the MFI framework topology of the H-NS samples. XRD patterns of bulk MFI and the H-NS samples as a function of d-spacing (d) are shown in figure 8. The H-NS samples display reflections characteristic of the MFI framework topology, thus confirming the MFI topology. For the H-NS samples, reflections in the [*h*0*l*] crystallographic directions appear, corresponding to in-plane (*ac* plane) reflections (Choi *et al.*, 2009).

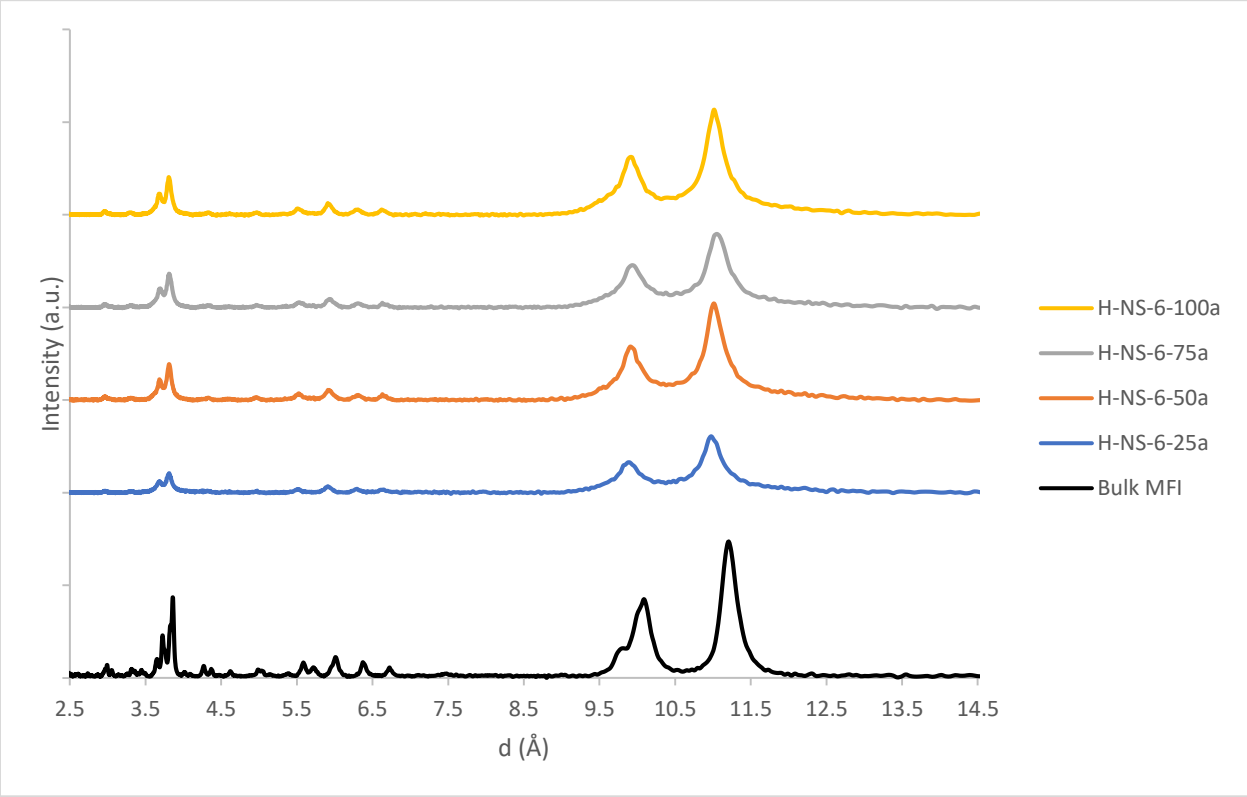

Figure 8: XRD patterns of bulk MFI and H-NS-6-ya samples.

5.1.1.2. TEM

TEM was used to confirm that the H-NS samples are nano-sheets. A TEM micrograph of bulk MFI is shown in figure 9. TEM micrographs of the H-NS samples are shown in figure 10 a – d. The micrographs of the H-NS samples confirm that the samples are nano-sheets. For each sample, the nanosheets exhibit a non-uniform thickness. The thickness range and corresponding average thickness are shown in table 19. MFI nano-sheets with a non-uniform thickness was reported by Wu *et al.* (2014). The average thickness of the C-NS samples is in reasonable agreement.

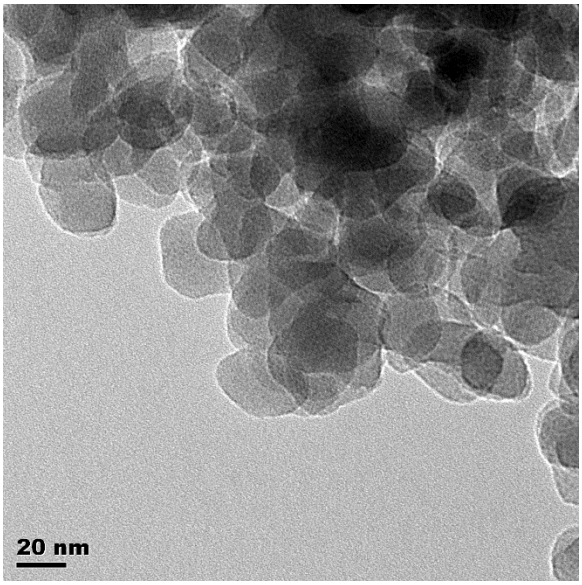

Figure 9: TEM micrograph of bulk MFI.

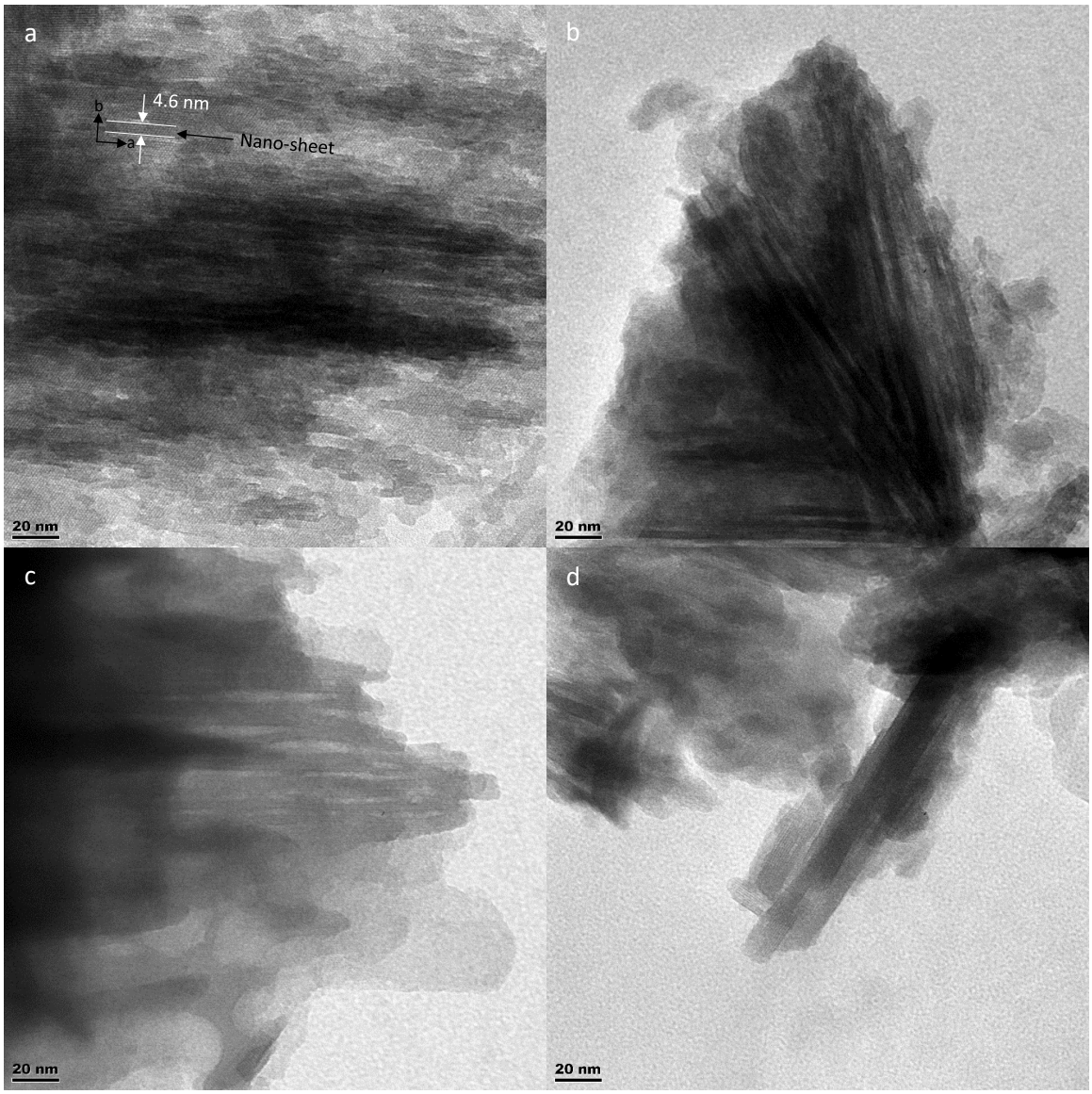

Figure 10: TEM micrographs of (a) H-NS-6-25a, (b) H-NS-6-50a, (c) H-NS-6-75a and (d) H-NS-6-100a.

Table 19: Thickness range and average thickness of H-NS-6-ya samples.

Zeolite	Thickness range (nm)	Average thickness (nm)
H-NS-6-25a	2.9 – 5.4	3.9 ± 0.7
H-NS-6-50a	2.5 – 6.0	3.5 ± 0.8
H-NS-6-75a	2.7 – 6.2	3.8 ± 0.6
H-NS-6-100a	3.0 – 9.6	3.8 ± 0.9

5.1.1.3. N_2 Physisorption

The V_{micro}, S_{ext} and mesopore PSD of the H-NS samples were determined by N_2 physisorption. The N_2 physisorption isotherms of bulk MFI and the H-NS samples are shown in figure 11.

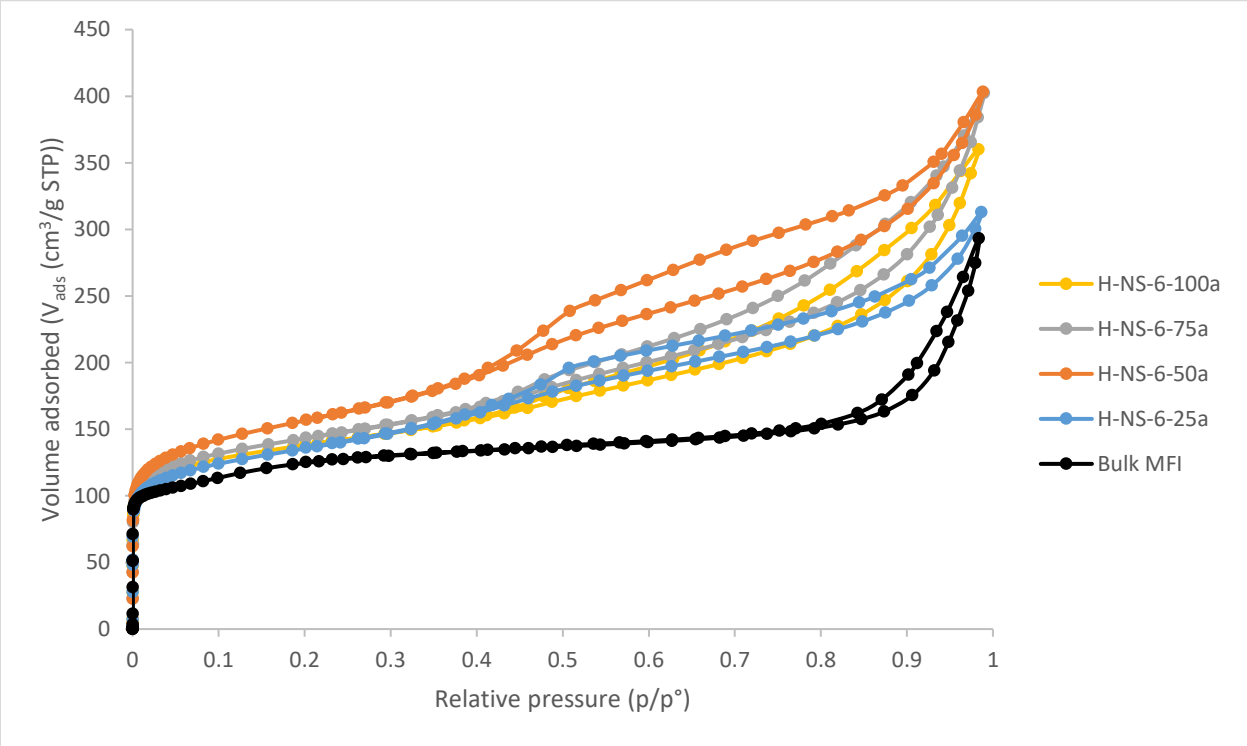

Figure 11: N_2 physisorption isotherms of bulk MFI and H-NS-6-ya samples.

The zeolites (bulk MFI and H-NS samples) display a combination of type I and type IV isotherms based on the International Union of Pure and Applied Chemistry (IUPAC) classification of isotherms (Sing *et al.*, 1985; Thommes *et al.*, 2015). For the zeolites, N_2 adsorption at low relative pressure (p/p_0) at approximately $0 < p/p_0 < 0.1$ corresponds to monolayer formation confirming the presence of micropores (Hudec *et al.*, 2002; Zhang, Yang & Yan, 2014). Bulk MFI displays a hysteresis loop at high p/p_0 at approximately $0.9 < p/p_0 < 1$. This can be attributed to capillary condensation owing to some macropores in the agglomerates of crystalline domains. H-NS samples display hysteresis loops from medium to high p/p_0 at approximately $0.45 < p/p_0 < 1$. The hysteresis loops are due to capillary condensation in mesopores between individual nano-sheets in the aggregates at approximately $0.45 < p/p_0 < 0.9$, and capillary condensation in some macropores between individual nano-sheets in the aggregates at approximately $0.9 < p/p_0 < 1$ (Sing *et al.*, 1985; Zhang, Yang & Yan, 2014; Thommes *et al.*, 2015).

The V_{micro} and S_{ext} of the zeolites derived from the isotherms are shown in table 20 (see 4.2.2.3).

Table 20: V_{micro} and S_{ext} of bulk MFI and H-NS-6-ya samples.

Zeolite	V_{micro} (cm^3/g)	S_{ext} (m^2/g)
Bulk MFI	0.13	141
H-NS-6-25a	0.08	300
H-NS-6-50a	0.08	382
H-NS-6-75a	0.10	271
H-NS-6-100a	0.10	234

As seen in table 20, the H-NS samples have a large V_{micro}, consistent with their zeolitic nature (Flanigen, 2001; Zhu *et al.*, 2015). The H-NS samples have a smaller V_{micro} than bulk MFI (> 20% difference). The *t*-plot method is known to underestimate the micropore volume of very small zeolite particles with high external surface area (Camblor, Corma & Valencia, 1998). An explanation for this is that the N_2 molecules that are adsorbed in the micropore apertures are counted as being adsorbed on the external surface of the particles (Aerts *et al.*, 2004). The smaller V_{micro} of the H-NS samples is most likely due to the much higher ratio of external surface compared to the surface of micropore channels. Another possible explanation for the smaller V_{micro} is structural mesoporosity (Lohse & Mildebrath, 1981). However, this is highly unlikely since structural mesopores could not be identified by TEM. Another possible explanation for the smaller V_{micro} is partial blockage of the micropore apertures by EFAl species (Marques *et al.*, 2003). However, this is highly unlikely for materials with these ultra-small dimensions and 3D pore structure. The H-NS samples have a larger S_{ext} than bulk MFI (> 20% difference) due to their higher dispersion (Verheyen *et al.*, 2013).

The mesopore PSDs of the zeolites derived from the isotherms are shown in figure 12 (see 4.2.2.3). The mode values of the mesopore sizes (maximum mesopore size in PSD) are shown in table 21. Application of the BJH method to bulk MFI confirms the absence of mesopores. The H-NS samples display narrow mesopore PSDs centred at approximately 4 nm. This could be due to the stacking of MFI nano-sheets during nano-sheet synthesis or to bulk MFI seeds in the synthesis mixture. Previously, when including bulk MFI in a synthesis mixture for MFI nano-sheets, it was found that an MCM-41-like phase initially formed, followed by zeolite formation (Jo *et al.*, 2014). Both materials exhibited uniform mesopore PSDs centred at approximately 4 nm. It is thought that during synthesis, bulk MFI seeds disintegrate into numerous sub-nanometre nuclei, which could be embedded everywhere in the MCM-41-like pore walls and could thereby start zeolite formation, resulting in the similarity of mesopore sizes between the MCM-41-like phase and nano-sheets.

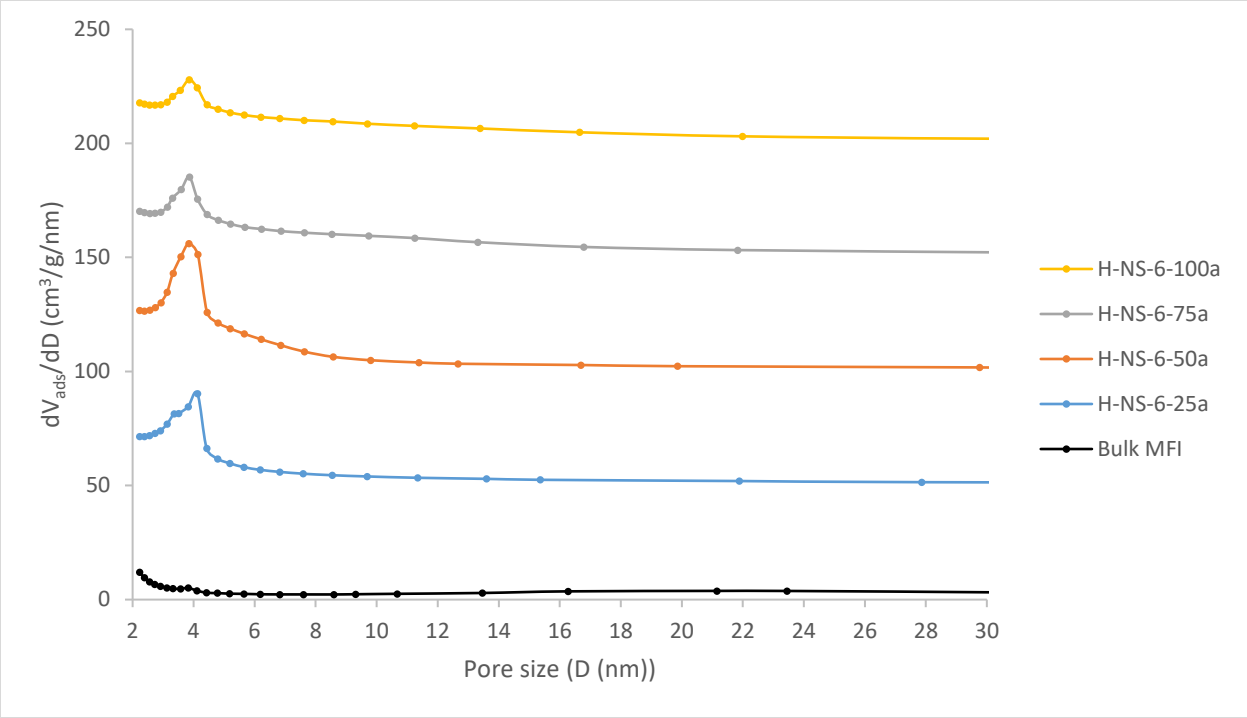

Figure 12: Mesopore PSDs of bulk MFI and H-NS-6-ya samples. The PSDs are vertically offset by equal intervals of 50 $cm^3/g/nm$.

Table 21: Mode value of the mesopore sizes of H-NS-6-ya samples.

Zeolite	Mesopore size mode value (nm)
H-NS-6-25a	4.1
H-NS-6-50a	3.8
H-NS-6-75a	3.9
H-NS-6-100a	3.9

5.1.1.4. NH_3-TPD

The acidity of zeolites can encompass Brønsted and Lewis acidity. Brønsted acidity is associated with FAl, as H^+ can compensate the negatively charged $Al(SiO)_4$ tetrahedra forming $H–Al(SiO)_4$ (Maxwell & Stork, 1991). Lewis acidity is associated with EFAl and extra-framework Si (EFSi) acting as electron pair acceptors. Lewis acidic EFAl include charged entities such as Al^{3+}, AlO^+ and $Al(OH)^{2+}$, the neutral entity $Al(OH)_3$, and lattice defect sites such as $Al(SiO)_3$, $Al(SiO)_2(OH)$ and $Al(SiO)(OH)_2$ (Uytterhoeven, Christner & Hall, 1965; Fyfe *et al.*, 1982; Klinowski *et al.*, 1983; Scherzer, 1984; Kazansky, 1988; Martens *et al.*, 1997; Wouters, Chen & Grobet, 1998; Lamberov *et al.*, 2000; Benco *et al.*, 2002; Jiao *et al.*, 2005; Huang *et al.*, 2008; Lisboa, Sánchez & Ruette,

2008). Lewis acidic EFSi includes the lattice defect site $Si(OAl)_3^+$ (Uytterhoeven, Christner & Hall, 1965; Kazansky, 1988). Since the TPD technique using NH_3 as a molecular probe is a well-known method of probing the acidity of zeolites, NH_3-TPD was conducted over bulk MFI and protonated (H)-NS samples. NH_3-TPD profiles of the zeolites are shown in figure 13. Hunger *et al.* (2002) suggested that NH_3 could be a suitable probe for all H^+ sites accessible through pores, channels, or windows with sizes ≥ 4 Å due to its small molecular dimensions (3.70 x 3.99 x 3.11 $Å^3$).

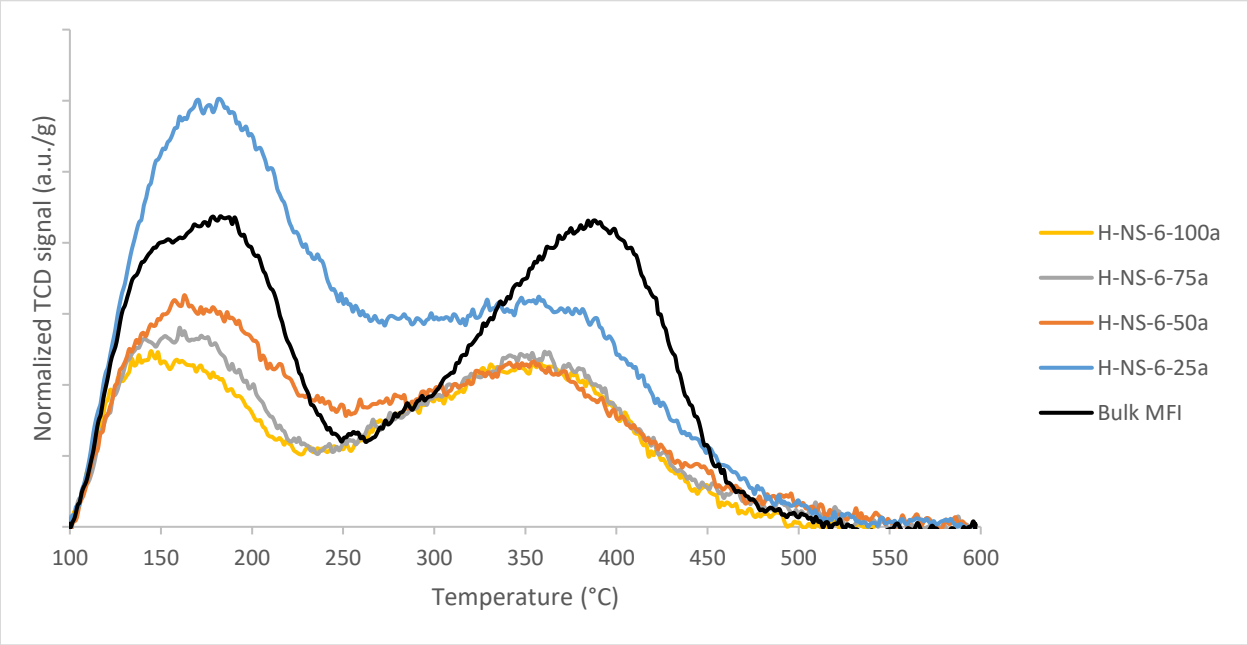

Figure 13: NH_3-TPD profiles of bulk MFI and H-NS-6-ya samples.

In the case of bulk MFI and H-NS samples, two separate peaks can be distinguished in the TPD profiles of the zeolites (figure 13). It has been generally accepted that the TPD peak position is directly related to the strength of the acid sites. Therefore, the low temperature desorption peaks, which can be observed from approximately 100 °C to approximately 275 °C, are due to weak acid sites, whereas the high temperature desorption peaks, which can be observed from approximately 275 °C to approximately 550 °C, are due to strong acid sites (Jentys & Lercher, 2001; Kim, Jung & Park, 2010; Zhu *et al.*, 2015). Wang, Wang & Li (2006) suggested that the low temperature peak mainly consists of the acid sites with strength H_0 in the range from -3.0 to +2.27 and the high temperature peak mainly consists of the acid sites with strength $H_0 \leq -3.0$ in bulk MFI. As seen in figure 13, for the H-NS samples, the strength of the acid sites is virtually constant with varying Si/Al ratio, in line with Kim *et al.* (2016). Bulk MFI with Si/Al = 45 contains slightly stronger acid sites than the H-NS samples, in line with Brosius, Kooyman and Fletcher

(2016). This could be due to a higher concentration of H^+ sites at the channel intersections in bulk MFI in comparison to the H-NS samples (Pushparaj *et al.*, 2013).

The [TAS] of bulk MFI and the H-NS samples estimated from the TPD profiles is shown in figure 14 with the corresponding $[Al]_T$ of the zeolites (see 4.2.2.4). In general, the $[Al]_T$ of zeolites can encompass FAl associated with Brønsted acidity, Lewis acidic EFAl, and non-Lewis acidic EFAl. Non-Lewis acidic EFAl can encompass Al in alumina-like polymeric phases (Scherzer, 1984; Martens *et al.*, 1997). The [TAS] of bulk MFI and H-NS-6-75a is in reasonable agreement with the corresponding $[Al]_T$. This implies that all the Al is associated with acidity (Brønsted + Lewis). On the other hand, the [TAS] of H-NS-6-25a, H-NS-6-50a and H-NS-6-100a deviates considerably from the corresponding $[Al]_T$. For H-NS-6-25a and H-NS-6-50a, the lower [TAS] compared to $[Al]_T$ implies that the samples may have a higher actual Si/Al ratio and therefore a lower actual Al concentration (using equation 8), which in turn suggests that not all the Al crystallized out of solution for the corresponding samples; and/or the lower [TAS] compared to $[Al]_T$ implies that the samples may contain non-Lewis acidic EFAl sites, on which NH_3 cannot chemisorb. Conversely, for H-NS-6-100a, the higher [TAS] compared to $[Al]_T$ implies that the sample may have a lower actual Si/Al ratio and therefore a higher actual Al concentration, which in turn suggests that not all the Si crystallized out of solution; and/or the higher [TAS] compared to $[Al]_T$ implies that the sample may contain Lewis acidic EFSi sites, on which NH_3 can chemisorb. Although NH_3-TPD is an important tool to obtain information on the strength and amount of acid sites on the zeolite surface, it cannot provide any direct information on the acid types such as Brønsted or Lewis acid (Jentys & Lercher, 2001; Kim, Jung & Park, 2010).

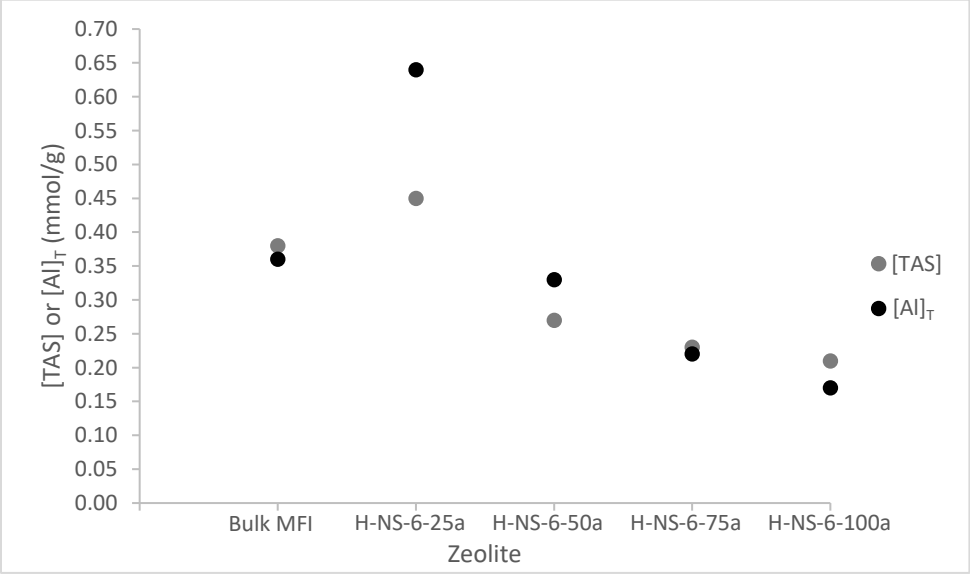

Figure 14: [TAS] and $[Al]_T$ of bulk MFI and H-NS-6-ya samples.

5.1.1.5. ^{27}Al MAS SSNMR Spectroscopy

^{27}Al MAS SSNMR Spectroscopy has been widely used to investigate the local environment and content of FAl and EFAl species in zeolites. FAl species contain Al in tetrahedral coordination with O. According to Löwenstein's rule, only a single tetrahedral environment, namely $Al(SiO)_4$, exists in the zeolite framework whereas AlOAl pairings are forbidden (Löwenstein, 1954). For EFAl species, pentahedral and octahedral coordination of Al with O have been identified (see 2.5.2).

Based on previous ^{27}Al MAS SSNMR studies of zeolites, the NMR signal of FAl in tetrahedral coordination (Al^{IV}) exhibits δ's approximately in the range 55 – 65 ppm (Fyfe *et al.*, 1982; Klinowski *et al.*, 1983; Pellet, Blackwell & Rabo, 1988; Yingcai *et al.*, 1996; Jo *et al.*, 2014; Wu *et al.*, 2014; Zhu *et al.*, 2015). EFAl in octahedral coordination (Al^{VI}) exhibits a δ at approximately 0 ppm (Fyfe *et al.*, 1982; Klinowski *et al.*, 1983; Pellet, Blackwell & Rabo, 1988; Yingcai *et al.*, 1996; Bourgeat-Lami *et al.*, 1991; Woolery *et al.*, 1997; Wouters, Chen & Grobet, 1998; van Bokhoven *et al*., 2000; Jo *et al.*, 2014; Wu *et al.*, 2014; Zhu *et al.*, 2015). Furthermore, EFAl in pentahedral coordination (Al^{V}) exhibits a δ at approximately 30 ppm (Gilson *et al.*, 1987; Pellet, Blackwell & Rabo, 1988; Jiao *et al.*, 2005; Huang *et al.*, 2008).

The FAl and EFAl of bulk MFI and H-NS samples were investigated by ^{27}Al MAS SSNMR. The spectra obtained are shown in figure 15 a – e.

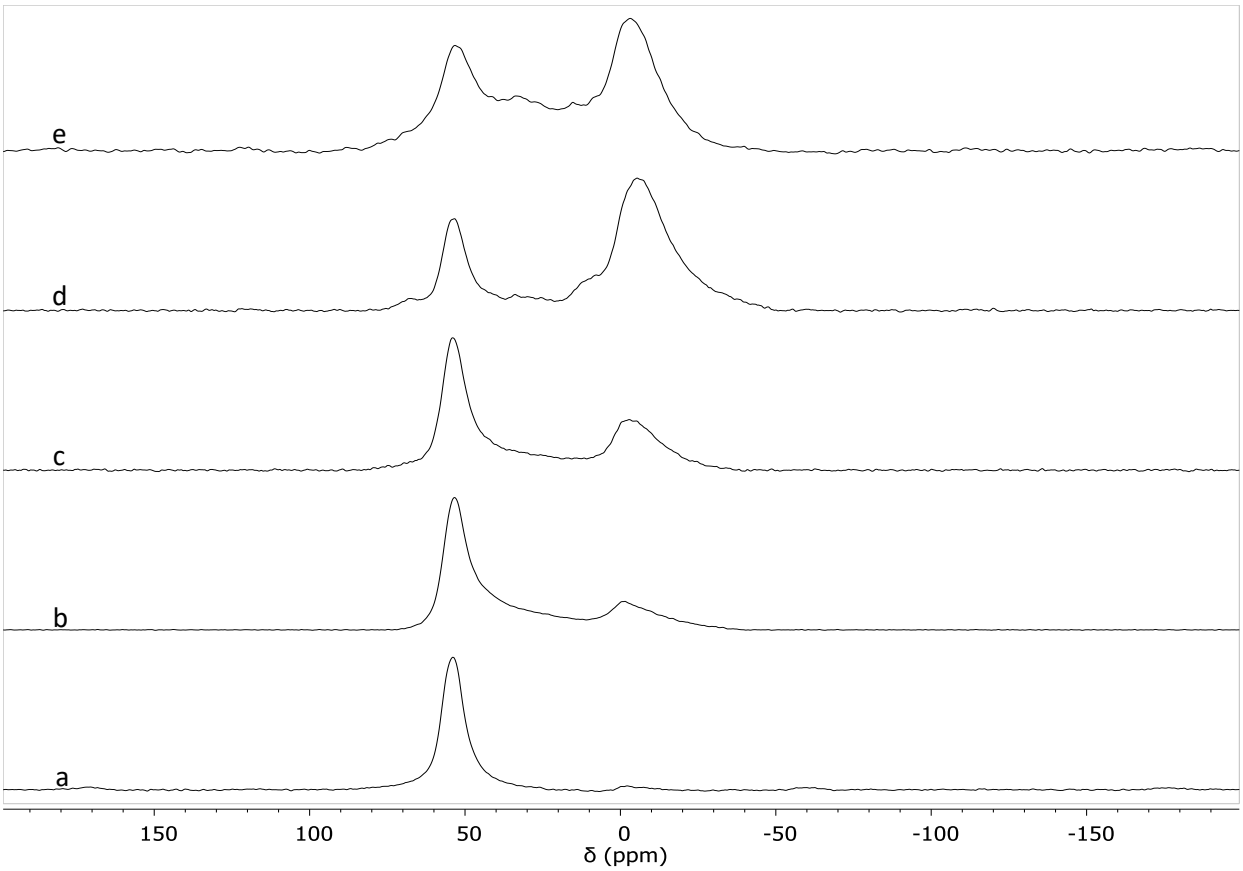

Figure 15: ^{27}Al MAS SSNMR spectra of (a) bulk MFI, (b) H-NS-6-25a, (c) H-NS-6-50a, (d) H-NS-6-75a and (e) H-NS-6-100a.

All the spectra are dominated by signals at δ's of approximately 55 ppm and 0 ppm, corresponding to Al^{IV} and Al^{VI}, respectively. In addition, the spectra of H-NS-6-100a and H-NS-6-75a contain a weaker signal at approximately 30 ppm, corresponding to Al^{V}. The signal at 0 ppm or 30 ppm can be assigned to one or more types of EFAl species (see 2.5.2).

From the spectra obtained, the % Al distribution was estimated using peak areas obtained from spectral deconvolution of the respective signal components (see 4.2.2.5). The deconvoluted spectra are shown in figures A3 – A7 in appendix 2. The δ's, peak areas and % peak areas obtained from the deconvoluted spectra are shown in tables A1 – A5 in appendix 2. The Brønsted acid site concentration ([BAS]) was estimated using the product of the % Al^{IV} estimated from the NMR spectra and [TAS] estimated from the NH_3-TPD profiles (figure 14). The % Al distribution and [BAS] of the zeolites are shown in table 22. For the H-NS samples, the % Al^{IV} content and [BAS] decrease in the order H-NS-6-25a > H-NS-6-50a > H-NS-6-100a > H-NS-6-75a, with H-NS-6-75a containing an oddly large % Al^{VI} content.

Table 22: % Al distribution and [BAS] of bulk MFI and H-NS-6-ya samples.

Zeolite	Al distribution (%)			[BAS] (mmol/g)
	FAl	EFAl		
	Al^{IV}	Al^{V}	Al^{VI}	
Bulk MFI	95	-	5	0.36
H-NS-6-25a	75	-	25	0.34
H-NS-6-50a	64	-	36	0.17
H-NS-6-75a	24	1	75	0.06
H-NS-6-100a	48	4	48	0.10

Another set of NS-6-y samples, namely the NS-6-yb samples, and a set of NS-3-y samples, namely the NS-3-ya samples, were synthesized (table 4). These samples were compared to investigate whether $C_{22\text{-}6\text{-}3}$ could result in a higher FAl content than $C_{22\text{-}6\text{-}6}$ at a given Si/Al ratio. The only difference between these sets and the NS-6-ya set is the number of calcinations performed. As mentioned in 4.1.3.1, the NS-6-yb and NS-3-ya samples were calcined twice to completely remove the surfactants, since for the NS-6-yb samples, a fraction of the sample appeared brown, whereas for the NS-3-ya samples, the whole sample appeared brown. The brown colour implies that surfactant is still present. Also, the NS-6-yb and NS-3-ya samples were calcined in the same manner to eliminate any differences that may arise from calcination. Characterization results of the NS-6-yb and NS-3-ya samples are analyzed in the next section.

5.1.2. NS-6-yb and NS-3-ya

C-NS-6-yb and C-NS-3-ya samples were characterized by XRD, TEM, N_2 physisorption and ^{27}Al MAS SSNMR spectroscopy. H-NS-6-yb and H-NS-3-ya samples were characterized by NH_3-TPD. Bulk MFI (Si/Al = 45) was used as a reference sample.

5.1.2.1. XRD

XRD patterns of bulk MFI and the C-NS-6-yb and C-NS-3-ya samples are shown in figure 16. The C-NS samples display reflections characteristic of the MFI framework topology, thus confirming the MFI topology. For the C-NS samples, reflections in the [*h*0*l*] crystallographic directions appear, corresponding to *ac* plane reflections (Choi *et al.*, 2009). For C-NS-3-50a and C-NS-3-75a, a reflection at d of approximately 9.7 Å with a *b* component (111) appears faintly as a shoulder and grows in intensity in C-NS-3-100a. The presence of (111) could be due to preferred orientation of nano-sheets along the [111] direction, or to thicker nano-sheets in comparison to

the other C-NS samples. The XRD patterns of the C-NS-6-yb samples correspond well with those of the H-NS-6-ya samples (figure 8).

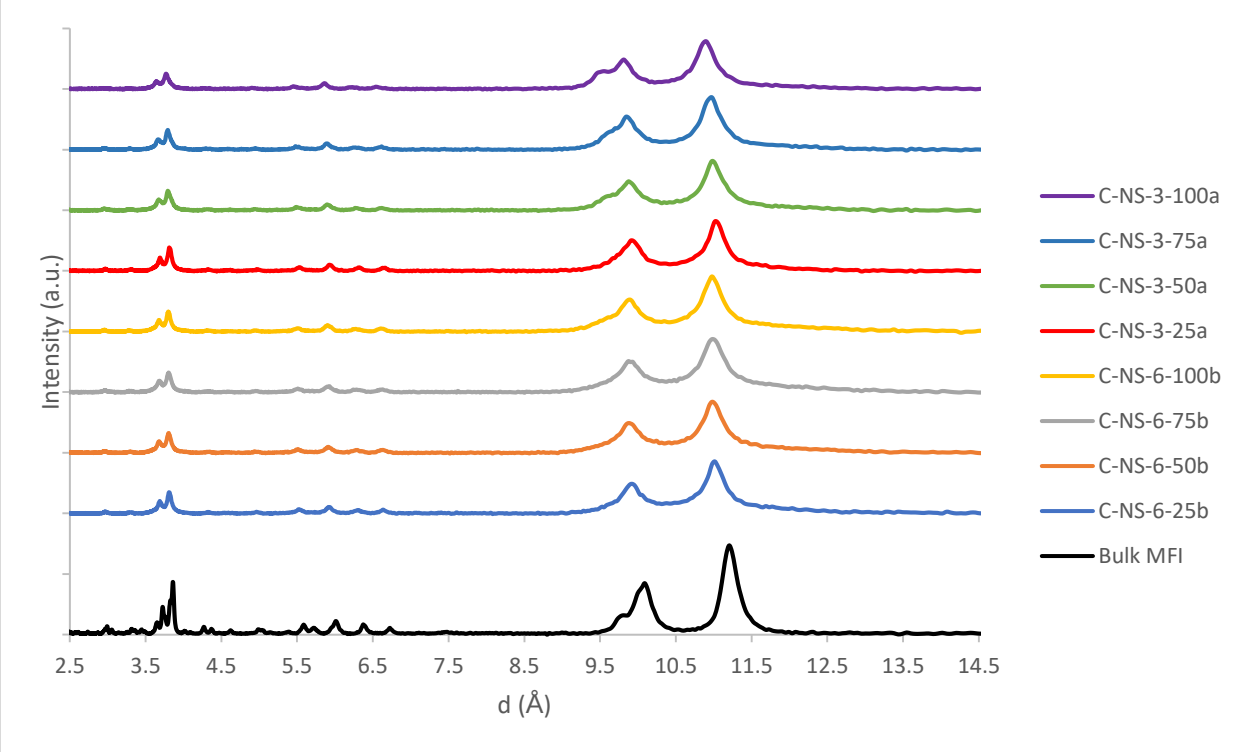

Figure 16: XRD patterns of bulk MFI and C-NS-6-yb and C-NS-3-ya samples.

5.1.2.2. TEM

TEM micrographs of the C-NS samples are shown in figures 17 – 19. The micrographs confirm that the samples are nano-sheets. For the C-NS-3-ya samples, a fraction of the nano-sheets exhibits shorter crystalline domains along the *ac* plane than the C-NS-6-yb samples. For each sample, the nanosheets exhibit a non-uniform thickness. The thickness range and corresponding average thickness are shown in table 23. MFI nano-sheets with a non-uniform thickness were reported previously (Wu *et al.*, 2014). The average thickness of the C-NS-6-yb samples, C-NS-3-50a, C-NS-3-75a and C-NS-3-100a is in reasonable agreement, whereas the average thickness of C-NS-3-25a is slightly larger than the other samples. This suggests that preferred orientation of nano-sheets along the [111] direction rather than thicker nano-sheets gives rise to the (111) reflection in the XRD patterns of C-NS-3-50a, C-NS-3-75a and C-NS-3-100a (figure 16). The average thickness of the C-NS-6-yb samples is in reasonable agreement with that of the H-NS-6-ya samples (table 19).

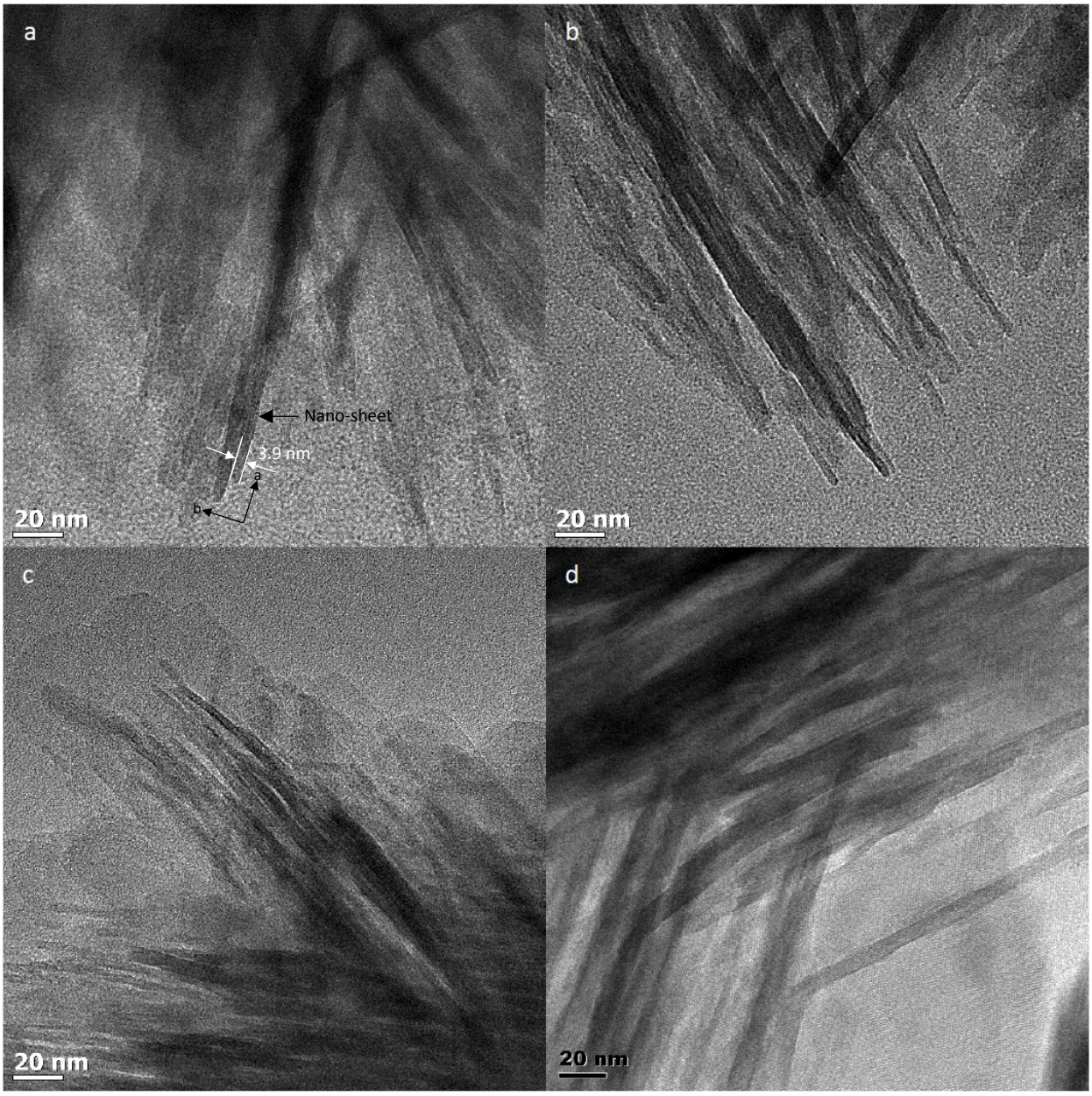

Figure 17: TEM micrographs of (a) C-NS-6-25b, (b) C-NS-6-50b, (c) C-NS-6-75b and (d) C-NS-6-100b.

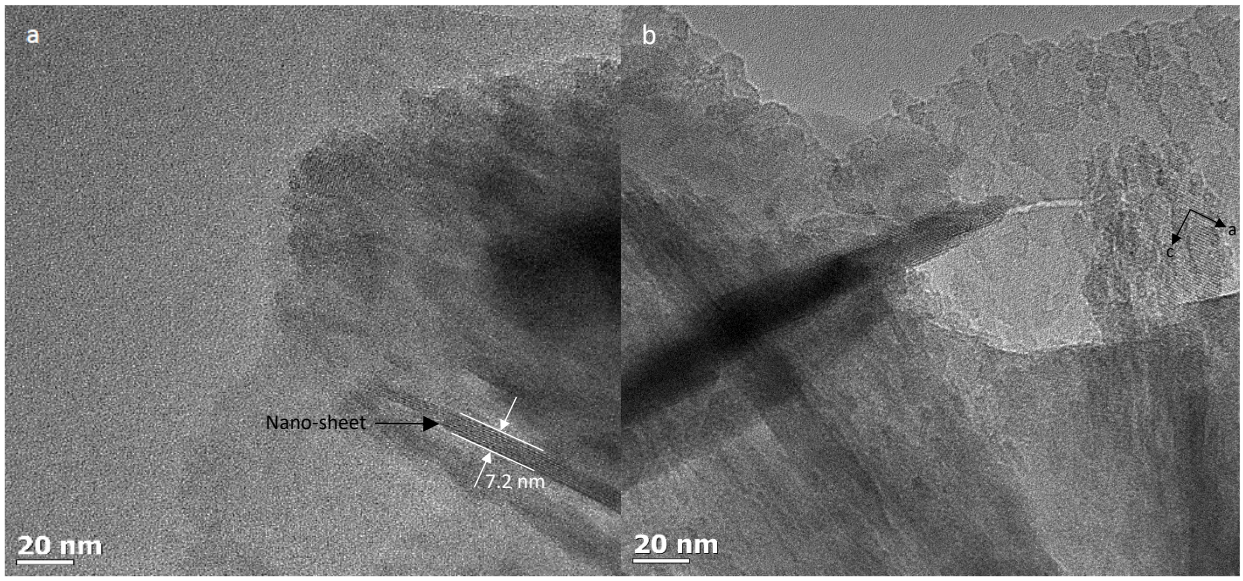

Figure 18: TEM micrographs of (a – b) C-NS-3-25a.

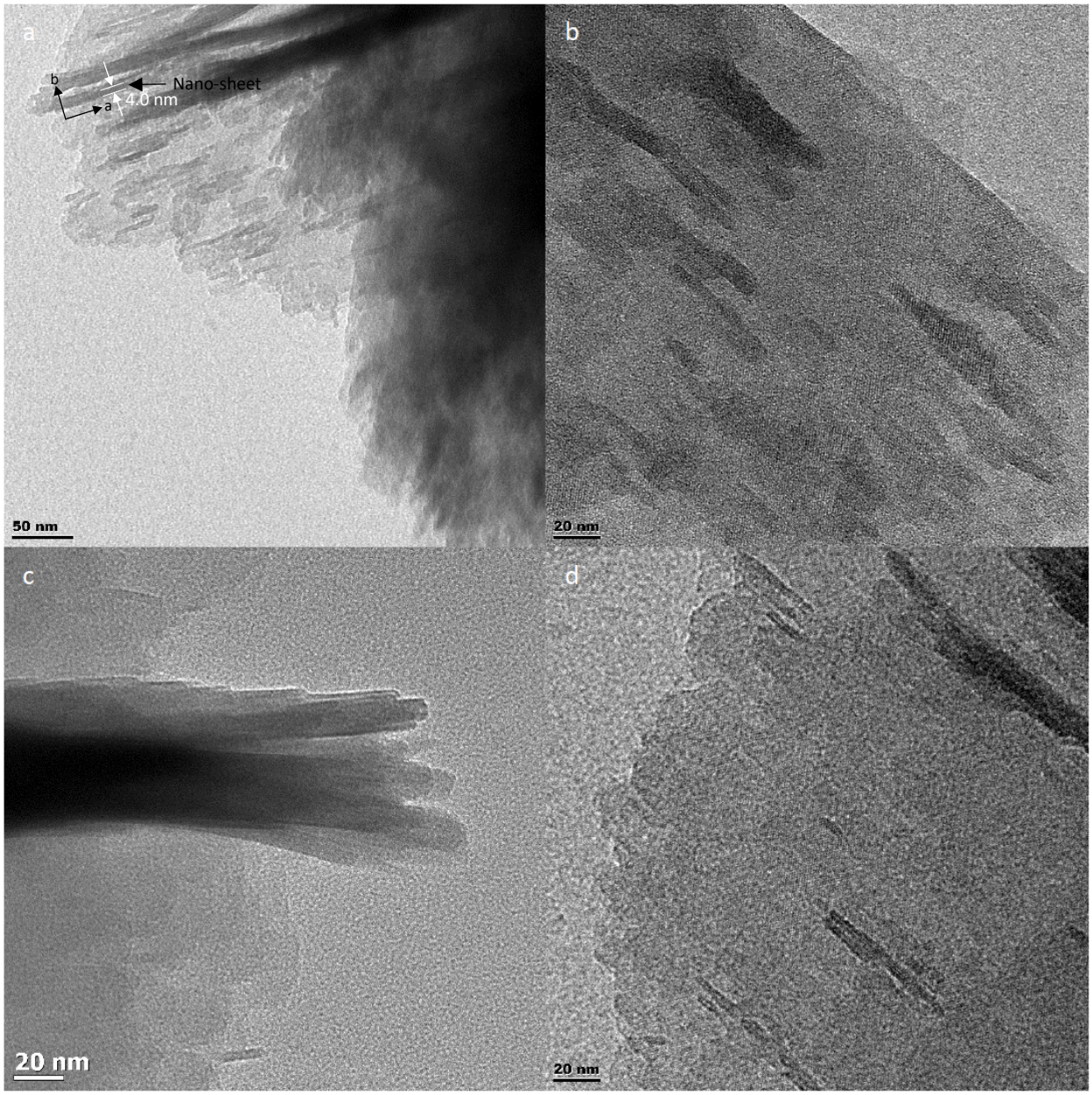

Figure 19: TEM micrographs of (a) C-NS-3-50a, (b) C-NS-3-75a and (c – d) C-NS-3-100a.

Table 23: Thickness range and average thickness of C-NS-6-yb and C-NS-3-ya samples.

Zeolite	Thickness range (nm)	Average thickness (nm)
C-NS-6-25b	2.6 – 5.3	3.7 ± 0.7
C-NS-6-50b	2.7 – 6.0	3.7 ± 0.7
C-NS-6-75b	2.8 – 6.3	4.1 ± 1.0
C-NS-6-100b	2.0 – 5.2	3.6 ± 0.6
C-NS-3-25a	2.7 – 7.6	4.7 ± 1.3
C-NS-3-50a	2.5 – 4.0	3.4 ± 0.4
C-NS-3-75a	2.7 – 4.8	3.9 ± 0.5
C-NS-3-100a	2.5 – 4.8	3.7 ± 0.6

5.1.2.3. N_2 Physisorption

N_2 physisorption isotherms of bulk MFI and the C-NS samples are shown in figure 20.

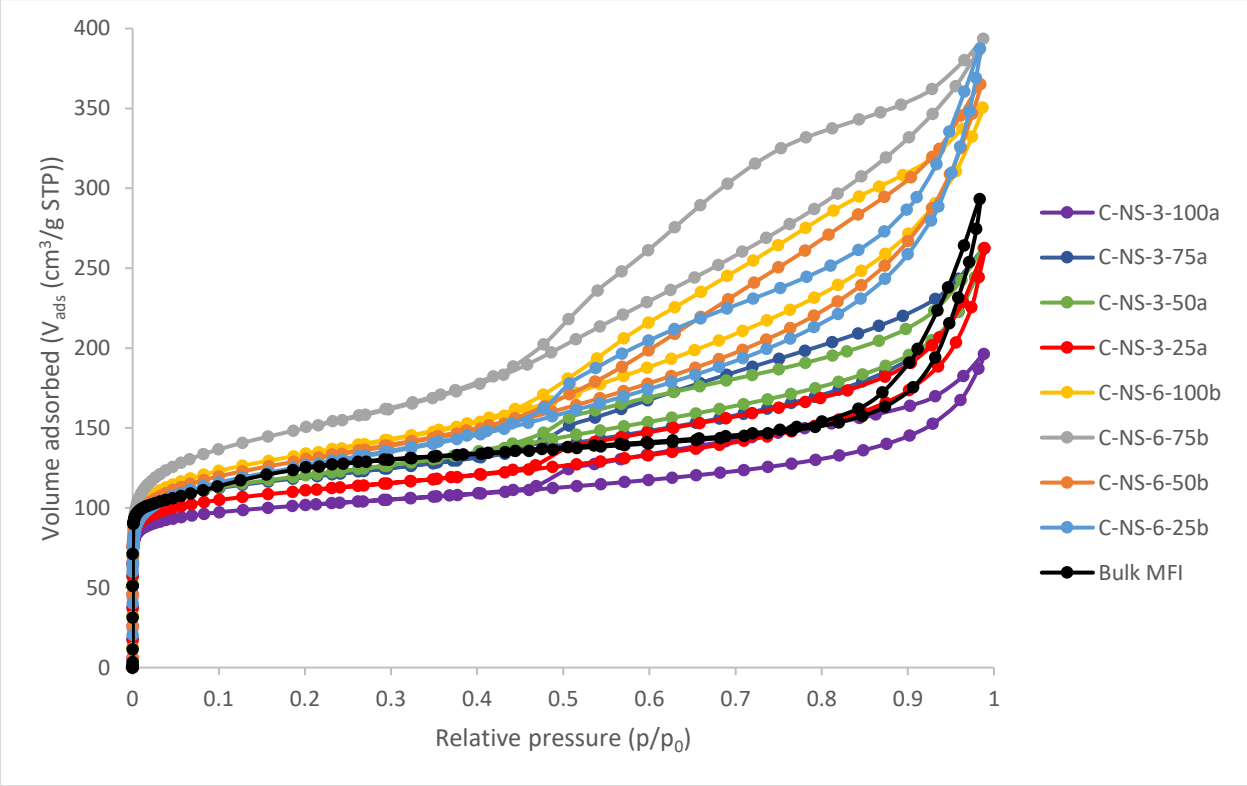

Figure 20: N_2 physisorption isotherms of bulk MFI and C-NS-6-yb and C-NS-3-ya samples.

The C-NS samples display a combination of type I and type IV isotherms based on the IUPAC classification (Sing *et al.*, 1985; Thommes *et al.*, 2015). N_2 adsorption at low p/p_0 at approximately $0 < p/p_0 < 0.1$ confirms the presence of micropores (Hudec *et al.*, 2002; Zhang, Yang & Yan, 2014).

The C-NS samples display hysteresis loops from medium to high p/p_0 at approximately $0.45 < p/p_0 < 1$, confirming the presence of mesopores and macropores (Sing *et al.*, 1985; Zhang, Yang & Yan, 2014; Thommes *et al.*, 2015). The V_{micro} and S_{ext} of the zeolites are shown in table 24.

Table 24: V_{micro} and S_{ext} of bulk MFI and C-NS-6-yb and C-NS-3-ya samples.

Zeolite	V_{micro} (cm^3/g)	S_{ext} (m^2/g)
Bulk MFI	0.13	141
C-NS-6-25b	0.09	231
C-NS-6-50b	0.09	227
C-NS-6-75b	0.09	322
C-NS-6-100b	0.10	237
C-NS-3-25a	0.12	119
C-NS-3-50a	0.11	169
C-NS-3-75a	0.12	147
C-NS-3-100a	0.12	88

As seen in table 24, the C-NS samples have a large V_{micro}, consistent with their zeolitic nature (Flanigen, 2001; Zhu *et al.*, 2015). The C-NS-6-yb samples have a smaller V_{micro} than bulk MFI (see 5.1.1.3). The C-NS-3-ya samples and bulk MFI have a comparable V_{micro}.

The C-NS-6-yb samples have a larger S_{ext} than bulk MFI due to their higher dispersion (Verheyen *et al.*, 2013). C-NS-3-25a, C-NS-3-50a, C-NS-3-75a and bulk MFI have a comparable S_{ext} and thus comparable dispersion, whereas C-NS-3-100a has a lower S_{ext} than bulk MFI and thus a lower dispersion. The lower S_{ext} of the C-NS-3-ya samples compared to the C-NS-6-yb samples correlates well with the shorter crystalline domains along the *ac* planes of the C-NS-3-ya samples compared to the C-NS-6-yb samples in TEM (see 5.1.2.2). Furthermore, the lower S_{ext} of the C-NS-3-ya samples compared to the C-NS-6-yb and H-NS-6-ya samples and comparable V_{micro} of the C-NS-3-ya samples and bulk MFI supports the underestimation of the V_{micro} of the C-NS-6-yb and H-NS-6-ya samples by the *t*-plot method.

The mesopore PSDs of the zeolites are shown in figure 21. The mode values of the mesopore sizes are shown in table 25. The C-NS samples display narrow mesopore PSDs centred at approximately 4 nm (see 5.1.1.3).

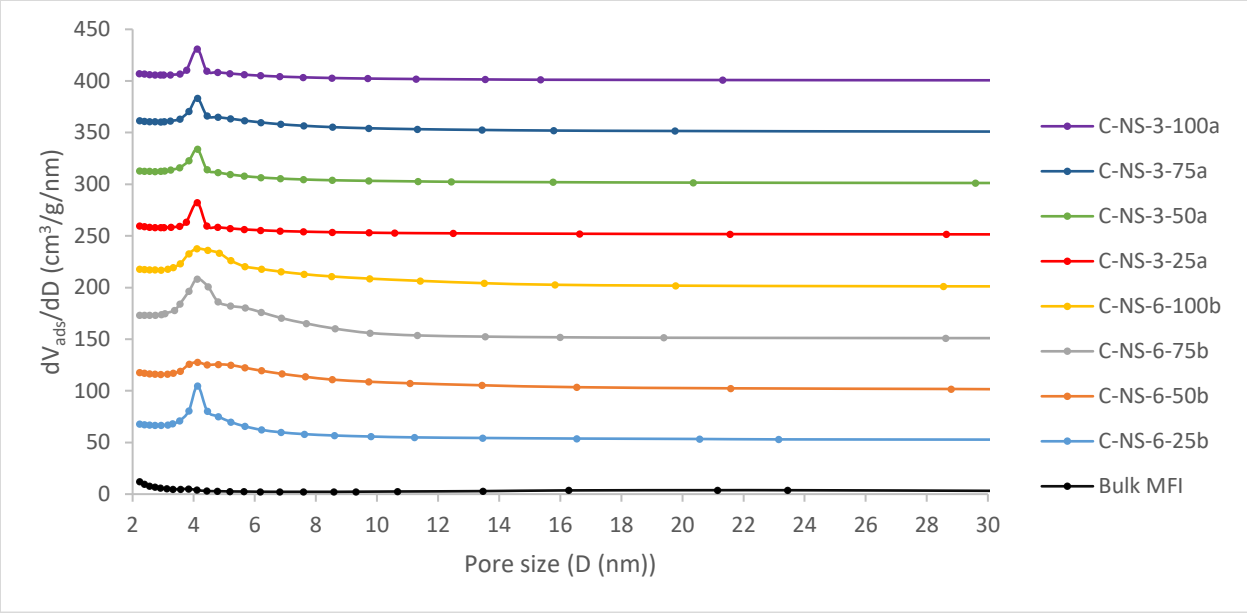

Figure 21: Mesopore PSDs of bulk MFI and C-NS-6-yb and C-NS-3-ya samples. The mesopore PSDs are vertically offset by equal intervals of 50 $cm^3/g/nm$.

Table 25: Mode value of the mesopore sizes of C-NS-6-yb and C-NS-3-ya samples.

Zeolite	Mesopore size mode value (nm)
C-NS-6-25b	4.1
C-NS-6-50b	4.1
C-NS-6-75b	4.1
C-NS-6-100b	4.1
C-NS-3-25a	4.1
C-NS-3-50a	4.1
C-NS-3-75a	4.1
C-NS-3-100a	4.1

Table 26 compares the V_{micro}, compares the S_{ext}, and compares the mode value of the mesopore sizes of the C-NS-6-yb and H-NS-6-ya samples at given Si/Al ratios. At a given Si/Al ratio, the V_{micro} of the C-NS-6-yb and H-NS-6-ya samples is similar. Also, at given Si/Al ratios of 75 and 100, the S_{ext} of the C-NS-6-yb and H-NS-6-ya samples is similar. In contrast, at given Si/Al ratios of 25 and 50, the S_{ext} of the C-NS-6-yb and H-NS-6-ya samples is significantly different. This could be due to the longer calcination of the as-synthesized forms of NS-6-yb samples compared to NS-6-ya samples. Furthermore, at a given Si/Al ratio, the mode values of the mesopore sizes of the C-NS-6-yb and H-NS-6-ya samples are similar.

Table 26: Comparison of V_{micro}, comparison of S_{ext}, and comparison of the mode value of the mesopore sizes of C-NS-6-yb and H-NS-6-ya samples at given Si/Al ratios.

y	V_{micro} (cm^3/g)		S_{ext} (m^2/g)		Mesopore size mode value (nm)	
	C-NS-6-yb	H-NS-6-ya	C-NS-6-yb	H-NS-6-ya	C-NS-6-yb	H-NS-6-ya
25	0.09	0.08	231	300	4.1	4.1
50	0.09	0.08	227	382	4.1	3.8
75	0.09	0.10	322	271	4.1	3.9
100	0.10	0.10	237	234	4.1	3.9

5.1.2.4. NH_3-TPD

NH_3-TPD profiles of bulk MFI and the H-NS-6-yb and H-NS-3-ya samples are shown in figure 22.

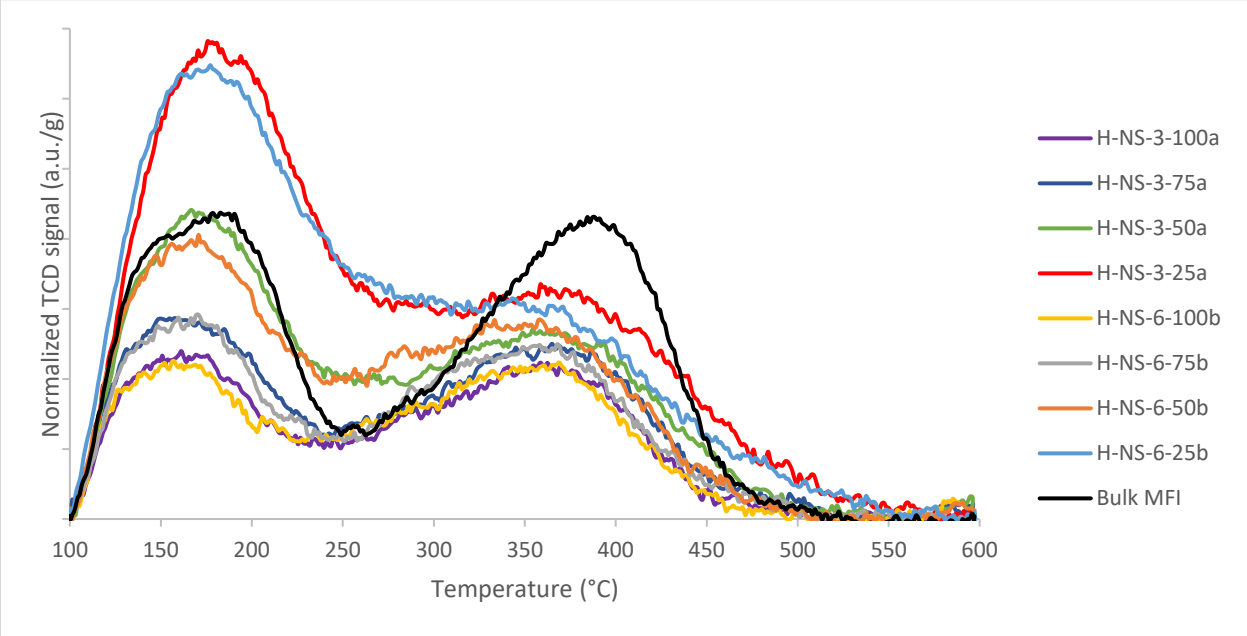

Figure 22: NH_3-TPD profiles of bulk MFI and H-NS-6-yb and H-NS-3-ya samples.

As seen in the profiles, the H-NS samples contain weak and strong acid sites (see 5.1.1.4). For the H-NS samples, the strength of the acid sites is virtually constant with varying Si/Al ratio (Kim *et al.*, 2016). At a given Si/Al ratio, for H-NS samples synthesized with $C_{22\text{-}6\text{-}6}$ or $C_{22\text{-}6\text{-}3}$, the strength of the acid sites is similar. Bulk MFI with Si/Al = 45 contains slightly stronger acid sites than the H-NS samples (see 5.1.1.4).

The [TAS] and $[Al]_T$ of bulk MFI and the H-NS samples are shown in figure 23. The [TAS] of H-NS-6-50b and H-NS-3-50a is in reasonable agreement with the corresponding $[Al]_T$, implying

that all the Al is associated with acidity. On the other hand, the [TAS] of the remaining H-NS samples deviates considerably from the corresponding $[Al]_T$. For H-NS-6-25b and H-NS-3-25a, the lower [TAS] compared to $[Al]_T$ implies that the samples may have a higher actual Si/Al ratio and/or may contain non-Lewis acidic EFAl sites (see 5.1.1.4). Conversely, for H-NS-6-75b, H-NS-6-100b, H-NS-3-75a and H-NS-3-100a, the higher [TAS] compared to $[Al]_T$ implies that the samples may have a lower actual Si/Al ratio and/or may contain Lewis acidic EFSi sites (see 5.1.1.4).

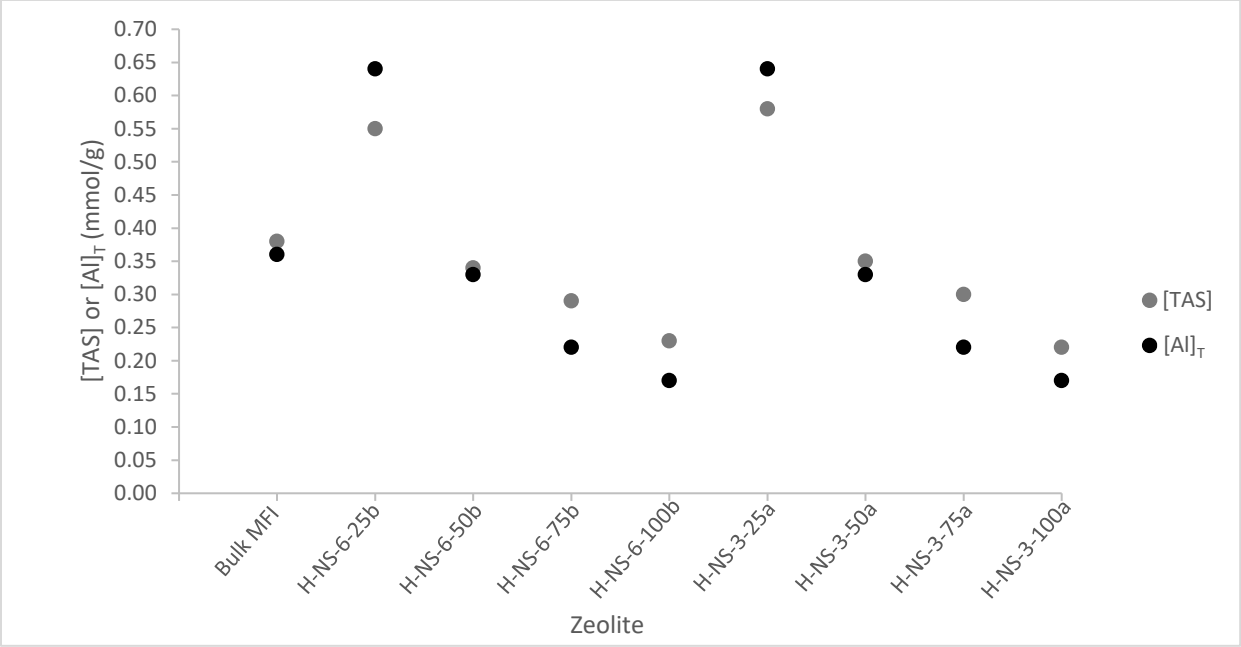

Figure 23: [TAS] and $[Al]_T$ of bulk MFI and H-NS-6-yb and H-NS-3-ya samples.

Figure 24 compares the [TAS] of the H-NS-6-yb and H-NS-6-ya samples at given Si/Al ratios. At given Si/Al ratios of 25, 50 and 75, considerable deviations occur between the [TAS] of H-NS-6-yb and H-NS-6-ya, which could be due to the longer calcination of the as-synthesized forms of NS-6-yb samples compared to the as-synthesized forms of NS-6-ya samples (see 5.1.1.4).

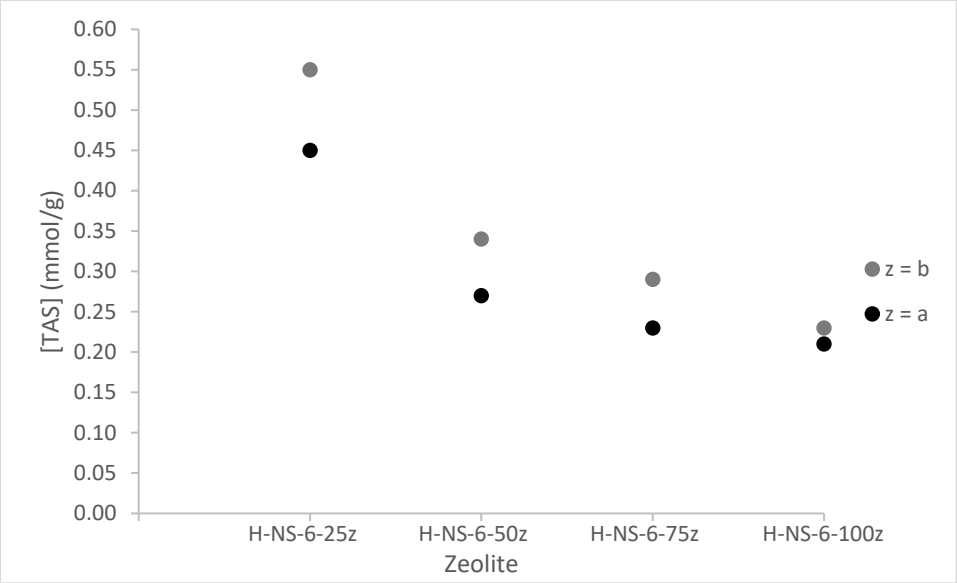

Figure 24: Comparison of [TAS] of H-NS-6-ya and H-NS-6-yb samples at given Si/Al ratios.

5.1.2.5. ^{27}Al MAS SSNMR Spectroscopy

^{27}Al MAS SSNMR spectra obtained for the C-NS-6-yb and C-NS-3-ya samples and bulk MFI are shown in figure 25 a – i. The deconvoluted spectra of the C-NS samples are shown in figures A8 – A15 in appendix 2. The δ's, peak areas and % peak areas obtained from the deconvoluted spectra are shown in tables A6 – A14 in appendix 2.

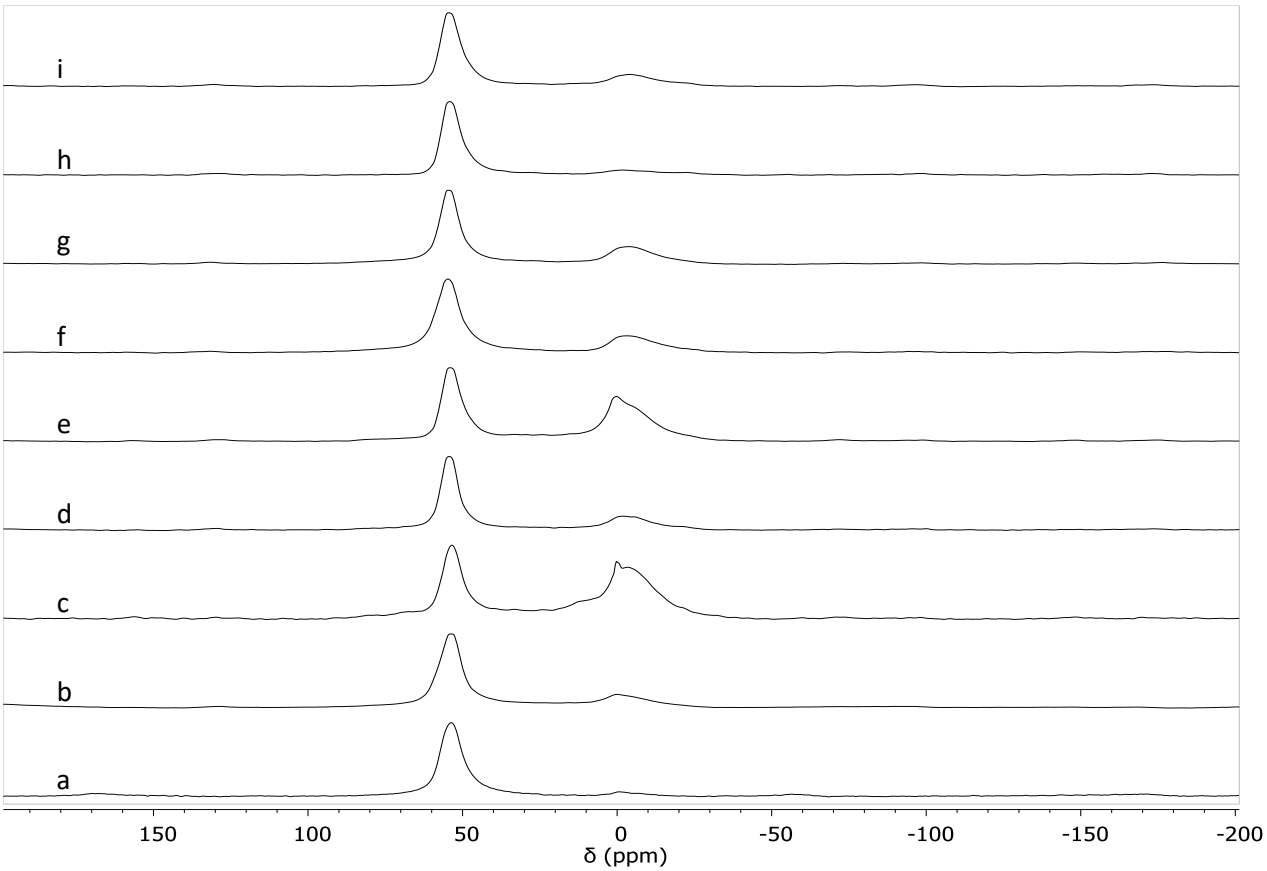

Figure 25: ^{27}Al MAS SSNMR spectra of (a) bulk MFI, (b) C-NS-6-25b, (c) C-NS-6-50b, (d) C-NS-6-75b, (e) C-NS-6-100b, (f) C-NS-3-25a, (g) C-NS-3-50a, (h) C-NS-3-75a and (i) C-NS-3-100a.

All the spectra are dominated by signals at δ's of approximately 55 ppm and 0 ppm, corresponding to Al^{IV} and Al^{VI}, respectively. In addition, upon close inspection, the spectra of C-NS-6-50b and C-NS-6-100b contain a weaker signal at approximately 30 ppm, corresponding to Al^{V}. The signal at 0 ppm or 30 ppm can be assigned to one or more types of EFAl species (see 2.5.2). The % Al distribution of the C-NS-6-yb and C-NS-3-ya samples estimated from NMR and the [BAS] of the C-NS-6-yb and C-NS-3-ya samples assuming complete protonation and estimated using % Al^{IV} from NMR and [TAS] from NH_3-TPD are shown in table 27.

Table 27: % Al distribution and [BAS] of bulk MFI, % Al distribution of C-NS-6-yb and C-NS-3-ya samples, and [BAS] of C-NS-6-yb and C-NS-3-ya samples assuming complete protonation.

Zeolite	Al distribution (%)			[BAS] (mmol/g)
	FAl	EFAl		
	Al^{IV}	Al^{V}	Al^{VI}	
Bulk MFI	95	-	5	0.36
C-NS-6-25b	73	-	27	0.40
C-NS-6-50b	36	3	61	0.12
C-NS-6-75b	68	-	32	0.20
C-NS-6-100b	42	4	54	0.10
C-NS-3-25a	76	-	24	0.44
C-NS-3-50a	69	-	31	0.24
C-NS-3-75a	81	-	19	0.24
C-NS-3-100a	73	-	27	0.16

Using the data in table 27, the % FAl content of the zeolites is compared in figure 26. At given Si/Al ratios of 25, 50, 75 and 100, the % increase in % FAl content for C-NS-3-ya samples relative to the C-NS-6-yb samples is 4%, 92%, 19% and 74%, respectively. Thus, replacing the terminal $–C_6H_{13}$ group in $C_{22\text{-}6\text{-}6}$ with $–C_3H_7$ in the new synthesis method results in an increase in the FAl content of MFI nano-sheets with Si/Al ≥ 50, with the increase being the most pronounced for nano-sheets with Si/Al = 50. The increase in FAl content is consistent with a previous study (Zhu *et al.*, 2015). It can be explained by the increased occupancy of the zeolite framework by the hydrophilic region of $C_{22\text{-}6\text{-}3}$ in comparison to the hydrophilic region of $C_{22\text{-}6\text{-}6}$ under the given set of synthesis conditions, since $–C_3H_7$ is less bulky than $–C_6H_{13}$ (figure 6).

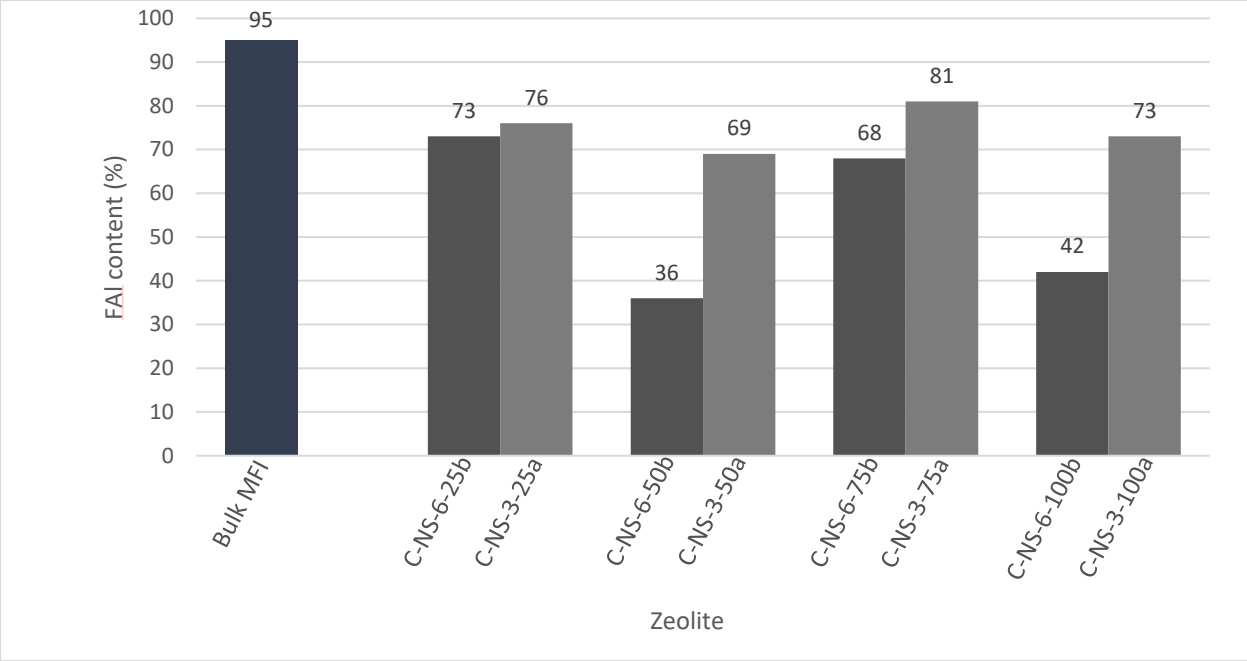

Figure 26: Comparison of % FAl content of C-NS-6-yb and C-NS-3-ya samples at given Si/Al ratios.

Figure 27 compares the % EFAl content of H-NS-6-ya samples with the % EFAl content of C-NS-6-yb samples at given Si/Al ratios.

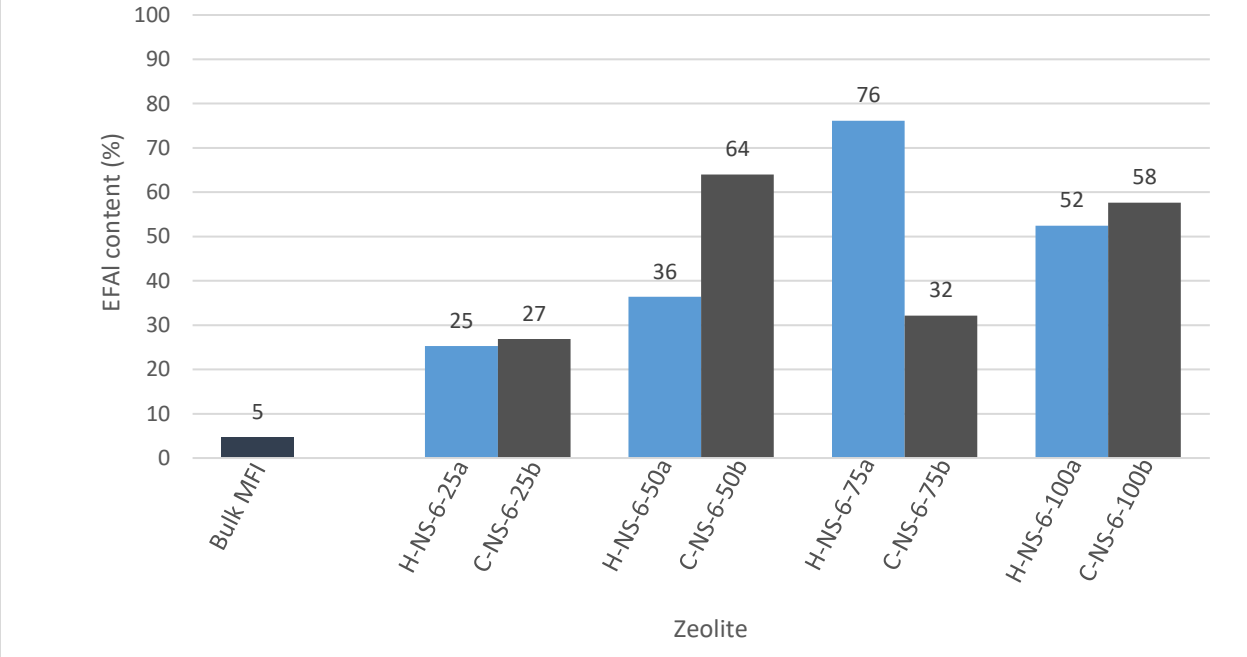

Figure 27: Comparison of % EFAl content of H-NS-6-ya and C-NS-6-yb samples at given Si/Al ratios.

The higher EFAl content of C-NS-6-50b compared to H-NS-6-50a (figure 27) could be due to the longer calcination of the as-synthesized form of NS-6-50b (see 4.1.3.1). Previously, calcining an

as-synthesized zeolite resulted in formation of EFAl species, which may be attributed to dealumination of the zeolite framework during the calcination process (Jo *et al.*, 2014).

H-NS-6-75a has considerably more EFAl than expected from the trend for the H-NS samples (expected EFAl content of H-NS-6-75a ≈ 44%), whereas C-NS-6-75b has considerably less EFAl than expected from the trend for the C-NS samples (expected EFAl content of C-NS-6-75b ≈ 44%) (figure 27). The excess EFAl of H-NS-6-75a (≈ 32%) may encompass Al^{VI} and Al^{V} species closely associated with the zeolite framework and the species may have formed during calcination of NH_4-NS-6-75a. In general, calcining an NH_4-zeolite releases NH_3, yielding the H-zeolite. In previous studies, it was found that calcining NH_4-zeolites lead to formation of Al^{VI} species at the expense of Al^{IV}, and upon transforming the H-zeolites back to the NH_4-forms, via NH_3 adsorption or NH_4^+ ion exchange, the original NMR spectra of the NH_4-forms were recovered (Bourgeat-Lami *et al.*, 1991; Woolery *et al.*, 1997; Wouters, Chen & Grobet, 1998; van Bokhoven *et al.*, 2000).

It has been suggested that formation of these 'flexible' Al^{VI} species during calcination of an NH_4-zeolite is induced by H_2O molecules (van Bokhoven *et al.*, 2000). Apparently, the H-zeolite attracts H_2O molecules to stabilize the strong electric fields in the framework induced by protons and the cationic charge is delocalized. Throughout the framework, the zeolite is unable to accommodate too many of these strong electrical field centres; hence, H_2O molecules are attracted and part of the framework Al^{IV} may convert to Al^{VI}, reducing the strong electrical fields in the framework. This could be accompanied by hydrolysis of part of the Al – O – Si linkages, while each zeolite shows a unique tendency toward this process of hydrolysis. No other cations induce such an effect, which can be understood while realizing that protons are catalysts for hydrolysis reactions. When transforming the H-zeolite back to the NH_4-zeolite, NH_4^+ serves as the cation, thereby removing H_2O, returning Al^{VI} back to Al^{IV} (van Bokhoven *et al.*, 2000).

The flexible Al^{VI} species has been proposed to be a species containing a Brønsted acid site such as $Al(SiO)_4(H_2O)(H_3O^+)$ (Bourgeat-Lami *et al.*, 1991) and lattice defects containing a Lewis acid site coordinated by three H_2O molecules such as $Al(SiO)_3(H_2O)_3$ (Woolery *et al.*, 1997). The connection of Al^{VI} with the zeolite framework was confirmed by van Bokhoven *et al.* (2000). Other species including lattice defects such as $Al(SiO)_2(OH)(H_2O)_3$ and $Al(SiO)(OH)_2(H_2O)_3$ have been identified (Wouters, Chen & Grobet, 1998). Flexible Al^{V} species could be lattice defects containing a Lewis acid site coordinated by two H_2O molecules such as $Al(SiO)_3(H_2O)_2$ (Cabral de Menezes *et al.*, 2006).

On the other hand, the deficient EFAl of C-NS-6-75b (≈ 12%) encompasses Al^{VI} and Al^{V} species that may have become so amorphous that they are no longer observable in the NMR spectrum.

The amorphous EFAl may be a result of the second calcination of the as-synthesized form of NS-6-75b.

5.2. Hydrocracking of n-C_{16}

5.2.1. Pt/H-NS-6-ya

H-NS-6-ya samples were loaded with 0.9 wt% Pt via IWI (see 4.1.3.3.1). The samples were calcined (see 4.3.2.2) and subsequently reduced *in-situ* (see 4.3.2.3) to form Pt^0 particles, resulting in the bifunctional catalysts. Following *in-situ* reduction, dry and wet hydrocracking of n-C_{16} was performed (see 4.3.3 – 4.3.4). After reaction, used Pt/H-NS-6-ya samples were characterized by TEM (see 4.2.2.2).

5.2.1.1. Average Pt Particle Size (d_{Pt}), Pt Dispersion (γ_{Pt}) and Pt Particle Size Distribution

The average Pt particle size (d_{Pt}), Pt dispersion (γ_{Pt}) and Pt particle size distribution of used catalysts were determined by TEM. TEM micrographs are shown in figures A16 – A19 in appendix 2. The d_{Pt} and γ_{Pt} are shown in table 28 and Pt particle size distributions in figure 28 a – d. A high, similar γ_{Pt} was obtained for Pt/H-NS-6-25a, Pt/H-NS-6-50a and Pt/H-NS-6-100a. Pt particles < 3 nm were obtained in each case. This corresponds well with a previous study (Brosius, Kooyman & Fletcher, 2016). In contrast, Pt/H-NS-6-75a displays a low γ_{Pt} and contains a large amount of Pt particles > 3 nm, despite being treated the same as the other catalysts. With such very large Pt particles supported by H-NS-6-75a, the Pt particles should be located predominantly on the external surface of the zeolite support (Philippaerts *et al.*, 2010; Kim *et al.*, 2013). The very large Pt particles supported by H-NS-6-75a may be related to the abundancy, nature and/or location of EFAl species present in the support (table 22). The V_{micro} of the H-NS-6-ya samples is large and similar (table 20), and blockage of micropore apertures by EFAl species is highly unlikely for zeolite nano-sheets (see 5.1.1.3). Thus, for Pt/H-NS-6-75a, Pt located predominantly on the external surface of the support would not be a result of blockage of the micropore apertures by EFAl species. Instead, EFAl species is most likely located on the external surface of the support and may serve as a preferential location for Pt. Sree *et al.* (2016) found that alumina on the external surface of bulk MFI served as a preferential location for Pt, resulting in a large d_{Pt}.

Table 28: d_{Pt} and γ_{Pt} of Pt/H-NS-6-ya catalysts.

Catalyst	d_{Pt} (nm)	γ_{Pt} (%)
Pt/H-NS-6-25a	1.30 ± 0.33	78 ± 20
Pt/H-NS-6-50a	1.20 ± 0.28	84 ± 19
Pt/H-NS-6-75a	4.66 ± 1.41	22 ± 7
Pt/H-NS-6-100a	1.28 ± 0.36	80 ± 22

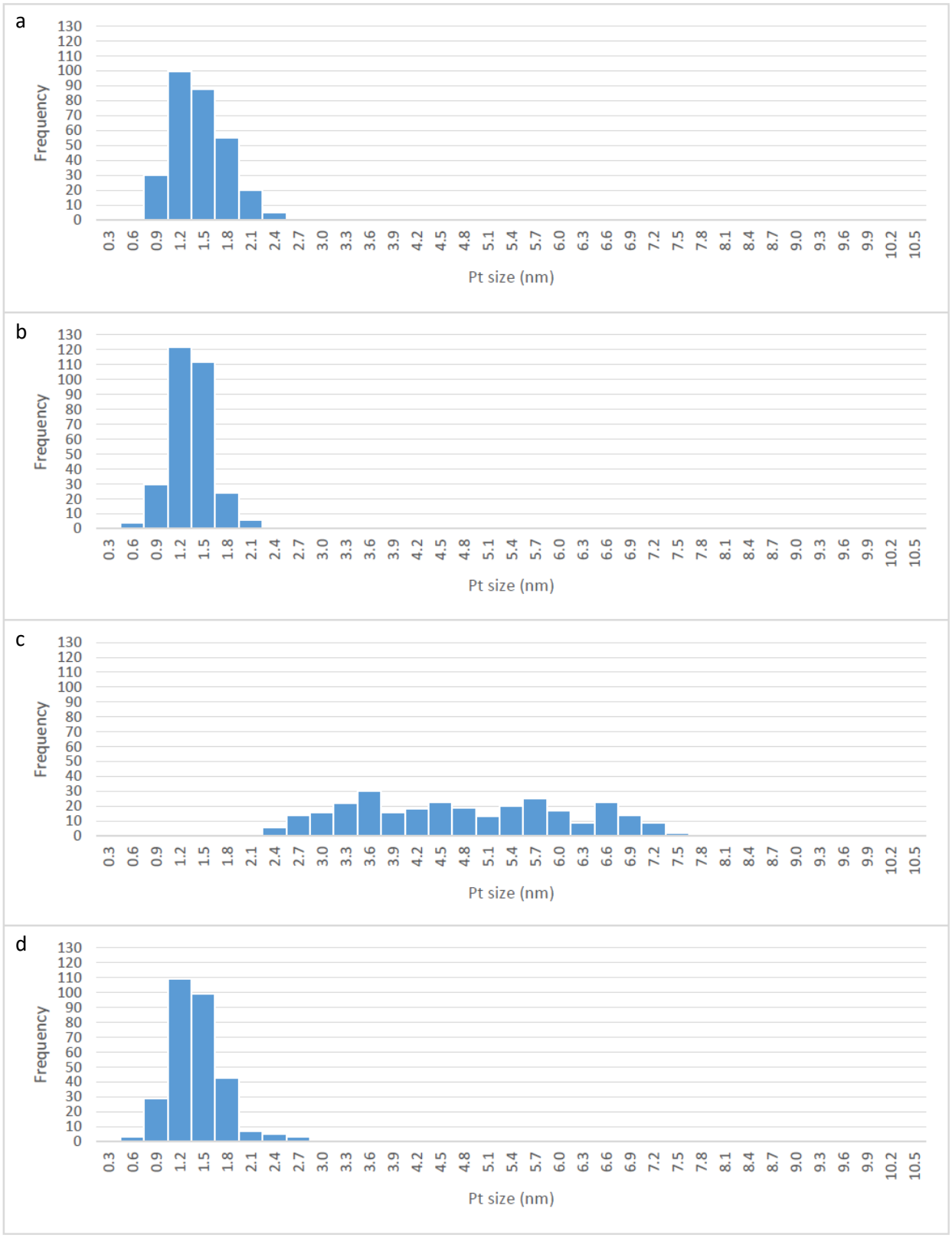

Figure 28: Pt particle size distributions of (a) Pt/H-NS-6-25a, (b) Pt/H-NS-6-50a, (c) Pt/H-NS-6-75a and (d) Pt/H-NS-6-100a.

5.2.1.2. Catalytic Activity

The Arrhenius plot for n-C_{16} dry and wet hydrocracking is shown in figure 29. The corresponding conversion versus temperature plot is shown in figure A28 in appendix 3. The plots show the hydrocracking performance under ideal plug flow conditions and in the absence of external diffusional limitations. In dry hydrocracking, the catalytic activity decreases with increasing Si/Al ratio. The reaction rates at 205 °C ($r_{205\ °C}$) and corresponding conversions at 205 °C ($X_{205\ °C}$) are shown in table 29.

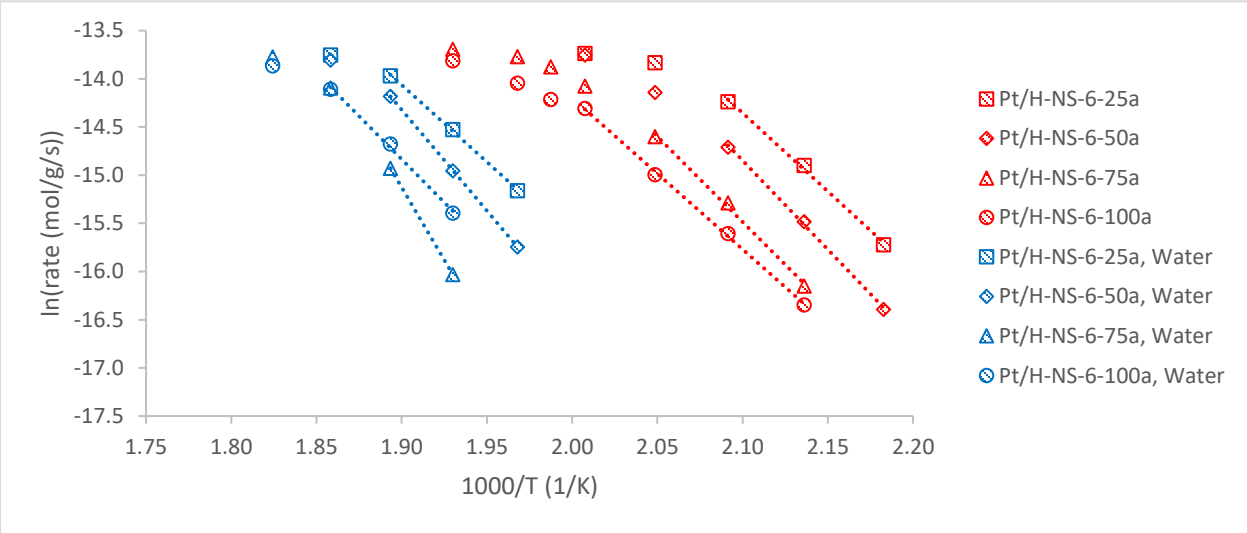

Figure 29: Arrhenius plot for n-C_{16} hydrocracking in the absence (red) and presence (blue) of H_2O over Pt/H-NS-6-ya catalysts (0.9 wt% Pt, 20 bar, W/F = 875 kg s/mol, H_2/n-C_{16} = 10 mol/mol, H_2O/n-C_{16} = 0.8 v/v).

Table 29: $r_{205\ °C}$ and $X_{205\ °C}$ in dry hydrocracking over Pt/H-NS-6-ya catalysts.

Catalyst	$r_{205\ °C}$ (mol/g/s)	$X_{205\ °C}$ (%)
Pt/H-NS-6-25a	6.56×10^{-7}	55.44
Pt/H-NS-6-50a	4.10×10^{-7}	33.22
Pt/H-NS-6-75a	2.30×10^{-7}	19.90
Pt/H-NS-6-100a	1.67×10^{-7}	15.69

Based on the NH_3-TPD profiles of the H-NS-6-ya samples (figure 13), the strength of the acid sites is virtually constant with varying Si/Al ratio and thus will most likely not play a role in the activity trend. For H-NS-6-25a, H-NS-6-50a and H-NS-6-100a, the trend in the [BAS] (table 22) correlates well with the activity trend between the corresponding catalysts in dry hydrocracking. Since the γ_{Pt} is similar for these catalysts (table 28), the correlation between [BAS] and activity implies that the reaction rate is controlled by the Brønsted acid function.

However, in dry hydrocracking, Pt/H-NS-6-75a has a higher activity than Pt/H-NS-6-100a, despite H-NS-6-75a having a lower [BAS] than H-NS-6-100a (table 22). Previously, increasing the d_{Pt} from approximately 1 nm to approximately 6 nm in Pt/bulk MFI lowered the activity, although the influence was limited (Brosius, Kooyman & Fletcher, 2016).

The higher activity of Pt/H-NS-6-75a compared to Pt/H-NS-6-100a strongly suggests the presence of additional H^+ sites present in H-NS-6-75a. H-NS-6-75a most likely contains some Al^{VI} species associated with Brønsted acidity. A species, namely $Al(SiO)_4(H_2O)(H_3O^+)$, was proposed by Bourgeat-Lami *et al.* (1991) and forms after calcining NH_4-zeolites (see 5.1.1.5) (Bourgeat-Lami *et al.*, 1991; van Bokhoven *et al.*, 2000). This further supports the presence of flexible Al^{VI} species in H-NS-6-75a (figure 27). The total [BAS] of H-NS-6-75a could encompass H^+ associated with Al^{IV} and Al^{VI}, which is more than the [BAS] of H-NS-6-100a and less than the [BAS] of H-NS-6-50a. Compared to Pt/H-NS-6-50a, the lower activity of Pt/H-NS-6-75a may be attributed to the lower total [BAS] of Pt/H-NS-6-75a.

In wet hydrocracking, with $H_2O/n\text{-}C_{16}$ = 0.8 v/v corresponding to 53 mol-% H_2O in the feed, the rate of hydrocracking for Pt/H-NS-6-25a, Pt/H-NS-6-50a, Pt/H-NS-6-75a and Pt/H-NS-6-100a is suppressed by 45, 43, 47 and 37 °C, respectively, in comparison to the rate of dry hydrocracking at 205 °C.

In ideal hydrocracking, the Brønsted acid-catalysed steps, namely skeletal isomerization and β-scission, are rate-limiting for the overall reaction (Coonradt & Garwood, 1964). The reactivity of n-paraffins in microporous zeolites is controlled by competitive adsorption rather than diffusion (Denayer *et al.*, 1997). The rate is suppressed by H_2O, since H_2O competes with the feed for adsorption at the H^+ sites (Brosius, Kooyman & Fletcher, 2016). In addition, the stronger deactivation of Pt/H-NS-6-75a in comparison to Pt/H-NS-6-100a may be a result of the very low γ_{Pt} of Pt/H-NS-6-75a (table 28, figure 28 c). This is similar to a previous study, in which Pt/bulk MFI with very large Pt particles (d_{Pt} ≈ 6 nm) showed a stronger deactivation by H_2O than Pt/bulk MFI with small Pt particles (d_{Pt} ≈ 1 nm) (Brosius, Kooyman & Fletcher, 2016). This underlines the importance of high γ_{Pt}.

5.2.1.3. Yields of Isomerization and Cracking Products

The yields of iso-hexadecane ($Y(iso\text{-}C_{16})$) and cracking products ($Y(C_1\text{-}C_{15})$) in dry and wet hydrocracking are shown in figure A29 a – d in appendix 3. In dry and wet hydrocracking, the yields of iso-C_{16} of the Pt/H-NS-6-ya catalysts are as high as can be expected for Pt/MFI nano-sheets (Brosius, Kooyman & Fletcher, 2016).

In dry hydrocracking, it was reported that the large pore Pt/HY zeolite displayed much higher yields of iso-C_{16} than Pt/bulk MFI and Pt/MFI nano-sheets (Brosius, Kooyman & Fletcher, 2016). Thus, the medium pores of the MFI framework play a role in the lower yields of iso-C_{16} of Pt/MFI zeolites in comparison to Pt/HY zeolite. The medium pores impose product shape-selectivity effects. Due to the long residence time of iso-C_{16} in the medium pores, iso-C_{16} undergoes cracking reactions, resulting in the low yields of iso-C_{16}.

In wet hydrocracking, the yields of iso-C_{16} increased in all Pt/H-NS-6-ya catalysts. This is due to H_2O, which facilitates desorption of iso-C_{16} by adsorbing on the H^+ sites, resulting in the increased iso-C_{16} yields and suppression of consecutive cracking (Brosius, Kooyman & Fletcher, 2016).

5.2.1.4. Hydrocracking Selectivity

5.2.1.4.1. Secondary Cracking

The degree of secondary cracking is presented as a ratio by moles of the C_4 and C_{12} fractions in figure 30. In dry hydrocracking, the occurrence of secondary cracking in MFI zeolites is due to product shape-selectivity imposed by the medium pores. The largest fragments are hindered from diffusing out of the zeolite pores and thus undergo secondary cracking (Weitkamp, Jacobs & Martens, 1983). The degree of secondary cracking (figure 30) increases from low to high conversions as the largest fragments gradually disappear (Weitkamp, Jacobs & Martens, 1983). In wet hydrocracking, secondary cracking for each catalyst is completely suppressed up to high conversions. The suppression of secondary cracking is due to competitive adsorption of H_2O, which facilitates desorption of primary cracking products from the H^+ sites (Brosius, Kooyman & Fletcher, 2016).

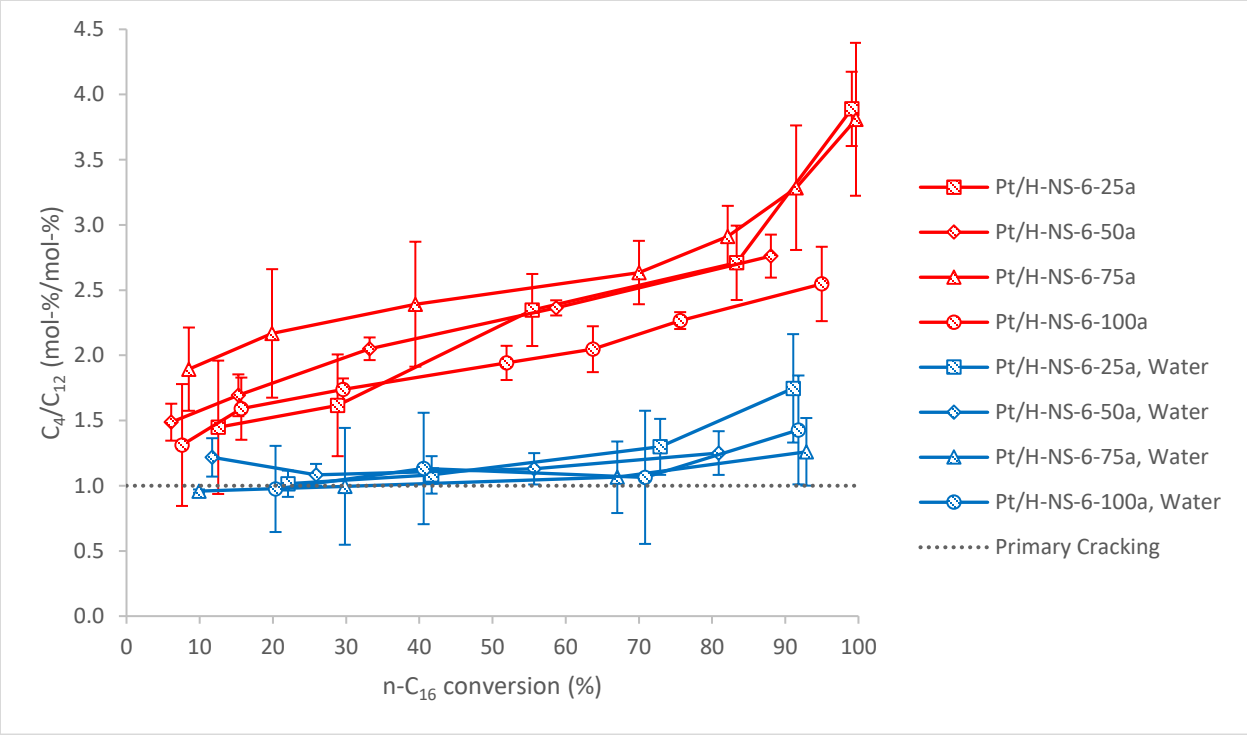

Figure 30: Degree of secondary cracking in the absence (red) and presence (blue) of H_2O over Pt/H-NS-6-ya catalysts (H_2O/n-C_{16} = 0.8 v/v). Error bars for the C_4/C_{12} molar ratio are shown at each conversion for each catalyst.

5.2.1.4.2. Secondary Isomerization

In MFI zeolites, the degree of branching of cracking products is limited due to transition-state shape-selectivity imposed by the medium pores. Type C β-scission is favoured over type A and B β-scissions, since the transition-state that would form via type A or B β-scission is sterically hindered in the medium pores, thus favouring linear cracking products (see 2.3.2) (Weitkamp, Jacobs & Martens, 1983). Under normal hydrocracking conditions, linear primary cracking products are isomerized in a consecutive step, and the reactivity order is determined by competitive adsorption (Weitkamp, Jacobs & Martens, 1983).

Figure 31 a – b shows the content of n-C_{12} in the C_{12} fraction in dry and wet hydrocracking.

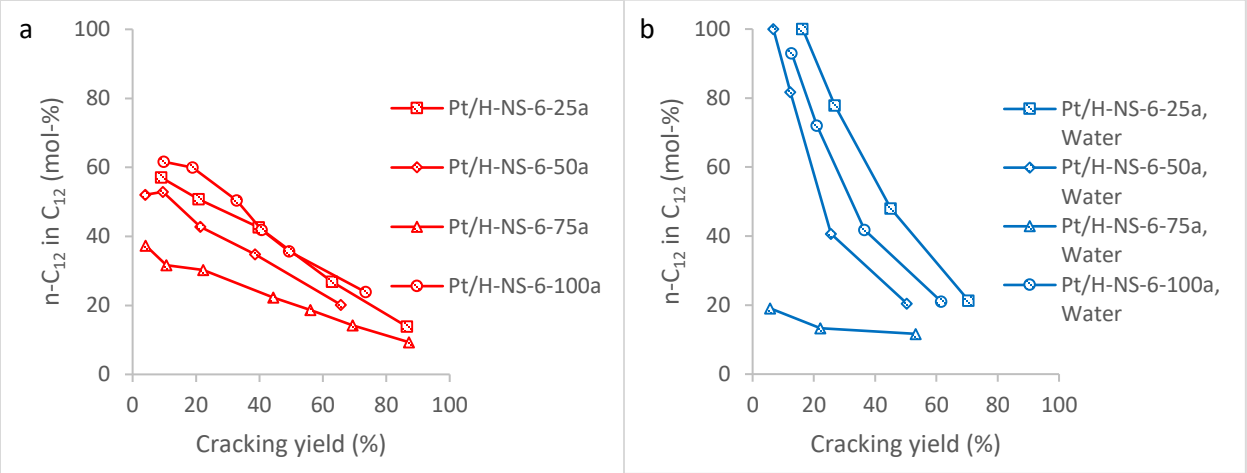

Figure 31: Content of n-C_{12} in the C_{12} fraction in (a) dry hydrocracking and (b) wet hydrocracking over Pt/H-NS-6-ya catalysts.

In dry hydrocracking, for each catalyst, the degree of C_{12} fraction branching increases with cracking yield, since the probability of secondary isomerization of C_{12} increases as iso-C_{16} is consumed by the reaction. In wet hydrocracking, for Pt/H-NS-6-25a, Pt/H-NS-6-50a and Pt/H-NS-6-100a, H_2O suppresses secondary isomerization of C_{12} at low cracking yields. H_2O outcompetes n-C_{12} for adsorption at the H^+ sites and as a result completely suppresses secondary isomerization of C_{12} at low cracking yields. On the other hand, for Pt/H-NS-6-25a, Pt/H-NS-6-50a and Pt/H-NS-6-100a, H_2O enhances secondary isomerization of C_{12} at higher cracking yields. The probability of secondary isomerization increases with cracking yield as iso-C_{16} is consumed by the reaction. Thus, with increasing cracking yields, n-C_{12} will eventually outcompete H_2O for adsorption at the H^+ sites, resulting in the enhancement of secondary isomerization at higher cracking yields.

For Pt/H-NS-6-75a, secondary isomerization of C_{12} is enhanced in the presence of H_2O. This may be related to the very low γ_{Pt} of Pt/H-NS-6-75a (table 28, figure 28 c). In wet hydrocracking, despite the very low γ_{Pt}, secondary cracking is completely suppressed up to high conversions (figure 30). This is in line with a previous study, where in wet hydrocracking, increasing the d_{Pt} from approximately 1 nm to approximately 6 nm in Pt/bulk MFI enhanced secondary isomerization, while secondary cracking remained completely suppressed (Brosius, Kooyman & Fletcher, 2016). The suppression of secondary cracking in Pt/H-NS-6-75a implies that cracking reactions occurred inside the micropores, since it is in the micropores where the reactions are subjected to the competitive adsorption effects of H_2O. With such very large Pt particles supported by H-NS-6-75a, the Pt particles should be located predominantly on the external surface of the zeolite support (Philippaerts *et al.*, 2010; Kim *et al.*, 2013). The Pt sites on the

external surface are probably too far from the H^+ sites inside the micropores, such that secondary isomerization reactions of olefinic intermediates on the H^+ sites are favoured.

For neither dry nor wet hydrocracking, does the trend in the content of n-C_{12} in the C_{12} fraction with Si/Al ratio correlate with V_{micro} (table 20), S_{ext} (table 20), [TAS] (figure 14), FAl content (table 22) or [BAS] (table 22) of the zeolites. Thus, it is not clear how Si/Al ratio influences differences in the content of n-C_{12} in the C_{12} fraction in dry and wet hydrocracking.

Thus, in wet bifunctional hydrocracking, for MFI nano-sheets with varying Si/Al ratios loaded with a constant and sufficient amount of metal, provided the metal dispersion is constant and sufficiently high, the activity increases with increasing number of H^+ sites (decreasing Si/Al ratio), while secondary cracking remains completely suppressed. Also, in this case, H_2O not only can prevent further cracking of isomerized cracking products but can also prevent isomerization of primary cracking products. This is advantageous with respect to maximizing diesel yield and CN in ideal hydrocracking of LTFT wax (see 2.2.3). Considering diesel production in high yield and high CN, in terms of selectivity, Pt/H-NS-6-25a is the best candidate, followed by Pt/H-NS-6-100a then Pt/H-NS-6-50a. In terms of both activity and selectivity, Pt/H-NS-6-25a is the best candidate.

Pt/H-NS-6-75a is the odd catalyst of the Pt/H-NS-6-ya series. H-NS-6-75a contains an abundant amount of EFAl species, of which a high fraction most likely encompasses flexible Al^{VI} species. Due to the trend in activity in dry hydrocracking, H-NS-6-75a most likely contains additional H^+ sites, probably associated with Al^{VI}, which supports the presence of flexible Al^{VI} species. The abundancy, nature and/or location of EFAl species most likely gives rise to the low γ_{Pt}. This in turn most likely results in the lower activity compared to Pt/H-NS-6-100a in wet hydrocracking. Also, it most likely favours selectivity towards branched cracking products in wet hydrocracking, thus making the catalyst an unsuitable candidate for production of high CN diesel.

5.2.2. Pt-H/C-NS-3-ya

C-NS-3-ya samples were loaded with 1 wt% Pt via CIE (see 4.1.3.3.2). The Pt-loaded samples were calcined (see 4.3.2.2) and subsequently reduced *in-situ* (see 4.3.2.3) to form Pt^0 particles and H^+ sites (equation 2), resulting in the bifunctional catalysts. Following *in-situ* reduction, dry and wet hydrocracking of n-C_{16} was performed (see 4.3.3 – 4.3.4). Fresh Pt-loaded samples were characterized by ICP-OES (see 4.2.2.6) and CO chemisorption (see 4.2.2.7).

5.2.2.1. Pt Loading and d_{Pt}

Prior to CO chemisorption, the Pt-loaded samples were calcined at 350 °C (heating rate: 0.3 °C/min) under O_2 flow (120 ml/min) and reduced at 225 °C (heating rate: 0.4 °C/min) under H_2 flow (120 ml/min) (see 4.2.2.7) (Philippaerts *et al.*, 2010; Brosius, Kooyman & Fletcher, 2016). The Pt loading and d_{Pt} are shown in table 30. The chemisorption isotherms are shown in figures A20 – A23 in appendix 2.

Table 30: Pt loading and d_{Pt} of Pt-H/C-NS-3-ya catalysts.

Catalyst	Pt loading (wt%)	d_{Pt} (nm)
Pt-H/C-NS-3-25a	0.92	2.23
Pt-H/C-NS-3-50a	0.81	1.72
Pt-H/C-NS-3-75a	0.87	2.00
Pt-H/C-NS-3-100a	0.88	2.10

As seen in table 30, the Pt-H/C-NS-3-ya catalysts have similar Pt loadings, in good agreement with the target loading of 1 wt%. Also, the catalysts have a similar d_{Pt}. Previously, it was reported that bulk MFI loaded with Pt via CIE and calcined at 350 °C using a slow heating rate (0.3 °C/min) in the presence of O_2 with a high flow rate (120 ml/min) gave rise to small Pt clusters (≈ 1 – 2 nm) with homogeneous particle size distribution throughout the zeolite crystal (Philippaerts *et al.*, 2010; Philippaerts *et al.*, 2011). In the present case, the d_{Pt} of the Pt-H/C-NS-3-ya catalysts is in good agreement with that reported previously.

5.2.2.2. Catalytic Activity

The Arrhenius plot for n-C_{16} dry and wet hydrocracking is shown in figure 32. The corresponding conversion versus temperature plot is shown in figure A30 in appendix 3. The plots show the hydrocracking performance under ideal plug flow conditions and in the absence of external diffusional limitations. In dry hydrocracking, the activity decreases with increasing Si/Al ratio. The $r_{205\,°C}$ and corresponding $X_{205\,°C}$ are shown in table 31. Since the catalysts have similar Pt loadings and a similar d_{Pt} (table 30), the trend in activity implies that the reaction rate is controlled by the Brønsted acid function.

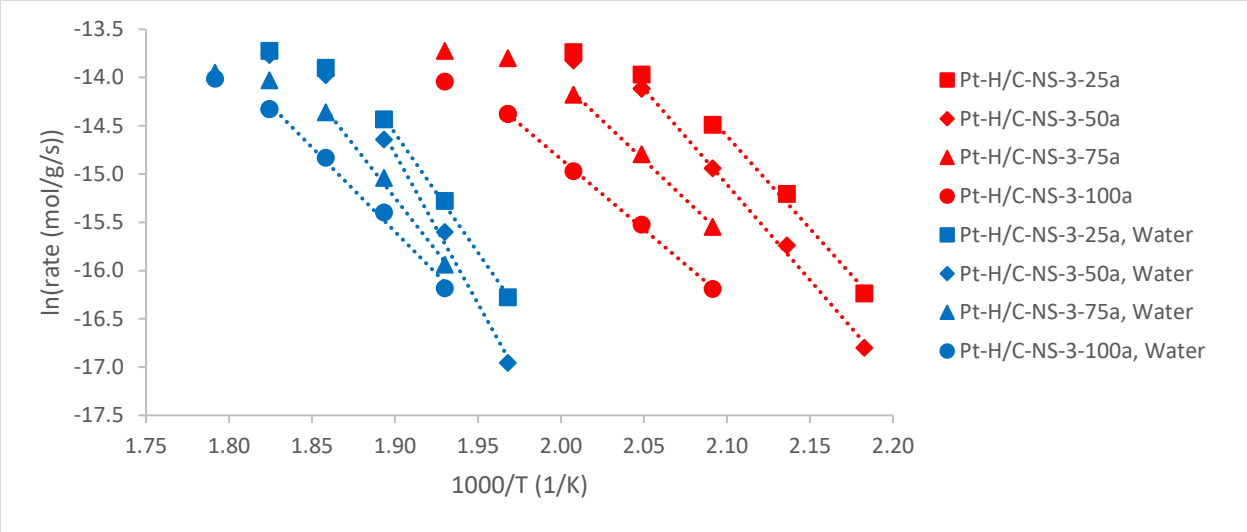

Figure 32: Arrhenius plot for n-C_{16} hydrocracking in the absence (red) and presence (blue) of H_2O over Pt-H/C-NS-3-ya catalysts (1 wt% Pt, 20 bar, W/F = 875 kg s/mol, H_2/n-C_{16} = 10 mol/mol, H_2O/n-C_{16} = 0.8 v/v).

Table 31: $r_{205\,°C}$ and $X_{205\,°C}$ in dry hydrocracking over Pt-H/C-NS-3-ya catalysts.

Catalyst	$r_{205\,°C}$ (mol/g/s)	$X_{205\,°C}$ (%)
Pt-H/C-NS-3-25a	5.10×10^{-7}	44.82
Pt-H/C-NS-3-50a	3.25×10^{-7}	28.56
Pt-H/C-NS-3-75a	1.77×10^{-7}	15.54
Pt-H/C-NS-3-100a	0.93×10^{-7}	9.09

In wet hydrocracking, the rate of hydrocracking for Pt-H/C-NS-3-25a, Pt-H/C-NS-3-50a, Pt-H/C-NS-3-75a and Pt-H/C-NS-3-100a is suppressed in decreasing order by 49, 47, 44 and 39 °C, respectively, in comparison to the rate of dry hydrocracking at 205 °C. The suppression of the rates by H_2O is due to competitive adsorption between H_2O and n-C_{16} at the H^+ sites (see 5.2.1.2) (Brosius, Kooyman & Fletcher, 2016).

Considering the catalysts have similar Pt loadings and the Pt clusters are well dispersed with a similar d_{Pt} (table 30), the trend in activity in dry and wet hydrocracking is probably due to differences in [BAS] between the catalysts. For the C-NS-3-ya supports loaded with Pt by CIE, 2 H^+ ions are formed for every Pt^0 after the *in-situ* reduction step (equation 2). All the catalysts were loaded with a constant amount of Pt (1 wt%). This implies that a constant amount of H^+ sites (≈ 0.10 mmol/g, using equation 2) should be generated after the *in-situ* reduction step in all the catalysts, which is less than the [BAS] of the C-NS-3-ya samples (table 27).

However, during calcination of as-synthesized forms of zeolites, removal of ammonium surfactant could generate H^+ sites (Parker, Bibby & Patterson, 1984; de Saldarriaga, Saldarriaga & Davis, 1987; Nowotny, Lercher & Kessler, 1991). After zeolite synthesis, the negative charge of the zeolite framework can be compensated by both Na^+ ions and ammonium surfactant. When calcining the zeolite, the ammonia moiety of the surfactant can be removed, leaving behind H^+ ions that can compensate the negative charge of the framework in addition to Na^+ ions. Thus, the total [BAS] of the *in-situ* reduced Pt/C-NS-3-ya catalysts could encompass both H^+ ions generated by surfactant removal during calcination and by the *in-situ* reduction step. The total [BAS] generated in this manner probably increases with decreasing Si/Al ratio, which accounts for the increasing trend in activity with decreasing Si/Al ratio observed in dry and wet hydrocracking.

5.2.2.3. Yields of Isomerization and Cracking Products

The yields of iso-C_{16} and cracking products in dry and wet hydrocracking are shown in figure A31 a – d in appendix 3. In dry and wet hydrocracking, the yields of iso-C_{16} of the Pt-H/C-NS-3-ya catalysts are as high as can be expected for Pt/MFI nano-sheets (Brosius, Kooyman & Fletcher, 2016). In wet hydrocracking, the yields of iso-C_{16} increased in all catalysts due to H_2O, which facilitates desorption of iso-C_{16} from H^+ sites (see 5.2.1.3) (Brosius, Kooyman & Fletcher, 2016).

5.2.2.4. Hydrocracking Selectivity

5.2.2.4.1. Secondary Cracking

The degree of secondary cracking (C_4/C_{12} molar ratio) is shown in figure 33. In dry hydrocracking, the degree of secondary cracking increases from low to high conversions as the largest fragments gradually disappear (see 5.2.1.4.1) (Weitkamp, Jacobs & Martens, 1983).

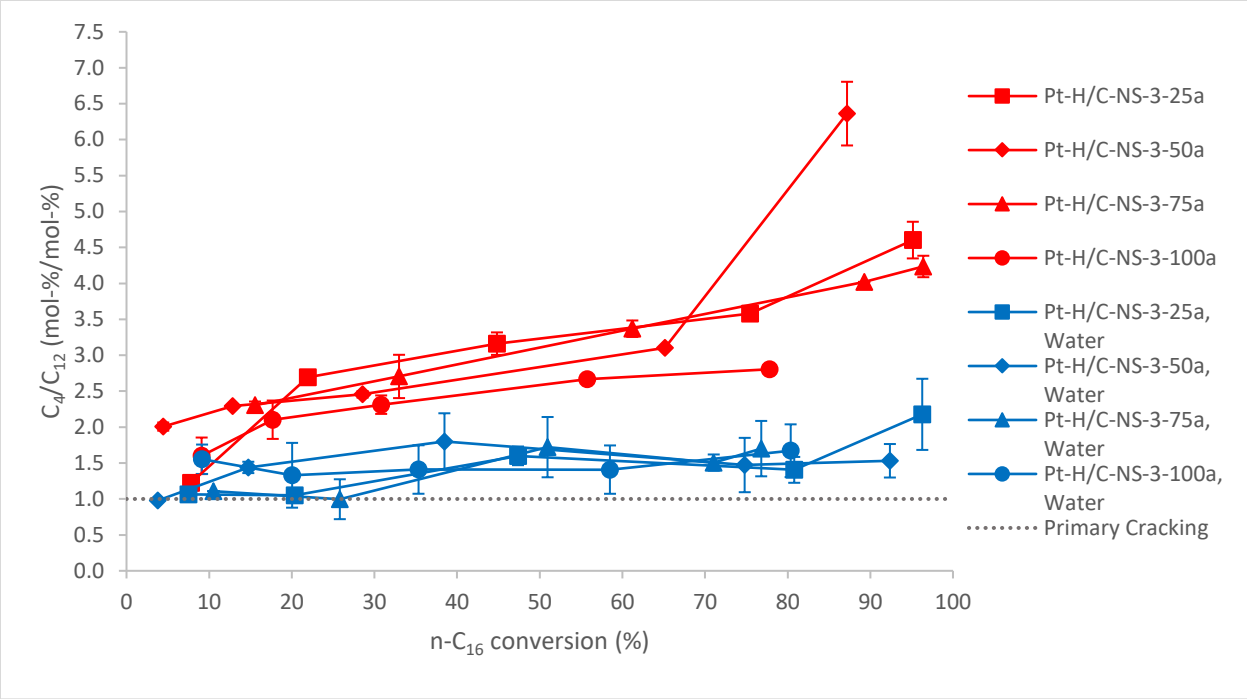

Figure 33: Degree of secondary cracking in the absence (red) and presence (blue) of H_2O over Pt-H/C-NS-3-ya catalysts (H_2O/n-C_{16} = 0.8 v/v).

In wet hydrocracking, H_2O suppresses secondary cracking in all catalysts. However, secondary cracking is not completely suppressed up to high conversions. The suppression of secondary cracking is due to competitive adsorption between H_2O and primary cracking products at the H^+ sites (see 5.2.1.4.1) (Brosius, Kooyman & Fletcher, 2016). As mentioned in 5.2.2.2, the total [BAS] of the Pt-H/C-NS-3-ya catalysts could encompass H^+ sites generated by surfactant removal during calcination and by the *in-situ* reduction step. The distribution of H^+ sites could be heterogenous with localized areas of abundant H^+ sites relative to Pt sites. This could increase the chance of primary cracking products encountering H^+ sites before encountering Pt sites, resulting in secondary cracking.

5.2.2.4.2. Secondary Isomerization

Figure 34 a – b shows the content of n-C_{12} in the C_{12} fraction in dry and wet hydrocracking. In dry hydrocracking, for each catalyst, the degree of C_{12} fraction branching increases with cracking yield, since the probability of secondary isomerization increases as iso-C_{16} is consumed by the reaction (see 5.2.1.4.2). In wet hydrocracking, H_2O suppresses secondary isomerization of C_{12} at low cracking yields. The suppression of secondary isomerization can be attributed to competitive adsorption between H_2O and n-C_{12} at the H^+ sites (see 5.2.1.4.2) (Brosius, Kooyman & Fletcher,

2016). On the other hand, H_2O enhances secondary isomerization of C_{12} at higher cracking yields (see 5.2.1.4.2).

For neither dry nor wet hydrocracking, does the trend in the content of n-C_{12} in the C_{12} fraction with Si/Al ratio correlate with V_{micro} (table 24), S_{ext} (table 24), [TAS] (figure 23), FAl content (table 27) or [BAS] (table 27) of the zeolites. Thus, it is not clear how Si/Al ratio influences differences in the content of n-C_{12} in the C_{12} fraction in dry and wet hydrocracking.

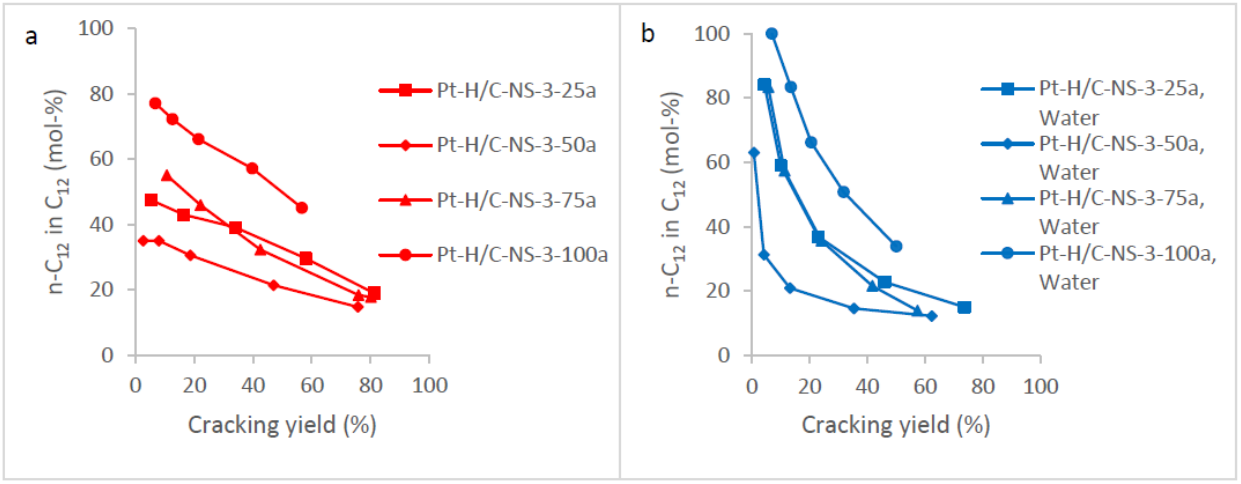

Figure 34: Content of n-C_{12} in the C_{12} fraction in (a) dry hydrocracking and (b) wet hydrocracking over Pt-H/C-NS-3-ya catalysts.

Thus, in wet bifunctional hydrocracking, for calcined MFI nano-sheets with varying Si/Al ratios loaded with 1 wt% of metal via CIE, the activity is not constant and secondary cracking is not completely suppressed up to high conversions. Although H_2O can prevent isomerization of primary cracking products at low cracking yields, it cannot prevent secondary cracking of isomerized cracking products up to high conversions. The incomplete suppression of secondary cracking is unfavourable with respect to maximizing diesel yield in ideal hydrocracking of LTFT wax (see 2.2.3). Thus, considering production of diesel in high yield and high CN, the Pt-H/C-NS-3-ya catalysts are unsuitable candidates.

5.2.3. Pt-H/Na-NS-6-yb

Prior to CIE, the C-NS-6-yb samples were ion exchanged to form the NH_4-forms, followed by another ion exchange to form the Na-forms to ensure that the samples are completely in their Na-forms (see 4.1.3.3.2). The Na-forms were loaded with 1 wt% Pt via CIE (see 4.1.3.3.2). Pt-loaded samples were calcined (see 4.3.2.2) and reduced *in-situ* (see 4.3.2.3) to form Pt^0 particles and H^+ sites (equation 2), resulting in the bifunctional catalysts. Following *in-situ* reduction, dry and wet hydrocracking of n-C_{16} was performed (see 4.3.3 – 4.3.4). Fresh

Pt-loaded samples were characterized by ICP-OES (see 4.2.2.6) and CO chemisorption (see 4.2.2.7).

5.2.3.1. Pt Loading and d_{Pt}

Prior to CO chemisorption, the Pt-loaded samples were oxidized and reduced in the same manner as the Pt-loaded C-NS-3-ya samples. The Pt loadings and d_{Pt} are shown in table 32. The chemisorption isotherms are shown in figures A24 – A27 in appendix 2.

Table 32: Pt loading and d_{Pt} of Pt-H/Na-NS-6-yb catalysts.

Catalyst	Pt loading (wt%)	d_{Pt} (nm)
Pt-H/Na-NS-6-25b	1.02	3.65
Pt-H/Na-NS-6-50b	1.07	3.68
Pt-H/Na-NS-6-75b	1.15	3.85
Pt-H/Na-NS-6-100b	0.99	2.96

As seen in table 32, the Pt-H/Na-NS-6-yb catalysts have similar Pt loadings, in good agreement with the target loading of 1 wt%. Also, the d_{Pt} of the catalysts is not significantly different. However, the d_{Pt} of the catalysts is larger than that of the Pt-H/C-NS-3-ya catalysts (table 30) and larger than that reported previously (Philippaerts *et al.*, 2010; Philippaerts *et al.*, 2011). With such a large d_{Pt}, the Pt clusters should be located predominantly on the external surfaces of the catalyst supports (Philippaerts *et al.*, 2010; Kim *et al.*, 2013).

Previously, bulk MFI in the Na-form loaded with Pt via CIE and pretreated in the same manner as the Pt-loaded Na-NS-6-yb samples gave rise to small Pt clusters (≈ 1 – 2 nm) with homogeneous particle size distribution throughout the zeolite crystal (Philippaerts *et al.*, 2010; Philippaerts *et al.*, 2011). Also, this holds for zeolite Y (Benesi, 1970) and mordenite (Ribeiro *et al.*, 1978). Thus, Na^+ ions most likely did not lead to the large d_{Pt} (table 32). The large d_{Pt} may be related to the nature and/or location of EFAl species present in the Na-NS-6-yb supports. The V_{micro} of the C-NS-6-yb samples is large and similar (table 24), and blockage of micropore apertures by EFAl species is highly unlikely for zeolite nano-sheets (see 5.1.2.3). Thus, for Pt/H-NS-6-yb samples, Pt located predominantly on the external surfaces of the supports would not be a result of blockage of the micropore apertures by EFAl species. Instead, EFAl species is most likely located on the external surfaces of the Na-NS-6-yb supports and may serve as a preferential location for Pt (Sree *et al.*, 2016).

5.2.3.2. Catalytic Activity

The Arrhenius plot for n-C_{16} dry and wet hydrocracking is shown in figure 35. The corresponding conversion versus temperature plot is shown in figure A32 in appendix 3. The plots show the hydrocracking performance under ideal plug flow conditions and in the absence of external diffusional limitations. In dry hydrocracking, a trend in activity is observed. There is a slight difference in the present activity trend compared to the Pt-H/C-NS-3-ya catalysts (figure 32). In the present case, the activity decreases in the order Pt-H/Na-NS-6-50b > Pt-H/Na-NS-6-25b > Pt-H/Na-NS-6-75b > Pt-H/Na-NS-6-100b. The $r_{205\ °C}$ and corresponding $X_{205\ °C}$ are shown in table 33.

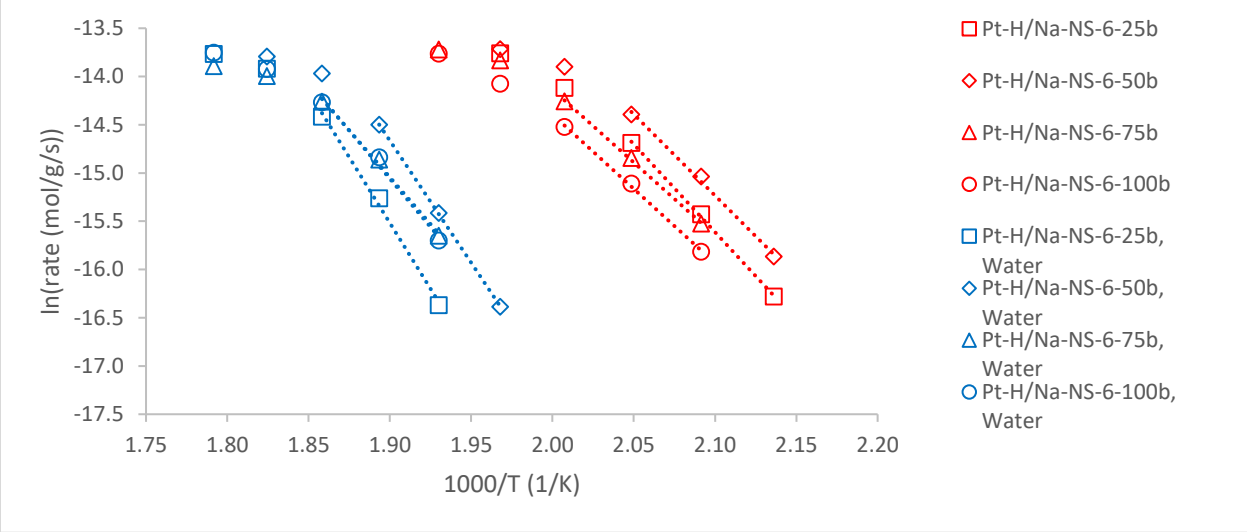

Figure 35: Arrhenius plot for n-C_{16} hydrocracking in the absence (red) and presence (blue) of H_2O over Pt-H/Na-NS-6-yb catalysts (1 wt% Pt, 20 bar, W/F = 875 kg s/mol, H_2/n-C_{16} = 10 mol/mol, H_2O/n-C_{16} = 0.8 v/v).

Table 33: $r_{205\ °C}$ and $X_{205\ °C}$ in dry hydrocracking over Pt-H/Na-NS-6-yb catalysts.

Catalyst	$r_{205\ °C}$ (mol/g/s)	$X_{205\ °C}$ (%)
Pt-H/Na-NS-6-25b	1.99×10^{-7}	17.48
Pt-H/Na-NS-6-50b	2.95×10^{-7}	25.90
Pt-H/Na-NS-6-75b	1.81×10^{-7}	15.87
Pt-H/Na-NS-6-100b	1.35×10^{-7}	11.88

In wet hydrocracking, the rate of hydrocracking for Pt-H/Na-NS-6-25b, Pt-H/Na-NS-6-50b, Pt-H/Na-NS-6-75b and Pt-H/Na-NS-6-100b is suppressed in decreasing order by 49, 44, 41 and 38 °C, respectively, in comparison to the rate of dry hydrocracking at 205 °C. The suppression of

the rates by H_2O is due to competitive adsorption between H_2O and n-C_{16} at the H^+ sites (Brosius, Kooyman & Fletcher, 2016).

The rate of n-C_{16} hydrocracking over all catalysts is probably controlled by diffusion of olefinic intermediates from H^+ sites to Pt sites (Weisz, 1962). This can explain differences in activities between the catalysts in dry hydrocracking and in wet hydrocracking (figure 35, figure A32). The catalysts have similar Pt loadings, the d_{Pt} of the catalysts are not significantly different, and the [BAS] formed after the *in-situ* reduction step should be constant in all catalysts (≈ 0.10 mmol/g, using equation 2). The [BAS] generated after the *in-situ* reduction step is less than the [BAS] of C-NS-6-25b, C-NS-6-50b and C-NS-6-75b (table 27) and equal to the [BAS] of C-NS-6-100b (table 27). However, the d_{Pt} of the catalysts is quite large (table 32). As mentioned in 5.2.2.1, with such a large d_{Pt}, the Pt clusters should be located predominantly on the external surfaces of the catalyst supports (Philippaerts *et al.*, 2010; Kim *et al.*, 2013).

The low [BAS] generated after the *in-situ* reduction step and the large d_{Pt} could lead to insufficient intimacy between the H^+ sites and Pt sites, resulting in the rate being controlled by diffusion of olefinic intermediates. Thus, in the operating window of diffusion, differences in activity between catalysts in dry hydrocracking and in wet hydrocracking are probably due to differences in the intimacy between the H^+ sites and Pt sites in the corresponding catalysts.

5.2.3.3. Yields of Isomerization and Cracking Products

The yields of iso-C_{16} and cracking products in dry and wet hydrocracking are shown in figure A33 a – d in appendix 3. In dry and wet hydrocracking, the yields of iso-C_{16} of the Pt-H/Na-NS-6-yb catalysts are as high as can be expected for Pt/MFI nano-sheets (Brosius, Kooyman & Fletcher, 2016). In wet hydrocracking, the yields of iso-C_{16} increased in all catalysts due to H_2O, which facilitates desorption of iso-C_{16} from H^+ sites (see 5.2.1.3) (Brosius, Kooyman & Fletcher, 2016).

5.2.3.4. Hydrocracking Selectivity

5.2.3.4.1. Secondary Cracking

The degree of secondary cracking (C_4/C_{12} molar ratio) is shown in figure 36. In dry hydrocracking, the degree of secondary cracking increases from low to high conversions as the largest fragments gradually disappear (see 5.1.2.4.1) (Weitkamp, Jacobs & Martens, 1983).

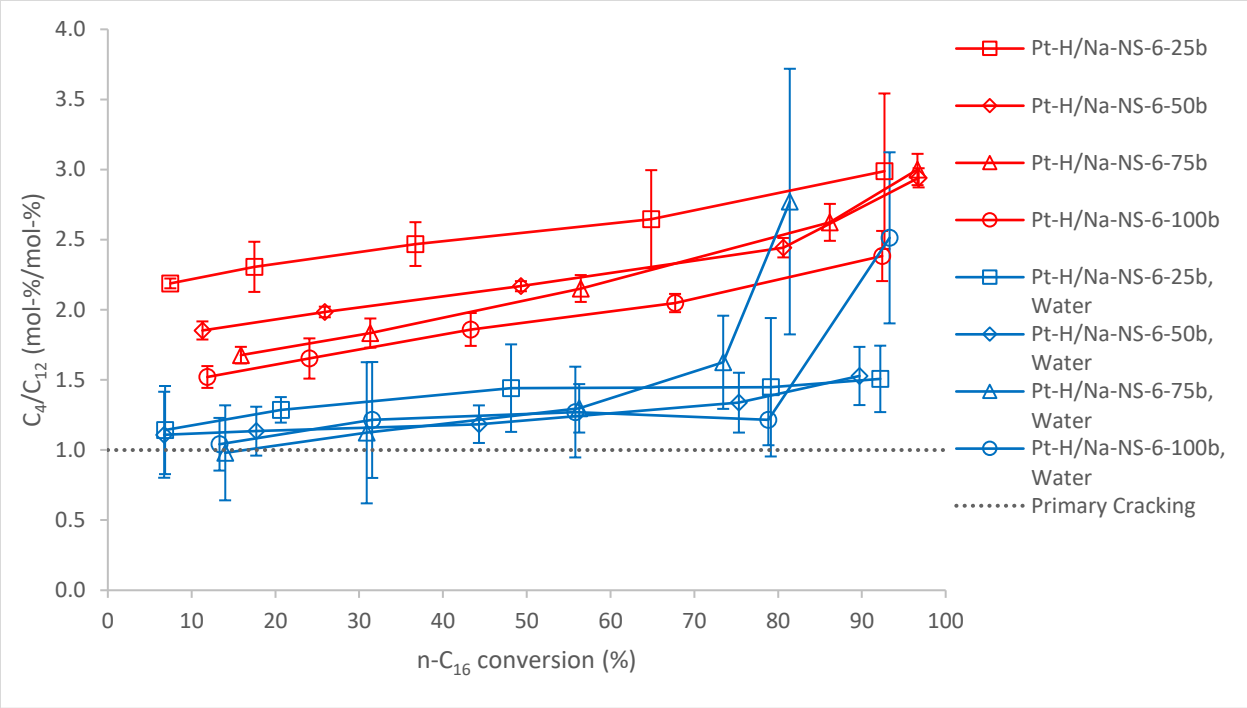

Figure 36: Degree of secondary cracking in the absence (red) and presence (blue) of H_2O over Pt-H/Na-NS-6-yb catalysts (H_2O/n-C_{16} = 0.8 v/v).

In wet hydrocracking, H_2O suppresses secondary cracking in all catalysts. However, similarly to the Pt-H/C-NS-3-ya catalysts, secondary cracking is not completely suppressed up to high conversions. The suppression of secondary cracking is due to competitive adsorption between H_2O and primary cracking products at the H^+ sites (Brosius, Kooyman & Fletcher, 2016). As mentioned in 5.2.2.2, the intimacy between the Pt sites and H^+ sites is probably insufficient such that the rate is controlled by diffusion of olefinic intermediates. With the presence of diffusion limitations, the primary cracking olefinic intermediates can undergo secondary cracking reactions on H^+ sites prior to encountering Pt sites, resulting in the secondary cracking (figure 36).

5.2.3.4.2. Secondary Isomerization

Figure 37 a – b shows the content of n-C_{12} in the C_{12} fraction in dry and wet hydrocracking. In dry hydrocracking, for each catalyst, the degree of C_{12} fraction branching increases with cracking yield, since the probability of secondary isomerization increases as iso-C_{16} is consumed by the reaction (see 5.2.1.4.2). In wet hydrocracking, similarly to the Pt-H/C-NS-3-ya catalysts (figure 34), H_2O suppresses secondary isomerization of C_{12} at low cracking yields. The suppression of secondary isomerization can be attributed to competitive adsorption between H_2O and n-C_{12} at the H^+ sites (see 5.2.1.4.2) (Brosius, Kooyman & Fletcher, 2016). On the other hand, H_2O enhances secondary isomerization of C_{12} at higher cracking yields (see 5.2.1.4.2).

For neither dry nor wet hydrocracking, does the trend in the content of n-C_{12} in the C_{12} fraction with Si/Al ratio correlate with V_{micro} (table 24), S_{ext} (table 24), [TAS] (figure 23), FAl content (table 27) or [BAS] (table 27) of the zeolites. Thus, it is not clear how Si/Al ratio influences differences in the content of n-C_{12} in the C_{12} fraction in dry and wet hydrocracking.

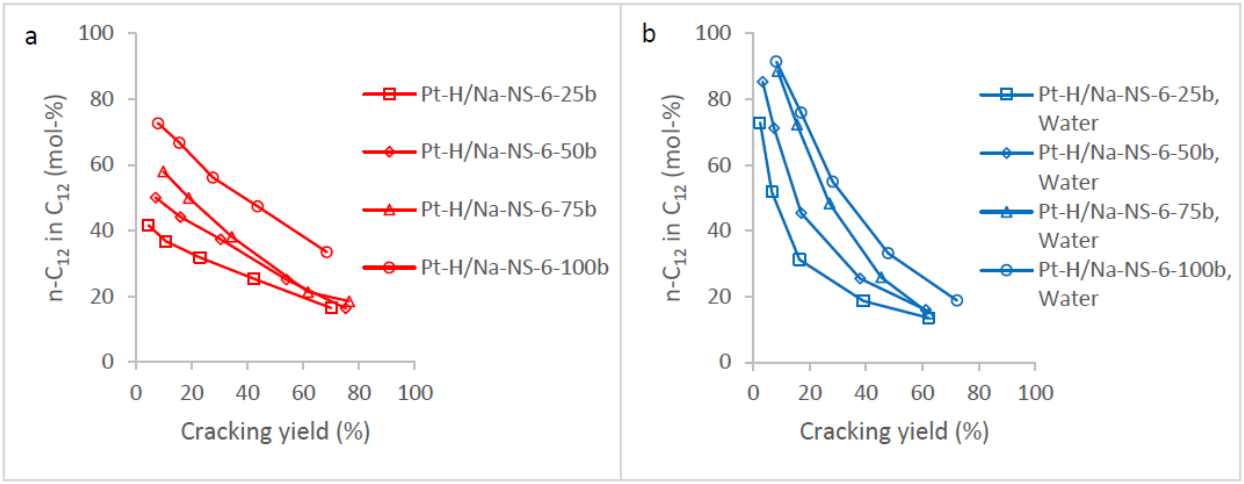

Figure 37: Content of n-C_{12} in the C_{12} fraction in (a) dry hydrocracking and (b) wet hydrocracking over Pt-H/Na-NS-6-yb catalysts.

Thus, in wet bifunctional hydrocracking, for Na^+ ion-exchanged MFI nano-sheets with varying Si/Al ratios loaded with 1 wt% of metal via CIE, the activity is not constant and secondary cracking is not completely suppressed up to high conversions. Although H_2O can prevent isomerization of primary cracking products at low cracking yields, it cannot prevent secondary cracking of isomerized cracking products up to high conversions. The incomplete suppression of secondary cracking is unfavourable with respect to maximizing diesel yield in ideal hydrocracking of LTFT wax (see 2.2.3). Thus, considering production of diesel in high yield and high CN, the Pt-H/Na-NS-6-yb catalysts are unsuitable candidates.

Chapter 6. Conclusions

In conclusion, the new synthesis method could be extended to various Si/Al ratios in the range 25 – 100. For each H-NS-6-ya sample, the nano-sheets had a non-uniform thickness. The average thickness of the H-NS-6-ya samples was in reasonable agreement. H-NS-6-ya samples had a smaller V_{micro} than bulk MFI, which was most likely due to the samples' much higher ratio of external surface compared to the surface of micropore channels. The H-NS-6-ya samples had a larger S_{ext} than bulk MFI due to their higher dispersion. The H-NS-6-ya samples exhibited uniform mesopore PSDs centred at approximately 4 nm, which could be due to the stacking of nano-sheets during synthesis or to bulk MFI seeds in the synthesis mixture.

For the H-NS-6-ya samples, the strength of the acid sites was virtually constant with varying Si/Al ratio. Bulk MFI (Si/Al = 45) contained stronger acid sites than the H-NS-6-ya samples, which could be due to a higher concentration of Brønsted acid sites at the channel intersections in bulk MFI in comparison to the H-NS-6-ya samples. All the Al atoms in bulk MFI and H-NS-6-75a was associated with acidity. H-NS-6-25a and H-NS-6-50a may have a higher actual Si/Al ratio and/or may contain non-Lewis acidic EFAl sites, whereas H-NS-6-100a may have a lower actual Si/Al ratio and/or may contain Lewis acidic EFSi sites. The H-NS-6-ya samples exhibited EFAl species, with H-NS-6-75a exhibiting an oddly large amount, of which a high fraction may have formed during calcination of the NH_4-form and may encompass flexible Al species with predominantly Al^{VI}.

Pt/H-NS-6-25a, Pt/H-NS-6-50a and Pt/H-NS-6-100a exhibited a similar and high γ_{Pt}. In contrast, Pt/H-NS-6-75a exhibited a very low γ_{Pt}, which was probably a result of the abundancy, nature and/or location of EFAl species present in the support. In dry hydrocracking of n-C_{16}, the trend in catalytic activity strongly suggested that the total [BAS] increased with decreasing Si/Al ratio. H-NS-6-75a most likely contained some Al^{VI} species associated with Brønsted acidity, supporting the presence of flexible Al^{VI} species. In wet hydrocracking of n-C_{16}, H_2O suppressed activity due to competitive adsorption between H_2O and the feed at the H^+ sites. At a constant and sufficiently high γ_{Pt}, the activity increased with increasing number of H^+ sites, while secondary cracking remained completely suppressed. The suppression of secondary cracking was due to competitive adsorption between H_2O and primary cracking products at the H^+ sites. Pt/H-NS-6-75a with a very low γ_{Pt} displayed a lower activity than Pt/H-NS-6-100a, which may be a result of the very low γ_{Pt} of Pt/H-NS-6-75a, underlining the importance of high γ_{Pt}. For Pt/H-NS-6-25a, Pt/H-NS-6-50a and Pt/H-NS-6-100a, H_2O favoured linear cracking products at low cracking yields due to competitive adsorption between H_2O and linear primary cracking products at the H^+ sites. In contrast, for Pt/H-NS-6-75a, H_2O favoured branched cracking products, which may be a result of Pt sites on

the external surface of the support being too far from the H^+ sites inside the micropores. Furthermore, it was not clear how Si/Al ratio influenced differences in selectivity towards linear primary cracking products in dry and wet hydrocracking.

The new synthesis method could be extended to $C_{22\text{-}6\text{-}3}$ at various Si/Al ratios in the range 25 – 100. The average thickness of the C-NS-6-yb samples was in reasonable agreement with that of the H-NS-6-ya samples. The C-NS-6-yb samples and H-NS-6-ya samples had a comparable V_{micro}. At given Si/Al ratios of 25 and 50, the S_{ext} of the C-NS-6-yb and H-NS-6-ya samples was significantly different. Also, C-NS-6-50b showed a higher EFAl content than H-NS-6-50a. Furthermore, at given Si/Al ratios of 25, 50 and 75, the [TAS] of the H-NS-6-yb and H-NS-6-ya samples was significantly different. The differences in S_{ext}, EFAl content and [TAS] could be due to the longer calcination of the as-synthesized forms of the corresponding NS-6-yb samples. C-NS-3-50a, C-NS-3-75a and C-NS-3-100a most likely contained nano-sheets oriented along [111]. For each C-NS-3-ya sample, the nano-sheets had a non-uniform thickness. The average thickness of the C-NS-6-yb samples, C-NS-3-50a, C-NS-3-75a and C-NS-3-100a was in reasonable agreement, whereas the average thickness of C-NS-3-25a was slightly larger than the other samples. For the C-NS-3-ya samples, a fraction of the nano-sheets exhibited shorter crystalline domains along the *ac* plane than the C-NS-6-yb samples. The C-NS-3-ya samples and bulk MFI had a comparable V_{micro}. C-NS-3-25a, C-NS-3-50a, C-NS-3-75a and bulk MFI had a comparable S_{ext} and thus comparable dispersion, whereas C-NS-3-100a had a lower S_{ext} than bulk MFI and thus a lower dispersion. The C-NS-6-yb and C-NS-3-ya samples exhibited uniform mesopore PSDs centred at approximately 4 nm, which could be due to the stacking of nano-sheets during synthesis or to bulk MFI seeds in the synthesis mixture.

For nano-sheets synthesized with $C_{22\text{-}6\text{-}6}$ or $C_{22\text{-}6\text{-}3}$, at a given Si/Al ratio, the strength of the acid sites was similar. For the H-NS-6-yb and H-NS-3-ya samples, the strength of the acid sites was virtually constant with varying Si/Al ratio. Bulk MFI contained stronger acid sites than the H-NS-6-yb and H-NS-3-ya samples, which could be due to a higher concentration of Brønsted acid sites at the channel intersections in bulk MFI in comparison to the H-NS-6-yb and H-NS-3-ya samples. All the Al atoms in H-NS-6-50b and H-NS-3-50a was associated with acidity. H-NS-6-25b and H-NS-3-25a may have a higher actual Si/Al ratio and/or may contain non-Lewis acidic EFAl sites, whereas H-NS-6-75b, H-NS-6-100b, H-NS-3-75a and H-NS-3-100a may have a lower actual Si/Al ratio and/or may contain Lewis acidic EFSi sites. Furthermore, replacing the terminal $–C_6H_{13}$ group in $C_{22\text{-}6\text{-}6}$ with $–C_3H_7$ resulted in an increase in the FAl content of nano-sheets with Si/Al ≥ 50, with the increase being the most pronounced for nano-sheets with Si/Al = 50. This was due to the increased occupancy of the zeolite framework by the hydrophilic region of $C_{22\text{-}6\text{-}3}$ in

comparison to the hydrophilic region of $C_{22\text{-}6\text{-}6}$ under the given set of synthesis conditions, since $–C_3H_7$ was less bulky than $–C_6H_{13}$.

For the Pt-H/C-NS-3-ya catalysts, the Pt loadings of the catalysts were similar, in good agreement with the target loading, and the d_{Pt} of the catalysts was low and similar. In dry and wet hydrocracking of n-C_{16}, the activity decreased with increasing Si/Al ratio, although a constant amount of H^+ would form after the *in-situ* reduction step. Also, in wet hydrocracking, secondary cracking was not completely suppressed up to high conversions. These were probably due to the presence of additional H^+ sites generated after SDA removal. Moreover, H_2O favoured linear cracking products at low cracking yields. Furthermore, it was not clear how Si/Al ratio influenced differences in selectivity towards linear primary cracking products in dry and wet hydrocracking.

For the Pt-H/Na-NS-6-yb catalysts, the Pt loadings of the catalysts were similar, in good agreement with the target loading, and the d_{Pt} of the catalysts was similar, but larger than the d_{Pt} of the Pt-H/C-NS-3-ya catalysts. This may be a result of the nature and/or location of EFAl species present in the Na-NS-6-yb supports. For the Pt-H/Na-NS-6-yb catalysts, differences in activity were observed in dry hydrocracking and in wet hydrocracking of n-C_{16}, although a constant amount of H^+ would form after the *in-situ* reduction step. Also, in wet hydrocracking, secondary cracking was not completely suppressed up to high conversions. These were probably due to insufficient intimacy between H^+ sites and Pt sites, such that the rate was controlled by diffusion of olefinic intermediates from H^+ sites to Pt sites and vice versa. Moreover, H_2O favoured linear cracking products at low cracking yields. Furthermore, it was not clear how Si/Al ratio influenced differences in selectivity towards linear primary cracking products in dry and wet hydrocracking.

The suppression of secondary cracking up to high conversions and suppression of secondary isomerization by H_2O is advantageous with regards to maximizing diesel yield and CN in ideal hydrocracking of LTFT wax. Considering diesel production in high yield and high CN from LTFT wax, in terms of selectivity, Pt/H-NS-6-25a is the best candidate, followed by Pt/H-NS-6-100a then Pt/H-NS-6-50a. In terms of both activity and selectivity, Pt/H-NS-6-25a is the best candidate. Due to high selectivity towards branched cracking products, Pt/H-NS-6-75a is an unsuitable candidate. Due to the incomplete suppression of secondary cracking up to high conversions, Pt-H/C-NS-3-ya and Pt-H/Na-NS-6-yb catalysts are unsuitable candidates.

Finally, this study has shown that in wet hydrocracking, for MFI nano-sheets with Si/Al ratios of 25 – 100 loaded with a constant and sufficient amount of metal, provided the metal dispersion is constant and sufficiently high, the activity increases with increasing number of H^+ sites

(decreasing Si/Al ratio), while secondary cracking remains completely suppressed. For MFI nano-sheets with Si/Al ratios of 25 – 100, modifying the structure of the $C_{22\text{-}6\text{-}6}$ SDA by replacing the terminal $–C_6H_{13}$ group with $–C_3H_7$ in the new synthesis method results in an increase in the FAl content of nano-sheets with Si/Al ≥ 50. Further research includes improving the activity of MFI nano-sheets beyond that of Pt/H-NS-6-25a while maintaining primary cracking up to high conversions in wet hydrocracking. Lowering the Si/Al ratio to below 25 and using $C_{22\text{-}6\text{-}3}$ as SDA presents a promising opportunity. To further increase the FAl content of MFI nano-sheets with various Si/Al ratios, increasing the crystallization temperature is another factor to consider (Zhu *et al.*, 2015). ^{27}Al NMR studies on as-synthesized, calcined and protonated forms can reveal whether EFAl results from synthesis, calcination involving SDA removal, or calcination involving NH_3 removal, respectively. Furthermore, ^{27}Al NMR studies on the ammonium forms and corresponding protonated forms can reveal whether EFAl encompasses flexible Al species. In addition, it will be interesting to investigate whether combining a Pt-containing surfactant with $C_{22\text{-}6\text{-}6}$ or $C_{22\text{-}6\text{-}3}$ can direct the structure of Pt-loaded MFI nano-sheets and thus eliminate the need for a Pt-loading post-treatment.

References

Aerts, A., van Isacker, A., Huybrechts, W., Kremer, S. P. B., Kirschhock, C. E. A., Collignon, F., Houthoofd, K., Denayer, J. F. M., Baron, G. V., Marin, G. B., Jacobs, P. A. & Martens, J. A. 2004. Decane Hydroconversion on Bifunctional Zeogrid and Nano-Zeolite Assembled from Aluminosilicate Nanoslabs of MFI Framework. *Applied Catalysis A: General.* 257:7 – 17.

Almutairi, S. M. T., Mezari, B., Pidko, E. A., Magusin, P. C. M. M. & Hensen, E. J. M. 2013. Influence of Steaming on the Acidity and the Methanol Conversion Reaction of HZSM-5 Zeolite. *Journal of Catalysis.* 307:194 – 203.

Alvarez, F., Ribeiro, F. R., Giannetto, G., Chevalier, F., Perot, G. & Guisnet, M. 1989. Hydroisomerization and Hydrocracking of Alkanes 5. Hydroisomerization and Hydrocracking of n Hexane and n Heptane on PtHY Catalysts. Effect of the Distribution of Metallic and Acid Sites. In *Zeolites: Facts, Figure, Future*, *Studies in Surface Science and Catalysis.* P. A. Jacobs & R. A. van Santen, Eds. Amsterdam: Elsevier. 1339 – 1348.

Alvarez, F., Ribeiro, F. R., Perot, G., Thomazeau, C. & Guisnet, M. 1996. Hydroisomerization and Hydrocracking of Alkanes 7. Influence of the Balance between Acid and Hydrogenating Functions on the Transformation of n-Decane on PtHY Catalysts. *Journal of Catalysis*. 164:179 – 189.

Argauer, R. J. & Landolt, G. R. 1972. *U.S. Patent No. 3 702 886*.

Avidan, A. A. 1993. Origin, Development and Scope of FCC Catalysis. In *Fluid Catalytic Cracking: Science and Technology, Studies in Surface Science and Catalysis.* J. S. Magee & M. M. Mitchell, Jr., Eds. Amsterdam: Elsevier. 1 – 39.

Bacha, J., Freel, J., Gibbs, A., Gibbs, L., Hemighaus, G., Hoekman, K., Horn, J., Gibbs, A. *et al.* 2007. *Diesel Fuels Technical Review.* (Technical Report 06/07). San Ramon, USA: Chevron Products Company, Chevron Corporation. Available: https://www.chevron.com/-/media/chevron/operations/documents/diesel-fuel-tech-review.pdf [2018, January 22].

Barret, E. P., Joyner, L. G. & Halenda, P. P. 1951. The Determination of Pore Volume and Area Distributions in Porous Substances. I. Computations from Nitrogen Isotherms. *Journal of the American Chemical Society.* 73:373 – 380.

Bartholomew, C. H. 2001. Mechanisms of Catalyst Deactivation. *Applied Catalysis A: General*. 212:17 – 60.

Basta, N. 1986. How to Convert Gradually to Oil-Refinery Hydrocracking. *Chemical Engineering*. 93:32 – 33.

BBC - GCSE Bitesize. n. d. *Analysing Substances*. Available: http://www.bbc.co.uk/schools/gcsebitesize/science/triple_aqa/further_analysis/analysing_substances/revision/3/ [2017, April 04].

Beck, J. S., Vartuli, J. C., Kennedy, G. J., Kresge, C. T., Roth, W. J. & Schramm, S. E. 1994. Molecular or Supramolecular Templating: Defining the Role of Surfactant Chemistry in the Formation of Microporous and Mesoporous Molecular Sieves. *Chemistry of Materials.* 6:1816 – 1821.

Benavent, V. J. M. 2012. Síntesis y Caracterización de Zeolitas Micro-Mesoporosas Obtenidas a Partir de Surfactantes Bifuncionales. MSc. Thesis. Instituto Technología Química.

Benco, L., Demuth, T., Hafner, J., Hutschka, F. & Toulhoat, H. 2002. Extraframework Aluminum Species in Zeolites: Ab Initio Molecular Dynamics Simulation of Gmelinite. *Journal of Catalysis.* 209:480 – 488.

Benesi, H. A. 1970. *U.S. Patent No. 3 527 835.* Washington, DC: Patent and Trademark Office.

Blomsma, E., Martens, J. A. & Jacobs, P. A. 1997. Isomerization and Hydrocracking of Heptane over Bimetallic Bifunctional PtPd/H-Beta and PtPd/USY Zeolite Catalysts. *Journal of Catalysis.* 165:241 – 248.

Bouchy, C., Hastoy, G., Guillon, E. & Martens, J. A. 2009. Fischer-Tropsch Waxes Upgrading via Hydrocracking and Selective Hydroisomerization. *Oil & Gas Science and Technology – Review IFP*. 64:91 – 112.

Bourgeat-Lami, E., Massiani, P., Di Renzo, F., Espiau, P., Fajula, F. & Des Courières, T. 1991. Study of the State of Aluminium in Zeolite-β. *Applied Catalysis*. 72:139 – 152.

Breck, D. W. 1974. *Zeolite Molecular Sieves, Structure, Chemistry and Use.* New York, USA: John Wiley & Sons.

Brosius, R. & Fletcher, J. C. Q. 2014. Hydrocracking under Fischer-Tropsch Conditions; the Effect of CO on the Mass Transfer Resistance by Metal Clusters. *Journal of Catalysis.* 317:318 – 325.

Brosius, R., Kooyman, P. J. & Fletcher, J. C. Q. 2016. Selective Formation of Linear Alkanes from n-Hexadecane Primary Hydrocracking in Shape-Selective MFI Zeolites by Competitive Adsorption of Water. *ACS Catalysis.* 6:7710 – 7715.

Brosius, R., Kooyman, P. J. & Fletcher, J. C. Q. 2016. Selective Formation of Linear Alkanes from n-Hexadecane Primary Hydrocracking in Shape-Selective MFI Zeolites by Competitive Adsorption of Water. *ACS Catalysis.* Suppl. (September, 30):1 – 14.

Brouwer, D. M. & Oelderik, J. M. 1968. HF-SbF_5 Catalysed Isomerization of 2-Methylpentane: Kinetics and Mechanism of Rearrangement and Hydride-Ion Transfer Steps in Alkylcarbonium Ion Reactions. *Recueil des Travaux Chimiques des Pays-Bas.* 87:721 – 736.

Business Dictionary. n.d. Cetane Number. Available: http://www.businessdictionary.com/definition/cetane-number.html [2017, February 19].

Buyan, F. M., Chen, N. Y., LaPierre, R. B., Pappal, D. A., Partridge, R. D. & Wong, S. F. 1995. *Hydrocarbon Technology International.* 14.

Cabral de Menezes, S. M., Lam, Y. L., Damodaran, K. & Pruski, M. 2006. Modification of H-ZSM-5 Zeolites with Phosphorus. 1. Identification of Aluminum Species by ^{27}Al Solid-State NMR and Characterization of their Catalytic Properties. *Microporous and Mesoporous Materials.* 95:286 – 295.

Calemma, V., Correra, S., Perego, C., Pollesel, P. & Pellegrini, L. 2005. Hydroconversion of Fischer-Tropsch Waxes: Assessment of the Operating Conditions Effect by Factorial Design Experiments. *Catalysis Today*. 106:282 – 287.

Camblor, M. A., Corma, A. & Valencia, S. 1998. Characterization of Nanocrystalline Zeolite Beta. *Microporous and Mesoporous Materials.* 25:59 – 74.

Chen, N. Y., Gorring, R. L., Ireland, H. R. & Stein, T. R. 1977. New Process Cuts Pour Point of Distillates. *Oil & Gas Journal.* 75:165 – 170.

Chevalier, F., Guisnet, M. & Maurel, R. 1977. Tracer Study of the Isomerization of Paraffins on Bifunctional Catalysts. *Proceedings of the 6th International Congress on Catalysis*. 1977. London: The Chemical Society. 478 – 487.

Choi, M., Na, K., Kim, J., Sakamoto, Y., Terasaki, O. & Ryoo, R. 2009. Stable Single-Unit-Cell Nanosheets of Zeolite MFI as Active and Long-Lived Catalysts. *Nature*. 461:246 – 249.

Choi, M., Na, K., Kim, J., Sakamoto, Y., Terasaki, O. & Ryoo, R. 2009. Stable Single-Unit-Cell Nanosheets of Zeolite MFI as Active and Long-Lived Catalysts. *Nature*. Suppl. (September, 10):1 – 6.

Coonradt, H. L. & Garwood, W. E. 1964. Mechanism of Hydrocracking. Reactions of Paraffins and Olefins. *Industrial & Engineering Chemistry Process Design and Development.* 3:38 – 45.

Csicsery, S. M. 1967. Equilibrium Distributions of the Dimethylethylbenzene and Methyldiethylbenzene Isomers. *Journal of Chemical & Engineering Data.* 12:118 – 122.

Csicsery, S. M. 1976. Shape Selective Catalysis. In *Zeolite Chemistry and Catalysis.* J. A. Rabo, Ed. Washington, DC: American Chemical Society. 680 – 713.

Csicsery, S. M. 1986. Catalysis by Shape Selective Zeolites – Science and Technology. *Pure and Applied Chemistry.* 58:841 – 856.

Database of Zeolite Structures. 2017. Framework Type MFI. Available: http://europe.iza-structure.org/IZA-SC/material_tm.php?STC=MFI [2018, January 19].

Degnan, T. F. & Kennedy, C. R. 1993. Impact of Catalyst Acid/Metal Balance in Hydroisomerization of Normal Paraffins. *AIChE Journal.* 39:607 – 614.

de Jong, K. P., Zečević, J., Friedrich, H., de Jongh, P. E., Bulut, M., van Donk, S., Kenmogne, R., Finiels, A., Hulea, V. & Fajula, F. 2010. Zeolite Y Crystals with Trimodal Porosity as Ideal Hydrocracking Catalysts. *Angewandte Chemie International Edition.* 49:10074 – 10078.

Denayer, J. F., Baron, G. V., Souverijns, W. S., Martens, J. A. & Jacobs, P. A. 1997. Hydrocracking of n-Alkane Mixtures on Pt/H-Y Zeolite: Chain Length Dependence of the Adsorption and the Kinetic Constants. *Industrial & Engineering Chemistry Research.* 36:3242 – 3247.

Department of the Interior. 1993. Testing for Chlorides with Silver Nitrate. *Conserve O Gram*. Available: https://www.nps.gov/museum/publications/conserveogram/06-03.pdf [2017, May 02].

de Saldarriaga, S. L., Saldarriaga, C. & Davis, M. 1987. Investigations into the Nature of a Silicoaluminophosphate with the Faujasite Structure. *Journal of the American Chemical Society.* 109:2686 – 2691.

Doolan, P. C. & Pujado, P. R. 1989. Make Aromatics from LPG. *Hydrocarbon Processing International Edition.* 68:72 – 74.

Dry, M. E. 2001. High Quality Diesel via the Fischer-Tropsch Process – A Review. *Journal of Chemical Technology and Biotechnology*. 77:43 – 50.

Dry, M. E. 2002. The Fischer-Tropsch Process: 1950 – 2000. *Catalysis Today*. 71:227 – 241.

Dufresne, P., Bigeard, P. H. & Billion, A. 1987. New Developments in Hydrocracking: Low Pressure High-Conversion Hydrocracking. *Catalysis Today*. 1:367 – 384.

Dune Sciences, Inc. 2011. *Particle Size Analysis SOP.* Available: http://www.dunesciences.com/files/Particle_Size_Analysis_SOP.pdf [2017, August 31].

Egeblad, K., Christensen, C. H., Kustova, M. & Christensen, C. H. 2008. Templating Mesoporous Zeolites. *Chemistry of Materials.* 20:946 – 960.

ExxonMobil Research and Engineering Company. 2002. ExxonMobil Catalytic Dewaxing – A Commercial Proven Technology, EMRE, August 2002. Available: http://citeseerx.ist.psu.edu/viewdoc/download;jsessionid=65E494E9C10CFC0AF71065305EFB24C0?doi=10.1.1.196.9147&rep=rep1&type=pdf [2018, August 5].

ExxonMobil Research and Engineering Company. 2011. Maximising Premium Distillate by Catalytic Dewaxing, EMRE, February 2011. Available: http://www.digitalrefining.com/article/1000235,Maximising_premium_distillate_by_catalytic_dewaxing.html#.W2Gn5NIzbIW [2018, August 5].

Flanigen, E. M. 2001. Zeolites and Molecular Sieves: An Historical Perspective. In *Introduction to Zeolite Science and Practice, Studies in Surface Science and Catalysis.* H. van Bekkum, E. M. Flanigen, P. A. Jacobs & J. C. Jansen, Eds. White Plains: Elsevier Science B. V. 11 – 35.

Fyfe, C., Gobbi, G., Hartman, J., Klinowski, J. & Thomas, J. 1982. Solid-State Magic-Angle Spinning Aluminum-27 Nuclear Magnetic Resonance Studies of Zeolites Using a 400-MHz High-Resolution Spectrometer. *The Journal of Physical Chemistry*. 86:1247 – 1250.

Gilson, J., Edwards, G., Peters, A., Rajagopalan, K., Wormsbecher, R., Roberie, T. & Shatlock, M. 1987. Penta-co-ordinated Aluminium in Zeolites and Aluminosilicates. *Journal of the Chemical Society, Chemical Communications*. 91 – 92.

Guild Associates, Inc. 2016. Molecular Gate® Adsorption Systems Nitrogen Rejection and CO_2 Removal Made Easy. Available: www.moleculargate.com [2008, August].

Guisnet, M., Alvarez, F., Giannetto, G. & Perot, G. 1987. Hydroisomerization and Hydrocracking of n-Heptane on PtH Zeolites. Effect of the Porosity and of the Distribution of Metallic and Acid Sites. *Catalysis Today.* 1:415 – 433.

Hedden, K. & Weitkamp J. 1975. Das Hydrocracken Schwerer Erdölfraktionen. Zur Flexibilität des Verfahrens und zum Reaktionsmechanismus. *Chemie Ingenieur Technik.* 47:505 – 513.

Henz, H. F., de Marco Meniconi, V. M. & Fuoco, J. M. 1986. Petrobas Experience with Octane Enhancement in Residual Catalytic Cracking. *Ketjen Catalyst Symposium.* 1986. Scheveningen.

Huang, J., Jiang, Y., Marthala, V., Thomas, B., Romanova, E. & Hunger, M. 2008. Characterization and Acidic Properties of Aluminum-Exchanged Zeolites X and Y. *The Journal of Physical Chemistry C*. 112:3811 – 3818.

Hudec, P., Smieskova, A., Zidek, Z., Schneider, P. & Solcova, O. 2002. Determination of Microporous Structure of Zeolites by t-Plot Method – State-of-the-Art. In *Impact of Zeolites and other Porous Materials on the New Technologies at the Beginning of the New Millennium*, *Studies in Surface Science and Catalysis.* R. Aiello, G. Giordano & F. Testa, Eds. Amsterdam: Elsevier Science B. V. 1587 – 1594.

Hunger, B., Heuchel, M., Clark, L. A. & Snurr, R. Q. 2002. Characterization of Acidic OH Groups in Zeolites of Different Types: An Interpretation of NH_3-TPD Results in the Light of Confinement Effects. *The Journal of Physical Chemistry B.* 106:3882 – 3889.

Institute of Chemistry, the Hebrew University of Jerusalem. n. d. *How to Make an NMR Sample*. Available: http://chem.ch.huji.ac.il/nmr/preparation/preparation.html [2017, April 03].

Ireland, H. R., Redini, C., Raff, A. S. & Fava, L. 1979. Distillate Dewaxing in Operation. *Hydrocarbon Processing.* 58:119 – 122.

IZA Structure Commission. 2017. Framework Type Codes. Available: http://www.iza-structure.org/index.htm [2018, January 19].

Jacobsen, C. J. H., Madsen, C., Houzvicka, J., Schmidt, I. & Carlsson, A. 2000. Mesoporous Zeolite Single Crystals. *Journal of the American Chemical Society.* 122:7116 – 7117.

Jager, B. 1998. Developments in Fischer-Tropsch Technology. In *Natural Gas Conversion V, Studies in Surface Science Catalysis*. A. Parmaliana, D. Sanfilippo, F. Frusteri, A. Vaccari & F. Arena, Eds. Giardini Naxos: Elsevier. 25 – 34.

Jentys, A. & Lercher, J. A. 2001. Techniques of Zeolite Characterization. In *Introduction to Zeolite Science and Practice, Studies in Surface Science and Catalysis.* H. van Bekkum, E. M. Flanigen, P. A. Jacobs & J. C. Jansen, Eds. Garching: Elsevier Science B. V. 345 – 418.

Jiao, J., Kanellopoulos, J., Wang, W., Ray, S., Foerster, H., Freude, D. & Hunger, M. 2005. Characterization of Framework and Extra-Framework Aluminum Species in Non-Hydrated Zeolites Y by ^{27}Al Spin-Echo, High-Speed MAS, and MQMAS NMR Spectroscopy at B_0 = 9.4 to 17.6 T. *Physical Chemistry Chemical Physics*. 7:3221 – 3226.

Jo, C., Cho, K., Kim, J. & Ryoo, R. 2014. MFI Zeolite Nanosponges Possessing Uniform Mesopores Generated by Bulk Crystal Seeding in the Hierarchical Surfactant-Directed Synthesis. *Chemical Communications.* 50:4175 – 4177.

Jung, J., Jo, C., Cho, K. & Ryoo, R. 2012. Zeolite Nanosheet of a Single-Pore Thickness Generated by a Zeolite-Structure-Directing Surfactant. *Journal of Materials Chemistry.* 22:4637 – 4640.

Kazansky, V. B. 1988. On the Nature of Lewis Acidic Sites in High Silica Zeolites and the Mechanism of their Dehydroxylation. *Catalysis Today.* 3:367 – 372.

Kim, Y. T., Jung, K. -D. & Park, E. D. 2010. Gas-Phase Dehydration of Glycerol over ZSM-5 Catalysts. *Microporous and Mesoporous Materials*. 131:28 – 36.

Kim, Y., Kim, J. -C., Jo, C., Kim, T. -W., Kim, C. -U., Jeong, S. -Y. & Chae, H. -J. 2016. Structural and Physicochemical Effects of MFI Zeolite Nanosheets for the Selective Synthesis of Propylene from Methanol. *Microporous and Mesoporous Materials*. 222:1 – 8.

Kim, J., Kim, W., Seo, Y., Kim J. -C. & Ryoo, R. 2013. n-Heptane Hydroisomerization over Pt/MFI Zeolite Nanosheets: Effects of Zeolite Crystal Thickness and Platinum Location. *Journal of Catalysis.* 301:187 – 197.

Klinowski, J., Thomas, J., Fyfe, C., Gobbi, G. & Hartman, J. 1983. A Highly Siliceous Structural Analog of Zeolite Y: High-Resolution Solid-State Silicon-29 and Aluminum-27 NMR Studies. *Inorganic Chemistry*. 22:63 – 66.

Koen, M. 2014. Hydrocracking of Long Chain n-Paraffins under Fischer-Tropsch Conditions. MSc. Thesis. University of Cape Town.

Kokotailo, G. T., Lawton, S. L. & Olson D. H. 1978. Structure of Synthetic Zeolite ZSM-5. *Nature (London)*. 272:437 – 438.

Kresge, C. T. & Dhingra, S. S. 2006. Molecular Sieves. In *Kirk-Othmer Encyclopedia of Chemical Technology*. Hoboken: John Wiley & Sons. 811 – 853.

Kresge, C. T., Leonowicz, M. E., Roth, W. J., Vartuli, J. C. & Beck, J. S. 1992. Ordered Mesoporous Molecular Sieves Synthesized by a Liquid-Crystal Template Mechanism. *Nature.* 359:710 – 712.

Kukard, R. S. 2008. The Effect of Zeolite Type on the Hydrocracking of Long n-Paraffins. MSc. Thesis. University of Cape Town.

Lamberov, A., Kuznetsov, A., Shapnik, M., Masliy, A., Borisevich, S., Romanova, R. & Egorova, S. 2000. Quantum-Chemical Investigation of the Formation of Lewis Acid Centers of High-Siliceous Zeolites. *Journal of Molecular Catalysis A: Chemical*. 158:481 – 486.

Leckel, D. 2007. Low-Pressure Hydrocracking of Coal Derived Fischer-Tropsch Waxes to Diesel. *Energy & Fuels*. 21:1425 – 1431.

Lilik, G. K. & Boehman, A. L. 2011. Advanced Diesel Combustion of a High Cetane Number Fuel with Low Hydrocarbon and Carbon Monoxide Emissions. *Energy Fuels*. 25:1444 – 1456.

Lisboa, O., Sánchez, M. & Ruette, F. 2008. Modeling Extra Framework Aluminum (EFAL) Formation in the Zeolite ZSM-5 Using Parametric Quantum and DFT Methods. *Journal of Molecular Catalysis A: Chemical.* 294:93 – 101.

Lohse, U. & Mildebrath, M. 1981. Dealuminierte Molekularsiebe vom Typ Y zur Porosität dealuminierter Molekularsiebe. *Zeitschrift für Anorganische und Allgemeine Chemie*. 476:126 – 135.

Lowell, S., Shields, J. E., Thomas, M. A. & Thommes, M. 2004. Micropore Analysis. In *Characterization of Porous Solids and Powders: Surface Area, Pore Size and Density*. B. Scarlett, Ed. New York: Springer Science + Business Media. 129 – 156.

Löwenstein, W. 1954. The Distribution of Aluminum in the Tetrahedra and Aluminates. *American Mineralogist*. 39:92 – 96.

Machoke, A. G., Knoke, I. Y., Lopez-Orozco, S., Schmiele, M., Selvam, T., Marthala, V. R. R., Spiecker, E., Unruh, T. *et al*. 2014. Synthesis of Multilamellar MFI-Type Zeolites under Static Conditions: The Role of Gel Composition on their Properties. *Microporous and Mesoporous Materials*. 190:324 – 333.

Maier, C. E., Bigeard, P. H., Lemaire, J. & Taoka, J. 1984. *NPRA Annual Meeting.* March 1984. San Antonio, Texas.

Marcilly, C. 2003. *Catalyse Acido-Basique, Application au Raffinage et à la Pétrochimie*. Paris, France: Institut Français du Pétrole Publications.

Marcilly, C. 2004. Zeolites in the Petroleum Industry. In *Encyclopedia of Supramolecular Chemistry*. J. L. Atwood & J. W. Steed, Eds. New York and Basel: Marcel Dekker. 1599 – 1609.

Marques, J. P., Gener, I., Ayrault, P., Bordado, J. C., Lopes, J. M., Ramôa Ribeiro, F. & Guisnet, M. 2003. Infrared Spectroscopic Study of the Acid Properties of Dealuminated BEA Zeolites. *Microporous and Mesoporous Materials.* 60:251 – 262.

Martens, J. A. & Jacobs, P. A. 2001. Introduction to Acid Catalysis with Zeolites in Hydrocarbon Reactions. In *Introduction to Zeolite Science and Practice, Studies in Surface Science and Catalysis.* H. van Bekkum, E. M. Flanigen, P. A. Jacobs & J. C. Jansen, Eds. Belgium: Elsevier Science B. V. 633 – 671.

Martens, J. A., Souverijns, W., van Rhijn, W. & Jacobs, P. A. 1997. Acidity and Basicity in Zeolites. In *Handbook of Heterogeneous Catalysis*. G. Ertl, H. Knözinger & J. Weitkamp, Eds. Weinheim: Wiley-VCH. 324 – 365.

Martens, J. A., Souverijns, W., Verrelst, W., Parton, R., Froment, G. & Jacobs, P. A. 1995. Selective Isomerization of Hydrocarbon Chains on External Surfaces of Zeolite Crystals. *Angewandte Chemie International Edition in English.* 34:2528 – 2530.

Maxwell, I. E. 1987. Zeolite Catalysis in Hydroprocessing Technology. *Catalysis Today.* 1:385 – 413.

Maxwell, I. E., Minderhoud, J. K., Stork, W. H. J. & van Veen, J. A. R. 1997. Hydrocracking and Catalytic Dewaxing. In *Handbook of Heterogeneous Catalysis.* G. Ertl, H. Knözinger & J. Weitkamp, Eds. Weinheim: Wiley-VCH. 2017 – 2038.

Maxwell, I. E. & Stork, W. H. H. 1991. Hydrocarbon Processing with Zeolites. In *Introduction to Zeolite Science and Practice, Studies in Surface Science and Catalysis*. H. van Bekkum, E. M. Flanigen, P. A. Jacobs & J. C. Jansen, Eds. Amsterdam: Elsevier Science B. V. 747 – 819.

Meisel, S. L., McCullough, J. P., Lechthaler, C. H. & Weisz, P. B. 1977. Recent Advances in the Production of Fuels and Chemicals over Zeolite Catalysts. *Leo Friend Symposium, 174th National Meeting of the American Chemical Society.* 30 August 1977. Chicago, Illinois: American Chemical Society.

Méthivier, A. 2005. Separation of Paraxylene by Adsorption. In *Zeolites for Cleaner Technologies.* M. Guisnet & J. -P. Gilson, Eds. London: Imperial College Press. 209 – 222.

Mills, G. A., Heinemann, H., Milliken, T. H. & Oblad, A. G. 1953. (Houdriforming Reactions) Catalytic Mechanism. *Industrial & Engineering Chemistry*. 45:134 – 137.

Na, K., Choi, M. & Ryoo, R. 2013. Recent Advances in the Synthesis of Hierarchically Nanoporous Zeolites. *Microporous and Mesoporous Materials.* 166:3 – 19.

Na, K., Park, W., Seo, Y. & Ryoo, R. 2011. Disordered Assembly of MFI Zeolite Nanosheets with a Large Volume of Intersheet Mesopores. *Chemistry of Materials.* 23:1273 – 1279.

Nowotny, M., Lercher, J. A. & Kessler, H. 1991. Ir. Spectroscopy of Single Zeolite Crystals. Part 1: Thermal Decomposition of the Template in MFI-Type Materials. *Zeolites*. 11:454 – 459.

Olson, D. H., Haag, W. O. & Borghard, W. S. 2000. Use of Water as a Probe of Zeolitic Properties: Interaction of Water with HZSM-5. *Microporous and Mesoporous Materials.* 35 – 36:435 – 446.

Olson, D. H., Haag, W. O. & Lago, R. M. 1980. Chemical and Physical Properties of the ZSM-5 Substitutional Series. *Journal of Catalysis.* 61:390 – 396.

Pappal, D. A., Hunter, M. G. & Groeneveld, L. R. 1997. Converting VGO HDS Units to Moderate Pressure Hydrocracking. Petroleum Technology Quaterly. June.

Park, W., Yu, D., Na, K., Jelfs, K. E., Slater, B., Sakamoto, Y. & Ryoo, R. 2011. Hierarchically Structure-Directing Effect of Multi-Ammonium Surfactants for the Generation of MFI Zeolite Nanosheets. *Chemistry of Materials*. 23:5131 – 5137.

Parker, L. M., Bibby, D. M. & Patterson, J. E. 1984. Thermal Decomposition of ZSM-5 and Silicalite Precursors. *Zeolites.* 4:168 – 174.

Patrigeon, A., Benazzi, E., Travers, Ch. & Bernhard, J. Y. 2001. Influence of the Zeolite Structure and Acidity on the Hydroisomerization of n-Heptane. *Catalysis Today.* 65:149 – 155.

Pellet, R., Blackwell, C. & Rabo, J. 1988. Catalytic Cracking Studies and Characterization of Steamed Y and LZ-210 Zeolites. *Journal of Catalysis*. 114:71 – 89.

Pérez-Ramírez, J., Christensen, C. H., Egeblad, K., Christensen, C. H. & Groen, J. C. 2008. Hierarchical Zeolites: Enhanced Utilisation of Microporous Crystals in Catalysis by Advances in Materials Design. *Chemical Society Reviews.* 37:2530 – 2542.

Philippaerts, A., Paulussen, S., Breesch, A., Turner, S., Lebedev, O. I., Tendeloo, G. V., Sels, B. & Jacobs, P. 2011. Unprecedented Shape Selectivity in Hydrogenation of Triacylglycerol Molecules with Pt/ZSM-5 Zeolite. *Angewandte Chemie International Edition.* 50:3947 – 3949.

Philippaerts, A., Paulussen, S., Turner, S., Lebedev, O. I., Van Tendeloo, G., Poelman, H., Bulut, M., De Clippel, F., Smeets, P., Sels, B. & Jacobs, P. 2010. Selectivity in Sorption and Hydrogenation of Methyl Oleate and Elaidate on MFI Zeolites. *Journal of Catalysis*. 270:172 – 184.

Pichler, H., Schulz, H., Reitemeyer, H. O. & Weitkamp, J. 1972. Über das Hydrocracken Gesättigter Kohlenwasserstoffe. *Erdöl & Kohle, Erdgas, Petrochemie.* 25:494 – 505.

Pushparaj, H., Mani, G., Muthiahpillai, P., Velayutham, M., Park, Y. -K., Choi, W. C. & Jang, H. T. 2013. Effects of Crystallinity of ZSM-5 Zeolite on *Para*-Selective *Tert*-Butylation of Ethylbenzene. *Chinese Journal of Catalysis.* 34:294 – 304.

Ribeiro, F., Marcilly, C. & Guisnet, M. 1982. Hydroisomerization of n-Hexane on Platinum Zeolites. *Journal of Catalysis*. 78:267 – 280.

Ribeiro, F., Marcilly, C. & Thomas, G. 1978. Homogeneous Platinum Deposit on Zeolite by Competitive Cation-Exchange. *Comptes rendus hebdomadaires* des *séances de l'Académie* des *Sciences Série C*. 287:431 – 434.

Scherzer, J. 1978. Dealuminated Faujasite-Type Structures with $SiO_2Al_2O_3$ Ratios over 100. *Journal of Catalysis.* 54:285 – 288.

Scherzer, J. 1984. The Preparation and Characterization of Aluminum-Deficient Zeolites. In *Catalytic Materials: Relationship between Structure and Activity.* T. E. White, R. A. Della Betta, E. G. Derouane & R. T. K. Baker, Eds. Washington, D.C.: American Chemical Society. 157 – 200.

Scherzer, J. & Gruia, A. 1996. *Hydrocracking Science and Technology*. New York, USA: CRC Press.

Scholle, K. F. M. G. J., Veeman, W. S., Frenken, P. & van der Velden, G. P. M. 1985. Characterization of Intermediate TPA-ZSM-5 Type Structures during Crystallization. *Applied Catalysis.* 17:233 – 259.

Schulz, H. F. & Weitkamp, J. H. 1972. Zeolite Catalysts. Hydrocracking and Hydroisomerization of n-Dodecane. *Industrial & Engineering Chemistry Product Research and Development.* 11:46 – 53.

Schüth, F. 2003. Endo- and Exotemplating to Create High-Surface-Area Inorganic Materials. *Angewandte Chemie International Edition.* 42:3604 – 3622.

Shah, P. P., Sturtevant, G. C., Gregor, J. H., Humbach, M. J., Padrta, F. G. & Steigleder, K. Z. 1988. *Fischer-Tropsch Wax Characterization and Upgrading: Final report*. (DOE/PC/80017-T1). Des Plaines, USA: UOP, Inc.

Shorey, S. W., Lomas, D. A. & Keesom, W. H. 1999. Use FCC Feed Pretreating Methods to Remove Sulfur. *Hydrocarbon Processing*. 78:43 – 57.

Sie, S. T., Senden, M. M. G. & Van Wechem, H. M. H. 1991. Conversion of Natural Gas to Transportation Fuels via the Shell Middle Distillate Synthesis Process (SMDS). *Catalysis Today*. 8:371 – 394.

Sing, K. S. W., Everett, D. H., Haul, R. A. W., Moscou, L., Pierotti, R. A., Rouquerol, J. & Siemieniewska, T. 1985. Reporting Physisorption Data for Gas/Solid Systems with Special Reference to the Determination of Surface Area and Porosity. *Pure and Applied Chemistry.* 57:603 – 619.

Sonnemans, J. W. M., Plantenga, F. L. & Desai, P. H. 1984. *Mild Hydrocracking of Heavy Oils in the Eighties*. (Technical Paper AM-84-60). San Antonio, USA: National Petrochemical & Refiners Association.

Sree, S. P., Dendooven, J., Magusin, P. C. M. M., Thomas, K., Gilson, J. -P., Taulelle, F., Detavernier, C. & Martens, J. A. 2016. Hydroisomerization and Hydrocracking Activity Enhancement of a Hierarchical ZSM-5 Zeolite Catalyst via Atomic Layer Deposition of Aluminium. *Catalysis Science & Technology.* 6:6177 – 6186.

Steijns, M., Froment, G., Jacobs, P., Uytterhoeven, J. & Weitkamp, J. 1981. Hydroisomerization and Hydrocracking. 2. Product Distributions from n-Decane and n-Dodecane. *Industrial & Engineering Chemistry Product Research and Development*. 20:654 – 660.

Stevenson, R. L. 1971. The Location of the Protons in Dehydrated Y-Faujasite. *Journal of Catalysis.* 21:113 – 121.

Tao, Y., Kanoh, H., Abrams, L. & Kanek, K. 2006. Mesopore-Modified Zeolites: Preparation, Characterization, and Applications. *Chemical Reviews.* 106:896 – 910.

Thommes, M., Kaneko, K., Neimark, A., Olivier, J., Rodriguez-Reinoso, F., Rouquerol, J. & Sing, K. 2015. Physisorption of Gases, with Special Reference to the Evaluation of Surface Area and Pore Size Distribution (IUPAC Technical Report). *Pure and Applied Chemistry*. 87:1 – 19.

Thybaut, J. W., Laxmi Narasimhan, C. S., Denayer, J. F., Baron, G. V., Jacobs, P. A., Martens, J. A. & Marin, G. B. 2005. Acid-Metal Balance of a Hydrocracking Catalyst: Ideal versus Non-Ideal Behaviour. *Industrial & Engineering Chemistry Research*. 44:5159 – 5169.

Toma, S. 2016. *Octane and Cetane Ratings – Your Guide to Diesel Fuel and Gasoline's Specs.* Available: https://www.autoevolution.com/news/octane-and-cetane-ratings-your-guide-to-diesel-fuel-and-gasoline-s-specs-113369.html [2018, January 11].

Tosheva, L. & Valtchev, V. P. 2005. Nanozeolites: Synthesis, Crystallization Mechanism, and Applications. *Chemistry of Materials.* 17:2494 – 2513.

Uytterhoeven, J. B., Christner, L. G. & Hall, W. K. 1965. Studies of the Hydrogen Held by Solids. VIII. The Decationated Zeolites. *The Journal of Physical Chemistry.* 69:2117 – 2126.

Valavarasu, G., Bhaskar, M. & Balaraman, K. S. 2007. Mild Hydrocracking – A Review of the Process, Catalysts, Reactions, Kinetics, and Advantages. *Petroleum Science & Technology.* 21:1185 – 1205.

van Bokhoven, J., Koningsberger, D., Kunkeler, P., van Bekkum, H. & Kentgens, A. 2000. Stepwise Dealumination of Zeolite Beta at Specific T-Sites Observed with ^{27}Al MAS and ^{27}Al MQ MAS NMR. *Journal of the American Chemical Society*. 122:12842 – 12847.

Van Veen, J. A. R. 2002. Hydrocracking. In *Zeolites for Cleaner Technologies.* M. Guisnet & J. -P. Gilson, Eds. London: Imperial College Press. 131 – 152.

Venuto, P. B. 1977. Aromatic Reactions over Molecular Sieve Catalysts: A Mechanistic Review. In *Catalysis in Organic Syntheses.* G. Smith, Ed. New York: Academic Press. 67 – 93.

Verheyen, E., Jo, C., Kurttepeli, M., Vanbutsele, G., Gobechiya, E., Korányi, T. I., Bals, S., Van Tendeloo, G., Ryoo, R., Kirschhock, C. E. & Martens, J. A. 2013. Molecular Shape-Selectivity of MFI Zeolite Nanosheets in n-Decane Isomerization and Hydrocracking. *Journal of Catalysis*. 300:70 – 80.

Vermeiren, W. & Gilson, J. -P. 2009. Impact of Zeolites on the Petroleum and Petrochemical Industry. *Topics in Catalysis*. 52:1131 – 1161.

Vogt, E. T. C., Whiting, G. T., Chowdhury, A. D. & Weckhuysen, B. M. 2015. Zeolites and Zeotypes for Oil and Gas Conversion. In *Advances in Catalysis.* Massachusetts: Academic Press. 143 – 314.

Wang, K., Wang, X. & Li, G. 2006. Quantitatively Study Acid Strength Distribution on Nanoscale ZSM-5. *Microporous and Mesoporous Materials.* 94:325 – 329.

Ward, J. W. 1967. The Nature of Active Sites on Zeolites: I. The Decationated Y Zeolite. *Journal of Catalysis.* 9:225 – 236.

Weisz, P. B. 1962. *Advances in Catalysis and Related Subjects*. D. D. Eley, P. W. Selwood & P. B. Weisz, Eds. New York, USA: Academic Press. 137 – 190.

Weisz, P. B. & Frilette, V. J. 1960. Intracrystalline and Molecular-Shape-Selective Catalysis by Zeolite Salts. *The Journal of Physical Chemistry.* 64:382 – 382.

Weisz, P. B. & Swegler, E. W. 1957. Stepwise Reaction on Separate Catalytic Centres: Isomerization of Saturated Hydrocarbons. *Science*. 126:31 – 32.

Weitkamp, J. 1975. The Influence of Chain Length in Hydrocracking and Hydroisomerization of n-Alkanes. In *Hydrocracking and Hydrotreating*. J. W. Ward & S. A. Qader, Eds. ACS Symposium Series: Washington, D. C. 1 – 27.

Weitkamp, J. 1978. Hydrocracken, Cracken und Isomerisieren von Kohlenwasserstoffen. *Erdöl & Kohle, Erdgas, Petrochemie.* 31:13 – 22.

Weitkamp, J. 1982. Isomerization of Long-Chain n-Alkanes on a Pt/CaY Zeolite Catalyst. *Industrial & Engineering Chemistry Product Research and Development*. 21:550 – 558.

Weitkamp, J. 2012. Catalytic Hydrocracking – Mechanisms and Versatility of the Process. *ChemCatChem*. 4:292 – 306.

Weitkamp, J., Ernst, S. & Karge, H. G. 1984. Peculiarities in the Conversion of Naphthenes on Bifunctional Catalysts. *Erdöl & Kohle, Erdgas, Petrochemie*. 37:457 – 462.

Weitkamp, J., Jacobs, P. A. & Martens, J. A. 1983. Isomerization and Hydrocracking of C9 through C16 n-Alkanes on Pt/HZSM-5 Zeolite. *Applied Catalysis*. 8:123 – 141.

Whitten, K. W., Davis R. E., Peck, L. & Stanley G. G. 2013. *Chemistry.* Massachusetts: Brookes/Cole. Available: http://www.chegg.com/homework-help/common-test-presence-chloride-ions-formation-heavy-white-pre-chapter-6-problem-88e-solution-9781133610663-exc [2017, May 03].

Woolery, G. L., Kuehl, G. H., Timken, H. C., Chester, A. W. & Vartuli, J. C. 1997. On the Nature of Framework Brønsted and Lewis acid sites in ZSM-5. *Zeolites*. 19:288 – 296.

Wouters, B., Chen, T. & Grobet, P. 1998. Reversible Tetrahedral−Octahedral Framework Aluminum Transformation in Zeolite Y. *Journal of the American Chemical Society*. 120:11419 – 11425.

Wu, L., Magusin, P. C. M. M., Degirmenci, V., Li, M., Almutairi, S. M. T., Zhu, X., Mezari, B. & Hensen, E. J. M. 2014. Acidic Properties of Nanolayered ZSM-5 Zeolites. *Microporous and Mesoporous Materials*. 189: 144 – 157.

Yan, T. Y. 1972. The Promotional Effect of Water in Hydrocracking. *Journal of Catalysis*. 25:204 – 2011.

Yingcai, L., Mingyang, J., Yaojun, S., Tailiu, W., Liping, W. & Lun, F. 1996. State of Aluminium in Hydrothermally Dealuminated MFI Zeolite. *Journal of the Chemical Society, Faraday Transactions*. 92:1647 – 1651.

Zhang, Q., Yang, H. & Yan, W. 2014. Effect of Ethanol on the Crystallinity and Acid Sites of MFI Zeolite Nanosheets. *RSC Advances.* 4:56938 – 56944.

Zhu, X., Wu, L., Magusin, P. C. M. M., Mezari, B. & Hensen, E. J. M. 2015. On the Synthesis of Highly Acidic Nanolayered ZSM-5. *Journal of Catalysis*. 327:10 – 21.

Appendices

Appendix 1: Characterization of SDAs

A 1.1. Proton (^{1}H) NMR Spectroscopy

A 1.1.1. $C_{22\text{-}6\text{-}6}Br_2$

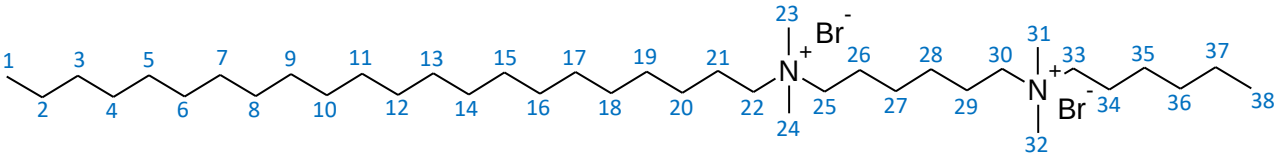

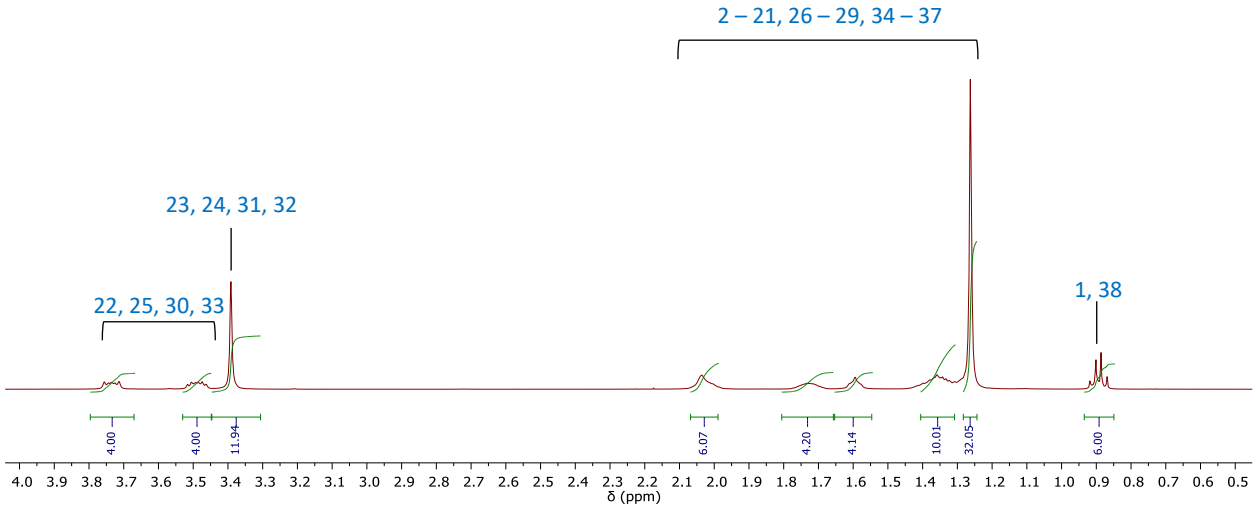

Figure A1: ^{1}H NMR spectrum of $C_{22\text{-}6\text{-}6}Br_2$.

A 1.1.2. $C_{22\text{-}6\text{-}3}Br_2$

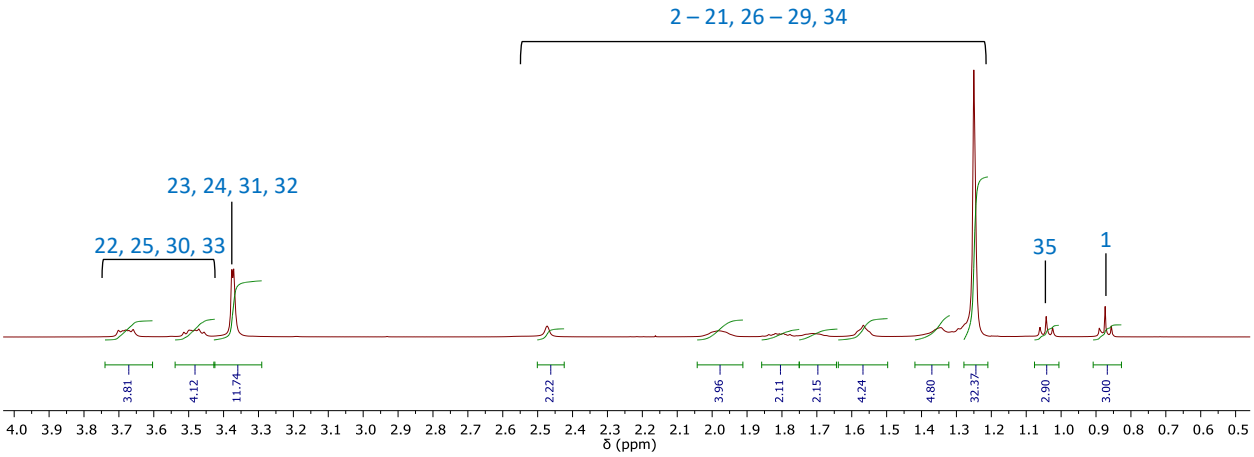

Figure A2: ^{1}H NMR spectrum of $C_{22\text{-}6\text{-}3}Br_2$.

Appendix 2: Characterization of Catalysts

A 2.1. ^{27}Al MAS SSNMR Spectroscopy

A 2.1.1. Deconvoluted Spectra: Bulk MFI

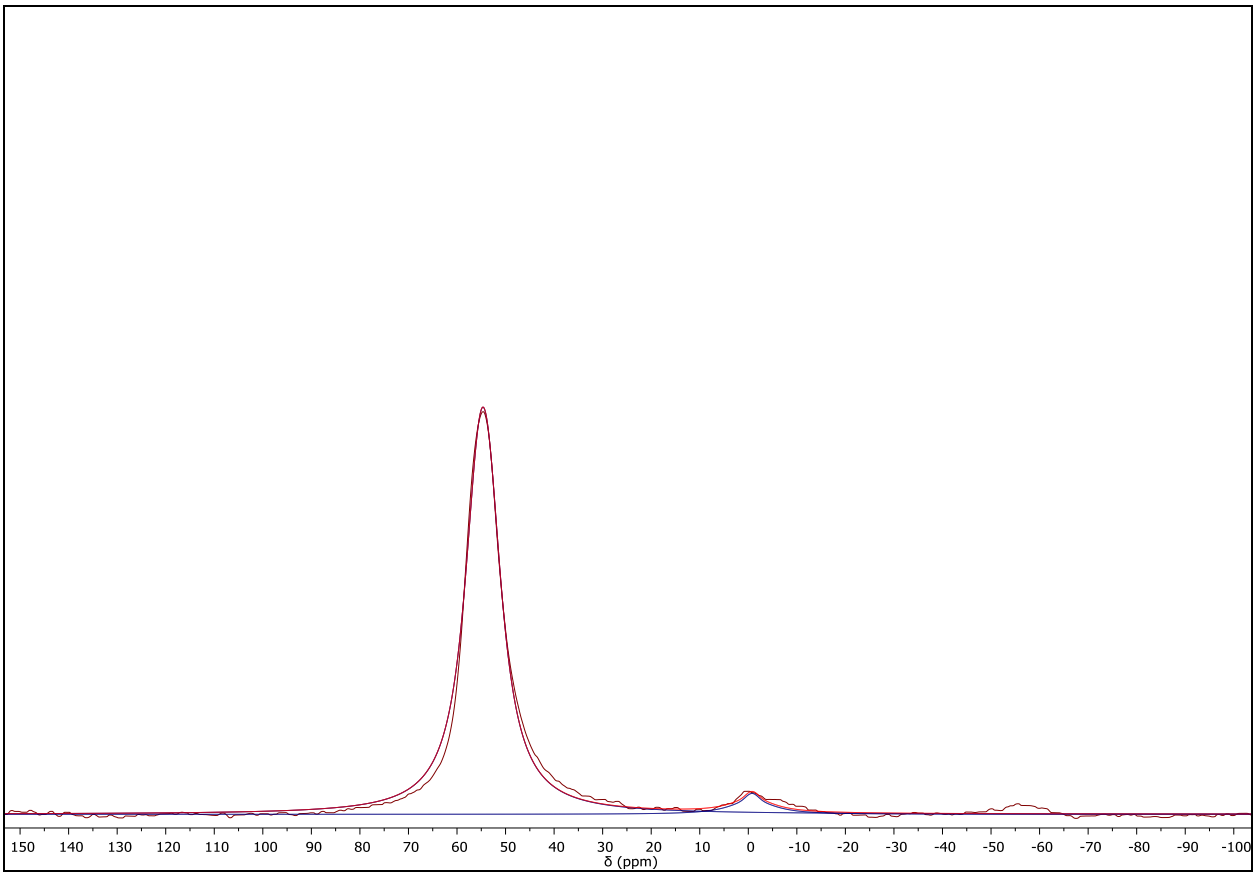

Figure A3: Deconvoluted ^{27}Al MAS SSNMR spectrum of bulk MFI.

Table A1: δ's, peak areas and % peak areas obtained from deconvoluted ^{27}Al MAS SSNMR spectrum of bulk MFI.

δ (ppm)	Peak area	% Peak area
54.65	23224.34	95
-0.78	1133.90	5

A 2.1.2. Deconvoluted Spectra: H-NS-6-ya

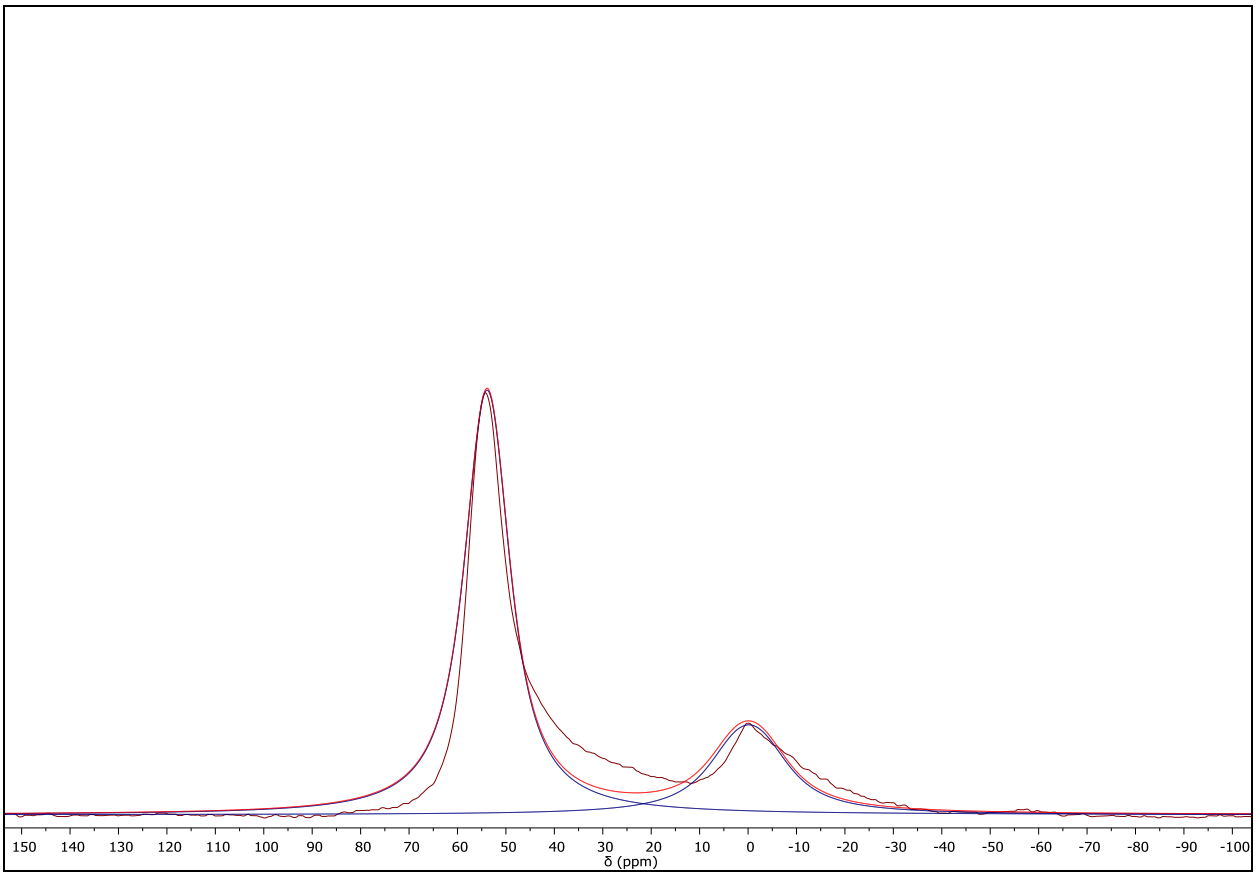

Figure A4: Deconvoluted ^{27}Al MAS SSNMR spectrum of H-NS-6-25a.

Table A2: δ's, peak areas and % peak areas obtained from deconvoluted ^{27}Al MAS SSNMR spectrum of H-NS-6-25a.

δ (ppm)	Peak area	% Peak area
53.88	88843.99	75
-0.16	29201.82	25

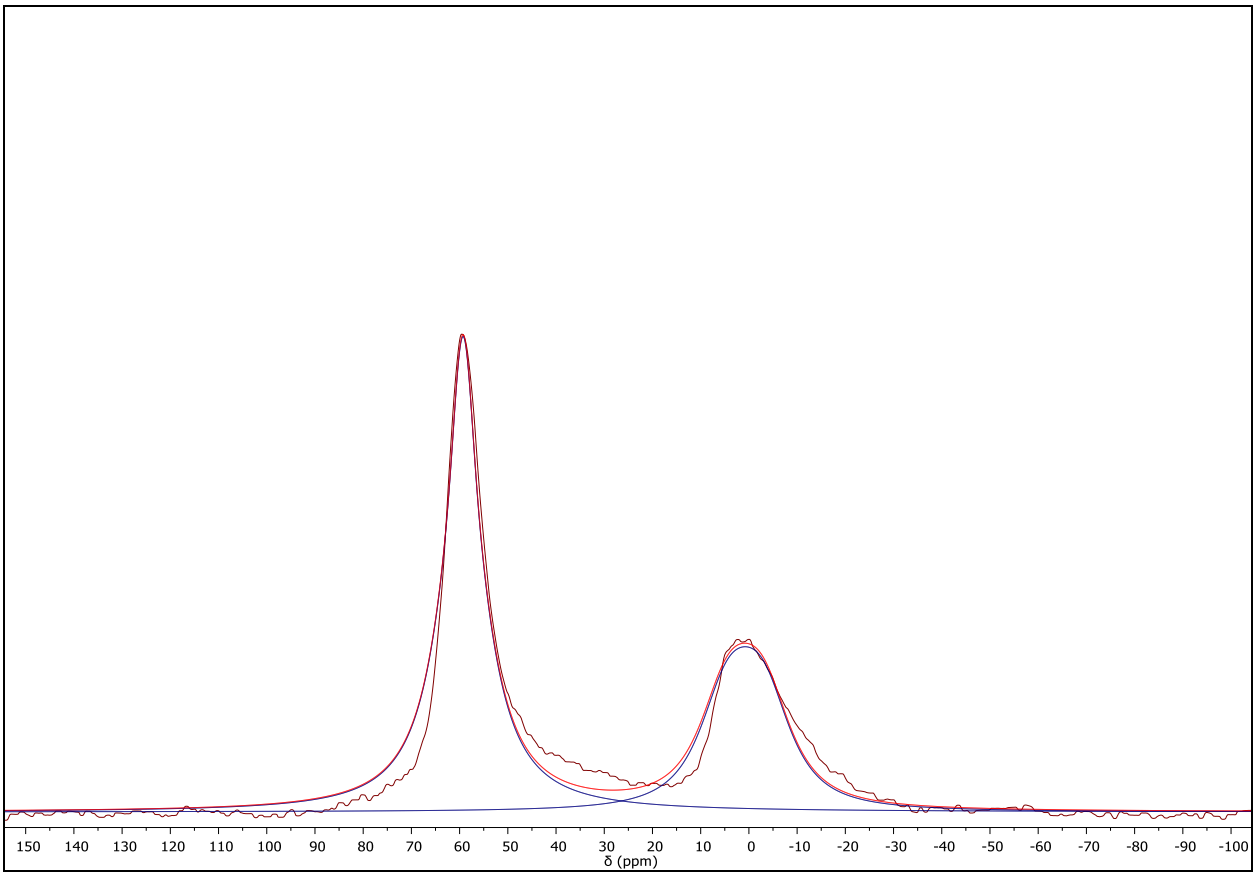

Figure A5: Deconvoluted ^{27}Al MAS SSNMR spectrum of H-NS-6-50a.

Table A3: δ's, peak areas and % peak areas obtained from deconvoluted ^{27}Al MAS SSNMR spectrum of H-NS-6-50a.

δ (ppm)	Peak area	% Peak area
59.29	25141.52	64
0.78	14372.34	36

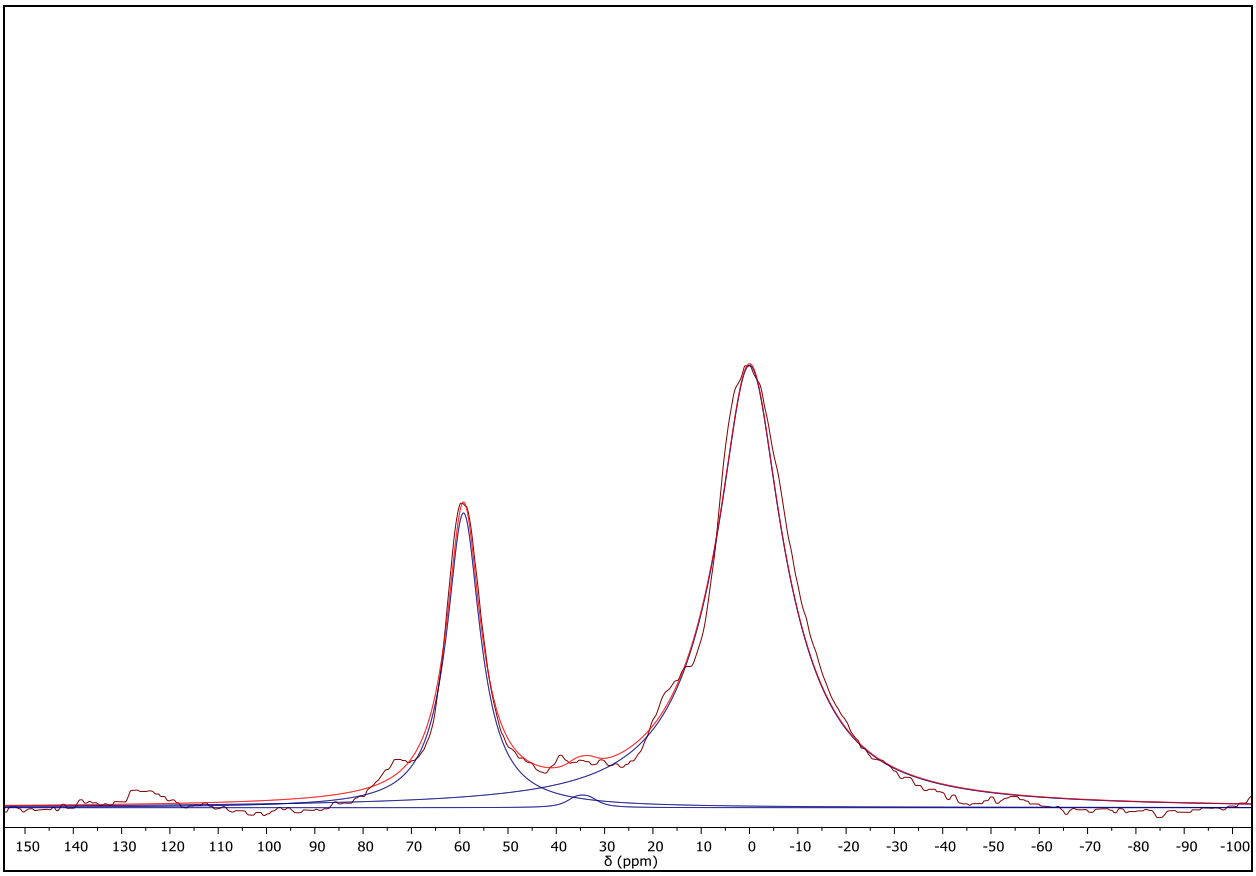

Figure A6: Deconvoluted ^{27}Al MAS SSNMR spectrum of H-NS-6-75a.

Table A4: δ's, peak areas and % peak areas obtained from deconvoluted ^{27}Al MAS SSNMR spectrum of H-NS-6-75a.

δ (ppm)	Peak area	% Peak area
59.21	14611.92	24
34.58	416.14	1
-0.03	46222.39	75

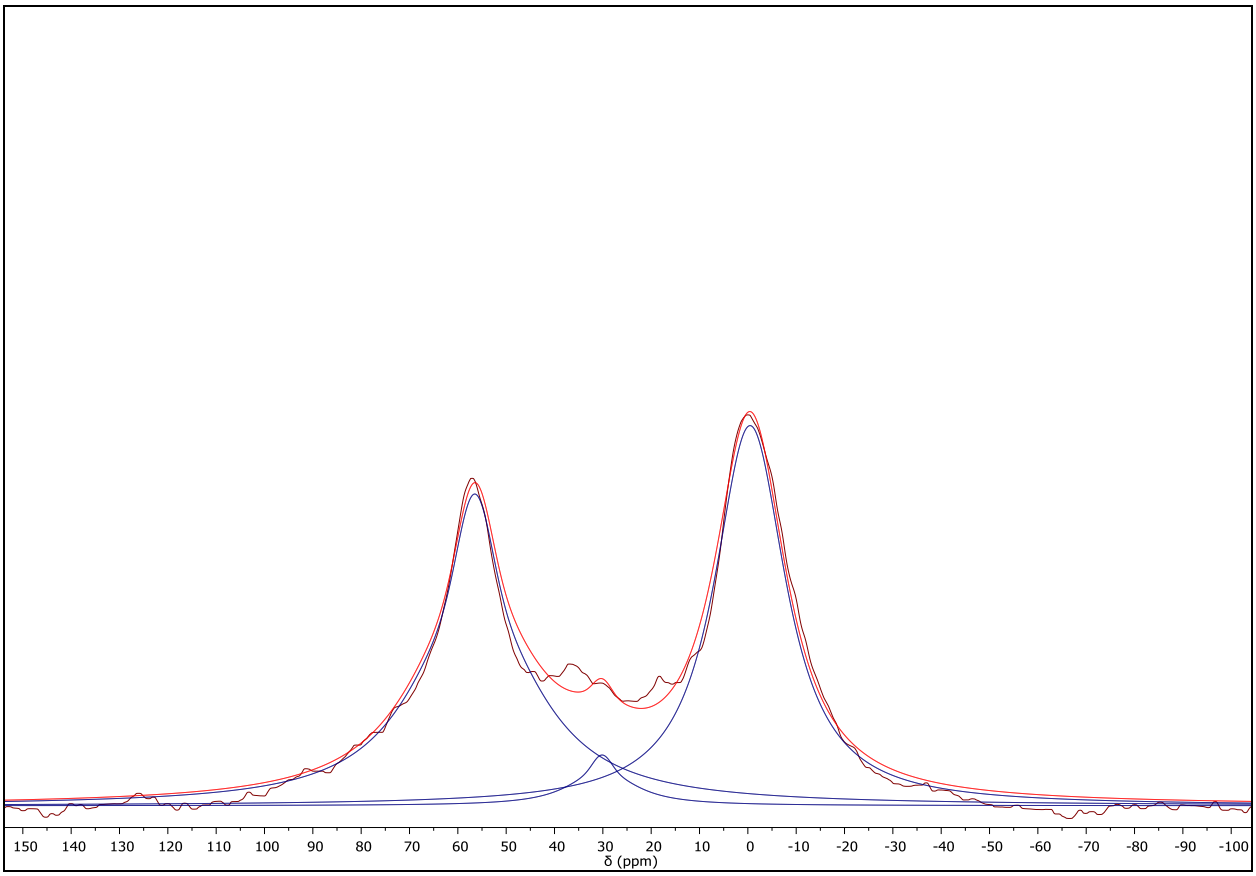

Figure A7: Deconvoluted ^{27}Al MAS SSNMR spectrum of H-NS-6-100a.

Table A5: δ's, peak areas and % peak areas obtained from deconvoluted ^{27}Al MAS SSNMR spectrum of H-NS-6-100a.

δ (ppm)	Peak area	% Peak area
56.50	37221.37	48
30.15	3355.57	4
-0.47	37627.44	48

A 2.1.3. Deconvoluted Spectra: C-NS-6-yb

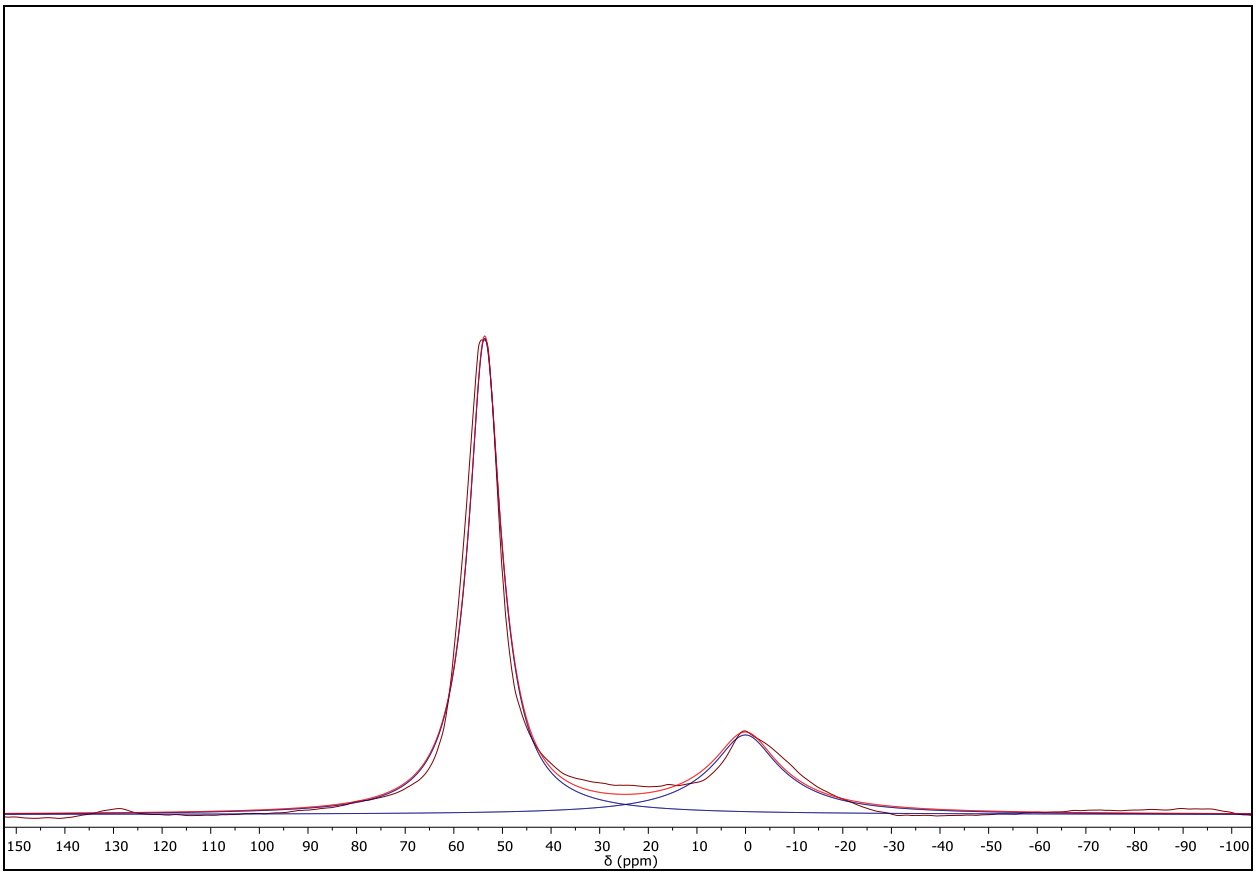

Figure A8: Deconvoluted ^{27}Al MAS SSNMR spectrum of C-NS-6-25b.

Table A6: δ's, peak areas and % peak areas obtained from deconvoluted ^{27}Al MAS SSNMR spectrum of C-NS-6-25b.

δ (ppm)	Peak area	% Peak area
53.65	219164.70	73
0.02	80435.41	27

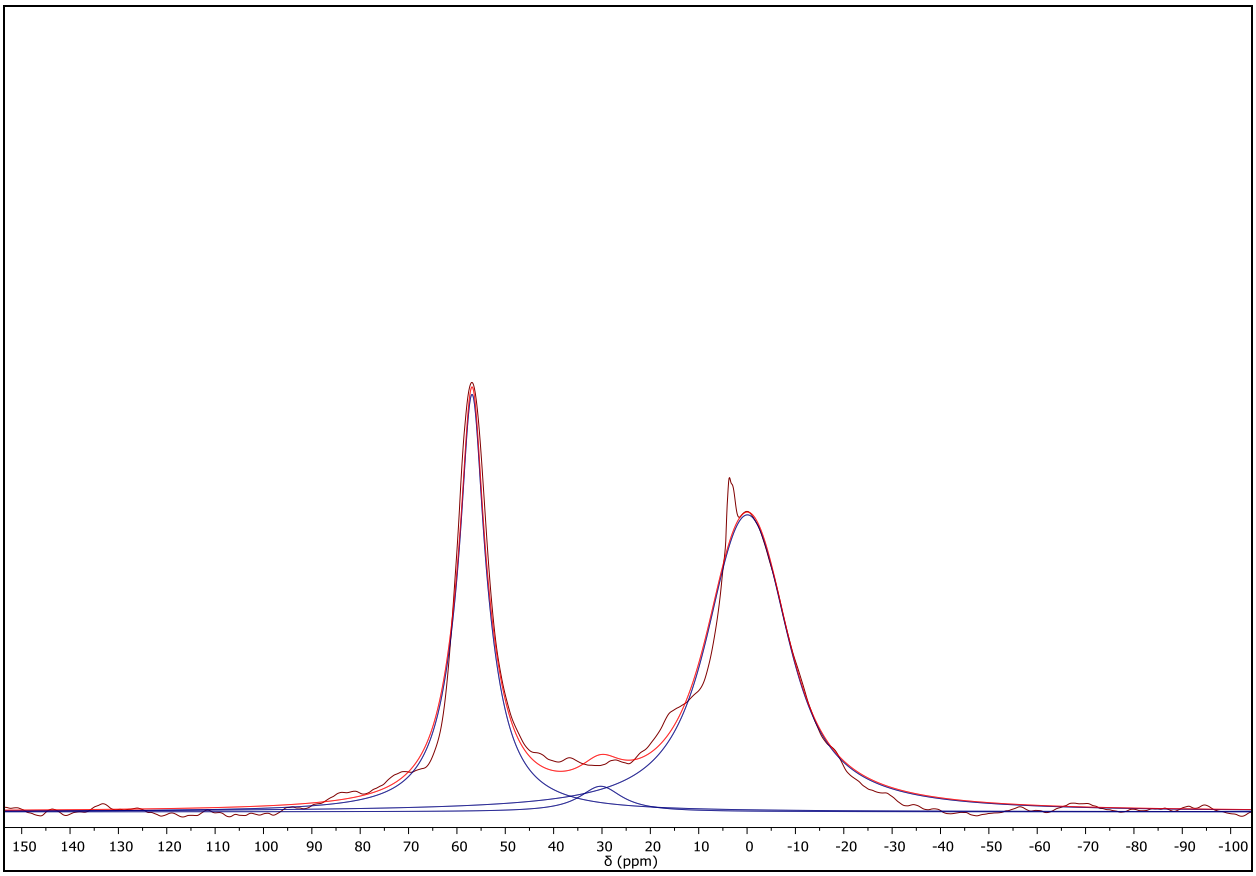

Figure A9: Deconvoluted ^{27}Al MAS SSNMR spectrum of C-NS-6-50b.

Table A7: δ's, peak areas and % peak areas obtained from deconvoluted ^{27}Al MAS SSNMR spectrum of C-NS-6-50b.

δ (ppm)	Peak area	% Peak area
56.87	14027.46	36
30.26	1188.20	3
-0.07	23781.33	61

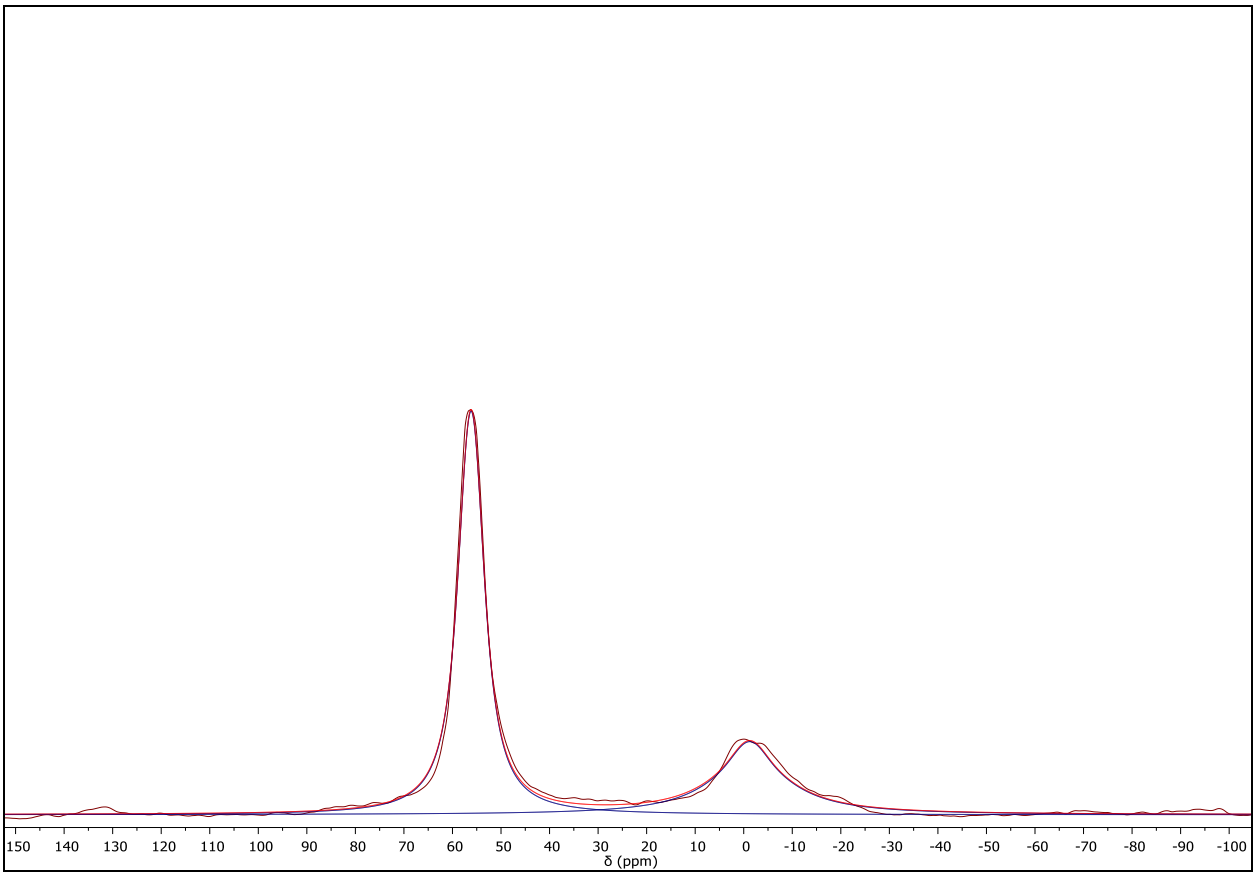

Figure A10: Deconvoluted ^{27}Al MAS SSNMR spectrum of C-NS-6-75b.

Table A8: δ's, peak areas and % peak areas obtained from deconvoluted ^{27}Al MAS SSNMR spectrum of C-NS-6-75b.

δ (ppm)	Peak area	% Peak area
56.16	29134.90	68
-1.24	13800.12	32

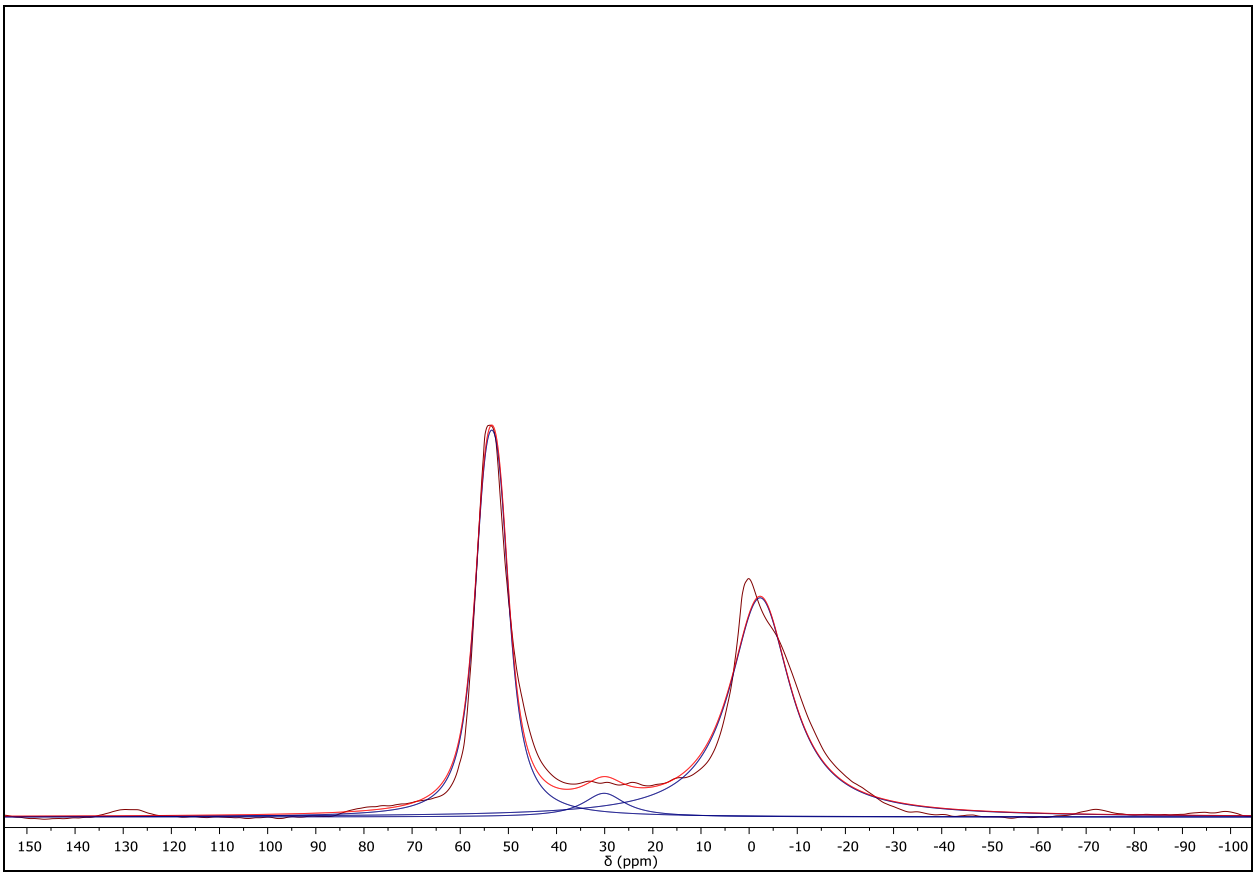

Figure A11: Deconvoluted ^{27}Al MAS SSNMR spectrum of C-NS-6-100b.

Table A9: δ's, peak areas and % peak areas obtained from deconvoluted ^{27}Al MAS SSNMR spectrum of C-NS-6-100b.

δ (ppm)	Peak area	% Peak area
53.45	106780.57	42
30.12	10233.01	4
-2.28	135083.67	54

A 2.1.4. Deconvoluted Spectra: C-NS-3-ya

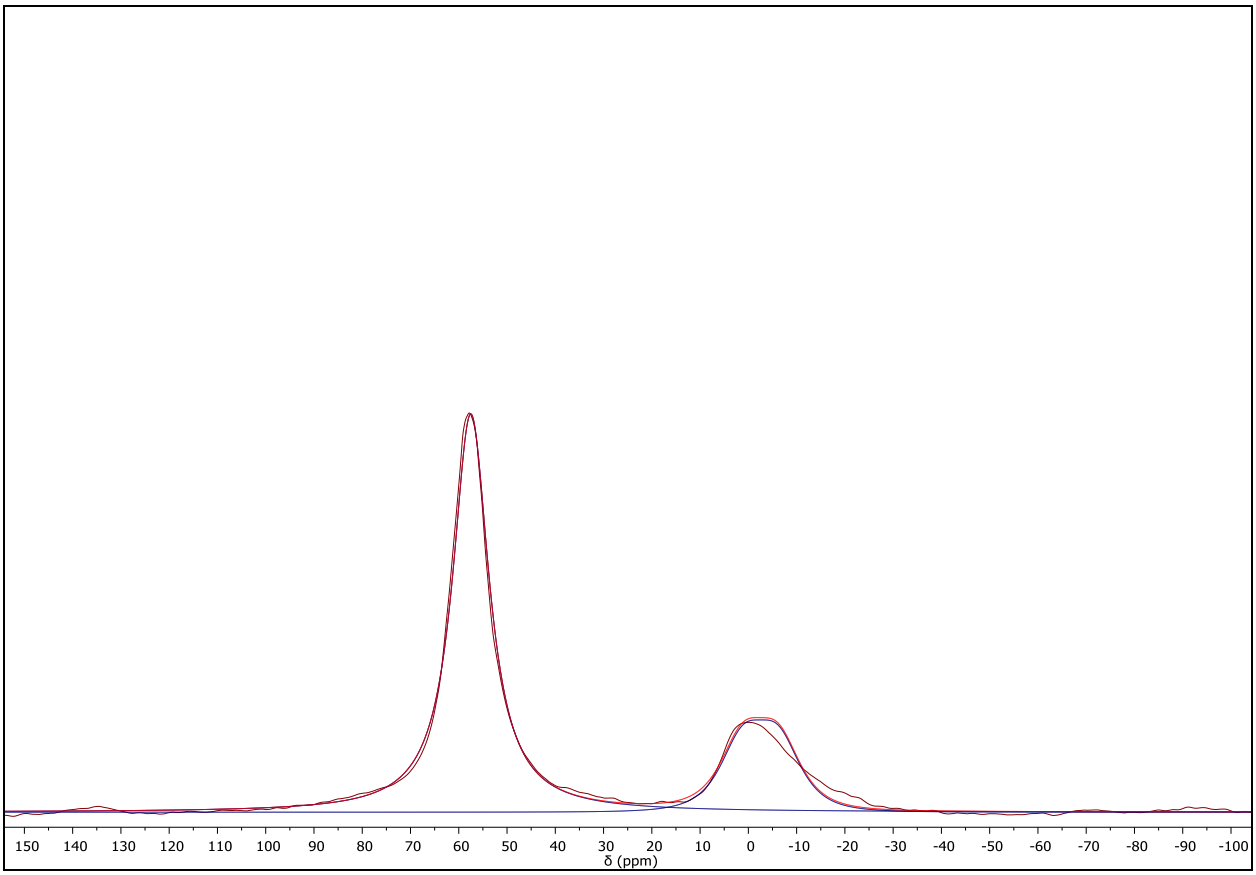

Figure A12: Deconvoluted ^{27}Al MAS SSNMR spectrum of C-NS-3-25a.

Table A10: δ's, peak areas and % peak areas obtained from deconvoluted ^{27}Al MAS SSNMR spectrum of C-NS-3-25a.

δ (ppm)	Peak area	% Peak area
57.51	62517.41	76
-2.50	19460.49	24

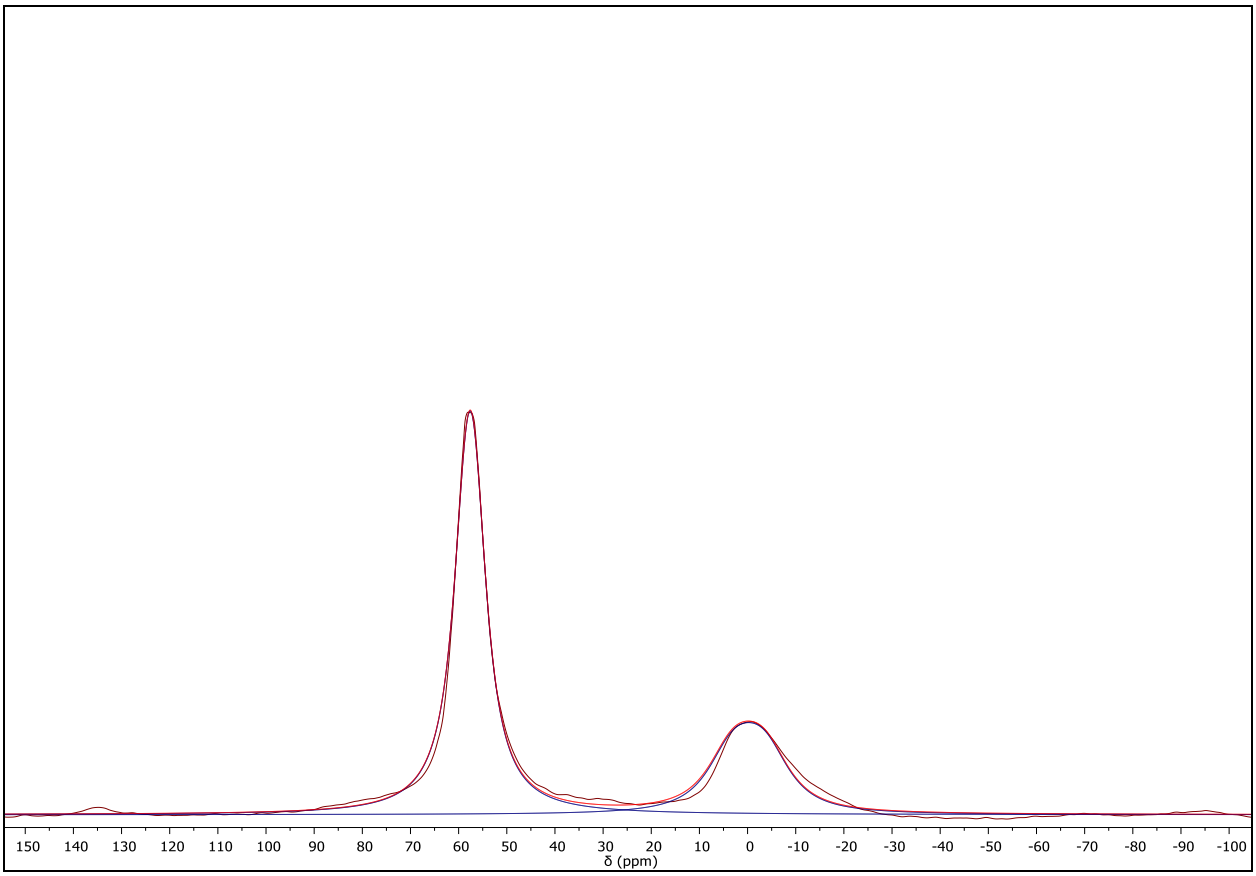

Figure A13: Deconvoluted ^{27}Al MAS SSNMR spectrum of C-NS-3-50a.

Table A11: δ's, peak areas and % peak areas obtained from deconvoluted ^{27}Al MAS SSNMR spectrum of C-NS-3-50a.

δ (ppm)	Peak area	% Peak area
57.61	108356.41	69
-0.21	48241.02	31

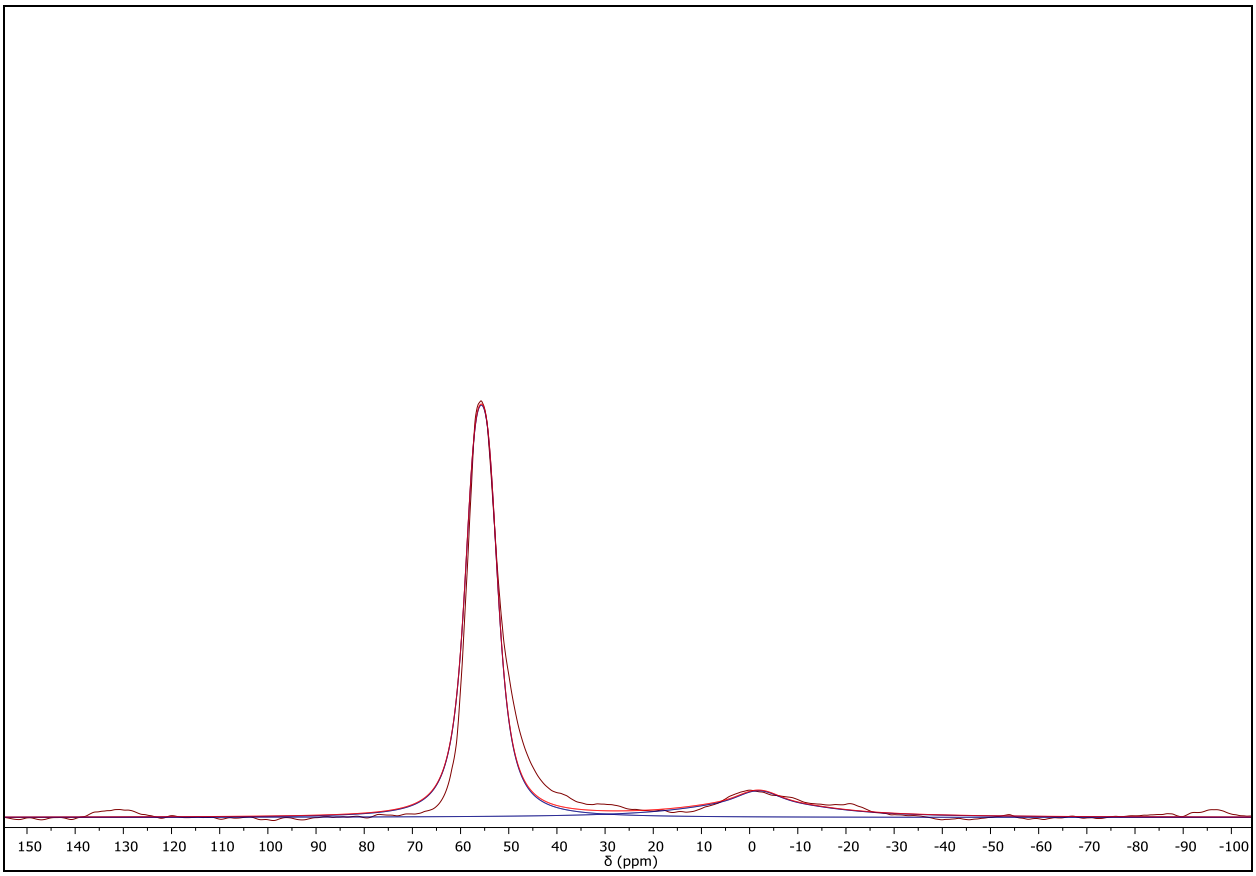

Figure A14: Deconvoluted ^{27}Al MAS SSNMR spectrum of C-NS-3-75a.

Table A12: δ's, peak areas and % peak areas obtained from deconvoluted ^{27}Al MAS SSNMR spectrum of C-NS-3-75a.

δ (ppm)	Peak area	% Peak area
55.69	36361.37	81
-1.84	8418.43	19

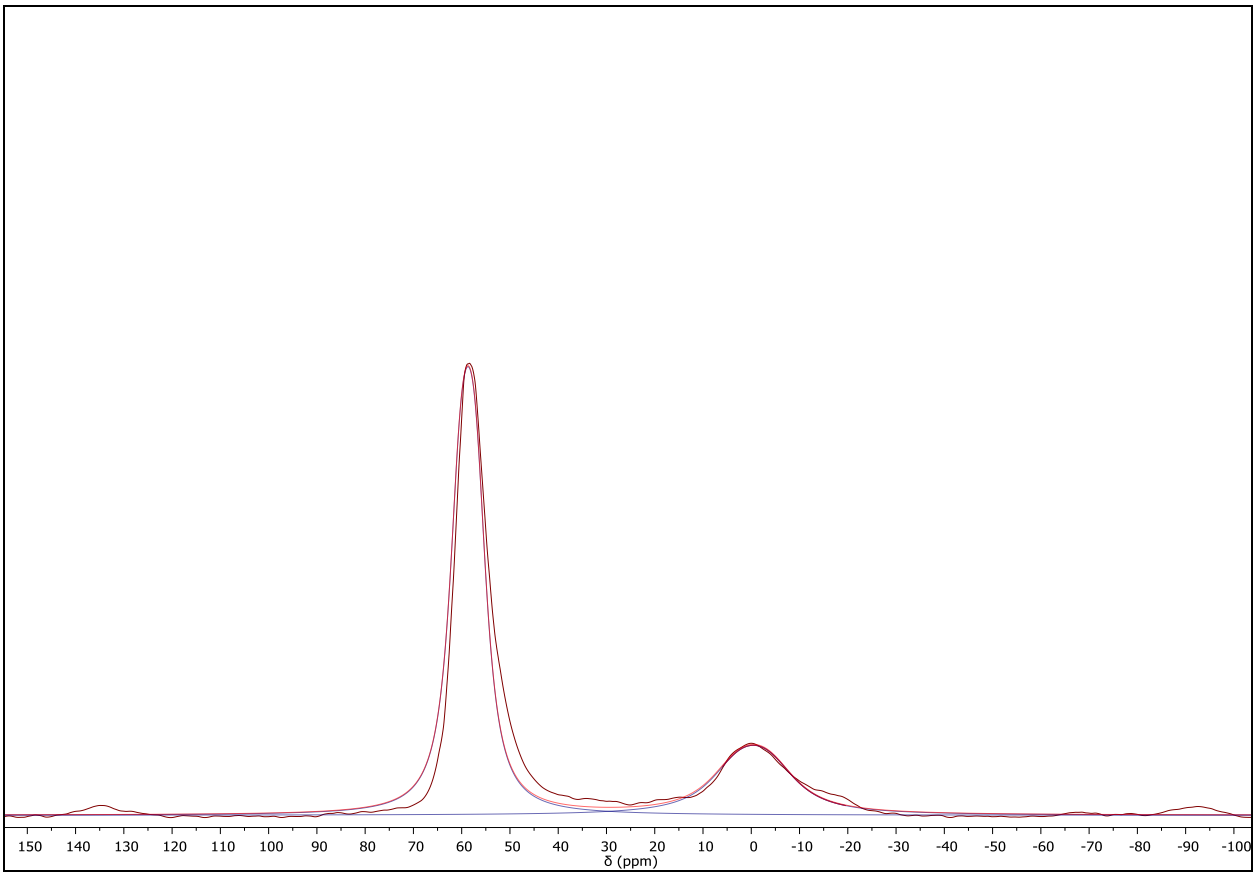

Figure A15: Deconvoluted ^{27}Al MAS SSNMR spectrum of C-NS-3-100a.

Table A13: δ's, peak areas and % peak areas obtained from deconvoluted ^{27}Al MAS SSNMR spectrum of C-NS-3-100a.

δ (ppm)	Peak area	% Peak area
58.69	85467.11	73
-0.43	32101.89	27

A 2.2. TEM

A 2.2.1. Pt/H-NS-6-ya

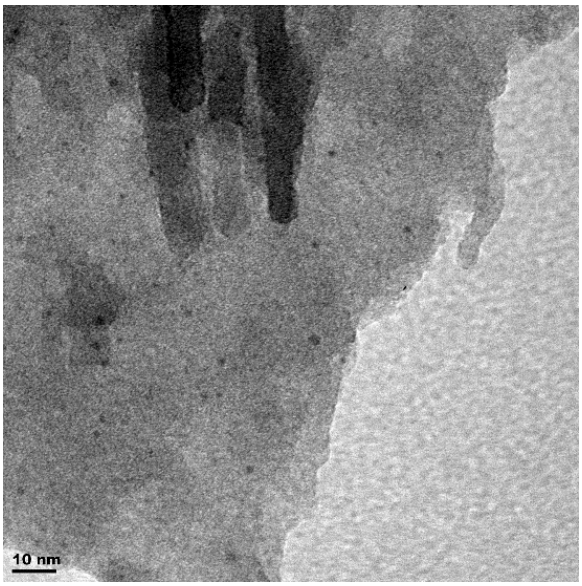

Figure A16: TEM micrograph of Pt/H-NS-6-25a.

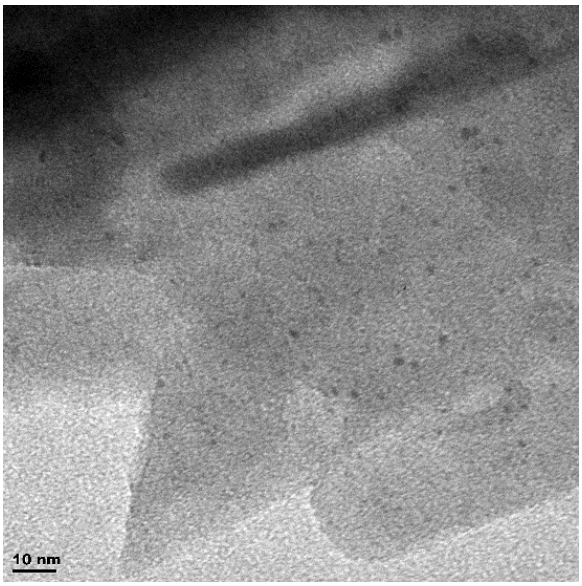

Figure A17: TEM micrograph of Pt/H-NS-6-50a.

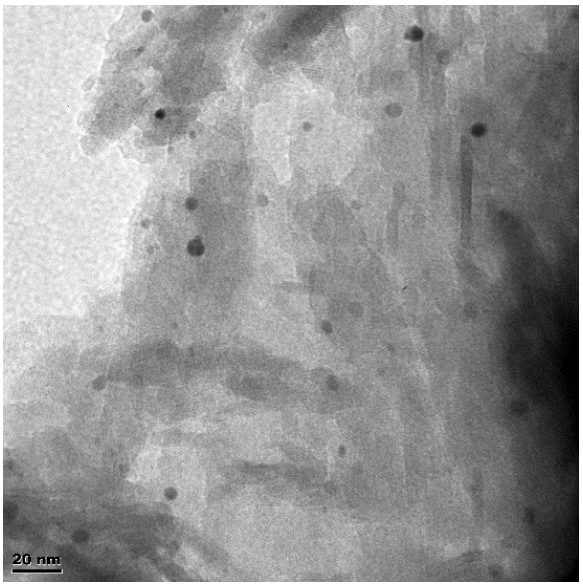

Figure A18: TEM micrograph of Pt/H-NS-6-75a.

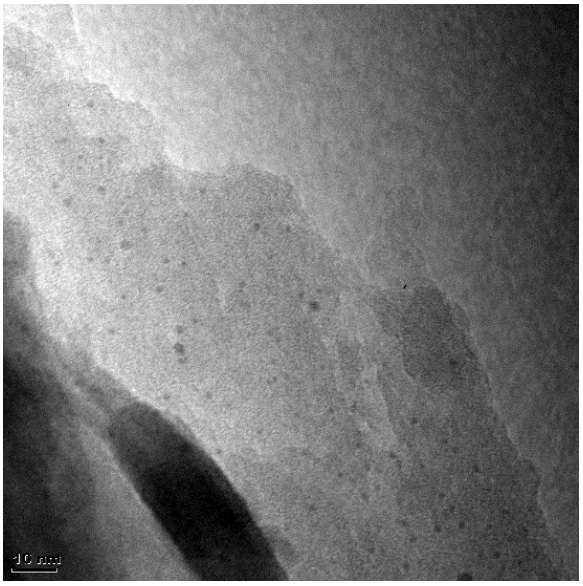

Figure A19: TEM micrograph of Pt/H-NS-6-100a.

A 2.3. CO Chemisorption

A 2.3.1. Pt-H/C-NS-3-ya

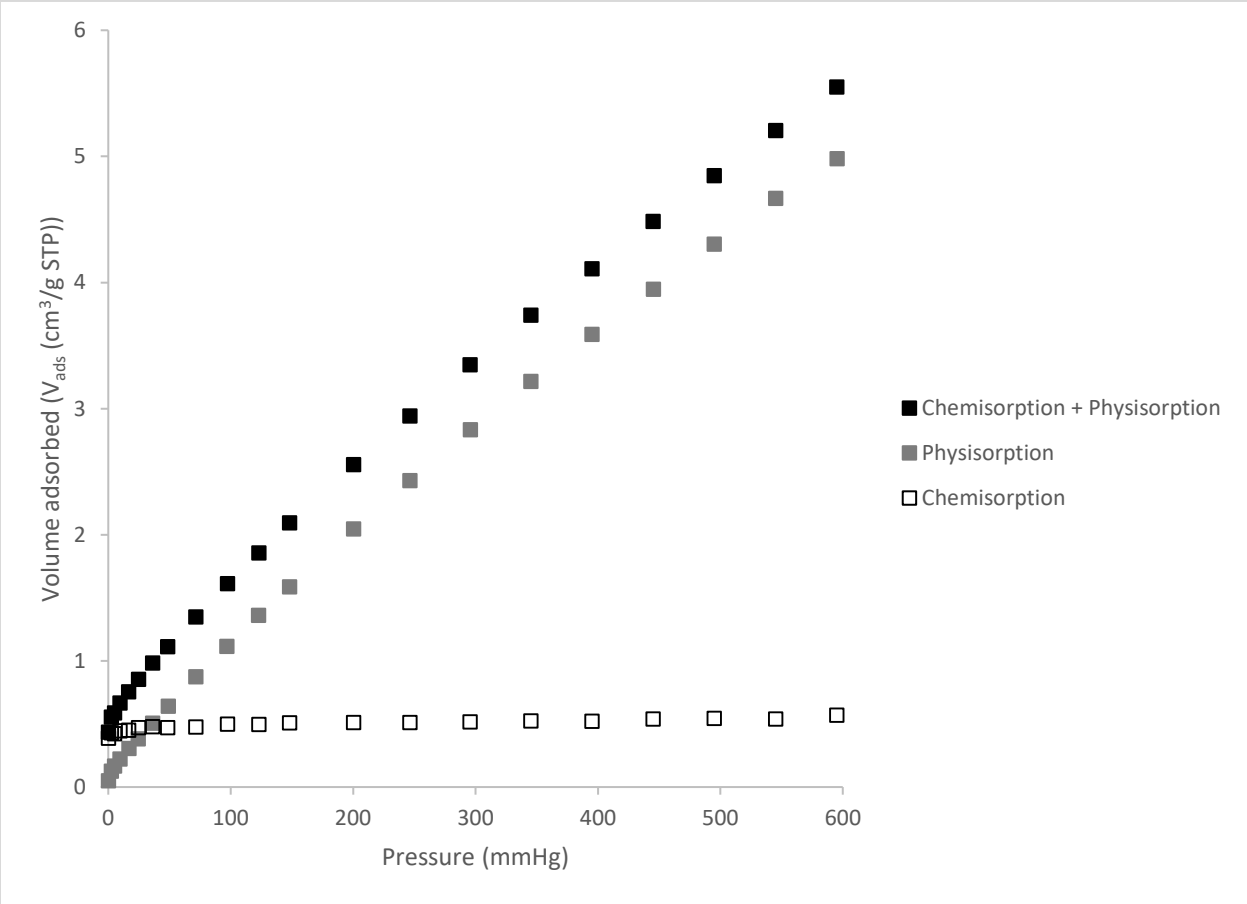

Figure A20: CO Chemisorption on Pt-H/C-NS-3-25a.

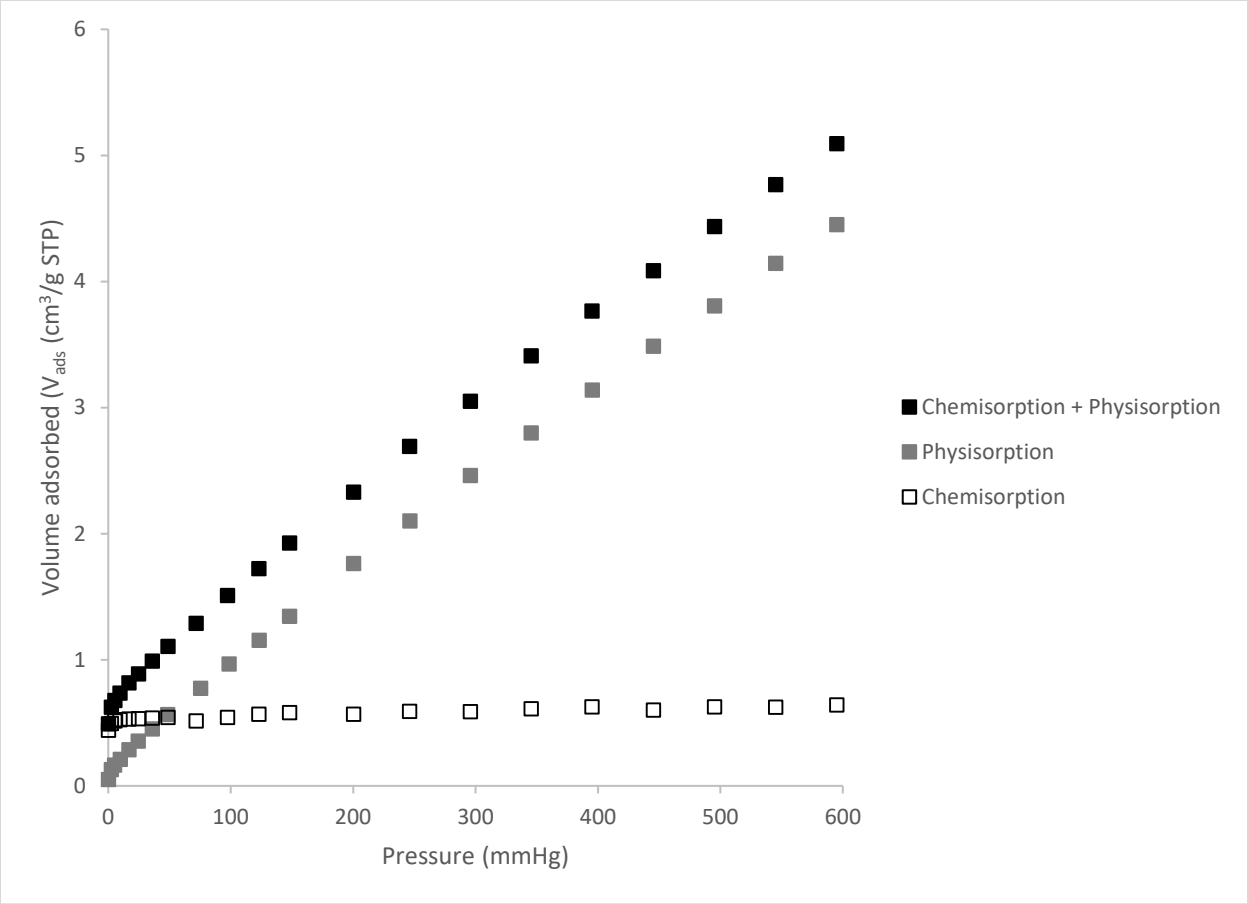

Figure A21: CO Chemisorption on Pt-H/C-NS-3-50a.

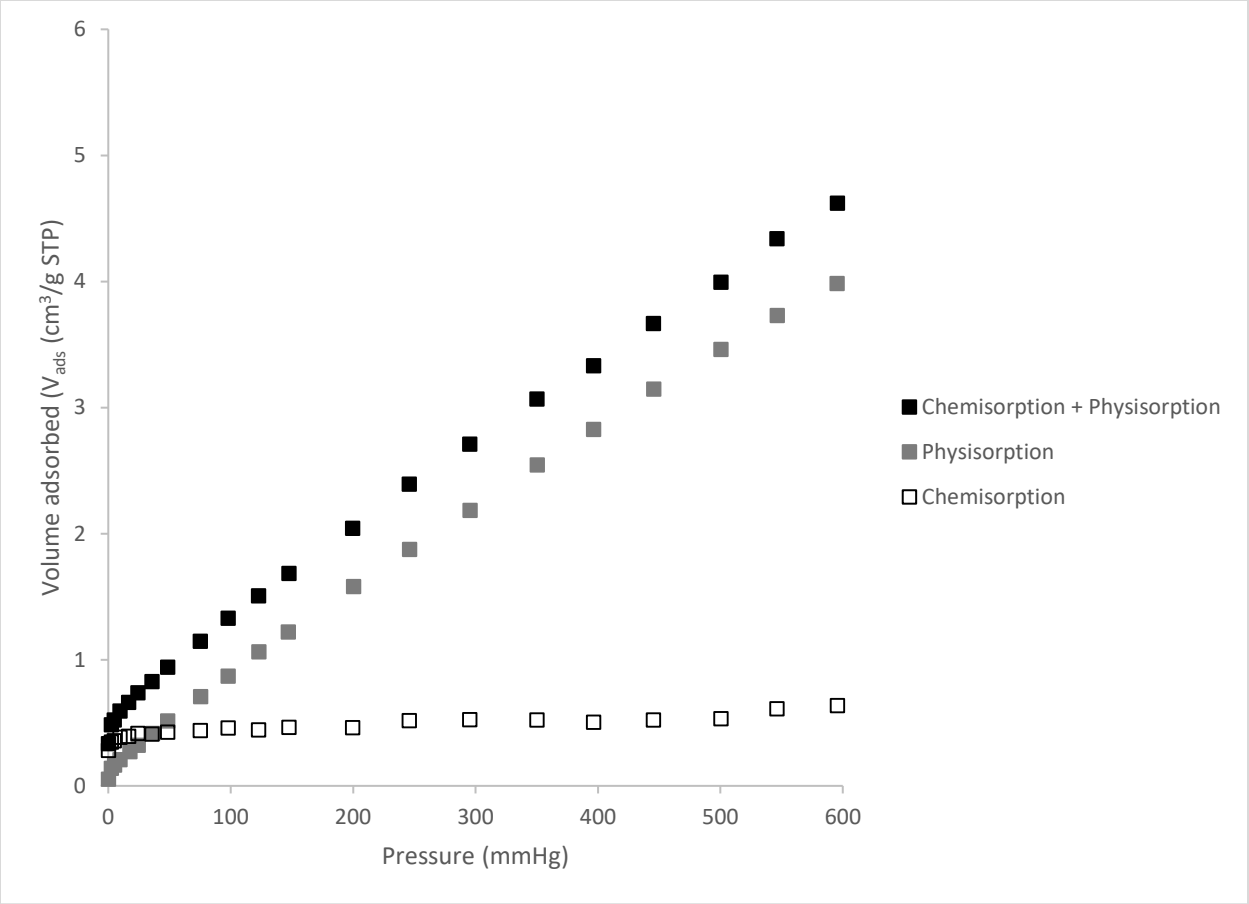

Figure A22: CO Chemisorption on Pt-H/C-NS-3-75a.

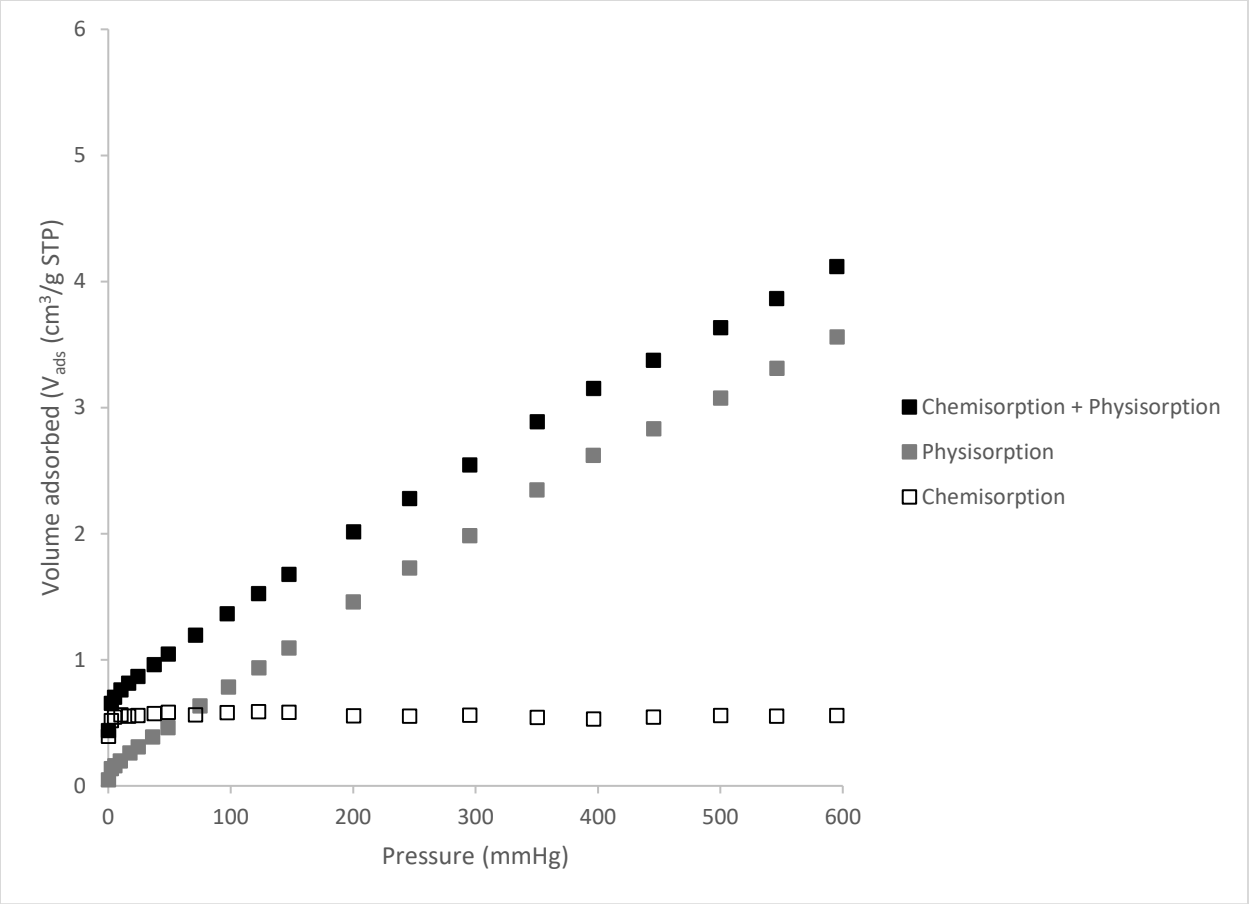

Figure A23: CO Chemisorption on Pt-H/C-NS-3-100a.

A 2.3.2. Pt-H/Na-NS-6-yb

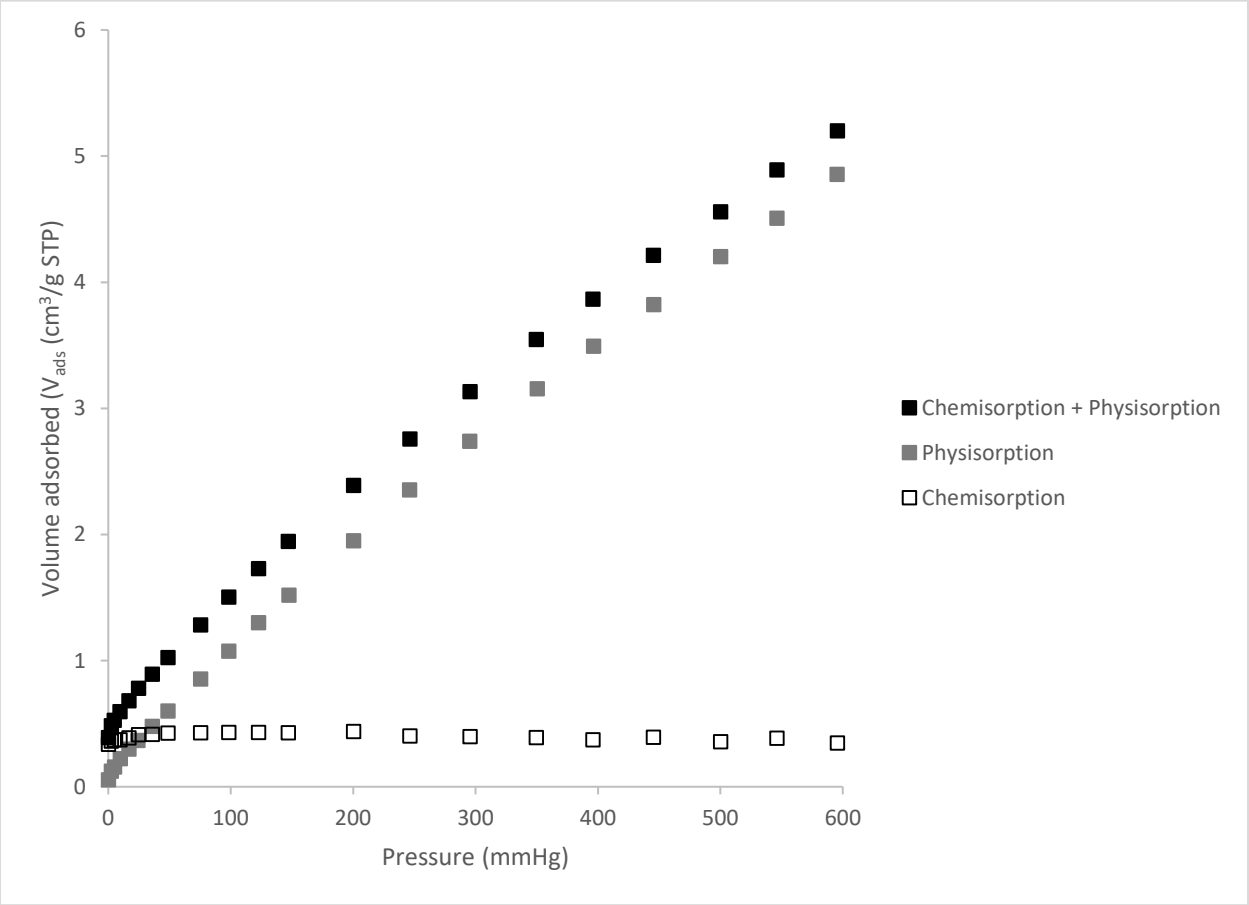

Figure A24: CO Chemisorption on Pt-H/Na-NS-6-25b.

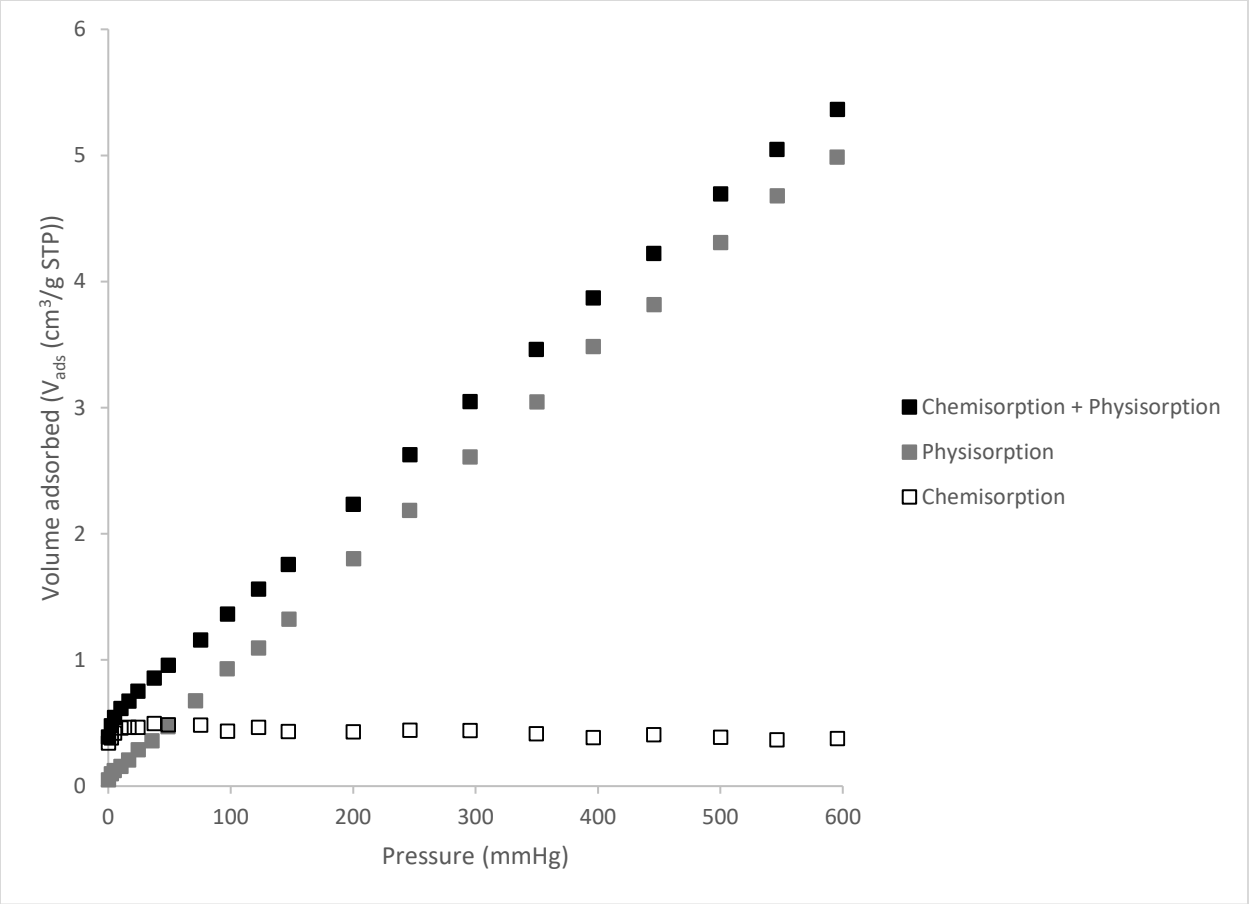

Figure A25: CO Chemisorption on Pt-H/Na-NS-6-50b.

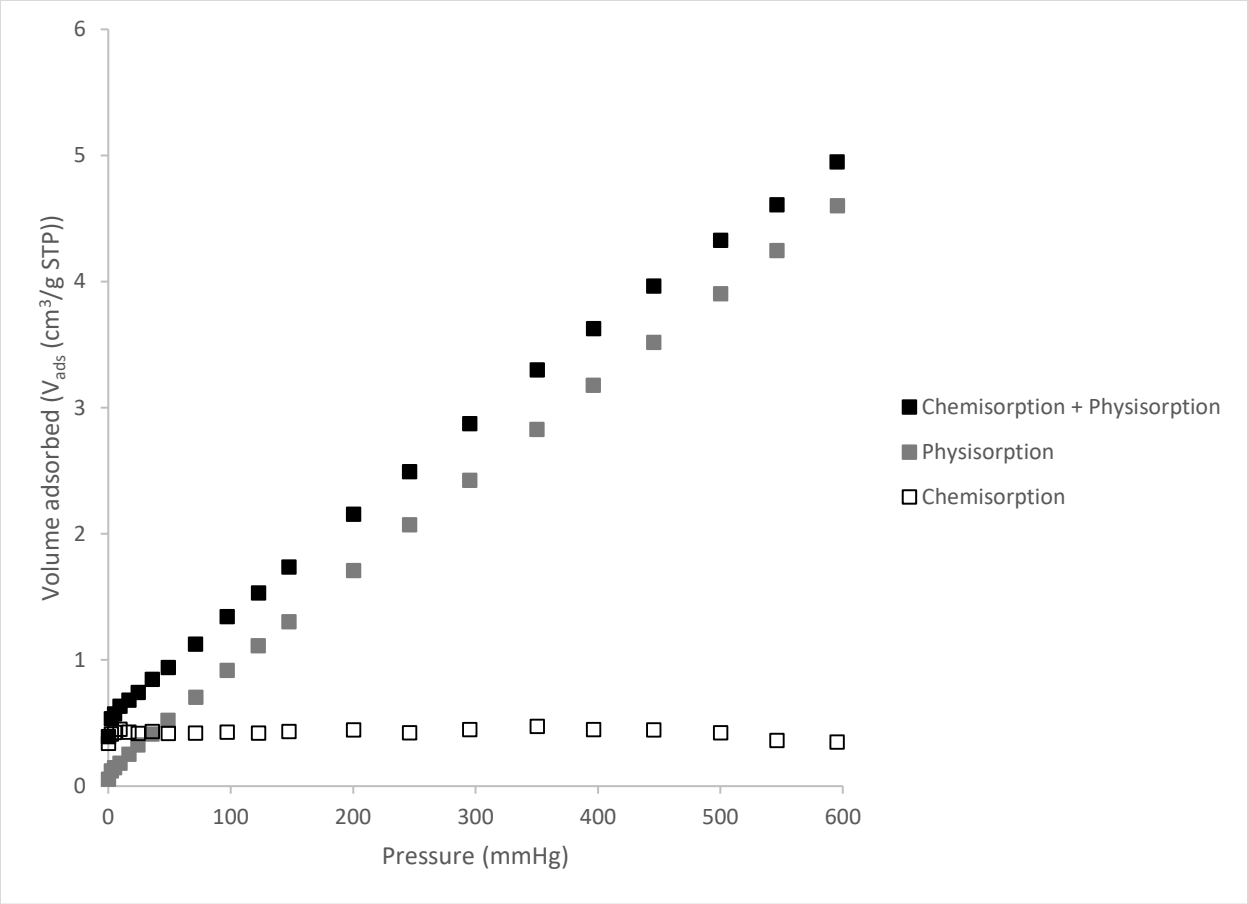

Figure A26: CO Chemisorption on Pt-H/Na-NS-6-75b.

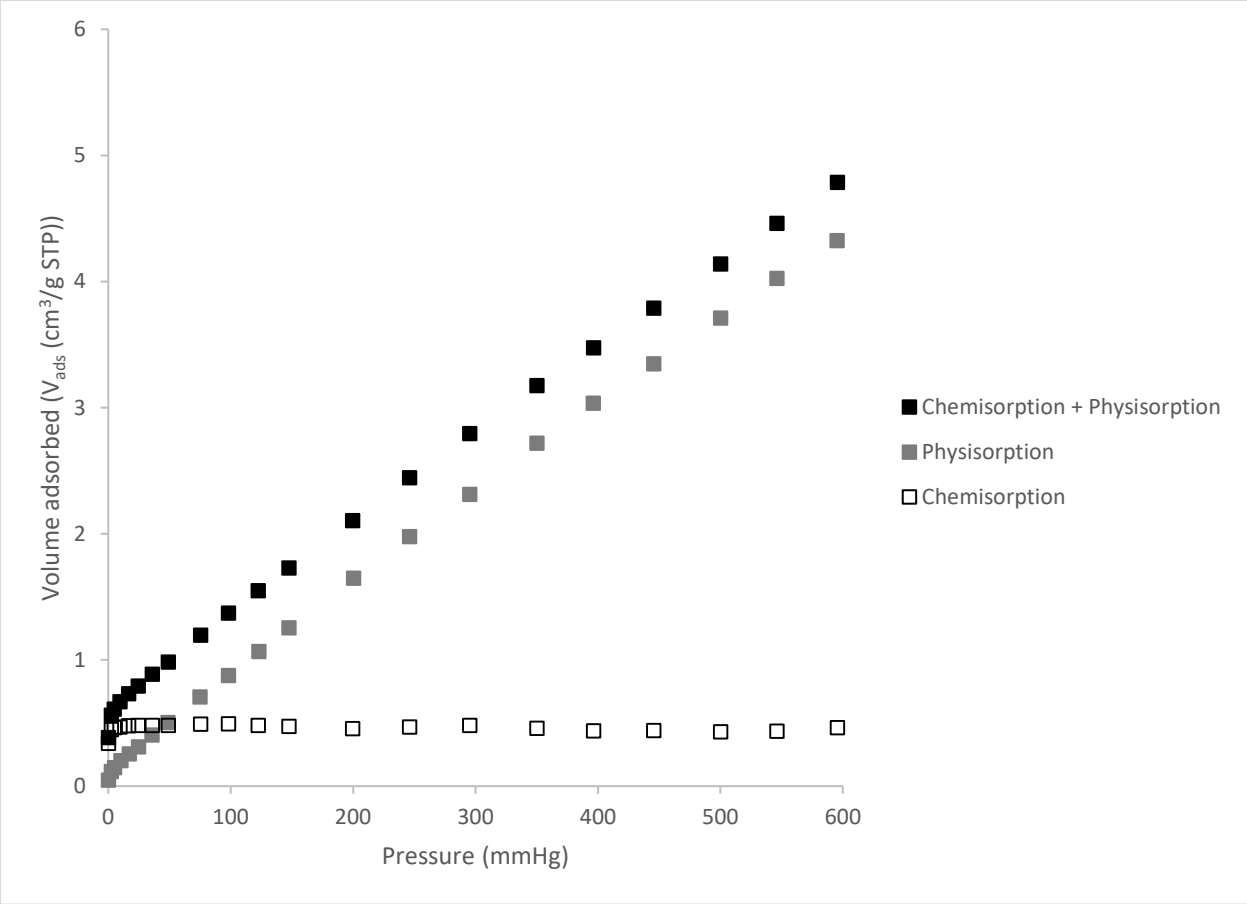

Figure A27: CO Chemisorption on Pt-H/Na-NS-6-100b.

Appendix 3: Hydrocracking of n-C_{16}

A 3.1. Pt/H-NS-6-ya

A 3.1.1. n-C_{16} Conversion vs. Temperature

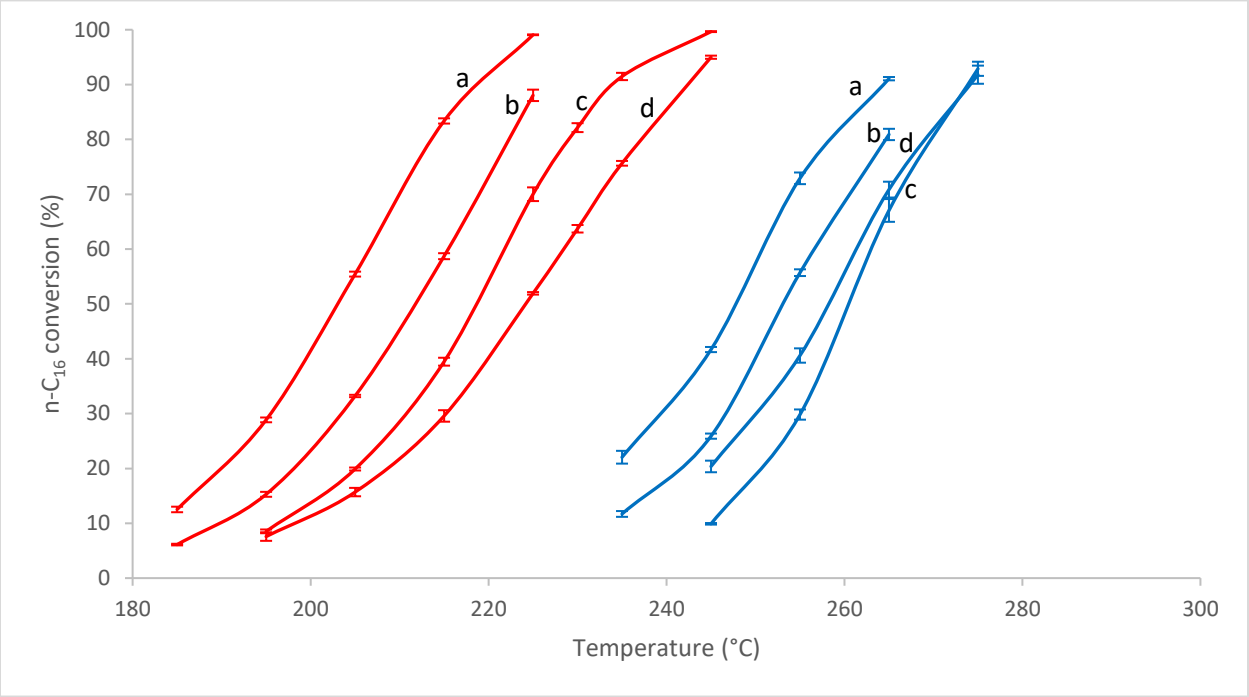

Figure A28: n-C_{16} conversion versus temperature plot for n-C_{16} hydrocracking in the absence (red) and presence (blue) of H_2O over (a) Pt/H-NS-6-25a, (b) Pt/H-NS-6-50a, (c) Pt/H-NS-6-75a and (d) Pt/H-NS-6-100a (0.9 wt% Pt via IWI, 20 bar, W/F = 875 kg s/mol, H_2/n-C_{16} = 10 mol/mol, H_2O/n-C_{16} = 0.8 v/v). Error bars for conversion are shown at each temperature for each catalyst.

A 3.1.2. Yields of Isomerization and Cracking Products

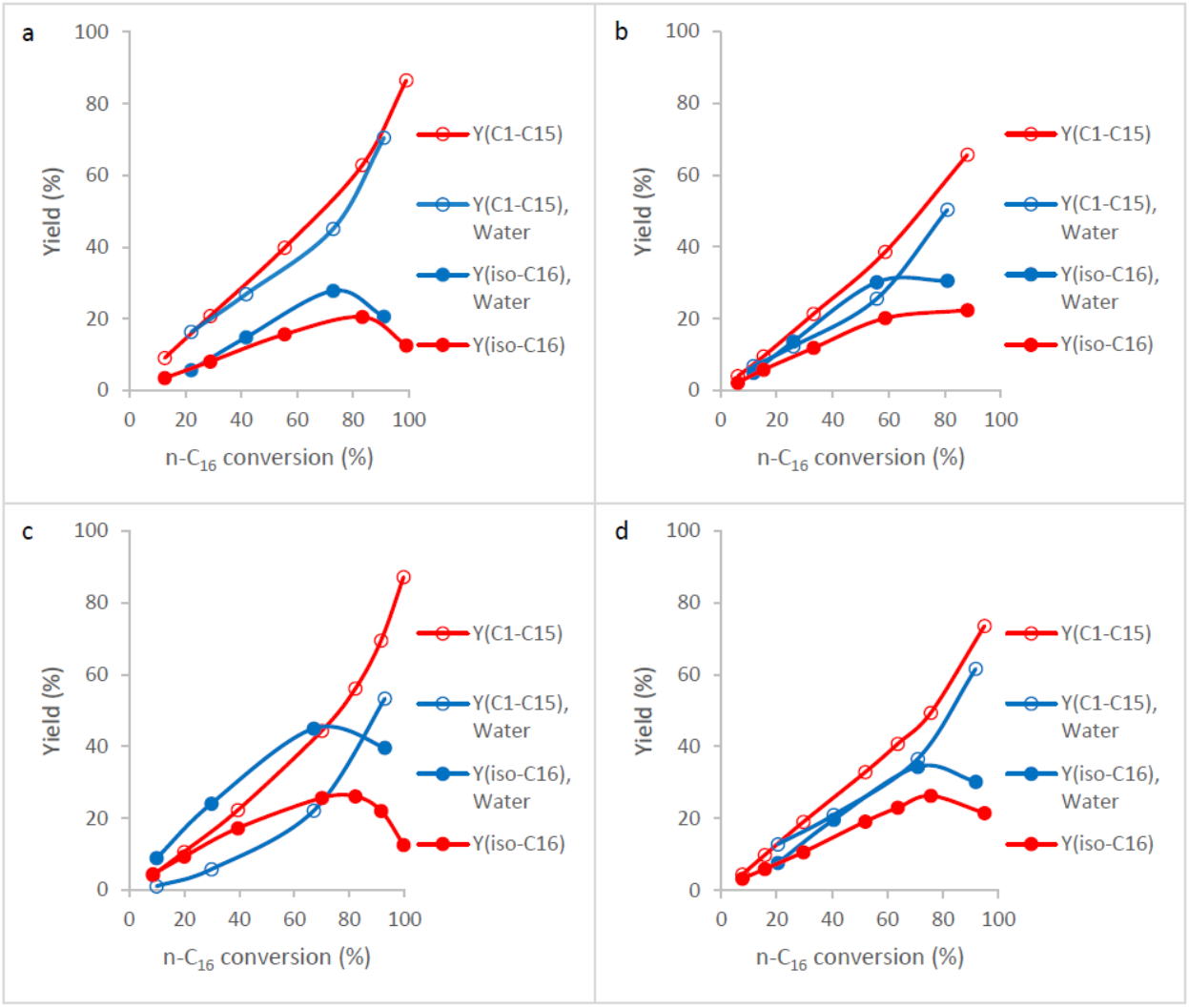

Figure A29: Yields of isomerization (Y(iso-C_{16})) and cracking products (Y(C_1-C_{15})) against n-C_{16} conversion in the absence (red) and presence (blue) of H_2O over (a) Pt/H-NS-6-25a, (b) Pt/H-NS-6-50a, (c) Pt/H-NS-6-75a and (d) Pt/H-NS-6-100a.

A 3.2. Pt-H/C-NS-3-ya

A 3.2.1. n-C_{16} Conversion vs. Temperature

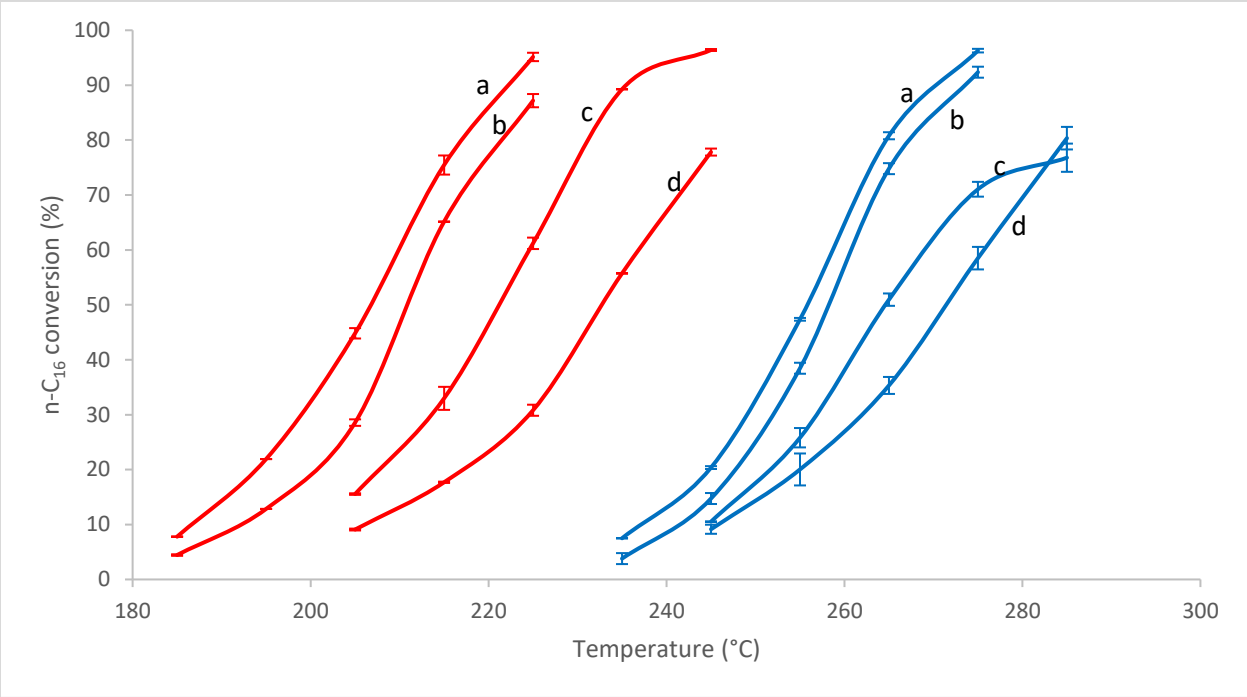

Figure A30: n-C_{16} conversion versus temperature plot for n-C_{16} hydrocracking in the absence (red) and presence (blue) of H_2O over (a) Pt-H/C-NS-3-25a, (b) Pt-H/C-NS-3-50a, (c) Pt-H/C-NS-3-75a and (d) Pt-H/C-NS-3-100a (1 wt% Pt via CIE, 20 bar, W/F = 875 kg s/mol, H_2/n-C_{16} = 10 mol/mol, H_2O/n-C_{16} = 0.8 v/v). Error bars for conversion are shown at each temperature for each catalyst.

A 3.2.2. Yields of Isomerization and Cracking Products

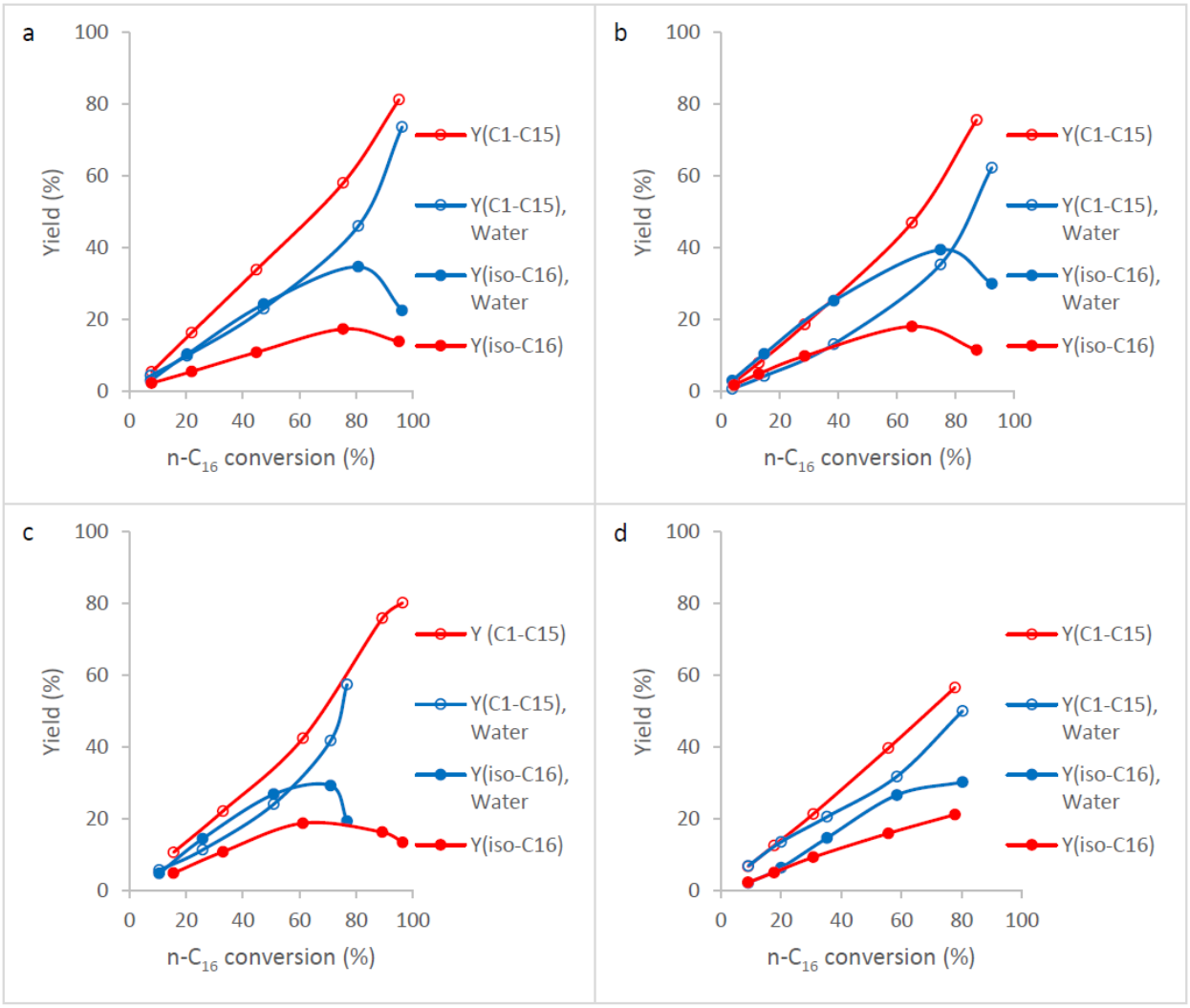

Figure A31: Yields of isomerization (Y(iso-C16)) and cracking products (Y(C1-C15)) against n-C_{16} conversion in the absence (red) and presence (blue) of H_2O over (a) Pt-H/C-NS-3-25a, (b) Pt-H/C-NS-3-50a, (c) Pt-H/C-NS-3-75a and (d) Pt-H/C-NS-3-100a.

A 3.3. Pt-H/Na-NS-6-yb

A 3.3.1. n-C_{16} Conversion vs. Temperature

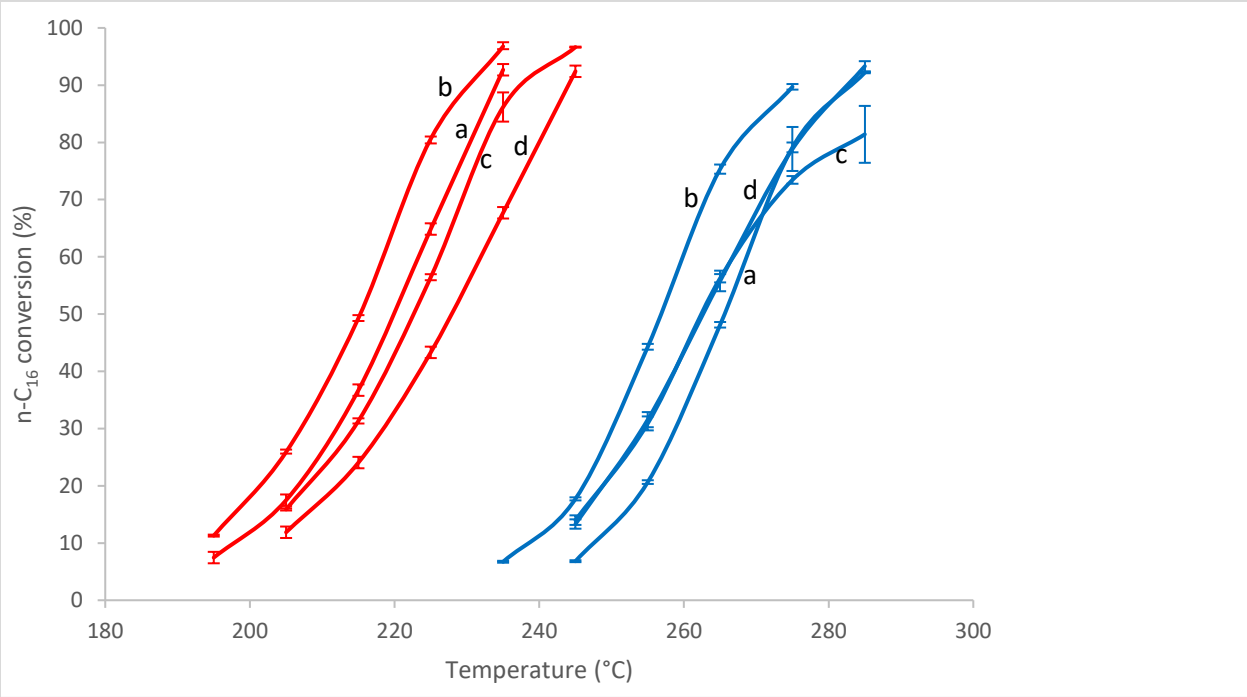

Figure A32: n-C_{16} conversion versus temperature plot for n-C_{16} hydrocracking in the absence (red) and presence (blue) of H_2O over (a) Pt-H/Na-NS-6-25b, (b) Pt-H/Na-NS-6-50b, (c) Pt-H/Na-NS-6-75b and (d) Pt-H/Na-NS-6-100b (1 wt% Pt via CIE, 20 bar, W/F = 875 kg s/mol, H_2/n-C_{16} = 10 mol/mol, H_2O/n-C_{16} = 0.8 v/v). Error bars for conversion are shown at each temperature for each catalyst.

A 3.3.2. Yields of Isomerization and Cracking Products

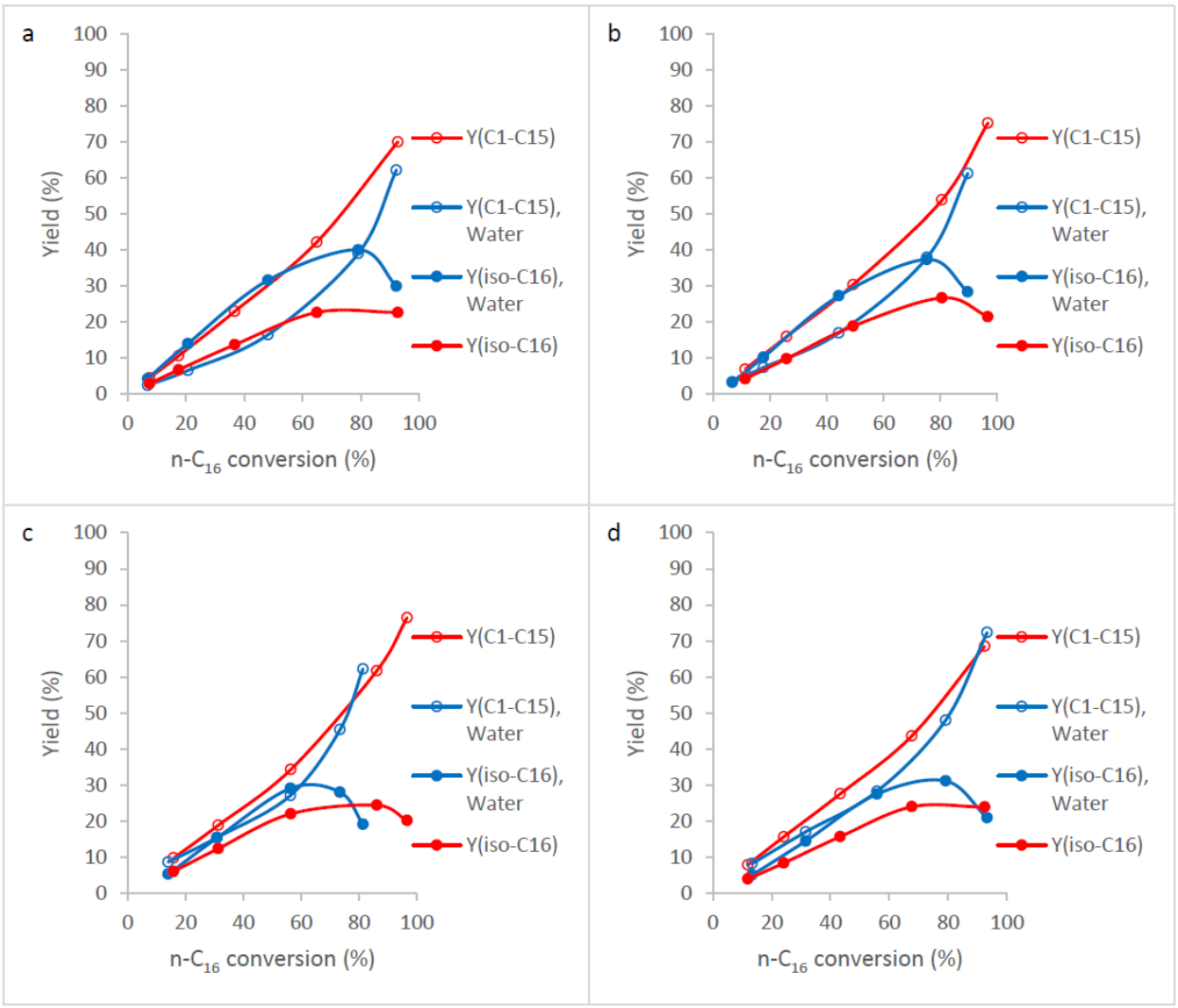

Figure A33: Yields of isomerization (Y(iso-C16)) and cracking products (Y(C1-C15)) against n-C_{16} conversion in the absence (red) and presence (blue) of H_2O over (a) Pt-H/Na-NS-6-25b, (b) Pt-H/Na-NS-6-50b, (c) Pt-H/Na-NS-6-75b and (d) Pt-H/Na-NS-6-100b.